Investigation of Immature Cu,Zn Superoxide Dismutase 1 Using Variable Temperature NMR

by

Jeffrey Alexander Palumbo

A thesis
presented to the University of Waterloo
in fulfillment of the
thesis requirement for the degree of
Master of Science
in
Chemistry

Waterloo, Ontario, Canada, 2020

AUTHOR'S DECLARATION

I hereby declare that I am the sole author of this thesis. This is a true copy of the thesis, including any required final revisions, as accepted by my examiners.

I understand that my thesis may be made electronically available to the public.

Abstract

Amyotrophic lateral sclerosis (ALS) is an adult onset neurodegenerative disease that results in the death of motor neurons in the spinal cord, cortex, and brain stem. The vast majority of ALS cases arise sporadically, but a small subset, fewer than 10%, acquire the disease through a hereditary mechanism, termed familial ALS (fALS). Clinical studies suggest that nearly 20% of fALS patients share mutations in the protein Cu,Zn superoxide dismutase (SOD1), an enzyme that scavenges superoxide radicals. SOD1 adopts a homodimeric β-barrel structure that contains a conserved disulfide bond and binds one structural zinc and one catalytic copper ion per monomer. Currently, there are 187 mutations known to be associated with fALS. These mutations are located in structurally and functionally important regions of the protein. It is accepted that these mutations result in a gain of toxic function that leads to the formation of protein aggregates, containing mature (holo) and immature SOD1. Protein aggregation has been observed in a number of other neurodegenerative diseases, such as Alzheimer's, Huntington's and Parkinson's disease. This thesis explores the effects of specific mutations on SOD1 folding and misfolding, using biomolecular NMR methods that provide structural information at a resolution of individual amino acid residues.

To achieve this goal, variable-temperature NMR, a well-established method that allows the correlation of protein structural stability with temperature, experiments were performed on a variety of SOD1 mutants. Specifically, amide proton (^{1}H) temperature coefficients serve as indicators of hydrogen bonding and provide valuable information on local unfolding events occurring within a protein. With the most immature form (apo2SH) of SOD1, mutant residues cause changes in temperature coefficients mostly within their own vicinity and provide insight into the disrupted processes observed in mutant SOD1. As SOD1 matures, the majority of residues experience a significant increase in structural stability, most notably following the binding of zinc.

To date, amide nitrogen (^{15}N) temperature coefficients have shown no discernable patterns, and therefore, their uses in structural interpretations have been limited. To determine their usefulness, ^{15}N temperature coefficients must be referenced to random coil, removing

their sequence-dependence. These referenced ^{15}N temperature coefficients are extremely sensitive to deviations from random coil and are useful for reporting on local structure. Similarly, secondary chemical shifts also report on local secondary structure. The structural data obtained with these methods agree well with those from crystallography. During SOD1 maturation, there is a widespread increase in structure; however, a small subset of hydrophobic residues in the dimer interface and core of the protein show decreased order. These residues may be reporting on either conformational strain or an altered packing structure that results from dimerization.

Curved temperature dependences report on the excursion of a residue to an excited state. The changes in curvature patterns in mutant SOD1 report on the structural and functional disruptions associated with the respective mutations. With native SOD1, maturation is accompanied by curvature decreases throughout the protein, notably in structurally and functionally important sites. In contrast, during the maturation of mutant SOD1 there are curvature increases through structurally important sites, identifying regions of the structure as dynamic hotspots that may be involved in aggregation. Additional curvature experiments determine that near the T_m of a protein there is a sharp increase in curvature, likely reporting on the onset of a global unfolding event.

Lastly, isoelectric focusing is an electrophoretic method that separates proteins by their isoelectric points (pI) and is used to determine a protein's diffusion coefficient. This method may be useful as a diagnostic tool for determining the mutant SOD1 and maturation states in patient samples. From experiments on various forms of purified SOD1, it is determined that the pI of SOD1 decreases as it matures, SOD1 is likely in a dimeric form during the experiments, and all SOD1 expressed in the wildtype (WT) background aggregated during focusing, likely as a result of the free cysteines in WT SOD1. From these studies, it appears that this method is likely not well-suited for studying the SOD1 present in patient samples.

Acknowledgements

I would like to thank all of the members of the Meiering Lab, past and present, for all of the help and training required to perform these studies. I especially would like to thank Dr. Kyle Trainor and Dr. Victor Galievsky for creating many of the programs and scripts used to analyze my data, without your help and guidance this project would have been in no way completed within two years. I would also like to thank other members of the Department of Chemistry who have helped in various capacities in the completion of this degree. These people include, but are not limited to, Jan Venne, Cathy Van Esch, David Beriashvili, Dr. Carol Tanner, and the members of my committee, Prof. Dieckmann and Prof. Palmer.

Lastly, I would like to thank and extend my heart-felt appreciation to my supervisor, Prof. Elizabeth Meiering, for allowing me to undertake these research endeavors, along with all of her advice and direction when I got stuck, for helping me to grow as both a scientist and person, and most importantly, for all of her encouragement and understanding during rough times.

Dedication

To my amazing family that I could always count on for advice, my ever-loving and supportive fiancée Jasmine, and all of my friends who have supported me over the years and have listened to me talk about everything under the sun for hours.

Table of Contents

List of Figures

List of Tables

List of Abbreviations

1D - one-dimensional

2D - two dimensional

3D - three-dimensional

ALS - Amyotrophic Lateral Sclerosis

apo2SH SOD1 - Disulfide reduced apo superoxide dismutase

CARA - Computer Aided Resonance Assignment

CCS - Copper chaperone for superoxide dismutase

CEST - ^{15}N chemical exchange saturation transfer

CIEF - Capillary Isoelectric Focusing

CPMG - ^{15}N Carr–Purcell–Meiboom–Gil

D - Diffusion Coefficient

DSS - 4,4-Dimethyl-4-silapentane-1-sulfonic acid

DTT - Dithiothreitol

E,Zn2SH SOD1 - Disulfide reduced one-zinc bound superoxide dismutase

fALS - Familial amyotrophic lateral sclerosis

FID - Free Induction Decay

HEPES - 4-(2-hydroxyethyl)-1-piperazineethanesulfonic acid

holo SOD1 - mature copper/zinc superoxide dismutase

HSQC - Heteronuclear single-quantum coherence correlation spectrum

IDPs - Intrinsically disordered proteins

LB - Luria broth

NMR - Nuclear magnetic resonance

NOESY - Nuclear Overhauser Effect Spectroscopy

Omp - Outer membrane protein

PD - Parkinson’s disease

pI - Isoelectric point

pWT - Pseudo-wildtype

SOD1 - Superoxide Dismutase 1

SUP - Cell supernatant

TCEP HCl - Tris (2- carboxyethyl) phosphine hydrochloride

T_m - Melting temperature

WCID - Whole-column imaging detection

WT - Wildtype

Chapter 1
Introduction

1.1 Protein Folding and Misfolding

Proteins are one of the four major classes of biological molecules that are required for life and cellular homeostasis, along with lipids, nucleic acids, and polysaccharides.[1] Of the classes listed, proteins may have the most diverse set of functions. For example, there are proteins involved in cell-to-cell signaling, structural proteins that maintain cell shape, and enzymes that catalyze biochemical reactions. The functions of any given protein are directly dependent on its complex three-dimensional structures. Despite proteins consisting of unique combinations of 20 amino acids, there are a large variety of protein structures found throughout the biological world.[1,2] Although we know that a protein's activity is regulated by its structure, it is not fully understood how living organisms control the protein folding process.[3–5]

1.1.1 Protein Folding Theory

In order for a protein to reach its fully functional native state, it must undergo a series of conformational changes known as protein folding. There is a hierarchy of complex structures that are sampled during folding.[1] The simplest description of a protein is the primary structure, which is the amino acid sequence of the polypeptide. This sequence of amino acids contains detailed information that directs the protein to fold into its native state.[2,3,6] The conclusion that a protein's primary sequence contains the information required for correct folding and self-assembly is based on Anfinsen's work in 1973, which demonstrated that ribonuclease can be reversibly denatured and renatured *in vitro*.[3]

Even though the information needed for a protein to fold correctly is contained within the amino acid sequence, the process of protein folding is complex and not completely understood.[4,6,7] Initially, there were a handful of theories on how protein folding occurred. The first theory is the "framework model", which postulates that the folding of a protein is directed down one or a few stepwise pathways with defined structural intermediates.[8,9] For example, the secondary structure of a protein would be formed early in the folding process and then interactions would occur between local structural elements, allowing the protein to assemble

into its tertiary structure.[8] The second theory is called the "diffusion-collision-adhesion model". This model suggests that segments of the unfolded protein chain fold independently into unstable microdomains that are able to diffuse and collide with each other. When several of these microdomains collide, they can fuse together and form a structural element found in the native protein.[10] Similarly, a third theory, known as the "jigsaw-puzzle model", suggests that the protein's tertiary structural elements are able to form without complete formation of the secondary structures. The folded protein can then be "pieced" together using these pre-formed structures.[11] The fourth theory is the hydrophobic collapse model, also known as the "cluster model", which proposes that protein folding is driven by the collapse of the nonpolar hydrophobic residues into the interior of the protein, inaccessible to water.[12] Following the hydrophobic collapse, the secondary structural elements of the protein are then able to form.[12] This theory is similar to the hybrid model, which suggests that the hydrophobic collapse can occur simultaneously with the folding of the secondary structural elements.[13]

A combination of these models has more recently led to the energy landscape model, which has come to be widely accepted. This theory approaches protein folding in terms of an "energy funnel" and is based on the idea that a protein has a minimum Gibbs free energy in its native conformation, located at the bottom of the "funnel" (Figure 1.1).[1–3,14] Initially, when a protein is unfolded, it has a high Gibbs free energy and is able to access a vast number of conformations, depicted by a broad top of the energy funnel. As the protein folds, it finds and retains energy-lowering favourable interactions, becomes more ordered, and accesses less conformations.[2,6] It is important to note that there is no unique pathway that alone leads to the native state, but instead, a large number of pathways that converge as the protein folds.[14,15]

In many cases, protein folding can be thought of as a two-state kinetic process; however more complex proteins can exhibit multi-state kinetics. In two state kinetics, the two states are the native state and the unfolded state, which encompasses all unfolded and intermediate states.[14,16] As the protein transitions from its unfolded state to native state, it encounters numerous free energy barriers that create many local energy minima that a protein can become momentarily trapped in. When proteins encounter these barriers, they need to acquire enough thermal energy to overcome the local maxima and continue the folding process.[2,6] The energy

landscape of each protein is unique and reflects the complexity of the folding process. For example, the native state of flexible proteins tend to exist in a conformational ensemble and, while still having a relatively deep folding funnel, have a series of minima close together at the bottom of the funnel with small energy barriers separating them. On the other hand, the native state of rigid proteins tend to have a deep and smooth minima, when compared to the rest of the folding funnel.[14] In contrast to the deep funnel observed for well-structured proteins, the folding funnels of intrinsically disordered proteins (IDPs) are relatively flat and highly rugged. This is due to the fact that IDPs do not fold into a specific structure.[17]

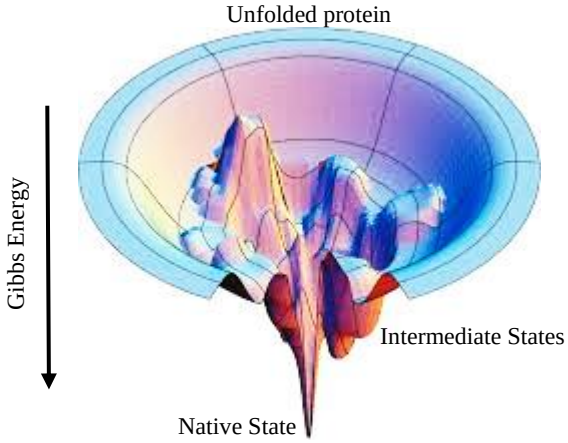

Figure 1.1: The Energy Landscape Model. This figure illustrates a potential energy landscape for a folding protein. The unfolded protein is shown to be able to access a large number of conformations, which decreases as the protein folds. Also, as the protein folds, the energy of the system decreases and reached a minimum when the protein is in its native conformation. Figure adapted from Voet & Voet.[1]

One important feature that is specific to every protein and heavily influences its ability to fold, is its melting temperature (T_m) of the protein. At the T_m, both the native and unfolded states have equal populations, and below this temperature, the native state is more thermodynamically favourable. Conversely, at temperatures above the T_m, the unfolded state becomes increasingly more favourable, which could potentially result in non-native interactions and protein misfolding.[14,18]

1.1.2 Protein Misfolding and Aggregation

Given that protein folding is a complex process with numerous conformations accessible at every step in the pathway, there is a probability for a protein to misfold and assume a non-native structure. Misfolding can arise from a myriad of causes, including mutations to the amino acid sequence of the protein and changes in the cell environment.[19] Also, along its path down the energy landscape funnel described in Section 1.1.1, a protein may encounter a large energy barrier and can become trapped in the associated intermediate state for a longer period of time, which may promote the acquisition of non-native interactions with other partially folded intermediates.[14] If these non-native interactions repeatedly occur and persist, they may stimulate the formation of protein aggregates (Figure 1.2).[19–22]

The structures of protein aggregates are largely dependent on the cellular environment and the specific proteins that make up the aggregate. Therefore, protein aggregates can be soluble or insoluble and are present in a variety of shapes and sizes, such as insoluble amyloid fibrils and large amorphous aggregates.[21,22] One mechanism that may describe the formation of protein aggregates is the "nucleated-polymerization model". In this model, protein monomers associate to form a soluble oligomer or a nucleus that undergoes a growth via chain polymerization, leading to the formation of an insoluble aggregate.[20] The initial formation of this nucleus is thermodynamically unfavourable; however, once formed, the nucleus facilitates the polymerization process.[22]

One method that cells use to prevent misfolding and aggregation of recently or currently translated proteins, is the use of various molecular chaperone proteins. Molecular chaperones are themselves proteins that bind and stabilize an unstable conformation of a target protein and help it to successfully reach its final form. This could involve helping the target protein to correctly fold, bind cofactors, switch to an active or inactive conformation, or being transported to another region of a cell.[21,23] Another method for controlling protein aggregation in cells uses the ubiquitin-proteasome system to degrade non-functional, misfolded or aggregated proteins. In the case that both methods fail to check the accumulation of protein aggregates cells may resort to autophagy to remove the depositions of proteins. Over time, continued cell death may lead to degenerative disorders, with those associated with aging

usually categorized as "toxic-gain-of-function" disorders.[21,22] In fact, the aggregation of proteins has been linked to several high profile diseases, such as type 2 diabetes, Alzheimer's, Huntington's, and Parkinson's, many of which are neurodegenerative diseases.[21,22,24]

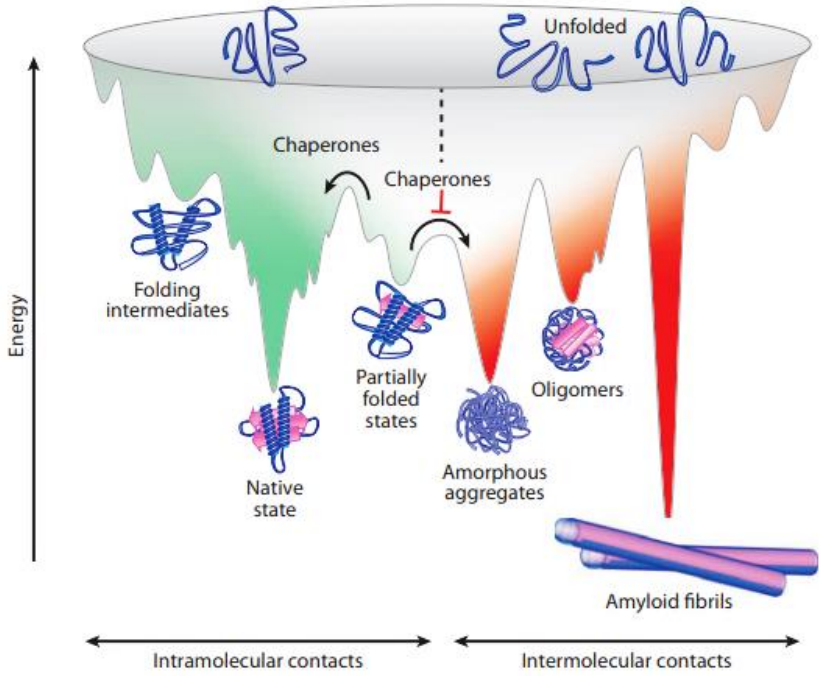

Figure 1.2: Competition Between Protein Folding and Aggregation. Energetically favourable intramolecular interactions help to stabilize the protein as it progresses towards the native state (green). Partially folded intermediates that are trapped in local minima along the rough energy landscape model can either be rescued by chaperones to continue folding towards the native state or form intermolecular interactions that promote aggregation (red). Copyright (2013) with permissions from Annu. Rev. Biochem.[21]

One example of a neurodegenerative disease associated with protein aggregation is Parkinson's disease (PD). Neurodegeneration in patients with PD is associated with the formation of Lewy bodies, intracellular inclusions that contain amyloid fibrils. These fibrils contain aggregated α-synuclein, an intrinsically disordered protein consisting of 140 residues.[24–27] This protein has been shown to aggregate through a two-step polymerization process, in which an oligomeric intermediate serves as a nucleus for elongation into fibrils, and is highly ubiquitinated in the final fibrils. In addition to containing ubiquitinated α-synuclein, inclusions also contain molecular chaperones for α-synuclein, suggesting that cells

containing these inclusions have activated their misfolded protein response and protein degradation pathways.[27] In a study performed by Burmann *et al.*, interactions between molecular chaperones and α-synuclein were investigated both *in vitro* and in cells at the atomic level using nuclear magnetic resonance spectroscopy (NMR) techniques. This study concluded that the molecular chaperones bind to α-synuclein at the N-terminus and the region surrounding Tyr39; however, under oxidative stress, Tyr39 is phosphorylated, which prevents the binding of the molecular chaperones to α-synuclein. This could then lead to α-synuclein aggregation, Lewy body formation, and, eventually, the disease progression of PD.[25]

1.2 Biomolecular NMR

To date, the study of biomolecules, such as proteins and nucleic acids, at atomic resolution has been performed using X-ray crystallography and NMR. More recently, cryo-electron microscopy has emerged as a viable alternative for determining biomolecular structures.[28–30] Of particular use in structural biology are solution state NMR methods. One key advantage NMR methods is their ability to capture the dynamics of protein folding and mobility over various timescales.[29,31–35] This is especially useful in the study of IDPs, which exhibit high flexibility and cannot be studied by crystallography, since IDPs do not adopt a single conformational native state.[32] Another benefit of solution NMR is that protein-protein and protein-ligand interactions can be studied under physiological conditions, as shown in the previous example in Section 1.1.2.[25] Experiments of this nature are also commonly performed in the pharmaceutical industry.[29,34] Despite these advantages, one of the major limitations of solution NMR is that it is limited to systems that are less than approximately 50 kDa.[28,34] This section aims to introduce key NMR concepts, as well as some uses of NMR techniques in protein chemistry and structural biology.

1.2.1 General NMR Background

Nuclear magnetic resonance is a spectroscopic technique that takes advantage of the magnetic spin properties of atomic nuclei. Several nuclei, such as the proton (^{1}H), possess a property called nuclear spin angular momentum. This property is characterized by the nuclear spin quantum number, which can be zero, a half-integer value, or an integer value.[36,37] For

example, the nuclear spin quantum number (I) for ^{1}H and ^{2}H are I=½ and I=1, respectively. One of the requirements for NMR is that the nuclei have nuclear spin, and therefore, nuclei with I=0 are invisible to NMR.[36] Common nuclei used in biomolecular NMR are ^{1}H, ^{13}C, ^{15}N, ^{19}F, and ^{31}P (all I=½), as well as 2H (I=1). The nonzero spin angular momentum that some nuclei possess gives rise to a nuclear magnetic moment (μ). This relationship is defined by:

$$\mu = \gamma I$$

where γ is the gyromagnetic ratio, a characteristic constant of a particular nucleus.[36,38] In addition, nuclei that have a spin number can exist in multiple spin states. For example, ^{1}H has a nuclear spin quantum number of I=½, which can give rise to two different spin states, denoted by the nuclear magnetic quantum number (m_I), of m_I = +½ and m_I = -½. These two states are degenerate, meaning they have the same energy, and can only be distinguished from each other in the presence of an external magnetic field (B_0).[37,38]

In the absence of a magnetic field, the spin states have the same energy and the magnetic moments of the nuclei are randomly oriented. When an external magnetic field is applied, the magnetic moments either align with or against the external magnetic field. The spin state (m_I = +½ or m_I = -½) that aligns with the magnetic field is considered the low-energy ground state, while the other spin state, which is oriented opposite to the external magnetic field, is considered the high-energy excited state. Both of these states have roughly equal populations, with a small excess of nuclei in the ground state.[37–39] The energy separation between the two spin states is proportional to the strength of the magnetic field. In order to excite a spin state from the ground state, energy, in the form of electromagnetic radiation, needs to be applied at a frequency equivalent to the energy gap. This frequency is dependent on the strength of the magnetic field and is commonly known as the Larmor frequency, ω_0, which is determined by the following equation.[36–39]

$$\omega_0 = \gamma B_0$$

When the electromagnetic radiation of the correct energy is applied, some of it is absorbed. This excites transitions from the ground state to the excited state and inverts the relative populations of the ground and excited states. If the electromagnetic radiation is removed, some

of the excited nuclei will relax back to their ground state and emit a frequency equal to that of the absorbed electromagnetic radiation.[38,39] In a pulsed NMR experiment, spins exposed to the static magnetic field are briefly subjected to a pulse that excited some of the spins. After the pulse is finished, the excited states produce an oscillating magnetic field that induces a current in a receiver coil. The current is measured as a function of time to provide the Free Induction Decay, also known as the FID. The FID then undergoes a Fourier transformation, which converts intensities detected as a function of time, to a function of frequency. This provides a traditional one-dimensional (1D) NMR spectrum, with absorption peaks appearing at frequencies equivalent to the energy difference between the ground and excited states of the irradiated nuclei (Figure 1.3).[34,37,38] The frequencies that the absorption peaks correspond to are termed the "chemical shift" (δ) of that specific nucleus. It is important to note that the actual strength of the magnetic field at a nucleus is usually shielded by the presence of the surrounding electrons participating in chemical bonds and is also influenced by the local chemical environment. This results in a slightly different frequency required to excite the nucleus, resulting in a slightly different chemical shift. Therefore, the chemical shift of a nucleus is dependent on the surrounding physicochemical environment.[34,37,40]

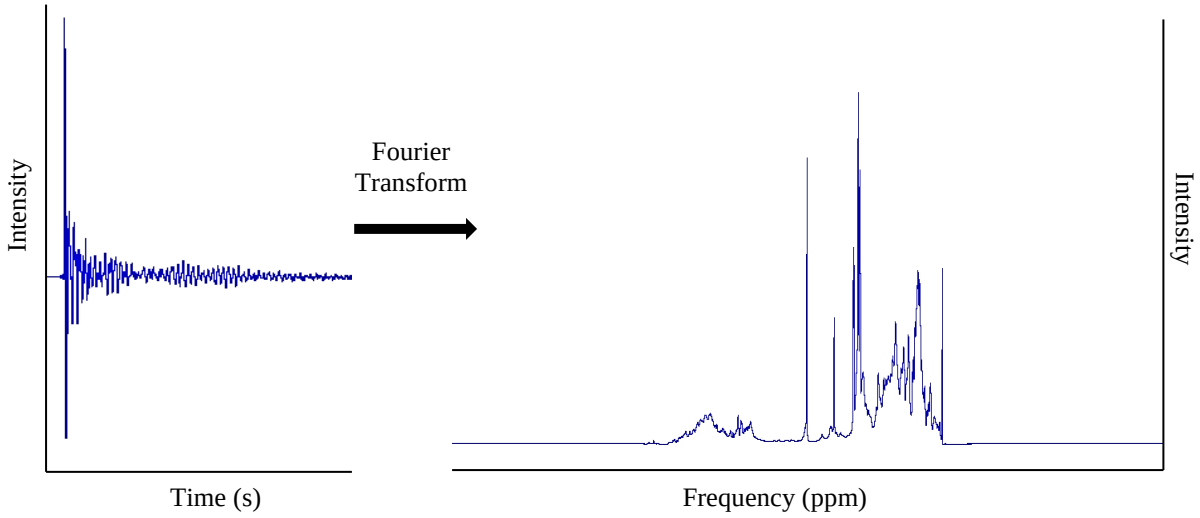

Figure 1.3: FID and Fourier Transformation. This figure illustrates the ^{1}H FID acquired from the NMR on a protein sample (left) and the 1D NMR spectrum following a Fourier Transform (right).

1.2.2 Multi-Dimensional NMR

In some cases, such as the study of proteins and other biomolecules, a 1D NMR spectrum is not as useful for analysis, since there are many nuclei that create NMR signals. This leads to the spectrum becoming crowded with overlapping signals that complicate and prevent spectral analysis. Therefore, the signal must be spread over a second frequency dimension to allow for more detailed analysis. In short, this occurs by the transfer of magnetization through bonds, termed J-coupling, or through space, termed dipole-dipole coupling. [30,36]

Two-dimensional (2D) NMR experiments consist of four basic elements: preparation, evolution, mixing, and detection. In the preparation period, the first spin is excited using electromagnetic radiation. Next, in the evolution period, also known as t_1, the chemical shift of the first state is encoded, due to evolution under a Hamiltonian operator. During this evolution period, t_1 begins at zero and is incrementally increased by a constant amount, with an FID being acquired at each value of t_1. In the next period, the mixing period, the events that occurred during t_1 cause the magnetization of the first spin to be transferred to the second spin. This also results in the transfer of the chemical shift information of the first spin to the second spin. Lastly, in the detection period, t_2, the FID is detected as described in Section 1.2.1.[36,38] A

Fourier transformation of these two time domains yields a 2D NMR spectrum with independent frequency dimensions (Figure 1.4). The first dimension is generated from the Fourier transformation on t_2, termed F_2, and is referred to the direct dimension since it is the dimension that is directly detected using the receiver coil. The second dimension is generated from the Fourier transformation on t_1, termed F_1, which is referred to as the indirect dimension since it is indirectly detected through the transfer of magnetization and chemical shift information to the second spin.[36] In the final spectrum, the Fourier transformation will produce peaks, termed crosspeaks, with the positions (F_2, F_1).[38]

There are many types of 2D NMR spectra, which can either be homonuclear or heteronuclear. In homonuclear methods, the magnetization is transferred between nuclei of the same type. For example, the magnetization of a ^{1}H nucleus can be transferred via J-coupling to other ^{1}H nuclei, up to a few bonds away. Notable 2D NMR experiments that utilize homonuclear methods are the correlation spectroscopy (COSY), which was the first 2D NMR experiment created, and the total correlation spectroscopy (TOCSY).[36–38] Another homonuclear 2D NMR experiment is the nuclear Overhauser effect spectroscopy (NOESY). This experiment utilizes magnetization transfer from one proton to others within a range of roughly 5Å, through cross-relaxation and dipole-dipole coupling, also known as the nuclear Overhauser effect (NOE). This results in spectra that show correlations between nearby nuclei.[36,38,41]

In contrast to homonuclear methods, heteronuclear methods involve the magnetization transfer between two different types of nuclei, such as between ^{1}H and ^{15}N or ^{13}C. There are numerous advantages to heteronuclear NMR methods that are not inherent to homonuclear methods, although homonuclear methods are still highly useful in certain circumstances. For example, the chemical shifts of heteronuclear atoms, such as ^{15}N or ^{13}C, are more dispersed than ^{1}H chemical shifts. Also, with respect to protein NMR, there are 2D experiments that can detect the one-bond coupling between an amide nitrogen and its amide proton or carbonyl carbon, allowing for specific resonance assignments. This is exploited in heteronuclear single quantum correlation (HSQC) experiments. An example of a HSQC experiment would be the ^{1}H-^{15}N HSQC, in which magnetization is transferred, through J-coupling, from a nitrogen

nucleus (t_1) to a proton nucleus (t_2). This results in a spectrum where each crosspeak represents a proton attached a nitrogen atom (Figure 1.4).[38,40]

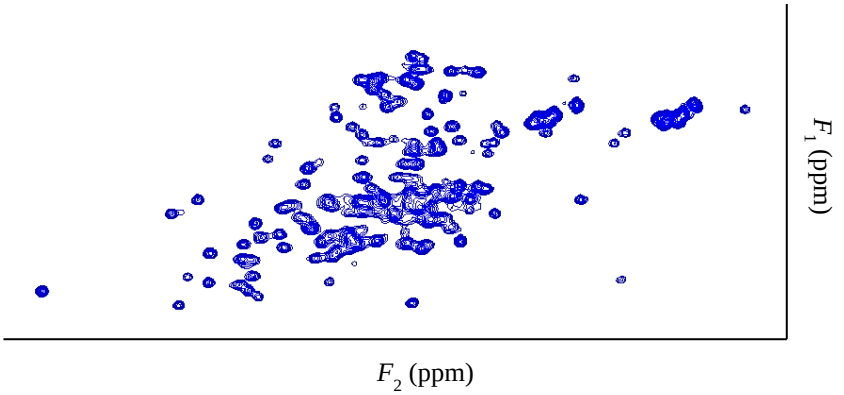

Figure 1.4: 2D NMR Spectrum. The 2D NMR spectrum displayed here is a ^{1}H-^{15}N HSQC with the direct dimension, F_2, representing the ^{1}H dimension and the indirect dimension, F_1, representing the ^{15}N dimension. This spectrum is of the metal-free, disulfide reduced form of pseudo-wildtype Cu,Zn superoxide dismutase 1.

In addition to 2D NMR, there are also three-dimensional (3D) and four-dimensional NMR experiments, though these are almost exclusively used in protein NMR for determining specific resonance assignments of nuclei. These heteronuclear-edited experiments resolve the ^{1}H-^{1}H crosspeaks obtained from a homonuclear experiment, often a NOESY or TOCSY, using the chemical shift of the heteronuclei bonded directly to the ^{1}H spins. A 3D heteronuclear-edited experiment would run a homonuclear experiment, often a NOESY or TOCSY, in combination with a heteronuclear experiment, such as an HSQC. For example, a 3D ^{15}N-edited NOESY-HSQC would consist of a NOESY experiment and a ^{1}H-^{15}N HSQC experiment.[36,38]

1.2.3 Protein NMR

The NMR signals generally used to analyze a protein's structure and dynamics originate from the amide functional group, more specifically the amide protons, within the backbone of the protein. The amide nitrogen and its attached carbonyl group are highly electronegative and attract the nearby electrons, causing the amide proton to become deshielded and shifting its chemical shift downfield; the corresponding region of the 1D NMR spectrum is called the amide region.[40,42] Since the 1D spectrum of a protein is generally too convoluted to analyze, a 2D spectrum is used.[30,36,38] The ^{1}H-^{15}N HSQC, introduced in Section

1.2.3, is one of the more commonly used 2D NMR experiments in protein NMR and generally provides one crosspeak for each directly bonded nitrogen and hydrogen. These crosspeaks mostly correspond to the amide protons found in the polypeptide backbone of a protein; however, proline residues do not appear in this spectrum because they do not contain an amide proton. In addition, some amino acid side chains can be observed in the HSQC spectrum, such as tryptophan, arginine, and glutamine.[29,40,43]

Many studies use the ^{1}H-^{15}N HSQC because the backbone resonances are easily obtained and analyzed; however, in order to interpret the NMR data as molecular information, specific resonance assignments are required. In order to acquire these assignments, 3D NMR experiments are often performed in combination with other 1D and 2D experiments, depending on the focus of the study and the extent of assignments needed. For example, a study aiming to create a 3D structure of a protein from NMR data will require more extensive assignments than a study that only requires the assignments of the protein backbone. Once assigned to their specific amino acid spin systems, the crosspeaks present in a spectrum can be further utilized in other analyses.[29,44,45] It should be noted that it may not be possible to obtain complete resonance assignments for a protein, especially for those undergoing conformational changes.[46]

1.2.4 Chemical Shifts

As mentioned earlier in Section 1.2.1, the chemical shift of a nucleus is dependent on the surrounding physicochemical environment. This means that, in both folded and unfolded proteins, nuclei will be sensitive to the presence of local secondary structure. A residue that lacks a defined local secondary structure is considered to be in random coil.[32,47–49] In the early 1990's Wishart proposed the idea of the secondary chemical shift and chemical shift index to help identify secondary structure elements in a protein.[47,48] The secondary chemical shift (δ_{sec}) is defined as the difference between a residue's experimentally measured chemical shift, originating from a crosspeak on a 2D NMR spectrum, and the random coil chemical shift for that residue. The random coil chemical shifts of residues, to which the experimental values are referenced, have been obtained using a series of short peptides under various experimental

conditions.[32,46,49] Generally, for $^{13}C_\alpha$ secondary chemical shifts, regions within a sequence that have consistent negative values are considered to be in a β-sheet structure, while those with consistent positive values are considered to be in an α-helical structure.[32,50]

Chemical shifts are influenced by protein structure, but also by dynamic processes. When dynamic processes occur, multiple NMR chemical shifts reflect the different environments that a nucleus experiences. If the dynamic process is a slow transition between two distinct states, the NMR will capture two distinct crosspeaks, each one corresponding to their respective state. If the exchange is occurring rapidly, a single crosspeak will be observed at a frequency representing the weighted average of the states. If the transition occurs on a time scale similar to that of the observed spin relaxation events, a single broadened peak would be observed.[45,51] One dynamic process that can make use of the chemical shift information obtained from NMR experiments is ligand binding. Binding studies often use the ^{1}H-^{15}N HSQC, which can detect changes in the backbone amide bonds as a ligand is added. After acquiring the NMR data, the change in amide proton chemical shift for a particular crosspeak can be plotted as a function of ligand concentration to determine the dissociation constant.[45]

1.2.5 The Temperature Dependence of Amide Proton Chemical Shifts

An application that takes advantage of the structural information that chemical shift data from 2D NMR experiments can provide is the temperature dependence of amide proton chemical shifts. As the name suggests, this method requires the acquisition of ^{1}H-^{15}N HSQCs at a series of temperatures and the resonance assignments of the amide proton crosspeaks, which are required to interpret the results (Figure 1.5). The chemical shift data for each assigned peak is then plotted against the temperature range and the slope of the resulting plot is calculated, yielding the temperature dependence of the amide proton chemical shift, termed the temperature coefficient ($\Delta\delta_{NH}/\Delta T$).[52,53]

Temperature coefficients were first described in 1969 by Ohnishi and Urry for the amide protons found in gramicidin S and valinomycin, two naturally occurring peptide antibiotics.[52] In this study, temperature coefficients were thought to be a useful alternative to

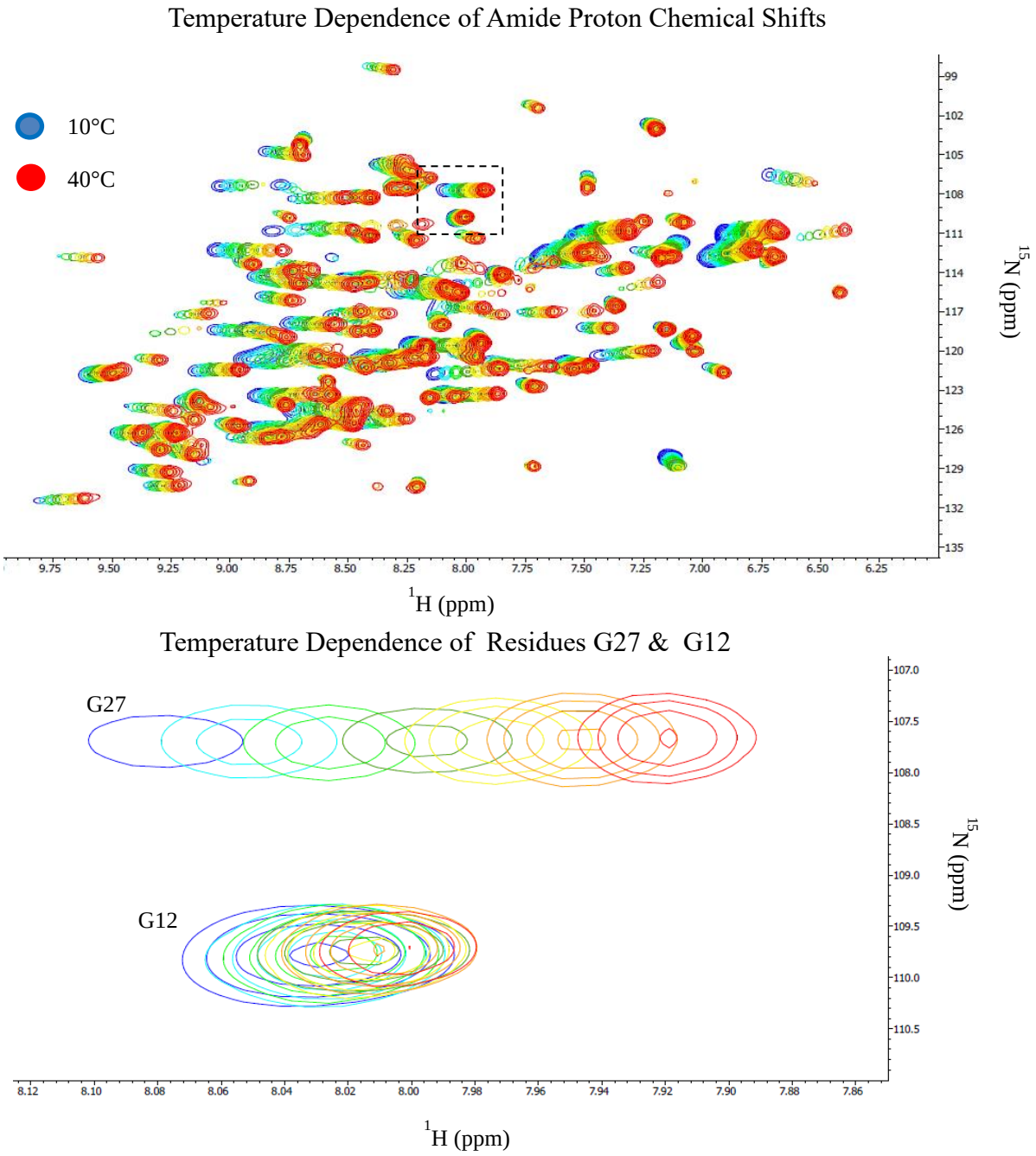

Figure 1.5: The Temperature Dependence of Amide Proton Chemical Shifts. The overlay of ^{1}H-^{15}N HSQCs acquired from 10°C (blue) to 40°C (red) in 2.5°C increments, with select spectra shown for readability. The protein used for these experiments is disulfide-reduced one zinc-bound pseudo-wildtype superoxide dismutase. The second panel shows the change in chemical shifts for two residues with increasing temperature. Overlays were made with Computer Aided Resonance Assignment (CARA) software.[54]

hydrogen/deuterium exchange experiments that determine if an amide proton is hydrogen-bonded or not. They concluded that hydrogen-bonded amide protons have more positive temperature coefficients than those of non-hydrogen-bonded, or solvent accessible, amide protons and that the temperature coefficients of the amide protons may be used to confirm secondary structure.[52] Later, in the late 1980s, one study using temperature coefficients investigated the hydrogen bonding patterns of an unstructured peptide in water and found that most of the unstructured protons have large, negative temperature coefficients. From this, and later experiments on select amide protons, it was determined that large negative temperature coefficients could also be attributed to the significant loss of local secondary structure in peptides upon heating.[55] Typically, amide proton temperature coefficients are linear and negative, reflecting that as temperature increases the chemical shifts move upfield. The explanation of this upfield shift is that as temperature increases, the hydrogen bonds that the amide protons participate in usually weaken and increase in length. The weakening of the hydrogen bonds results in an increasing shift of electron density back towards the nucleus of the amide proton, further shielding the nucleus and causing the chemical shift to move upfield.[53,56,57]

In the 1990s, temperature coefficients started being studied as indicators of hydrogen bonding in globular proteins to determine if temperature coefficients could inform on the increased structure and stability of globular proteins, relative to peptides. Generally, there are two types of hydrogen bonds that amide protons can participate in, intramolecular and intermolecular. In the case of intramolecular hydrogen bonding, the amide protons are bound to carbonyl or other electronegative groups within the protein. Amide protons that do not participate in intramolecular hydrogen bonding are usually solvent-accessible and participate in intermolecular hydrogen bonds with bulk water.[53,56] In a study published in 2001 by Cierpicki & Otlewski, correlations between the temperature coefficients and hydrogen bonds of 793 amide protons, originating from 14 globular proteins, were investigated. They observed that temperature coefficients more positive than -4.6 ppb/K are mainly associated with intramolecular hydrogen bonds, while temperature coefficients more negative than -4.6 ppb/K are most often intermolecularly hydrogen-bound amide protons.[57] This correlation can be

explained as follows: the chemical shifts used to calculate temperature coefficients depend on the inverse third power of the distance between the amide proton and the hydrogen bond acceptor. The more negative temperature coefficients associated with intermolecularly hydrogen-bound amide protons indicate that these hydrogen bond lengths increase more than the hydrogen bonds found in intramolecularly hydrogen-bound amide protons. This matches expectations, since intermolecular hydrogen bonds are generally weaker and are therefore more susceptible to a loss of local structure, resulting in more negative temperature coefficients.[56,57]

In addition to the effect that hydrogen bonding patterns have on temperature coefficients, there are also other factors that determine an amide proton's temperature coefficient. These include, but are not limited to, nearby aromatic side chains and the presence of secondary structure elements. Aromatic side chains exhibit ring currents, which may deshield neighboring amide protons, resulting in more positive temperature coefficients than expected. With respect to the effect that secondary structure may have on the temperature coefficients of amide protons, it has been observed that at the same hydrogen bond length, the temperature coefficients in α-helices are up to 1.2 ppb/K more negative than the temperature coefficients observed in β-sheets. Conversely, hydrogen bonds in α-helices are generally longer than those in β-sheets. This means that the relative increase in length with temperature is less in α-helices, resulting in temperature coefficients more positive than -4.6 ppb/K, on average.[57]

More recently, amide proton temperature coefficients have been interpreted in terms of local protein stability. A study performed by Tomlinson & Williamson in 2012 examined the amide temperature coefficients in the B1 domain of protein G at different pH values. They found that, while intramolecularly hydrogen-bound amide protons had more positive temperature coefficients than intermolecularly hydrogen-bound amide protons, the correlation between the temperature coefficients for amide protons involved in strong hydrogen bonds and hydrogen bond strength was poor. They concluded that amide protons participating in strong hydrogen bonds are generally found in more structured regions of a protein and, therefore, will display more negative observed temperature coefficients as the strong hydrogen bonds are

interrupted and the local structure is disturbed.[58] Regardless of attribution to hydrogen bonding or local structure, temperature coefficients can still provide detailed high-resolution information on local protein structure and stability.

1.2.6 The Temperature Dependence of Amide Nitrogen Chemical Shifts

While temperature coefficients have mostly been reported for amide protons, experiments have been performed on other nuclei present in the protein backbone, namely the amide nitrogens and $C_\alpha H$.[56,58] Currently, even though some amide nitrogen temperature coefficients have been published, there is no consensus as to their interpretation. For example, when measured in the B1 domain of protein G, the ^{15}N temperature coefficients spanned a much larger range than seen in the amide proton temperature coefficients, from approximately -30 to +30 ppb/K. These raw ^{15}N temperature coefficients were found to be very weakly correlated to amide proton temperature coefficients and thought to be uninterpretable.[58] With that said, the factors that affect amide nitrogen temperature coefficients are much more complex than those that affect amide proton temperature coefficients and may need to be considered during analysis for meaningful interpretation.[59–61]

1.2.7 Conformational Heterogeneity

Typically, temperature coefficients are predominately linear; however, some studies have shown the existence of curved temperature dependences.[56,62–65] This deviation from linearity, also known as curvature, originates from the temperature-dependent shift in population from the native state to a low-energy excited state.[62] This observed curvature is therefore able to report on the conformational heterogeneity found within a protein, visualized by a rough bottom of the free energy landscape of proteins that exist in a native ensemble. These low-energy alternate conformations that a residue may adopt within the native ensemble may be vital in either structural stability or functions such as binding, allostery, and catalysis.[14,63,66]

As mentioned above, curvature arises if a proton, for example, participates in the transition between two conformational states in fast exchange. This leads to the presence of

one crosspeak on a ^{1}H-^{15}N HSQC, that has a proton chemical shift equal to the average of the chemical shift in each of the two contributing states:

$$\delta_{observed} = \delta_1 f_1 + \delta_2 f_2$$

Here, δ_1 and δ_2 refer to the chemical shift of each conformation, while f_1 and f_2 refer to their relative populations. In order to observe curvature, the relative populations of the two states need to change with temperature and the population of the contributing states needs to be large enough. Generally, a contributing state needs to have a relative population of at least 5% and be within 5 kcal/mol of the native state. This limits the number of states that can contribute to the observed curvature.[62,65] It is important to note here that a lack of curvature does not imply that a proton, or other nucleus, is not accessing another state. It may just be that the state is too far apart in energy from the native state and that the population of the excited state is not large enough to be observed, such as in the case of a completely unfolded state, or that the proton is accessing a large number of alternate states.[62,63,65]

In previous experiments, curvature has been suggested to arise from a variety of processes. Examples are the "fraying" of the ends of helices present in cytochrome c, disulfide bond isomerization, new hydrogen bonds forming to buried water molecules, and other slight adjustments to a protein's structure that may be needed for function.[62,65] Also, in a study by Baxter & Williamson, it was demonstrated that when bovine pancreatic trypsin inhibitor is heated to its T_m, many of peaks that show linear dependences at lower temperatures start to deviate from linearity, beginning at approximately 15 °C below the T_m. Therefore, the curvature that appears in this situation may be interpreted as the beginning of a global unfolding event.[56] In addition to the variety of processes that may manifest curved temperature dependences, different proteins also exhibit different amounts of curvature. For example, in hen egg-white lysozyme, which is particularly stable and well-structured, roughly 5% of the residues exhibit curved temperature dependences. In contrast, 30% of the residues exhibit curvature in the bovine pancreatic trypsin inhibitor, which has a number of alternate conformations that affect hydrogen bonding.[62]

Furthermore, detailed information about the excited states is gathered by examining the curved temperature dependences. For instance, if curvature found in a nucleus' temperature dependence is present in a concave down shape, *i.e.* the slope starts relatively shallow and becomes steeper as temperature increases, it implies the native state is relatively structured and the excited state is moving towards random coil. Conversely, if the curvature is present in a concave up shape, *i.e.* the slope starts steep and becomes shallower as temperature increases, the excited state could be more structured than the native state. Usually, curvature is manifested in a concave down shape.[56,63,65] On top of the direction of curvature, the extent of curvature is inversely proportional to the energy difference between the ground and excited state.[63,65] Currently, experiments examining temperature coefficients and conformational heterogeneity are being used to explore the behaviour of numerous proteins, such as cardiac troponin C, hisactophilin, adnectins, and Cu,Zn superoxide dismutase (SOD1).[61,63,64,67]

1.3 Cu,Zn Superoxide Dismutase

One protein that has been widely characterized and would be highly useful in elucidating information about protein folding pathways is SOD1. In short, this model metalloenzyme undergoes several post translational modifications, including metal binding, disulfide bond formation, and dimerization, as well as being prone to mutation and is associated with the neurodegenerative disease amyotrophic lateral sclerosis (ALS).[68] In addition, SOD1 and its variants would be excellent for determining more uses, or the extent of usefulness, of temperature coefficients and conformational heterogeneity, as viewed by curved temperature dependences.

1.3.1 Structure and Function

Mature copper/zinc SOD1 (holo SOD1) is a homodimeric metalloenzyme predominantly found in the cytoplasm, with smaller amounts also being present in the nucleus, peroxisomes, and the mitochondrial intermembrane space of eukaryotic cells. In Gram-negative bacterial cells, a similar protein can be found in the periplasmic space.[68,69] The dimeric, functional form of SOD1 is 32 kDa in size, with each monomer consisting of 153 residues. Each monomer forms an eight-stranded β-barrel structure with a conserved disulfide

bond between Cys57 and Cys146 and two functionally important loops, the zinc-binding loop and the electrostatic loop (Figure 1.6 A). These two loops are relatively long, together accounting for roughly one-third of the residues found in the protein, and bracket the metal binding region and the active site of the enzyme.[68,70,71]

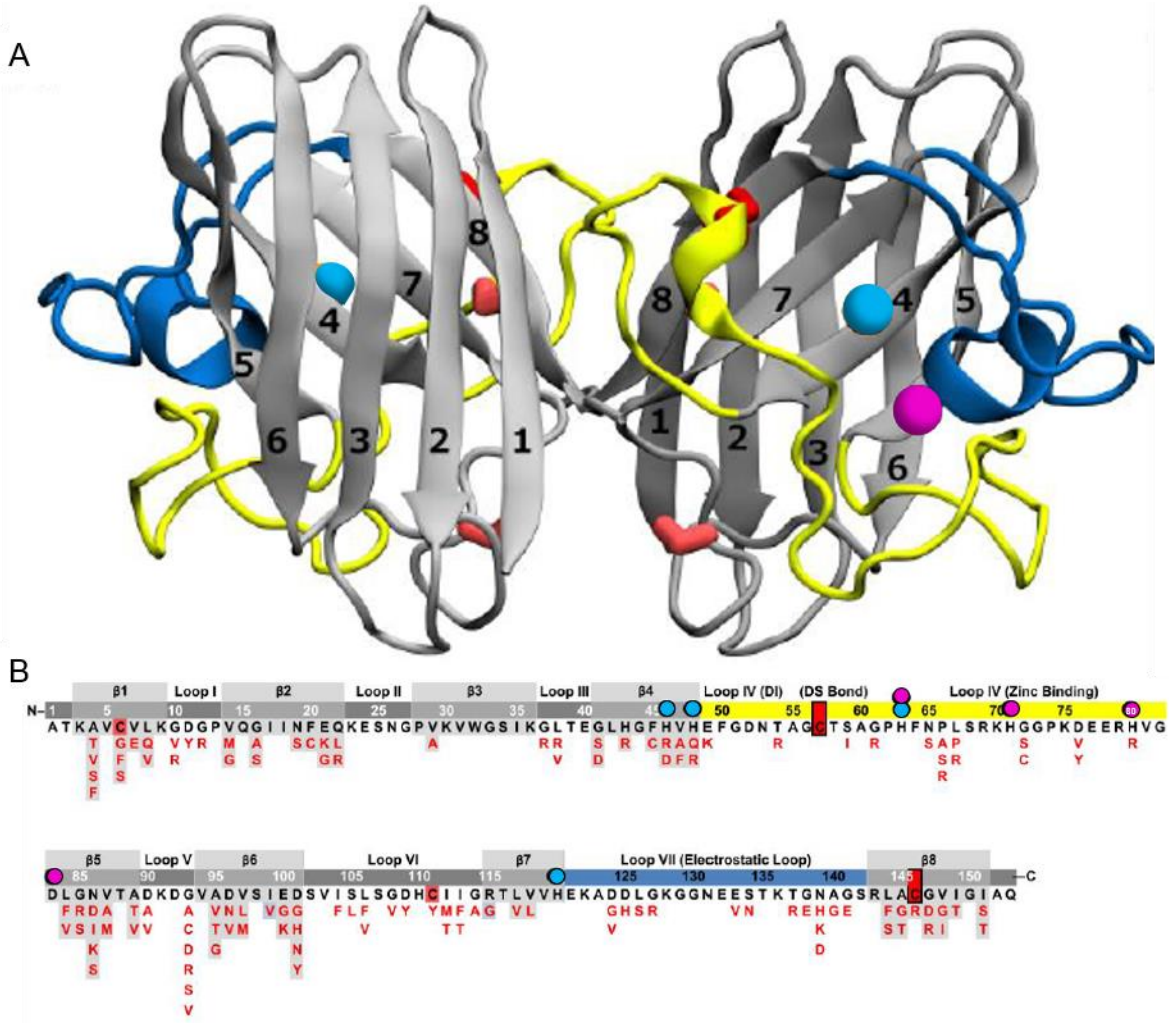

Figure 1.6: The Structure of Dimeric Holo SOD1. This figure (A) is a ribbon representation of the properly metallated homodimeric SOD1. The individual strands that make up the two β-sheets are labelled. The copper and zinc ions are shown as cyan and magenta spheres, respectively. In addition, the zinc binding loop (Loop IV) is shown in yellow, the electrostatic loop (Loop VII) is shown in blue, and the conserved intramolecular disulfide bond between Cys57 and Cys146 is shown as red spheres. The fALS-associated mutations and residues involved in metal-binding (spheres) are displayed on the sequence of SOD1 (B). Figure reproduced from Broom (2015) using PyMOL and PDB code 1HL5.[70,72,73]

Each of the two monomers of SOD1 bind one copper and one zinc ion. It is thought that the first metal to bind SOD1 is zinc, which confers structural stability to the protein and is coordinated in the zinc-binding loop by residues His63, His71, His80, and Asp83. The second metal, copper, confers catalytic activity to the enzyme and is coordinated by residues His46, His48, His63, and His120.[68,71] The channel that leads to the active site of SOD1 is formed by the zinc-binding and electrostatic loops, with several charged residues in the electrostatic loop, mainly lysines and glutamines, being responsible for guiding the substrate to the active site.[74]

SOD1 acts as an antioxidant defense enzyme; protecting the cells from toxic superoxide molecules (O_2^-) that are formed as a byproduct of respiration and other cellular processes.[71,75,76] Superoxide molecules are particularly toxic to cells due to their ability to react with hydrogen peroxide to form a more powerful oxidant, hydroxide radicals ($HO^{\cdot}$).[76] Hydroxide radicals are the strongest and most dangerous oxygen radicals as they interact and cause oxidative damage to macromolecules such as lipids, proteins, DNA, and carbohydrates.[76,77] SOD1 is able to rid cells of the superoxide molecules through a two-step ping-pong mechanism, involving the cyclic reduction and re-oxidation of copper (Figure 1.7).First, one superoxide molecule is oxidized to molecular oxygen, reducing the Cu^{2+} in the holo SOD1 to Cu^{1+}. Next, the reduced Cu^{1+} is oxidized to Cu^{2+} by reducing another superoxide molecule to hydrogen peroxide, regenerating the original form of SOD1.[70,71]

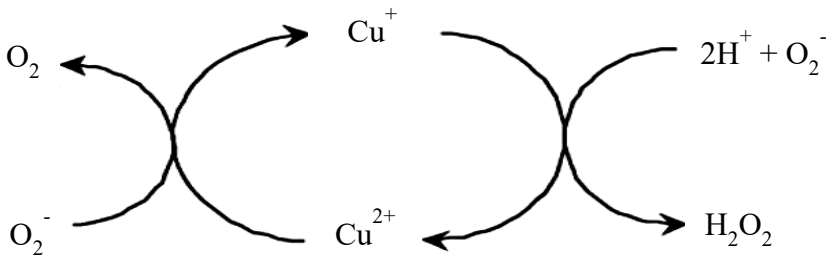

Figure 1.7: The Ping-Pong Mechanism of the Catalysis of Superoxide Molecules by SOD1. This figure shows the two reactions involved in the ping-pong mechanism performed by SOD1, using its catalytic copper ion. Two superoxide molecules and two protons are consumed and transformed to molecular oxygen and hydrogen peroxide.[71,74]

1.3.2 SOD1 Maturation and Immature SOD1

As alluded to earlier, SOD1 undergoes several posttranslational processes to become a fully mature and functional metalloenzyme (Figure 1.8). Initially, SOD1 is in an unmetallated monomeric form with reduced sulfhydryl groups, referred to as reduced apo-SOD1 (apo2SH SOD1). The subsequent modifications that occur are the binding of zinc and copper ions, the formation of a disulfide bond between Cys57 and Cys146, and dimerization.[68,78,79] In addition, other possible modifications include phosphorylation, N-acetylation in eukaryotic cells, and glutathionylation.[80,81] In the absence of post-translational modifications, the stability of apo2SH SOD1 is low when compared to other single-domain proteins and holo SOD1.[79,82,83] For example, differential scanning calorimetry experiments have shown the melting temperature of pseudo-wildtype (pWT) SOD1, in which Cys6 and Cys111 are mutated to Ala6 and Ser111, in the apo2SH and holo states to be 47.6°C and 92.7°C, respectively.[82,84,85]

As mentioned above, the major modifications that the apo2SH SOD1 monomer needs to undergo are zinc and copper binding, the oxidation of the disulfide bond, and dimerization. Currently, the mechanism of how zinc binds to SOD1 is not known, however, it is thought that zinc is the first metal to bind, and it greatly stabilizes the SOD1 monomer. The binding of zinc to apo2SH SOD1, produces the disulfide-reduced one zinc-bound SOD1 monomer (E,Zn2SH SOD1) and increases the affinity for binding with the copper chaperone protein for SOD1 (CCS).[86] The CCS is a 28 kDa homodimeric protein with each subunit comprised of three domains and is thought to form a heterodimer with monomeric E,Zn2SH SOD1. This loads the E,Zn2SH SOD1 with copper and assists in the formation of the disulfide bond.[78,87] The first domain of the CCS contains a copper-binding motif that binds Cu^{1+} and transfers the ion to the E,Zn2SH SOD1.[78] The second domain of the CCS is highly homologous to SOD1 and is vital for protein-protein recognition and the binding to SOD1. In human CCS, this domain binds an equimolar amount of zinc, which is essential for the proper functioning of the CCS.[87] The third domain of the CCS is a short polypeptide that is used to oxidize the disulfide bond in SOD1. It lacks secondary structure but contains two crucial cysteine residues, Cys244 and Cys246, that are involved in the formation of the SOD1 disulfide bond.[78] Following the addition of copper and the formation of the disulfide bond by the CCS, SOD1 dimerizes and forms the

final functional form of the protein. In the native protein, SOD1 forms a tight dimer with a dissociation constant of approximately 1.0×10^{-10} M^{-1}.[88]

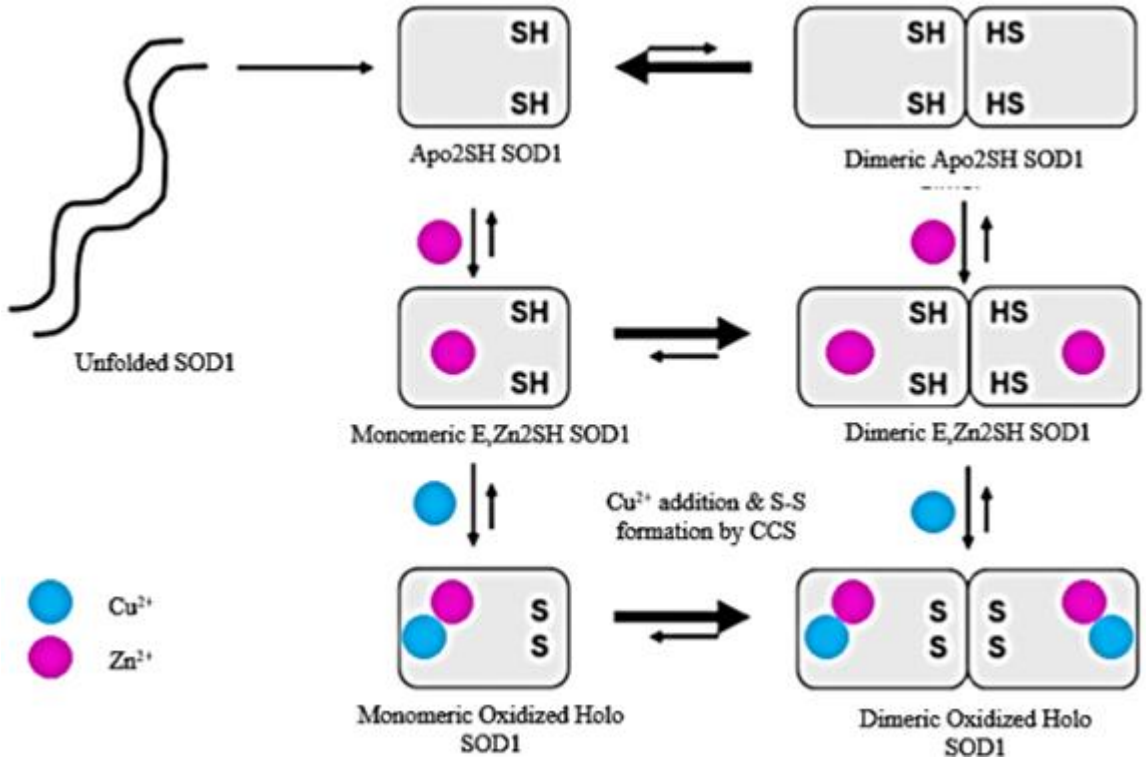

Figure 1.8: Key Maturation States of Cu,Zn SOD1. This schematic displays some potential maturation pathways for Cu,Zn SOD1. Following the initial folding events, the predominantly monomeric apo2SH SOD1 must bind copper and zinc ions, have a disulfide bond formed between Cys57 and Cys146, and dimerize to become fully functional holo SOD1. The binding of copper and the oxidation of the disulfide bond is carried out by the copper chaperone for SOD1 (CCS). Adapted from Banci *et al.*[78]

1.3.3 ALS and SOD1

In addition to being a well characterized protein, SOD1 has also been associated with the disease ALS. This adds to the value of studying the local structure and stability of SOD1 variants, since these studies may provide insights into pathways and mechanisms relevant to protein misfolding diseases. ALS is a fatal adult-onset neurodegenerative disease that causes the progressive degradation and death of the lower motor neurons in the brainstem and spinal cord, as well as the upper motor neurons in the motor cortex. ALS results in a loss of muscle

control that concludes in total paralysis and death, often by respiratory failure. The typical patient survival after the onset of symptoms is approximately 2-5 years.[68,75,89,90]

ALS can be classified as either sporadic or familial (fALS). Sporadic ALS has no known causes and accounts for approximately 90-95% of occurrences. The remaining 5-10% of cases are termed fALS and involve a family history of the disease.[68,89] Approximately 20-25% of fALS cases are associated with mutations in the *sod1* gene, which encodes the SOD1 protein.[68,75] The *sod1* gene is located on chromosome 21 and has 187 mutations identified (http://alsod.iop.kcl.ac.uk/), to date.[68,91] These mutations generally promote the formation of toxic misfolded and aggregated SOD1, which have been found in the spinal cords of transgenic SOD1 mice and deceased fALS patients.[68,92] Initially, it was hypothesized that the mutations associated with fALS affected the structure of SOD1, causing a decrease in dismutase activity and increasing oxidative stress in cells.[93] This was later rejected when further experiments on fALS-associated mutations concluded that different mutants displayed varying levels of SOD1 activity.[75,94] In addition, experiments on SOD1 knockout-mice showed that the mice did not develop any ALS symptoms.[95] However, when an fALS-associated mutant, such as G93A (a mutation of glycine to alanine at position 93), is expressed with endogenous mouse SOD1, the transgenic mice develop ALS symptoms, specifically the death of lower motor neurons.[96,97] These experiments have helped to determine that SOD1 experiences a gain of toxic function when mutations occur, hypothesized to be due to protein misfolding and aggregation.[68,96]

1.3.4 SOD1 Mutations and Gain of Toxic Function

The fALS-associated mutations, of which there are now 187, are dispersed throughout the entire structure of the protein and are predominantly autosomal dominant.[68,69,91] Some of these mutations are located in functionally important sites, such as the metal binding region and the dimer interface, which may promote improper metal binding or the disruption and dissociation of the dimer interface.[68,69,71] In general, the dissociation of SOD1 to its monomeric form and the loss of metals has been thought to be required for oligomerization and aggregation.[88,98–100] With respect to metal binding, the loss of metals may result in decreased stability of the zinc-binding loop, and also may promote dissociation of the SOD1 dimer since

a portion of the zinc-binding loop is present in the dimer interface region.[101,102] It is also possible for a mutation to change a residue's net charge, hydrophobicity, or side-chain orientation, which in turn may alter the stability of both immature and mature forms of SOD1, with respect to wildtype (WT) SOD1, and promote protein misfolding.[103–105] Furthermore, mutant SOD1s have displayed a greater aggregation propensity than WT SOD1, and both monomeric SOD1 and zinc-deficient SOD1 have been shown to have a greater aggregation propensity than holo SOD1.[83,88,99,100] The formation of aggregates containing misfolded mutant SOD1 has been observed in cell cultures, transgenic mice, and fALS patients.[68,92] Surprisingly, the stability of the mutants or their aggregation propensity does not always correlate to the disease duration. For example, V148I is more thermodynamically stable than, and has an aggregation propensity similar to that of, WT SOD1 but has an average disease duration of approximately 1.7 years.[84,106]

1.4 Research Objectives

Currently, not much is known regarding the potential mechanisms of pathogenic misfolding and aggregation of SOD1 in disease.[63,107] One focus of the Meiering lab is to elucidate the effects that fALS-associated mutations and the maturation process have on the physical and chemical properties of SOD1 and how these properties may influence the protein misfolding and aggregation observed in fALS patients, mice models, and cell cultures. Of particular interest is determining these various effects at high resolution, on a residue-specific level, since changes in global stability do not always reflect the changes in local stability.[108] NMR is a powerful technique that can be utilized to study these effects and shed light onto the potential mechanisms of misfolding of SOD1 in disease. More specifically, variable temperature NMR experiments have been performed and high-resolution chemical shift and temperature dependence data has been acquired to study the effects mentioned above.

Chapter 2 examines the effects that various mutations have on the local structural stability of SOD1 using amide proton secondary shifts, as well as both amide proton and amide nitrogen temperature coefficients and conformational heterogeneity patterns. Next, Chapter 3 investigates the effects of maturation from the apo2SH state to the holo SOD1 state using the

same methodologies as Chapter 2. Temperature coefficients and conformational heterogeneity data for the holo SOD1 variants have previously been reported and described in Doyle *et al.*[63] In both chapters 2 and 3, the implications of linear temperature coefficients and nonlinear temperature dependences, as well as amide proton secondary shift data, for the various mutants and maturation states studied will be discussed. Lastly, Chapter 4 reports initial capillary isoelectric focusing (CIEF) experiments examining the effects that mutations and maturation have on the isoelectric points and diffusions coefficients of SOD1 variants.

Chapter 2

Effects of Mutation on Immature SOD1 Studied by NMR

2.1 Introduction

Mutations arise from changes in the DNA sequence of a gene, and may result in changes to the codons contained within the respective gene, thus changing the amino acid sequence of a protein. These changes in amino acid sequence can result in changes to a proteins physical and chemical properties.[1,109] For example, a protein's structure, stability, binding partner specificity and activity may be changed as a result of mutation.[109] Most commonly, mutations have destabilizing, or deleterious, effects on a protein; however, there are some that result in stabilizing effects. Mutations have been widely associated with various forms of cancer and numerous other diseases.[1,19,109–111]

A protein's free energy landscape describes the conformations accessible to a protein at a given energy level and is generally rough, with many local minima and maxima. These local minima and maxima correspond to the intermediate states and the free energy barriers a protein must overcome to continue folding, respectively.[2,6,110] Mutations can cause perturbations in the free energy landscape of a protein, affecting the protein's ability to convert between states by either increasing or decreasing the free energy barriers.[18,110,112] This in turn alters the populations of the protein's states and affects how a protein regulates its intramolecular interactions and its interactions with molecular partners, which may result in non-native interactions and protein misfolding.[110,111] To date, there are many questions remaining regarding the effects mutations may have on the structures, functions, and dynamics of proteins.

2.1.1 Properties and Structural Changes of Selected SOD1 Mutants of Interest

In order to determine the various effects that mutations may have on the local (and global) structural stability of SOD1, protein denaturation must be reversible in all the studied variants, some of which have a high aggregation propensity.[83] To achieve reversible denaturation, all SOD1 variants studied using temperature coefficients and conformational

heterogeneity were expressed in a pWT background. In WT SOD1, there are four cysteine residues. Two of these residues, Cys57 and Cys146, form the intramolecular disulfide bond (Figure 1.6). The two remaining cysteine residues, Cys6 and Cys111, are able to form non-native intermolecular disulfide bonds, which may help promote the initiation of the aggregation process and have been shown to help stabilize aggregates *in vivo*.[113,114] Also, throughout the aggregation process, these intermolecular disulfide bonds could interrupt the intramolecular disulfide bonds between Cys57 and Cys146 through disulfide exchange reactions, further promoting SOD1 aggregation.[113,114] In the pWT background, the two free cysteine residues that are not involved in the formation of the intramolecular disulfide bond, Cys6 and Cys111, have been mutated to Ala6 and Ser111. The pWT has been well characterized and displays a high degree of reversible unfolding, in addition to possessing a similar stability, activity, and structure to WT SOD1.[82,84,85,115] These properties make the pWT background of SOD1 highly amenable to use in variable temperature NMR methods.

In addition to reversible unfolding, the mutations studied should be representative of the many that have been found throughout the SOD1 structure and be involved in, or thought to disrupt, various processes (http://alsod.iop.kcl.ac.uk/). In addition, the T_m of each form of SOD1 to be studied using temperature coefficients should be known. The reason for this is, as described in Section 1.2.7, that as the temperature approaches the T_m of the protein, the majority of the temperature dependences begin to curve. This may indicate the onset of a global unfolding event, which would prevent observation and interpretation of the local events occurring when the protein is properly folded, in each state.[56] The SOD1 variants to be studied by NMR are listed in Table 1, along with the average disease duration associated with each mutant and other thermodynamic parameters.[82,84,106]

The 6 mutations studied here, described in Table 1, are spread across the structure of SOD1 and are involved in, or disrupt, various processes (Figure 2.1). Two of these mutations (A4V and V148I) are in the dimer interface, one (G93A) is in a tight turn, two (G85R and E100G) are in the β5-β6 hairpin, and one (H46R) is a copper-coordinating residue in the metal binding region of β4. In addition, two of these mutations (H46R and G85R) affect the binding of metals to SOD1.[68]

Mutant	Location	Disease Duration (Years)	Holo T_m (°C)	Apo2SH T_m (°C)	ΔG, 37°C (kcal/mol)
pWT	N/A	N/A	92.7	47.6	1.8 ± 0.1
A4V	β1	1.2	86.7	36.3	N.D.
H46R	β4	17.6	77.5	52.6	3.1 ±0.1
G85R	β5	6.0	77.5	40.7	0.6 ± 0.0
G93A	Loop 5	3.1	87.7	33.0	N.D.
E100G	β6	4.7	86.2	33.2	-0.6 ± 0.2
V148I	β8	1.7	92.7	51.0	2.2 ± 0.0

Table 1: Summary of Disease Duration and Mutant pWT Thermodynamic Parameters. The disease duration of each mutant was obtained from Wang *et al.*[106] The holo SOD1 T_m data was obtained from Stathopulos *et al.*[82] The apo2SH T_m data and $\Delta G_{37°C}$ was obtained from Vassall *et al.*[84] N.D. denotes no data. E,Zn2SH pWT SOD1, not included in the table above, has a T_m of approximately 55 °C (unpublished).

The first of these mutations, A4V, is in the first β-strand that forms a part of the dimer interface region. This mutation is the most common and lethal of the mutations studied, with an average disease duration of approximately 1.2 years.[106] Mutations at the A4 position affect both the ability of SOD1 to dimerize and the structure of the β-barrel, since the side chain packs into the hydrophobic core of the protein.[101,112,116–121] With respect to the dimer interface, it has been shown by crystallography that A4V alters the packing of the dimer interface.[122] In the crystal structure of metal-free A4V, the residues that are in close proximity and displaced the most are L106 and I113, with F20 being moderately displaced.[116] In addition, V4 forms a close contact with I149 and a hydrogen bond is disrupted between the backbones of T2 and Q22, which in WT SOD1 is one of the hydrogen bonds that helps to stabilize the protein chain at the N terminus.[122]

The second mutation of interest is H46R, which involves one of the copper binding ligands. Of the mutations studied here, this mutant is associated with one of the longest fALS disease duration and has the highest T_m of the apo2SH variants tested.[84,106] This mutation allows for the successful binding of either zinc or copper at the zinc-binding site; however, the copper-binding site, for which H46 is one of the copper-coordinating side chains, is unable to bind metal ions, thus eliminating this variant's dismutase activity.[123] This mutation is thought

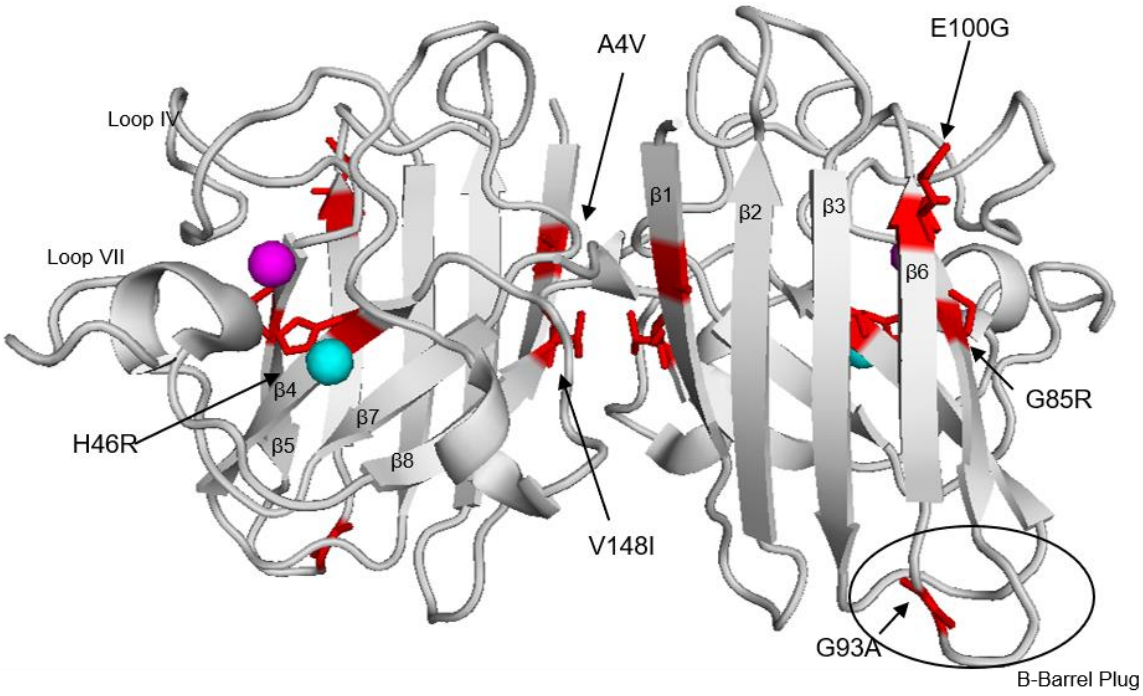

Figure 2.1: Sites of SOD1 Mutations of Interest. The locations of the 6 mutations studied in this work are shown on the structure for holo SOD1. The mutations are shown in red, with their side chains shown as sticks. The copper and zinc ions are shown in cyan and magenta, respectively. This figure was generated using PyMOL and PDB structure 1HL5.[70,72]

to disturb the H63, D124, and T137 side chains, which will weaken the interactions between the metal binding region and the electrostatic loop.[124–126]

The third mutation is another that affects metal binding, G85R. This mutation is close to one of the ligands that coordinate Zn, D83, and greatly decreases metal ion affinity and destabilizes the β5-β6 hairpin.[68,84,101,112,118,121,127] In the spinal cord lysates of mice overexpressing G85R, the protein has been found in a monomeric, copper-free, and disulfide reduced state, which may indicate that it has decreased interactions with the CCS due to decreased metal affinity.[127,128] In an extensive study on the crystal structures of various forms of G85R, the R85 sidechain was found to affect the position of P74, which is only two residues away from the zinc-binding ligand H71, and changes the orientation of its five-membered ring.[127] This rearrangement of the P74 ring disrupts a hydrogen bond between P74 and R79, one of two hydrogen bonds that secures the zinc-binding loop to the β-barrel, along with a hydrogen bond between R79 and D101. This change in structure would impose a conformation

on the zinc-loop which displaces one or more zinc-binding ligands. In addition, it has been shown that the hydrogen bonding network between β4 and β5 is weakened in G85R, such that a water molecule is able to form hydrogen bonds with the sidechain of D124 and the amide nitrogen of F45. In WT SOD1, the carbonyl oxygen of G85 forms a hydrogen bond with the amide nitrogen of F45 forming a part of the hydrogen bond network between β4 and β5.[127]

The next mutation, G93A, is in Loop V, a short loop connecting β-strands 5 and 6. This loop is also in close proximity to Loop III (residues 37-40), which connects the two β-sheets and is the location of the "β-barrel plug" that is critical for maintaining the structure SOD1.[116,129] Mutations at the highly conserved G93 position are thought to destabilize the β-barrel by affecting the packing of the residues that form the β-barrel plug. In the crystal structure of metal-free disulfide G93A, the residues that are displaced the most are L38 and D92, both found as a part of the β-barrel plug.[116] Furthermore, experiments on G93A have shown that the β5-β6 hairpin is destabilized, leading to the formation of linear filamentous fibrils.[112] These fibrils are stabilized by the disordered zinc-binding (loop IV) and electrostatic loops (loop VII), that are often found in metal-deficient pathogenic SOD1, forming non-native interactions with SOD1 monomers at the unprotected edge strands, such as β-strands 5 and 6. This aggregation model is also supported by the crystal structure of apo-oxidized H46R, which shows non-native interactions between the β5-β6 hairpin and the electrostatic loop of the adjacent monomer. This model may also be applicable to the mutations G85R and E100G, as they are present in the β5-β6 hairpin and have a destabilizing effect on SOD1.[125]

The fifth mutation studied in this work is E100G, another in the β5-β6 hairpin and one of the more common fALS mutations.[130] In addition, this mutant has one of the lowest T_m values of the apo2SH SOD1 variants studied.[84] Similar to G85R, this mutation decreases the net negative charge of the protein. To date, there have been no studies determining the structure of E100G SOD1; however, information obtained from the structures of G85R and D101G may provide some insight into the effects of the E100G mutation. D101 has two structural roles, the first is to form a bond with R79 that connects the edge strands β5 and β6 at their widest point. This most likely helps to protect the edge strands by stabilizing the closeness of β5 and β6, preventing the opening of the β5-β6 hairpin. The second is to provide conformational

specificity to the zinc-binding loop, as R79 is involved in hydrogen bonds that connect P74, H80, V81, and D83, two of which are residues involved in the coordination of zinc.[127,131] Furthermore, the zinc-binding loop contains D76, which has been posited to form a bond with K128 in the electrostatic loop, helping to associate these two loops. This residue falls between P74 and R79, and the bond between D76 and K128 may be influenced by the conformation of the zinc-binding loop.[131,132] Therefore, it could be expected that mutations near D101, such as E100G, could affect the formation of the bond between the D101 and R79 sidechains and affect the structure of the β5-β6 hairpin and the zinc-binding loop.[131] Also, the E100G mutation could disrupt the electrostatic along the surface of β-sheet 1, as it forms a salt bridge with residue K30.[63,131]

Lastly I studied V148I, which is in the dimer interface and has a similar T_m to that of pWT SOD1, despite having one of the lowest disease durations.[84,106] Previous studies on this mutant have shown that the protein is able to metallate properly and shows a decreased aggregation propensity compared to WT SOD1.[133,134] Also, immature forms of this have increased monomer stability and a slightly weakened dimer interface.[84,119] The sidechain of V148 points into the dimer interface and is buried in dimeric SOD1; however, the mutation to I148 introduces a larger hydrophobic residue. This mutation may have stabilizing effects due to the increase in hydrophobicity; but the steric hinderance of a larger sidechain may also have destabilizing effects on its immediate surroundings.[63]

2.1.2 Previous SOD1 Conformational Heterogeneity and Temperature Coefficient Studies

Numerous previous studies have examined the dynamics of WT and mutant SOD1. As mentioned in Section 1.3.2, SOD1 binds copper and zinc ions, forms a conserved intramolecular disulfide bond, and dimerizes as it matures to holo SOD1. Each of these steps increasingly limit the flexibility of the loops, particularly the long electrostatic and zinc-binding loops, and increases protein stability.[68,112,135] Without the presence of metals, which many mutations can affect, the disulfide bond, or a formed dimer, the apo2SH SOD1 has been shown to be more dynamic, with many stabilizing interactions between the metal binding

region and electrostatic and zinc-binding loops found to be missing. This causes these two long loops to become highly disordered, leading to an increased tendency to misfold.[85,126]

Studies performed by Sekhar *et al.* on pWT and mutant apo2SH SOD1 identified four low-energy conformational states that are thermally accessible on a millisecond time scale.[112,135] Using ^{15}N chemical exchange saturation transfer (CEST) and ^{15}N Carr-Purcell-Meiboom-Gill (CPMG) relaxation dispersion experiments, the free energy landscapes and previously determined excited states of pWT and mutant were characterized. The first excited state of apo2SH SOD1 corresponds to a dimeric form, similar to what is present in holo SOD1, is populated by roughly 3% of the protein, with a lifetime of 3 ms. One reporter of the dimerization process is G61, for which this residue's CEST profile was used alongside those of G51, N53, and T54 to determine if a dimer transiently forms in the disease mutants studied. Mutants G37R, G93A, and E100G, along with the metal-binding mutants H46R and G85R, all showed evidence of dimer formation. Conversely, the mutations A4V and V148G, which are both in the dimer interface region, do not show evidence of native dimer formation.[112,135]

The second excited state described in these studies involved the formation of a short helix in the electrostatic loop that is also present in holo SOD1. This state is populated by roughly 2% of the pWT protein and has a lifetime of 13 ms. Two residues that report on the formation of a more structured electrostatic loop are T135 and T137. Mutants G37R and G93A both showed evidence for the formation of this helix; however, mutants H46R and G85R, which interfere with metal binding, as well as mutants E100G and V148G, did not.

The other two excited states described involve the formation of nonnative dimers. One of these two states is stabilized by interactions between the native dimer interface region of one monomer and the electrostatic loop of another. The mutations that disrupted the transient native dimer, A4V and V148G, also showed no evidence of these two non-native dimers.[112,135]

In addition to the four excited states described above, there were additional conformations for mutants G85R and G93A that were not present in pWT SOD1. Closer investigation of these states revealed that multiple conformations, involving a large number of residues, are accessible in the β5-β6 hairpin. This was attributed to the opening of the β5-β6

hairpin, as observed in experiments performed on holo G93A by Elam *et al.*[112,125] Also, other NMR experiments on holo G93A have shown that loops III and V have more mobility than in WT SOD1 on a time scale faster than the rate of protein tumbling.[136] This was interpreted as the transient opening of the β-barrel, which may become more apparent if the protein is metal-deficient, leading to amyloid fibrillogenesis through non-native interactions, such as the edge-to-edge interactions described in Section 2.1.1.[136]

Another important study examining the conformational heterogeneity in SOD1 was published in 2016 by Doyle *et al.*[63] This study utilized temperature coefficients to examine the local stability and conformational heterogeneity in variants of holo SOD1.[63] As discussed in Sections 1.2.5 and 1.2.7, temperature coefficients are a measure of the local structural stability of a protein, with more negative temperature coefficients corresponding to lower local structural stability. Also, the non-linearity observed in temperature coefficients can report on the population of alternate low-energy excited states.[56–58,63] With respect to holo pWT SOD1, the average amide proton temperature coefficient value is more positive than other proteins, matching previously acquired thermodynamic data that describes holo SOD1's high thermodynamic stability.[63,82] Also, in holo pWT, the edge strands β1, β6, and β8 all have a decreased stability when compared to other β-barrel strands and the electrostatic and zinc-binding loops have similar average temperature coefficient values to those of the β-strands, owing to their structured states in holo SOD1. Furthermore, residues that exhibit more negative temperature coefficients, indicating they are less structured, more commonly appear at the ends of the β-strands, in loops, and in the edge strands. In contrast, the residues with more positive temperature coefficients are found in the core and more structured regions of the protein.[63]

Doyle *et al.* also found that the mutations cause changes in the local structural stability of the protein that correlated with global stability. For example, holo V148I has the largest T_m, and also had the most positive average temperature coefficient, when compared to holo G93A and E100G. Also, the location of changes in temperature coefficients, when compared to pWT, localize to varying extents to the sites of mutation. For example, in holo G93A, in which the mutation is present in loop V and near the β-barrel plug found in loop III, a decrease in stability of loops III and V was observed . In E100G, where the mutation is present in the widest part

of the β5-β6 hairpin, the changes in temperature coefficients were all near the site of mutation. In holo V148I, present in β8 and the dimer interface, many of the residues that experience a change in temperature coefficient compared to pWT show an increase in local stability and the majority of the changes are near the site of mutation and in the dimer interface region.[63]

Upon examining the curvature with temperature, Doyle *et al.* found that a variety of residues populate alternate energy states. Generally, the mutants have similar curvature patterns to holo pWT; however, all show an increase in curvature in the β6 strand. Some of these residues form hydrogen bonds that connect the edge strands to the main structure of SOD1, and curvature in this region may indicate the edge strands are beginning to separate from the rest of the structure. Also, all mutants either show curvature or changes in hydrogen bond patterns near the β-barrel plug, potentially showing the opening of the structure. Lastly, this study also looked at the amide nitrogen temperature coefficients for the variants discussed. The authors concluded that, at the time, the ^{15}N temperature coefficients were largely uninterpretable.[63]

In this chapter, high resolution NMR data as a function of temperature has been gathered for the apo2SH forms of each SOD1 variant described in Table 1 and compared to each other. In addition, previous NMR data acquired for holo SOD1 variants by Doyle *et al.* that were not interpretable at the time will be discussed.[63] These NMR data were analyzed to determine amide proton secondary chemical shifts, amide proton and nitrogen temperature coefficients, and curved temperature dependences. Each of these analyses provides valuable structural information about the apo2SH form of SOD1 and the effects of mutations. The amide proton secondary shifts for apo2SH and holo SOD1 correlate well with structural data previously reported in crystal structures, indicating a structured β-barrel and less structured loop regions. The results obtained from the amide proton temperature coefficients studies support the use of temperature coefficients as indicators of intramolecular hydrogen bonding and local stability. The changes in temperature coefficients largely occur around the sites of mutation and provide insight into many of the disrupted processes in mutant SOD1. In the amide nitrogen temperature coefficient studies, when secondary temperature coefficients are derived by referencing to random coil, theses appear to be extremely sensitive to deviations

from random coil and are useful for reporting on local structure. The curvature present in the amide proton and nitrogen temperature dependences was also analyzed. The curvature patterns in mutant SOD1 report on the disruptions to both the structure and function associated with the respective mutations, as well as excursions to sparsely populated excited states. These data specifically highlight the β5-β6 hairpin as a hotspot for the temperature-dependent loss of folded structure in mutant SOD1. Also discussed is an alternate purification protocol for SOD1 that shows promise for SOD1 variants that have relatively high T_m values.

2.2 Methods

2.2.1 Growth and Expression of pWT SOD1

The conditions for recombinant expression of SOD1 in bacterial cells for these NMR experiments followed the procedures previously developed by Getzoff *et al.* and Stathopulos *et al.*[83,137] Human cytosolic SOD1 variants in a pWT background, were expressed in BL21 *E.coli* cells using a pHSOD1ASlacI1 vector containing a tacI promoter, ampicillin resistance gene, and the lac repressor. The BL21 cells were transformed with the vector by electroporation and successfully transformed cells were selected for by growing overnight in 10 mL LB media containing 0.1 mg/mL ampicillin at 37°C with shaking, to aerate the culture. This overnight culture was used to inoculate 1 L of M9 minimal medium, consisting of the M9 supplements and 100 mL 10x M9 salts from Table 2, made up to 1 L with MilliQ water. For ^{15}N-labelled samples, 0.5 g of $^{15}NH_4Cl$ was added to each liter of M9 minimal media instead of NH_4Cl. The *E.coli* cells were grown at 37°C until an OD_{600} of approximately 0.6 was reached, after which protein expression was induced by adding isopropyl β-D-1-thiogalactopyranoside, to a final concentration of 0.250 mM. At this point, $CuSO_4$ and $ZnSO_4$ was added to final concentrations of 0.05 and 0.1 mM, respectively. The cells were then grown at 25°C for 36 hours, at which point they were harvested by 15 minutes of centrifugation at 4000 g. Cell pellets were stored at -80°C until further processing.

Media	Composition
Luria Broth (LB)	20 g LB (Lennox) per liter, which is a mixture of 20 g bacto-tryptone, 5 g bacto-yeast extract, 10 g NaCl
10x M9 Salts	67.8 g Na_2HPO_4, 30 g KH_2PO_4, 5 g NaCl per liter
M9 Supplements	0.5 mg/mL NH_4Cl, 2 mM $MgSO_4$, 0.1 mM $CaCl_2$, 0.4% glucose, 0.0001% thiamine HCl (w/v)

Table 2: Composition of Growth Buffers. This table described the composition of the growth media used to grow and express ^{15}N-labelled SOD1.

2.2.2 SOD1 Purification

Pseudo-wildtype SOD1 was purified using the methods previously described in Getzoff *et al.* and Doyle *et al.*[63,137] One modification to this procedure was the replacement of the diethyl-amino-ethyl column with a Poros HP2 hydrophobic interaction column.[101] The SOD1 was first released from the *E.coli* periplasmic space by an osmotic shock. Then, the protein was copper-charged by adding $CuSO_4$ to a final concentration of 1.4 mM. This ensured proper metalation, producing holo SOD1, which was then heated for at 70°C for 20 minutes to precipitate contaminating or misfolded proteins. The mutant proteins were heated at lower temperatures, typically between the T_m of their holo and disulfide-oxidized apo states.

After cooling, the precipitated protein was removed by centrifugation at 10000 x g for 20 minutes before ammonium sulphate and trisaminomethane, pH 8.0, were added to a final concentration of 3 M and 20 mM, respectively. The solution was then filtered through nitrocellulose paper and run through the hydrophobic interaction column, which separated SOD1 from any remaining contaminant proteins. SOD1 was eluted from the column by a gradient of decreasing ammonium sulphate before being dialyzed against water and concentrated to approximately 7 mg/mL by ultrafiltration using a 10 kDa cutoff membrane. The exact concentration of SOD1 was determined using an ε_{280nm} of 5400 $M^{-1}cm^{-1}$ per monomer. The protein was then flash-frozen using liquid nitrogen and stored at -80 °C until further processing.

2.2.3 New SOD1 Purification Procedure

Partway through this study, additional SOD1 was required to prepare the apo2SH A4V sample. The protein was grown as described in Section 2.2.1; however, was purified using a

procedure being tested by Dr. Tridib Mondal at the Weizmann Institute of Science (Mondal, unpublished). This procedure aims to eliminate the use of the hydrophobic interaction column and the subsequent dialyses, to remove the large amount of ammonium sulfate, in an effort to improve the yield of SOD1, as well as reducing the time and cost of the purification process.

The purification process begins the same as the one described in Section 2.2.2, with an osmotic shock to release the SOD1 from the *E. coli* periplasmic space, copper charging with $CuSO_4$, and a heat treatment. The heat treatment was performed at 65 °C for 25 minutes to reflect the lower T_m of holo A4V. Following the heat treatment, the protein was allowed to cool to room temperature on a bench for approximately 4 hours, before the precipitated protein was removed by centrifugation. The remaining soluble proteins were concentrated to approximately 15 mL using a 10 kDa membrane and ultrafiltration. To remove the excess copper from the copper charging, the protein was dialyzed twice against 1 L of 20 mM HEPES buffer, pH 7.8. Following dialysis, the protein was diluted thrice with the HEPES buffer above and concentrated to approximately 4 mg/mL using a 10 kDa membrane and ultrafiltration. The protein was then flash-frozen using liquid nitrogen and stored at -80 °C until further processing.

2.2.4 Removal of Metals from SOD1

The removal of metals from SOD1 was performed using the procedure from Vassall *et al.*[101] Briefly, the purified protein was unfolded at pH 3.80 and dialyzed against ethylenediaminetetraacetic acid (EDTA). The metal-free SOD1 was then dialyzed against a solution containing 50 mM sodium acetate and 100 mM sodium chloride, pH 3.8, to remove the remaining EDTA. Finally, the protein was dialyzed against fresh MilliQ water, followed by dialysis against 1 mM 4-(2-hydroxyethyl)-1-piperazineethanesulfonic acid (HEPES) buffer, pH 7.8. This yielded apo SOD1 containing an oxidized disulfide bond.

Once SOD1 was metal-free, great care was taken to avoid re-introducing metals to the protein. Therefore, all glassware, Eppendorf tubes, and pipette tips were washed using 50% nitric acid and rinsed extensively with fresh MilliQ water. Any membranes used for concentrating the protein were soaked in EDTA and then rinsed extensively with chelexed water, prepared by passing MilliQ water through a column packed with Chelex® 100 resin. In

addition, all aqueous solutions made for preparing apo samples for NMR experiments were made using chelexed water.

2.2.5 Reduction of the SOD1 Disulfide Bond and Reconstitution of Zinc

The SOD1 disulfide bond was reduced as described previously in Vassall *et al.*[84] In summary, using nitric acid-washed glassware and pipette tips, disulfide-oxidized apo SOD1 was denatured by adding guanidine hydrochloride and HEPES buffer, pH 7.8, to final concentrations of 2M and 20 mM, respectively. Next, tris (2-carboxyethyl) phosphine hydrochloride (TCEP HCl) was added to a final concentration of 10 mM. TCEP HCl was used to reduce the disulfide bond between Cys57 and Cys146. Following the addition of TCEP HCl, the denatured protein was incubated for approximately one hour in a desiccator at 37°C before being exchanged into a refolding buffer containing 1 mM TCEP HCl and 20 mM HEPES, pH 7.4. This process yielded apo2SH SOD1, which will be used in both the preparation of E,Zn2SH SOD1 and apo2SH NMR samples. Following the reduction of the disulfide bond and the refolding of the protein, the concentration of apo2SH SOD1 was determined using an ε_{280nm} of 5400 $M^{-1}cm^{-1}$ per monomer. For the E,Zn2SH pWT SOD1 sample, zinc was then reconstituted by adding an equimolar amount of $ZnSO_4$ to apo2SH SOD1.[138]

2.2.6 Preparation of the NMR Sample

After the removal of metals and the reduction of the disulfide bond the resulting apo2SH SOD1 was ready to be prepared into NMR samples. The samples are prepared by concentrating the protein of interest to approximately 1 mM monomer in 450 µL of 20 mM HEPES buffer and 1 mM TCEP, pH 7.4.[63] After the protein is concentrated, 4,4-dimethyl-4-silapentane-1-sulfonic acid (DSS) was added as an internal standard to a final concentration of 1 mM for chemical shift referencing.[63] Next, deuterium oxide (D_2O) was added to the sample to a final concentration of approximately 10% (v/v). The final sample, approximately 500 µL, was then transferred to a nitric acid washed NMR tube and purged multiple times with argon. This step replaced any oxygen in the NMR tube with argon, since any oxygen present will contribute to oxidizing the TCEP HCl and the SOD1 disulfide bond. Lastly, a cap was placed on the NMR tube and sealed with parafilm.

2.2.7 NMR Experiments

The NMR experiments for all SOD1 variants were performed on a Bruker Avance 600 MHz spectrometer with a triple-resonance (TXI) probe (Bruker, Billerica, MA, USA). Depending on the thermostability of the SOD1 variants, the lowest set temperatures for the variable temperature NMR experiments ranged between 6 and 10 °C to higher temperatures ranging between 24 and 40 °C. Additional temperatures for select variants were also studied to determine the effects that heating to the T_m of the protein may have on individual temperature coefficients and conformational heterogeneity. The exact temperature ranges studied for each variant are displayed in Table 3. For all apo2SH SOD1 variants, the temperature was increased in roughly 2 °C increments. For E,Zn2SH pWT SOD1, the temperature was increased in 2.5 °C increments from 10 to 45 °C, before increasing in 5°C increments to 55 °C.

Variant	T_m (°C)	Lowest Set Temperature (°C)	Highest Set Temperature (°C)	Extended Temperature Range (°C)
Apo2SH pWT	47.6	6.0	32.0	N/A
Apo2SH A4V	36.3	6.0	24.0	36.0
Apo2SH H46R	52.6	10.0	38.0	N/A
Apo2SH G85R	40.7	8.0	24.0	N/A
Apo2SH G93A	33.0	8.0	24.0	N/A
Apo2SH E100G	33.2	8.0	24.0	32.0
Apo2SH V148I	51.0	10.0	36.0	N/A
E,Zn2SH pWT	55.0	10.0	40.0	55.0

Table 3: Variable Temperature NMR Temperature Ranges. This table displays the temperature ranges studied by variable temperature NMR for each SOD1 variant, as well as their T_m values.[82,84]

One dimensional excitation sculpting NMR experiments (Bruker pulse program 'zgesgp') were performed to determine the location of the DSS peak, to assist with chemical shift referencing.[139] The location of the ^{1}H-^{15}N crosspeaks used in the subsequent analyses were determined using a ^{1}H-^{15}N HSQC (Bruker pulse program 'hsqcfpf3gpphwg').[140–143] Specific resonance assignments for E,Zn2SH pWT SOD1 were obtained using a three-dimensional ^{15}N-edited NOESY HSQC (Bruker pulse program 'noesyhsqcfpf3gpsi3d').[144–147]

Acquisition and processing parameters for the ^{1}H-^{15}N HSQC can be found in Appendices A and B, respectively.

2.2.8 Resonance Assignments

Resonance assignments for the SOD1 backbone amides have been reported previously for the apo2SH SOD1 variants.[112,135] Resonance assignments were made for E,Zn2SH pWT SOD1 using the NOE crosspeaks obtained from the ^{15}N-edited NOESY HSQC experiment performed at 25 °C and CARA software.[54,148] Reference spectra for each SOD1 variant acquired in this study can be found in Appendix C.

2.2.9 Data Analysis

The NMR data acquired in this project were processed and analyzed using Bruker TopSpin 4.0.6 and CARA softwares.[54,148] Amide proton chemical shifts for each SOD1 variant were directly referenced to DSS in TopSpin 4.0.6, and in CARA, previously reported resonance assignments were transferred onto the re-referenced spectra collected at 24 °C.[112,135] At this temperature, a peak list was created for each re-referenced peak that was assigned to a backbone amide and their respective peak in the non-referenced spectrum. Peak lists were created for the non-referenced spectrum using the peak picking algorithm in TopSpin 4.0.6. The algorithm was set up to locate the 200 most intense peaks in the spectrum between roughly 6.5 and 10.5 ppm in the ^{1}H dimension and between 95 and 135 ppm in the ^{15}N dimension. The algorithm was also set to find the center of each peak using parabolic interpolation. These peak lists were then submitted to the ShiftTrack script of the Shift-T Webserver, created by Dr. Kyle Trainor, along with their respective nominal temperatures and DSS chemical shifts, as well as the peak list containing the backbone amide assignments at the reference temperature, 24 °C.[149] The ShiftTrack script performs numerous tasks such as: calculating temperature differentials, referencing the crosspeaks using the well-established relationship between water and DSS, tracking the crosspeaks over the temperature range, and finally plotting and calculating the temperature coefficient for individual backbone amides.[149]

Following the determination of individual temperature coefficients by Shift-T, the peak tracking data was manually reviewed and corrected, where appropriate. These corrected data were then submitted to Curvalyzer, another script contained within the Shift-T Webserver. Curvalyzer detects and analyzes curvature in the temperature dependences through statistical tests. More specifically, Curvalyzer uses an extra sum-of-squares F-test to determine the statistical significance that a quadratic model is a better fit to the data than a linear model.[149] The curvature data obtained from Curvalyzer is manually reviewed and corrections are made, where appropriate. Curvature in the amide nitrogen temperature dependences was detected and analyzed by swapping the amide nitrogen chemical shift with the amide proton chemical shift data, and resubmitting to Curvalyzer. The temperature coefficient and curvature results were then mapped onto structures of SOD1 using PyMOL and the appropriate PDB files, to assist with interpretation.[72]

In addition to analysis by the Shift-T Webserver, the amide proton chemical shifts were compared to their respective random coil chemical shifts as a measure of the presence of secondary structure elements within apo2SH pWT SOD1. The random coil chemical shifts were obtained by using a chemical shift calculator, coded by Alex Maltsev for Dr. Flemming Poulsen.[49,150–152] This entailed submitting the sequences of the SOD1 variants, along with information about the experiments, such as the reference temperature and the pH of the buffer. Secondary chemical shifts were then calculated by subtracting the random coil chemical shifts from the observed experimental chemical shifts.[46,49] Amide nitrogen temperature coefficients were analyzed by referencing experimentally determined nitrogen temperature coefficients to their random coil temperature coefficients using a script developed by Dr. Kyle Trainor.[61]

2.3 Results and Discussion

2.3.1 New Purification Protocol

The osmotic shock of the A4V SOD1 cells for this new protocol was performed on two samples, each from 1 L of growth media. SDS-PAGE analysis of the samples following the osmotic shock (Figure 2.2) shows the presence of SOD1 in the pellet, water fraction, and sucrose fraction of each sample. The pWT SOD1 gel standard used in this experiment is

partially degraded, which has the benefit of showing where the monomeric form and the partially degraded forms of the protein run on the gel. The pellet fractions are quite impure, as expected; however, due to the presence of proteins in empty lanes, it is likely that one of the pellet samples was overloaded by volume. The sucrose fraction contains two predominant proteins, one of which is A4V SOD1. The water fraction contains numerous proteins present at low concentration, and A4V SOD1, which is present at a much higher concentration than the other proteins, indicating that the osmotic shock was successful.

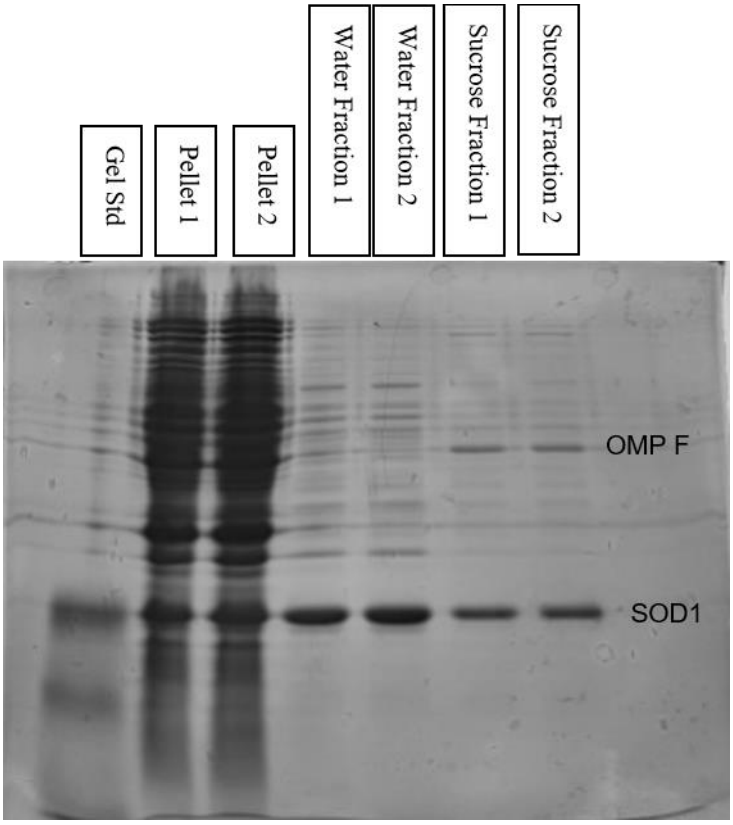

Figure 2.2: SDS PAGE of A4V Osmotic Shock. This gel shows the different fractions following an osmotic shock on two separate 1 L growths (labelled 1,2) of A4V SOD1. The most intense band present in the water and sucrose fractions is A4V SOD1. The other intense band in the sucrose fractions is OmpF.[153]

Almost All Contaminant Proteins Are Removed During Heat Treatment, Method Results in Increased Yield of SOD1

As discussed in Section 2.2.3, following copper-charging and heat treatment at 65 °C for 20 minutes, the precipitated proteins were removed by centrifugation, the supernatant

concentrated by ultracentrifugation, dialyzed against 20 mM HEPES buffer, and finally concentrated to approximately 4 mg/mL by ultracentrigufation. Figure 2.3 shows the SDS PAGE results for the new purification procedure, following the heat treatment step. During the heat treatment, almost all of the contaminating proteins are removed, except for one. The most intense band in the concentrated samples is the desired "holo" A4V SOD1, with the light band below it representing partially degraded SOD1. In the lane containing the final concentrated A4V SOD1, there is also a small proportion, roughly 2-3%, of a protein that is approximately 39 kDa in size. This is most likely the outer membrane protein (Omp) F that is found in the outer membrane of gram negative bacteria such as *E. coli*. OmpF has been previously reported to be approximately 37.5 kDa in size and has a T_m of 87 °C, which is also the melting temperature of holo A4V SOD1.[82,153–155] The T_m of OmpF is well above the temperature for the heat treatment and, therefore, this purification protocol would not be sufficient to remove it. With that said, it is present in such a low concentration, which would only decrease as further steps are taken to prepare the apo2SH A4V needed for the NMR sample, that it should not have an effect on the NMR spectra obtained in the variable temperature NMR experiments. In the NMR experiments performed on the apo2SH A4V SOD1 sample, there was not a noticeable increase in the number of peaks in the ^{1}H-^{15}N HSQC spectra or many peaks whose position had changed relative to apo2SH pWT SOD1, with the exception of peaks that moved due to the A4V mutation that were either close in sequence or in the structure of the protein. This indicates that the OmpF was either degraded or removed during later steps to prepare apo2SH A4V SOD1, or was present in a concentration below the NMR detection. The final yield of "holo" A4V SOD1 is approximately 20 mg per litre of growth media, which is higher than previous purifications performed on A4V SOD1 in the Meiering Lab, which yielded 10-15 mg/L.

The Alternate Purification Protocol may not be Applicable to Mutants with Lower Thermostability

While this method may work on SOD1 variants that have relatively high thermostablity, such as holo A4V, G93A, E100G, and V148I, it may not work as well with less thermostable variants. These less thermostable variants would include metal-binding

mutants such as H46R and G85R, which have melting temperatures between 75 and 80 °C. The heat treatment is generally performed at 20 °C or more below the T_m of the holo form of the variant; however, metal-binding mutants have decreased structural stability due to a lack of one or both metals, meaning that the heat treatment would potentially have to be performed at a lower temperature.[82,84] This would especially be the case for G85R, since it does not show a strong affinity for zinc, which confers structural stability to SOD1.[127] A heat treatment performed at a lower temperature may increase the number of contaminant proteins found in the final concentrated protein, reducing the protocol's effectiveness.

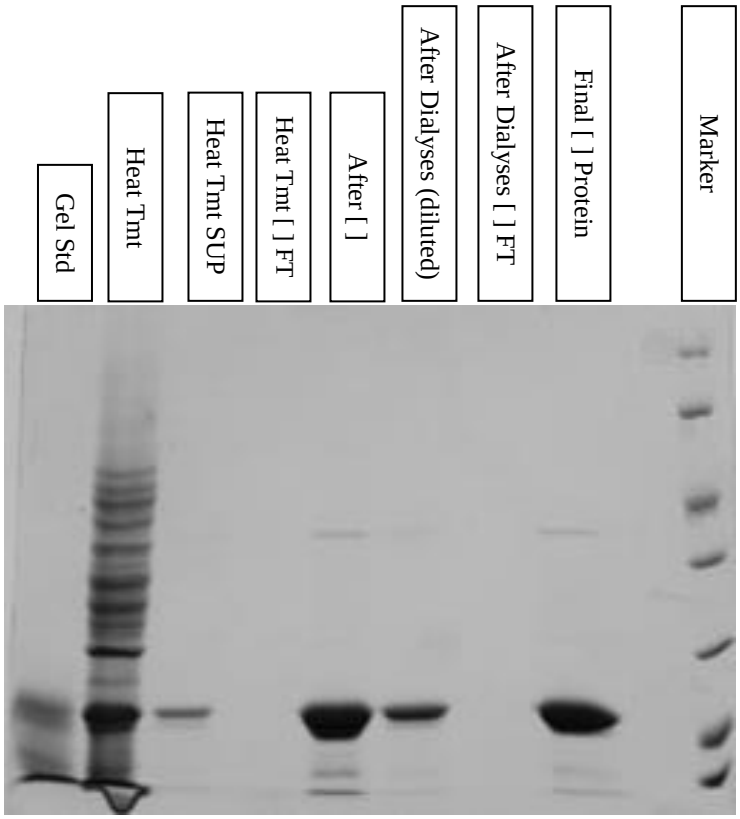

Figure 2.3: SDS PAGE of New SOD1 Purification Procedure. This gel shows samples of A4V SOD1 as it is purified to "holo" A4V SOD1, the final concentrated protein. The protein markers from top to bottom are the following sizes: 116, 64, 45, 35, 25, 18, 14 kDa (Biobasic, Amherst, New York, USA).

2.3.2 Amide Proton Secondary Shifts

As discussed in Section 1.2.4, chemical shifts and secondary chemical shifts are useful information that can provide insight into the local secondary structure elements contained within a protein.[46,48,49] Given that the chemical shift index and secondary chemical shifts for alpha protons and ^{13}C are well established methods of determining the presence of secondary structure elements, it is of interest to use amide ^{1}H secondary chemical shifts to derive low resolution structural information of the apo2SH SOD1 variants.[47,156] Amide ^{1}H secondary chemical shifts are sensitive to secondary structure but are also sensitive to other structural influences, such as changes in the geometry of hydrogen bonds, fluctuations in backbone and side chain torsion angles, and changes in aromatic side chain position.[156,157] Currently, there is no high resolution structure available for apo2SH SOD1; however, it has been suggested that apo2SH SOD1 maintains an 8-stranded β-barrel with disordered loops.[63,135] By determining low resolution structural information of the apo2SH SOD1 variants, valuable information regarding the effects mutations have on the structure of apo2SH SOD1 may be obtained. This structural information would also assist in the interpretation of temperature coefficients and curved temperature dependencies.

Residues Participating in β-strands Often Have Secondary Chemical Shift More Negative than -0.4 ppm, More Positive than 0.4 ppm for Residues in Structured Loops

The secondary chemical shifts were first determined for holo SOD1 variants, using the chemical shift data for holo pWT, G93A, E100G, and V148I obtained by Colleen Doyle, and plotted to investigate if the ^{1}H secondary chemical shift patterns match known SOD1 crystal structures.[158] In holo SOD1, there are 2 beta sheets, consisting of 4 beta strands each, and 2 structured loops, the zinc binding loop, loop 4, which contributes to forming the dimer interface and the zinc binding site, and the electrostatic loop, loop 7, that forms on the other side of the active site.[68] The holo SOD1 secondary chemical shifts are shown in Figure 2.4, along with the changes in secondary chemical shifts ($\Delta\delta_{sec}$) for each mutant, relative to pWT SOD1, in Figure 2.5. From these secondary chemical shift data, regions of the protein that are known to be participating in a β-strand structure generally have secondary chemical shifts more negative than -0.4 ppm.[70,135] In addition to the β-strands, a portion of the electrostatic loop,

residues 124-127, also displays large negative secondary chemical shifts. This region of the electrostatic loop is near β4, which contains residues involved in coordinating the zinc and copper ions, as well as being directly beside K128, which bonds to D76 in the zinc-binding loop.[131,132] This may indicate that this region is highly structured in holo SOD1. We also noted in the experimentally obtained secondary chemical shift data that regions with large positive secondary chemical shifts, greater than 0.4 ppm, correlate well with more structured loop elements.[70] For example, the zinc-binding loop and electrostatic loops is much more structured following the binding of the zinc and copper ions. Furthermore, the loop regions that form part of the dimer interface of holo SOD1, the beginning of loop IV and the C-terminal portion of loop VI, also display large positive secondary chemical shift values, indicating they are also different from random coil.

Secondary Structure in Mutant SOD1 is Identical to that of pWT SOD1 and Any Changes Occur Near the Site of Mutation

When comparing the secondary chemical shift values obtained for the holo mutant SOD1 to pWT, almost all of the secondary chemical shift values remain unchanged, indicating a conserved SOD1 structure across these mutations. Changes greater than 0.1 ppm are seen almost exclusively at or near that sites of mutations. For example, in holo G93A, changes in secondary chemical shift, relative to pWT, are found in loop V, where the mutation is located, and loop III, which is directly beside the site of mutation. From the structural studies mentioned earlier, loop III connects the two β-sheets and is the location of the "β-barrel plug" that is essential to maintaining the structure of the folded SOD1.[116,129] Mutations at the G93 position have been thought to destabilize the β-barrel by affecting the packing of the residues that form the β-barrel plug. In the structure of metal-free G93A, the residues that are displaced the most are residues L38 and D92, both of which are a part of the β-barrel plug.[116] Both of these residues, as well as a couple residues surrounding them, show altered secondary chemical shifts.

When comparing the holo E100G SOD1 secondary chemical shift data to that of pWT, there is only one large noticeable change, at residue V97, which is located in the β5-β6 hairpin.

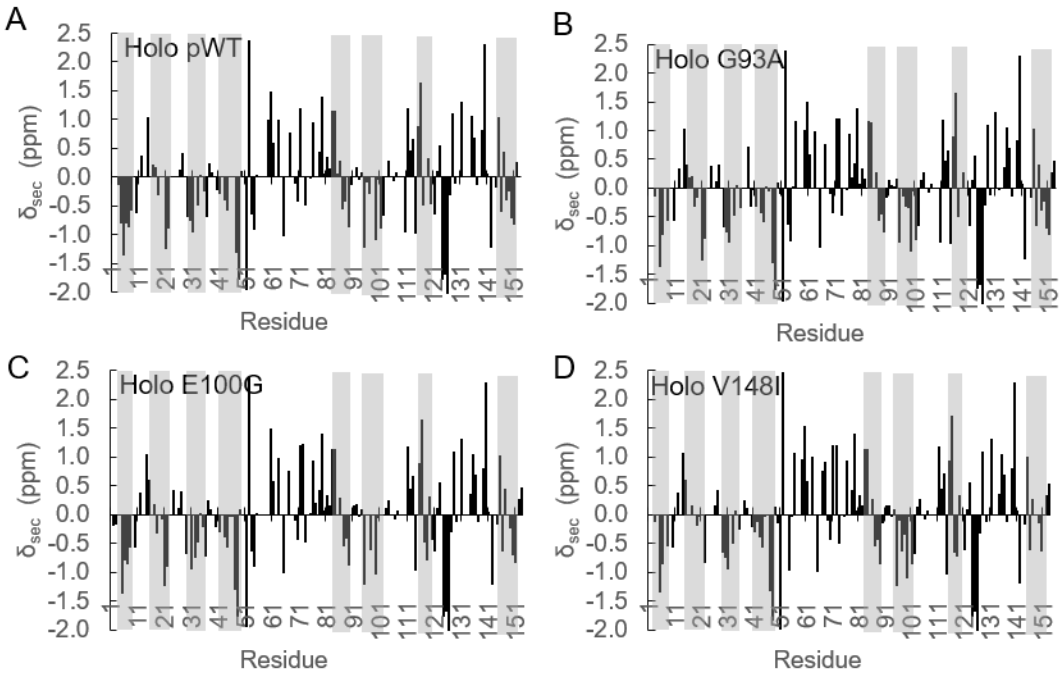

Figure 2.4: Amide ^{1}H Secondary Chemical Shift Data for Holo SOD1 Variants. These graphs display the secondary chemical shift data for holo pWT, G93A, E100G, and V148I SOD1. The dark grey bars on the graphs correspond to the location of the 8 β-strands that make up the SOD1 β-barrel.[70] The chemical shift data used for these comparisons were reported by Doyle *et al.*[63]

While more changes may be expected in the secondary chemical shifts, key residues such as K30, which participates in a salt bridge with the E100 side chain in pWT SOD1, as well as residues D101 and S102, which are directly beside the site of mutation, do not have resonance assignments in holo E100G.[63,131]

Lastly, the changes in secondary chemical shift when the V148I mutation is introduced are relatively consistent with the results for the other mutants, in that the changes occur close to the side of mutation. More specifically, residues G147 and L117, which are both beside the site of mutation in the structure show altered secondary chemical shifts. In addition, residue V97, shows an altered secondary chemical shift, illustrating that mutations may have long range effects on other regions of a protein's structure. Residues A6, D52, G114, T116, I149, and G150, which are all near the site of mutations, also all have $\Delta\delta_{sec}$ values just below the ±0.1 ppm cutoff, indicating that these residues may also experience a slightly altered structure.

Overall, the use of amide ^{1}H secondary chemical shifts appears to be a good indicator of protein secondary structure in SOD1, as seen from these holo SOD1 results.

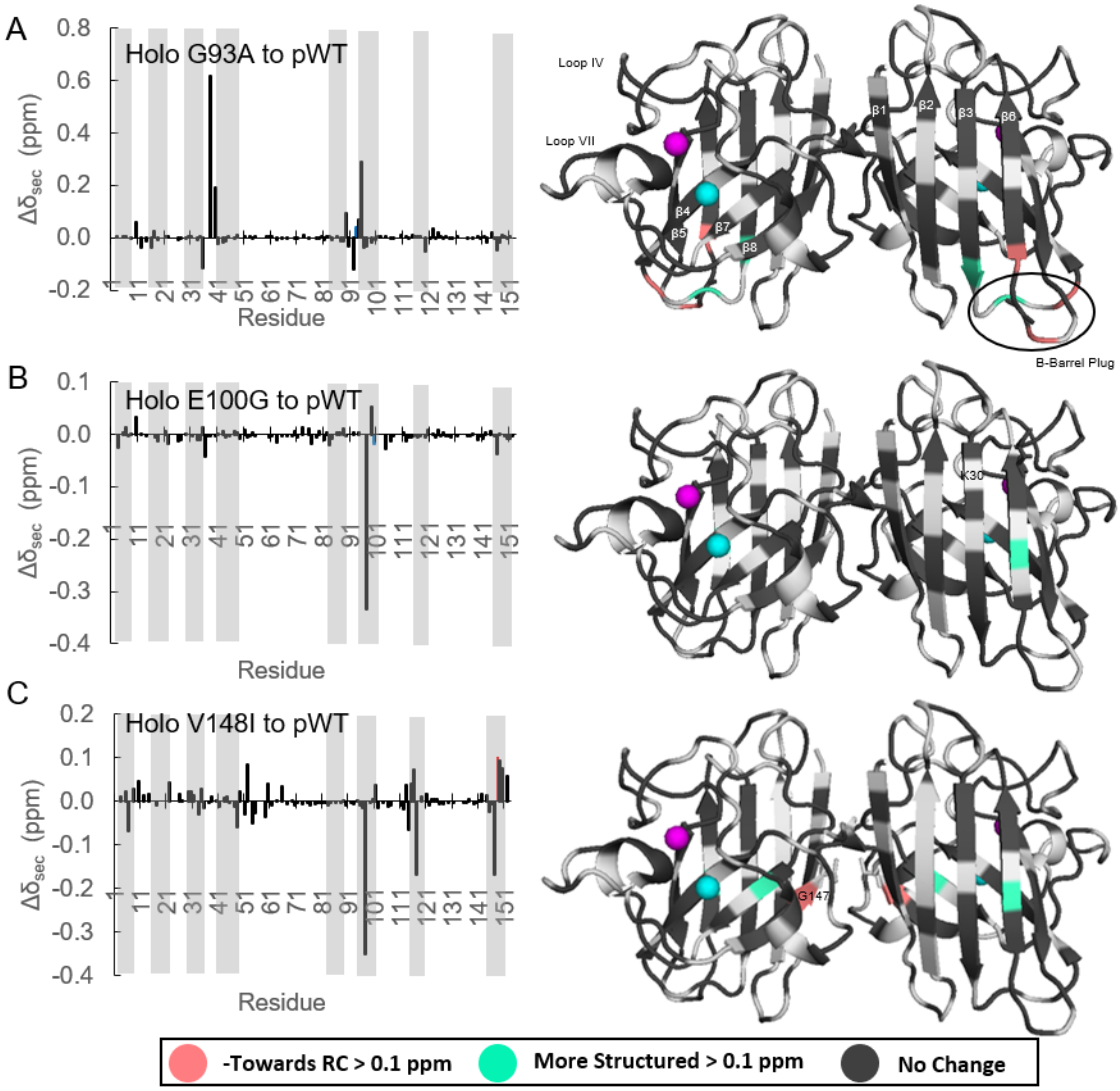

Figure 2.5: Secondary Chemical Shift Data for Holo SOD1 Variants Relative to pWT. These graphs display the changes in secondary chemical shifts for each mutant relative to holo pWT SOD1. The dark grey bars on the graphs correspond to the location of the 8 β-strands that make up the SOD1 β-barrel.[70] Residues coloured white occur where no comparisons could be made. A93 and G100 are shown as blue bars and I148 appears as a red bar (signifying there is no data for this residue) in the respective graphs and the sidechains are shown as sticks in the structural representations of the data. Figures were made using PyMOL and PDB code 1HL5.[70,72] The chemical shift data used for these comparisons was reported by Doyle *et al.*[63]

β-strand Location is Similar in Apo2SH SOD1, Less Structured Loops

Since positive results were obtained for the use of ^{1}H secondary chemical shifts as indicators of protein secondary structure in SOD1, the secondary chemical shifts of apo2SH SOD1 variants and EZn,2SH pWT SOD1 were investigated. Figure 2.6 displays the secondary chemical shifts for a number of apo2SH variants and E,Zn2SH pWT SOD1. Both Figure 2.7 and Figure 2.8 display the change in secondary chemical shifts for the mutant apo2SH SOD1, relative to apo2SH pWT SOD1. First, from each of the secondary chemical shift datasets for the apo2SH variants, most of the residues previously assigned to be in β-strand structure, generally have secondary chemical shifts below -0.4 ppm. Also, given that the loops in apo2SH SOD1 are unstructured and there is very little evidence for helical structure in apo2SH SOD1, there are little to no residues that have secondary chemical shift values larger than 0.4 ppm. The residues that do show secondary chemical shift values larger than 0.4 ppm are generally at the ends of β-strand structure, which corresponds to the first residue in a loop or turn. Notably there are no residues with large positive secondary chemical shifts in the zinc-binding and electrostatic loops of each apo2SH SOD1 variant, indicating that they are largely unstructured without the presence of metal ions and the disulfide bond between Cys57 and Cys 146.[68,135] Conversely, in the top right graph in Figure 2.6, E,Zn2SH SOD1 shows generally well-structured loops, with secondary chemical shift values more positive than 0.4 ppm, and defined β-strands, as described above.

Changes in Secondary Structure Are Largely Localized Near the Site of Mutation, Correlate Well to Data Obtained from Crystal Structures

When examining the effect mutations have on the secondary chemical shifts found in the apo2SH SOD1 variants, the patterns are similar to the ones observed in holo SOD1 variants, with the majority of changes occurring near the site of mutation. In A4V, the residues that show the largest changes in secondary chemical shift are V5, A6, S105, G114, and A152. Each of these residues are in the vicinity of V4, with the exception of S105, which is beside L106, a residue whose sidechain points directly at the V4 sidechain. As mentioned in Section 2.1.2, in the crystal structure of metal-free disulfide-intact (dimeric) A4V, the residues that are in

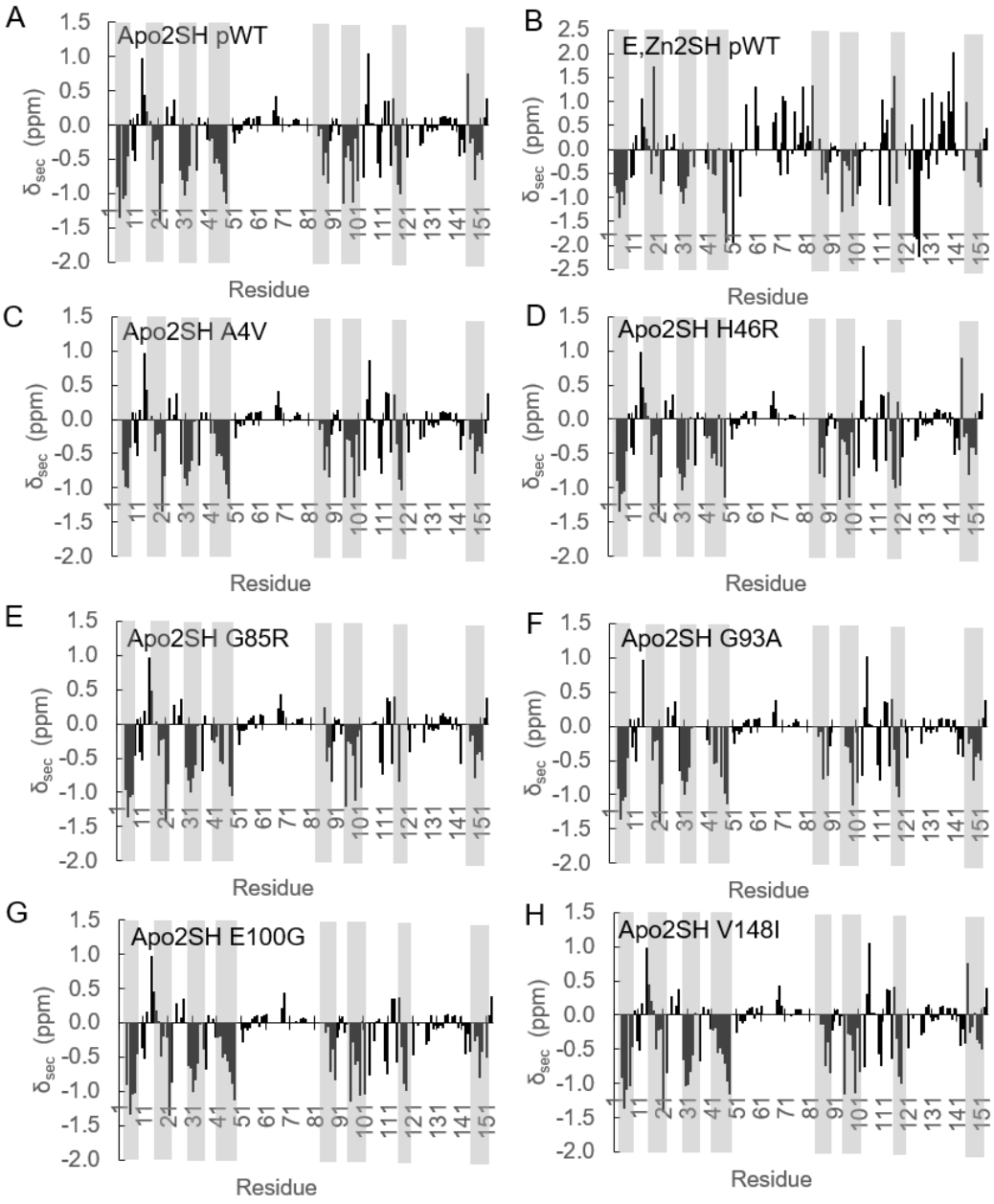

Figure 2.6: Secondary Chemical Shift Data for apo2SH and E,Zn2SH SOD1. These graphs display the secondary chemical shift data for the SOD1 variants mentioned above. The dark grey bars on the graphs correspond to the location of the 8 β-strands that make up the SOD1 β-barrel in holo SOD1.[70]

close proximity and displaced the most are L106 and I113.[116] As expected both L106 and I113 are beside residues that have an altered secondary chemical shift, both of which become more random coil-like. Mutations that disrupt the dimer interface, such as A4V and I113T, may

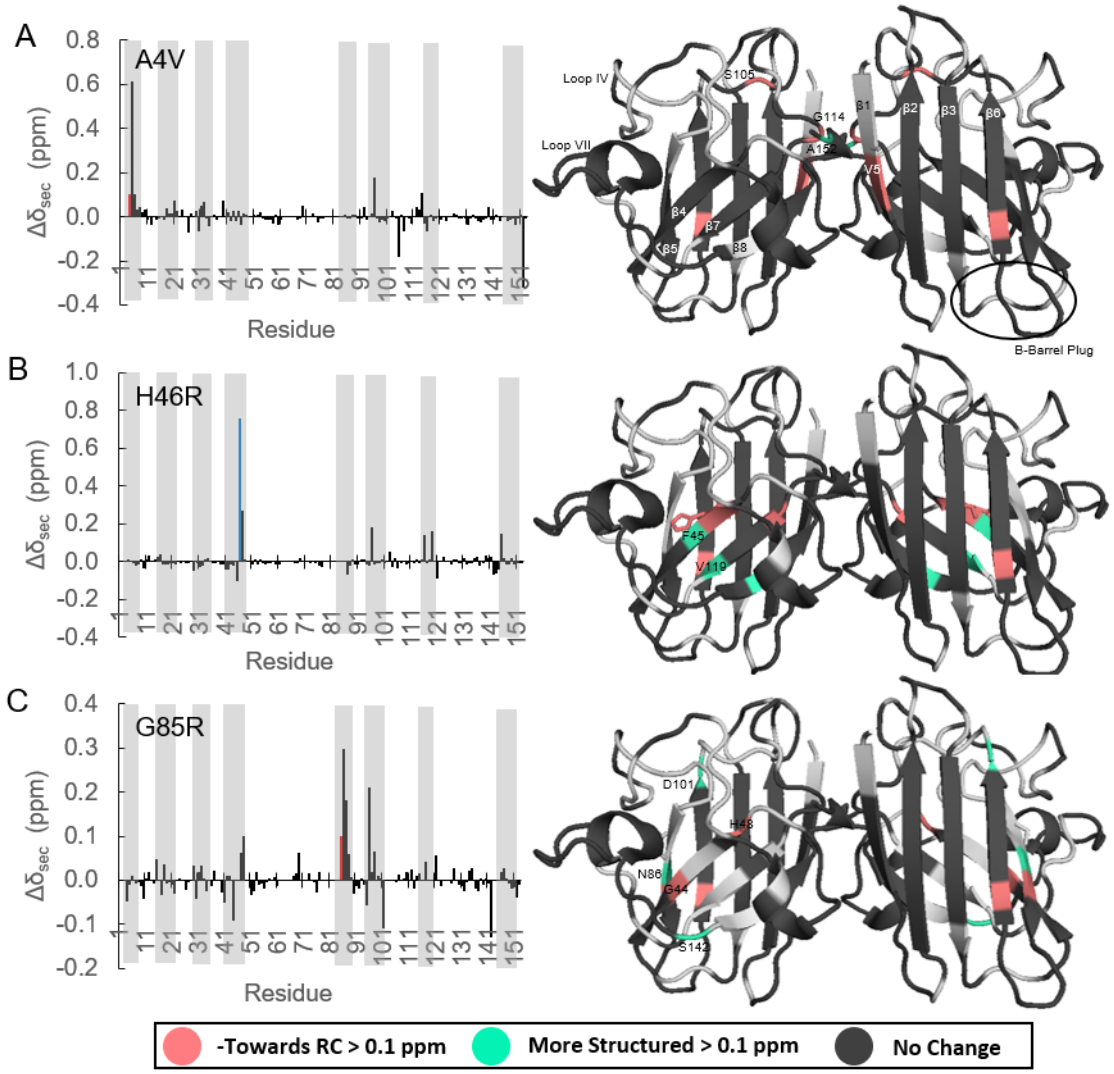

Figure 2.7: Secondary Chemical Shift Data for apo2SH A4V, H46R, and G85R SOD1 Relative to pWT. These graphs display the secondary chemical shift data for the SOD1 variants mentioned above and the changes in secondary chemical shift for (A) A4V, (B) H46R, and (C) G85R relative to apo2SH pWT SOD1. The dark grey bars on the graphs correspond to the location of the 8 β-strands that make up the SOD1 β-barrel in holo SOD1.[70] Residues coloured white occur where no comparisons could be made. R46 is shown as a blue bar and both V4 and R85 appears as red bars (signifying there is no data for these residues) in the respective graphs. The sidechains are shown as sticks in the structural representations of the data. Figures were made using PyMOL and PDB code 1HL5.[70,72]

affect the hydrogen bonding pattern of G114. This residue is involved, in dimeric SOD1, in intermolecular hydrogen bonding with another SOD1 monomer at the dimer interface, strengthening the dimer interface.[122] Therefore, the loss of structure at residue G114 may contribute to the destabilization of the dimer interface observed in this mutant.[119,122]

In H46R, the largest changes in secondary chemical shift are found at residues F45, H46, V47, T116, V119, and A145. These residues surround R46 in the structure of the protein. For example, F45 is immediately beside V119, which is also directly beside A145. Also, V47 and T116 are beside each other. All of these residues are located at or around the copper binding site, which agrees with the weakened copper binding of this mutant.[123]

In G85R, the most notable changes occur at H48, N86, V87, D96, D101, and S142. Some of these residues are located beside the R85 mutation and in the β5-β6 hairpin. The most notable of these is D101, which forms a hydrogen bond with R79. This hydrogen bond is one of two securing the zinc-binding loop to the β-barrel.[127] Also, the change in secondary chemical shift for G44 is just below the cutoff of ±0.1 ppm. This value may reflect a real change in the structure of the protein, as the hydrogen bonding network between β4 and β5 is weakened in G85R due a water molecule forming hydrogen bonds to the sidechain of D124 and the amide nitrogen of F45, which does not occur in WT SOD1.[127] The change in secondary chemical shift of G44, may reflect the change in F45's structure, which does not have a resonance assignment in G85R, and the weakening of the hydrogen bond network between β4 and β5. The other two residues, H48 and S142 are both present in or around the copper binding site. One of these, H48, is a copper ligand, while the other, S142, is directly beside the catalytically important R143.[87] These structural changes may account for the decreased copper affinity and lower catalytic activity of G85R.[159]

G93A is also in the β5-β6 hairpin and near the β-barrel plug, which is made of portions of loops III and V. The most striking changes in secondary chemical shift are in residues A89 and D96, both at the bottoms of β5 and β6, respectively. Also, in previous structural studies on metal-free G93A, the residues that are displaced the most are L38 and D92, both forming part of the β-barrel plug.[116] Interestingly, assignments for the residues previously assigned in all other apo2SH SOD1 variants, within or on the edges of loops III (residues 36, 37, & 39) and V (residues 91-95), encompassing the β-barrel plug have been lost in G93A, supporting a potentially different structure of the β-barrel plug in G93A.

The last of the mutations in the β5-β6 hairpin, E100G, also causes numerous changes in secondary chemical shift around the site of mutation. For example, the largest changes in

secondary chemical shift occur at residues K30, D96, V97, G100, D101, and S105. Most of these are in the β6 strand, indicating an altered structure compared to pWT, while S105 is a

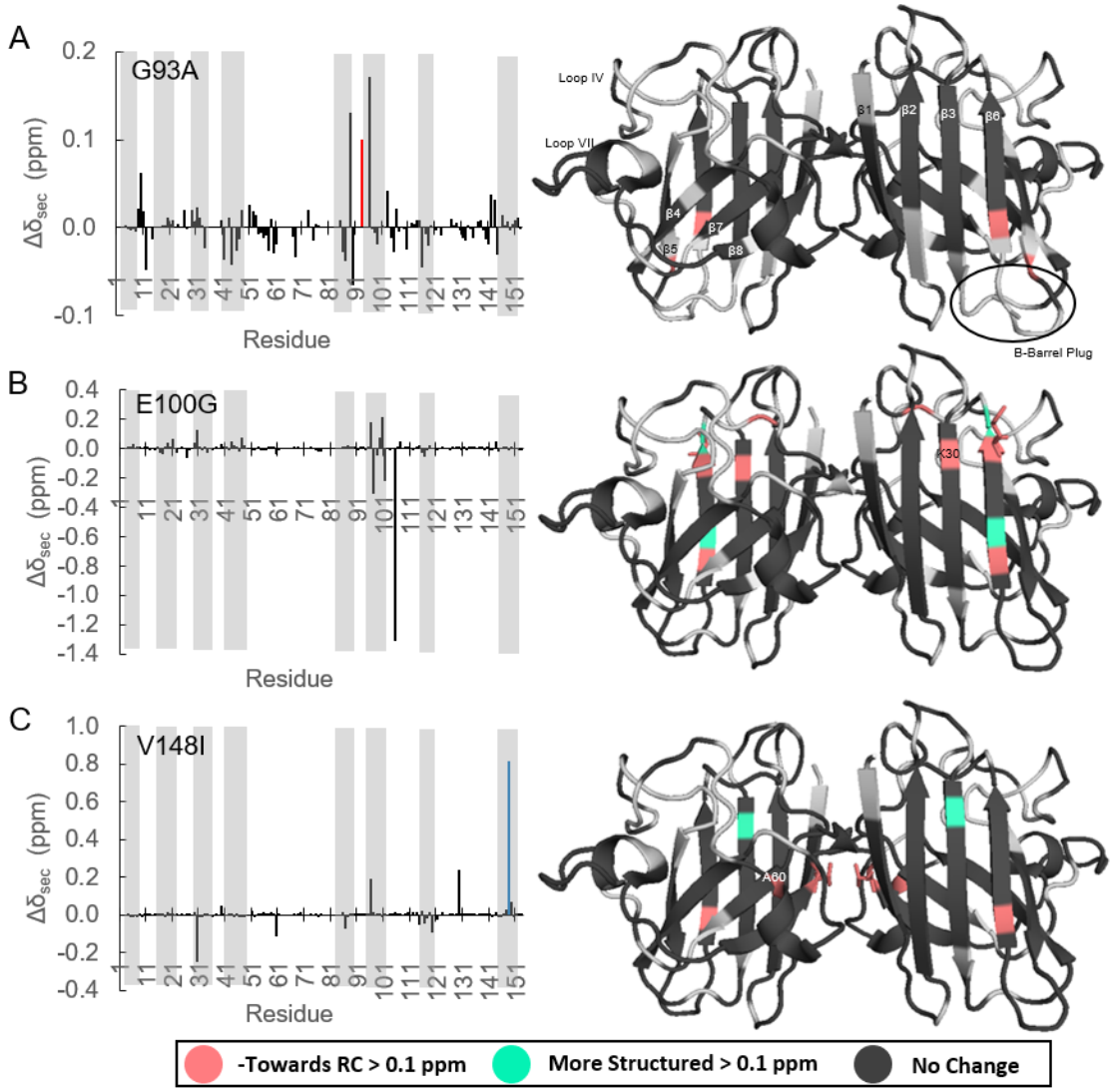

Figure 2.8: Secondary Chemical Shift Data for apo2SH G93A, E100G, and V148I SOD1 Relative to pWT. These graphs display the secondary chemical shift data for the SOD1 variants mentioned above and the changes in secondary chemical shift for (A) G93A, (B) E100G, and (C) V148I relative to apo2SH pWT SOD1. The dark grey bars on the graphs correspond to the location of the 8 β-strands that make up the SOD1 β-barrel in holo SOD1.[70] Residues coloured white occur where no comparisons could be made. G100 and I148 are shown as blue bars and A93 appears as a red bar (signifying there is no data for this residue) in the respective graphs. The sidechains are shown as sticks in the structural representations of the data. Figures were made using PyMOL and PDB code 1HL5.[70,72]

part of the loop directly following β6. As expected, changes are observed for D101, which is directly beside the site of mutation and, as discussed earlier, forms one of two hydrogen bonds that tethers the zinc-binding loop to the β-barrel and bridges the β5-β6 hairpin at its widest point. A disruption to the bond between R79 and D101 may result in the opening of the β5-β6 hairpin, decreasing the protection of the two edge strands and promoting aggregation.[127,131] Also discussed earlier in Section 2.2.2, a disruption to the salt bridge between D101 and R79, may result in an altered zinc-binding loop and, through the bond between D76 and K128, an altered electrostatic loop.[131,132] Also, a change is observed for K30, a residue beside the site of mutation in β3, part of the electrostatic network across the first β-sheet and forms a salt bridge with E100 in pWT SOD1.[63,131] As a consequence of the mutation from E to G, this salt bridge is disrupted.

Lastly, V148I, shows fewer changes in secondary chemical shifts, indicating that it is the most similar in structure to apo2SH pWT SOD1. The changes in secondary chemical shift occur for residues K30, A60, G129, and I148; however, the secondary chemical shift for G129 changes in sign (from negative to positive) but not in magnitude, indicating that it is still close to random coil. Other than the secondary chemical shift for the site of mutation (I148) changing, another residue nearby and also in the dimer interface region, A60, experiences a change in secondary chemical shift. In addition, K30 shows a change in secondary chemical shift, which may indicate a long distance effect of the V148I mutation that either could affect the electrostatic network across the first β-sheet, or a slight change in the β5-β6 hairpin, observed through the salt bridge connecting K30 and E100.[63,131]

In many of the cases discussed above, the results illustrate how the effects of a mutation can propagate through a protein, disrupting secondary structure elements, especially those near the site of mutation. In general, these disruptions in secondary structure elements, as determined by changes in secondary chemical shifts, match well with the changes in structure and disruptions observed in the crystal structures of SOD1 variants. In addition, there are more disruptions to the apo2SH forms of SOD1 than the holo forms of SOD1. This matches expectations as apo2SH SOD1 has been shown to be less structurally stable than holo SOD1, as a result of the monomeric form lacking metals and possessing a reduced disulfide

bond.[63,79,82,83] While amide proton secondary shifts may be influenced by other structural factors, these data suggest that they may be useful in defining regions of a protein where structure is altered, and typically disrupted, in mutants.

2.3.3 Amide Proton Temperature Coefficients

As discussed earlier, amide proton temperature coefficients are a valuable high resolution probe of local temperature-dependent loss of structure, also known as the structural stability, of a protein.[58,63] In addition, temperature coefficients have the benefits of being sensitive to hydrogen bond formation, with intramolecularly hydrogen bonded amides generally exhibiting temperature coefficients more positive than -4.6 ppb/K and intermolecular hydrogen bonded amides generally exhibiting temperature coefficients more negative than -4.6 ppb/K.[53,56,57] This section aims to discuss the various effects mutations have on the local structural stability of apo2SH SOD1, using amide proton temperature coefficients. The temperature ranges studied for each mutant are summarized in Table 3.

Stabilizing Mutations Result in More Positive Average Temperature Coefficients While Destabilizing Mutations Result in More Negative Values

The temperature coefficients for each of the SOD1 variants studied are displayed in the ribbon diagrams in Figure 2.9. All apo2SH SOD1 variants are shown on the structure of holo pWT SOD1, 1HL5, since no high resolution structures are available.[70] While the apo2SH state of SOD1 exists in a monomeric form, Figure 2.9 displays the data as a dimer, both to highlight the region that would participate in forming the dimer interface in later maturation states and to display the temperature coefficient patterns found in both β-sheets. The average temperature coefficient of each variant, along with the average temperature coefficient of each structural feature is given in Table 4 and Table 5. Table 4 summarizes the average temperature coefficients of all residues assigned in each of the variants. Table 5 also summarizes the average temperature coefficients for the SOD1 variants and the secondary structure elements, but with residues that are assigned across all variants. Notably, the destabilizing mutants A4V, G85R, G93A and E100G, all have more negative average temperature coefficients than pWT, while the stabilizing mutations, H46R and V148I, have similar or more positive values. In

general, unstructured regions in apo2SH SOD1, such as the dimer interface, zinc-binding loop, and electrostatic loop, all have large negative amide proton temperature coefficients. Conversely, regions that are thought to be more structured, namely the β-strands, show more positive temperature coefficients.[135] This supports that more positive temperature coefficients are often associated with an increased structural stability. In fact, the majority of the residues present in the β-strands have temperature coefficients more positive than -4.6 ppb/K, indicating that they are involved in intramolecular hydrogen bonds, while the residues in less structured regions, such as the electrostatic loop and zinc binding loop, have temperature coefficients indicative of intermolecular hydrogen bonding with bulk water.[57,58]

The average temperature coefficients for each apo2SH SOD1 variant are compared to other thermodynamic parameters, obtained by Vassall *et al.*, in Figure 2.10.[84] Here, it is observed that the ΔG_{37C} and T_m values obtained by Vassall *et al.* correlate well to each other, as do the average temperature coefficients of each variant to both the variants' T_m and ΔG_{37C} values.[84] In Figure 2.10 (B), the average temperature coefficient of G85R is more negative than expected; however, this could be attributed to fewer assignments in this mutant when compared to other apo2SH variants, as a result of a more altered structure. For E,Zn2SH pWT SOD1, there are fewer large negative temperature coefficients, especially in the dimer interface region, metal-binding region, and the electrostatic loop, which can be attributed to the increase in structural stability as a result of zinc-binding (Figure 2.9). Changes in temperature coefficients as a result of SOD1 maturation from apo2SH to E,Zn2SH pWT SOD1 will be further discussed in Section 3.3.2.

Mutations Affect the Structural Features They are Contained Within and Those Nearby

The average temperature coefficients of each structural feature, displayed in Table 4, provide an assessment of each feature's overall stability and may also provide insights into dynamic regions in apo2SH SOD1. In general, the average temperature coefficients of the β-strands are more positive than those for the loops, as expected. The average temperature coefficients are relatively consistent across all variants for β-strands 1, 2, and 3, as well as loops I, II, and II. In contrast, loop III exhibits a larger variation in average temperature

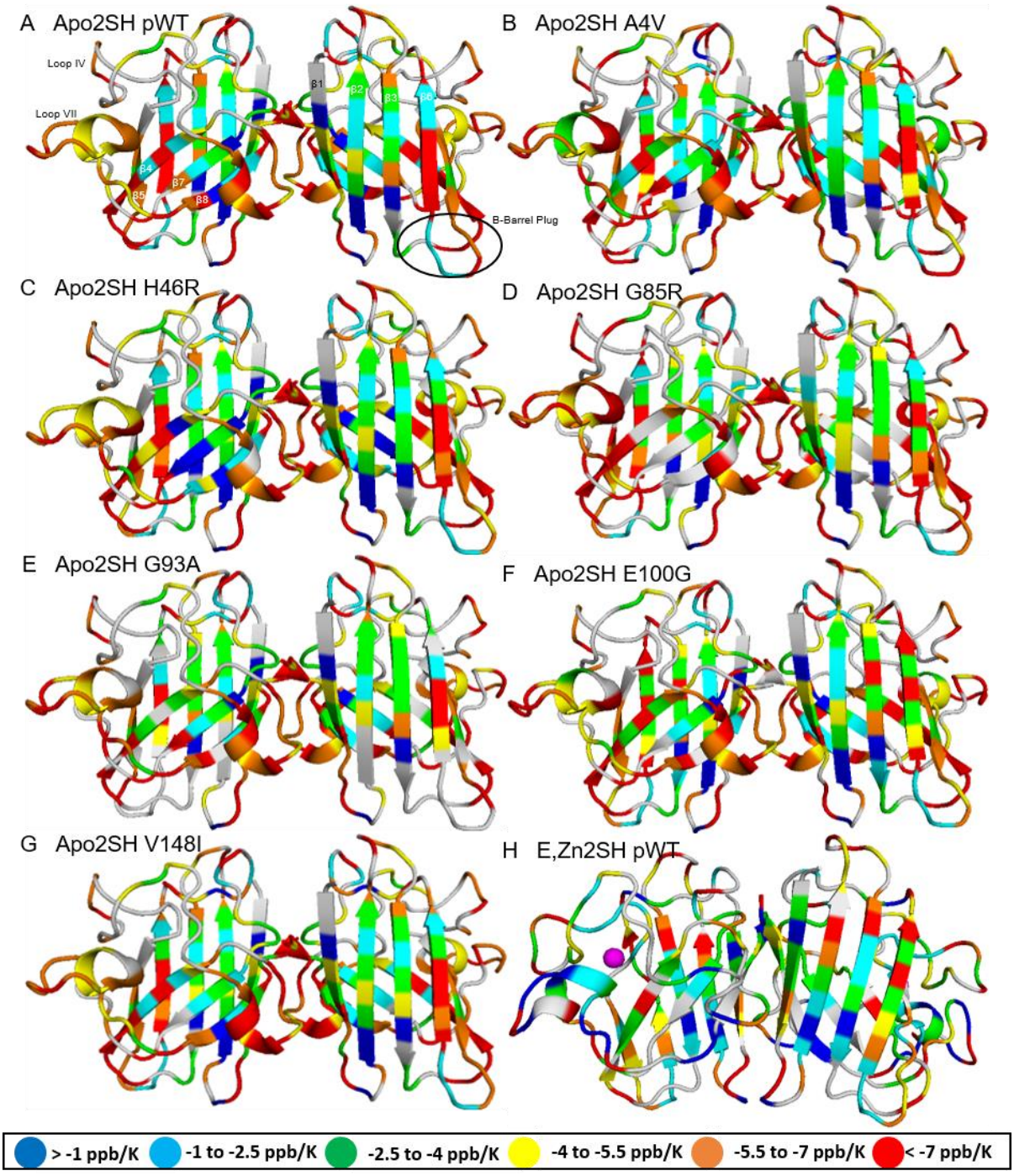

Figure 2.9: ^{1}H Temperature Coefficients of apo2SH Variants and E,Zn2SH pWT SOD1. Displayed are ^{1}H temperature coefficients for apo2SH SOD1 variants (A) pWT, (B) A4V, (C) H46R, (D) G85R, (E) G93A, (F) E100G, and (G) V148I, and (H) E,Zn2SH pWT SOD1. The zinc ion in E,Zn2SH SOD1 is coloured magenta. Residues coloured white are unassigned. Figures were made using PyMOL and PDB codes 1HL5 (apo2SH SOD1) and 2AF2 (E,Zn2SH pWT SOD1).[70,72,160]

coefficients, especially for G85R and G93A; however, these mutants also have less assignments in this region, while the residues that are assigned have temperature coefficients similar to those residues in the other variants. In β-strand 4, there is a wider range of average temperature coefficient values. Apo2SH A4V, H46R, and G93A all have more positive values; however, G93A has less assignments here and when comparing values for similar assignments, its β4 average temperature coefficient is similar to those of pWT, E100G, and V148I. Conversely, apo2SH G85R has a more negative average temperature coefficient and despite having less assignments, the individual temperature coefficients of these residues are more negative than those in other variants. This indicates that β4, which is involved in metal binding, has decreased structural stability in apo2SH G85R.

The first portion of the zinc-binding loop, which is comprised of residues 50-62, is in the dimer interface region of the protein. While most of the average temperature coefficients are similar, that region in A4V has a more negative value, suggesting that this region has decreased structural stability. The second portion of the zinc-binding loop, comprising residues 63-82, is involved in metal-binding. G85R, a mutation which affects the binding of zinc, is the only mutant that shows a more negative average temperature coefficient in this region. G85R is also the only mutant, that has a decreased average temperature coefficient in β-strand 5, where the site of mutation is located. In the next structural feature, loop V, both A4V and G93A display more negative temperature coefficients. Even though only one residue is assigned in this loop in G93A, the value of this temperature coefficient is significantly more negative than in other apo2SH SOD1 variants. In both β-strand 6 and loop VI, the average temperature coefficients are fairly consistent; however, E100G displays the most negative temperature coefficients for both of these structural features. With respect to β-strand 7, one of the strands that contains residues involved in metal-coordination, the average temperature coefficient is more positive in H46R, a mutation that results in increased stability but decreased affinity for copper binding, and more negative in both A4V, which is nearby in the structure, and G85R, which displays decreased metal affinity.[123,159] In addition, G85R also exhibits the most negative average temperature coefficient in loop VII, the electrostatic loop, and H46R displays the most positive value. This matches expectations, as the G85R mutation decreased zinc-

	pWT	A4V	H46R	G85R	G93A	E100G	V148I
Average	-5.35	-5.53	-5.00	-5.86	-5.69	-5.66	-5.38
# Res	119	116	117	104	100	113	117
Average Tamperature Coefficient by Structural Feature (ppb/K)							
N	N/A	N/A	N/A	N/A	N/A	N/A	N/A
β1	-4.21 (5)	-4.66 (5)	-4.15 (5)	-4.24 (5)	-4.49 (5)	-4.33 (5)	-4.67 (5)
Loop I	-5.71 (4)	-5.73 (4)	-5.54 (4)	-5.90 (4)	-5.99 (4)	-5.99 (3)	-5.29 (4)
β2	-2.25 (9)	-2.06 (9)	-2.17 (9)	-2.58 (9)	-3.77 (6)	-2.24 (9)	-2.18 (9)
Loop II	-6.03 (3)	-6.09 (3)	-5.98 (3)	-5.96 (3)	-6.28 (3)	-6.24 (3)	-6.04 (3)
β3	-3.26 (7)	-3.21 (7)	-2.90 (7)	-3.53 (7)	-3.54 (6)	-3.66 (8)	-3.18 (7)
Loop III	-11.26 (3)	-12.39 (2)	-11.80 (3)	-6.29 (2)	-9.29 (1)	-11.59 (3)	-11.66 (3)
β4	-6.73 (8)	-5.44 (8)	-5.92 (8)	-8.43 (6)	-5.47 (6)	-6.99 (8)	-6.97 (8)
Loop IV (part 1)	-6.68 (11)	-7.10 (11)	-6.38 (10)	-6.59 (10)	-6.73 (11)	-6.86 (11)	-6.78 (11)
Loop IV (part 2)	-5.71 (7)	-5.89 (7)	-5.71 (7)	-6.73 (7)	-5.95 (6)	-5.84 (6)	-5.72 (7)
β5	-5.61 (5)	-5.34 (5)	-5.58 (3)	-6.40 (4)	-5.65 (4)	-5.75 (5)	-5.74 (5)
Loop V	-4.02 (4)	-5.44 (4)	-3.70 (4)	-4.07 (4)	-8.59 (1)	-3.80 (4)	-3.83 (4)
β6	-5.75 (8)	-5.53 (8)	-5.18 (8)	-5.88 (8)	-5.98 (5)	-6.02 (8)	-5.38 (8)
Loop VI	-4.47 (10)	-4.44 (10)	-4.12 (10)	-4.56 (7)	-4.80 (10)	-4.93 (9)	-4.43 (10)
β7	-2.84 (5)	-4.52 (5)	-1.54 (6)	-4.22 (2)	-3.03 (5)	-3.30 (4)	-2.94 (4)
Loop VII	-6.51 (19)	-6.83 (19)	-6.39 (19)	-7.87 (18)	-7.04 (17)	-6.83 (18)	-6.66 (18)
β8	-4.38 (9)	-5.40 (7)	-3.87 (9)	-5.63 (6)	-6.11 (8)	-5.55 (7)	-4.21 (9)
C	-7.42 (2)	-8.52 (2)	-7.29 (2)	-7.66 (2)	-7.25 (2)	-7.45 (2)	-7.52 (2)

Table 4: Temperature Coefficients for Apo2SH SOD1 Variants. Temperature coefficient data for each of the apo2SH SOD1 variants studied are summarized here. The first portion of the table describes the average temperature coefficients for each apo2SH variant and the number of residues that data is available for. The second portion of the table describes the average temperature coefficient for each structural feature of SOD1, with the average temperature coefficient found beside the parentheses containing the number of residues for which data is available. Loop IV is separated into two parts, the first passes through the dimer interface region while the second is involved in the binding of the zinc ion.

	pWT	A4V	H46R	G85R	G93A	E100G	V148I
Average of Same Res. (87)	-5.43	-5.45	-5.31	-5.97	-5.70	-5.59	-5.45
β-Sheet 1 (21)	-4.43	-4.34	-4.11	-4.36	-4.40	-4.52	-4.35
β-Sheet 1 (15)	-4.98	-5.04	-5.11	-6.09	-5.28	-5.43	-5.18
Average Tamperature Coefficient by Structural Feature (ppb/K)							
N-terminus (0)	N/A	N/A	N/A	N/A	N/A	N/A	N/A
β1 (5)	-4.21	-4.66	-4.15	-4.24	-4.49	-4.33	-4.67
Loop I (3)	-6.47	-5.46	-6.21	-5.72	-5.94	-5.99	-6.01
β2 (6)	-4.12	-4.05	-3.98	-4.05	-4.18	-4.24	-4.09
Loop II (3)	-6.03	-6.09	-5.98	-5.96	-6.28	-6.24	-6.04
β3 (6)	-3.27	-3.17	-2.88	-3.62	-3.54	-4.11	-3.11
Loop III (1)	-3.01	-2.67	-3.41	-3.07	N/A	-3.20	-3.49
β4 (5)	-5.63	-4.87	-6.01	-8.01	-5.99	-5.88	-6.03
Loop IV Part 1 (10)	-6.43	-6.91	-6.38	-6.59	-6.50	-6.59	-6.48
Loop IV Part 2 (6)	-5.81	-5.48	-5.79	-6.41	-5.95	-5.84	-5.88
β5 (2)	-4.53	-3.87	-5.12	-5.79	-5.21	-4.91	-4.99
Loop V (1)	-5.73	-5.10	-5.11	-5.72	-8.59	-4.85	-5.65
β6 (5)	-7.03	-6.67	-6.27	-6.20	-5.98	-6.18	-6.38
Loop VI (7)	-4.40	-4.51	-4.29	-4.56	-4.64	-4.71	-4.27
β7 (2)	-3.51	-6.04	-3.18	-4.22	-3.45	-6.32	-4.06
Loop VII (18)	-6.17	-6.29	-6.05	-7.79	-7.04	-6.34	-6.29
β8 (5)	-5.13	-5.02	-5.00	-5.21	-5.49	-4.95	-4.89
C-terminus (2)	-7.42	-8.52	-7.29	-7.66	-7.25	-7.45	-7.52

Table 5: Average Temperature Coefficients of Same Residues Across Apo2SH SOD1 Variants. Temperature coefficient data for each of the apo2SH SOD1 variants studied are summarized here. The first portion of the table describes the average temperature coefficients for each apo2SH variant and the two β-sheets that form the β-barrel. The second portion of the table describes the average temperature coefficient for each structural feature of SOD1. Loop IV is separated into two parts, the first passes through the dimer interface region while the second is involved in zinc binding. The number of residues assigned across all apo2SH SOD1 variants for each structural feature are in parentheses.

binding affinity and has shown to possess an altered hydrogen bonding network in the vicinity and the H46R mutation is known to stabilize the protein, one part of which is the association of the metal-binding region with the electrostatic loop.[123,127] In β-strand 8, there is a distinct separation between the average temperature coefficients for the destabilizing mutation, A4V,

G85R, G93A, and E100G, and pWT and the stabilizing mutations, H46R and V148I. The destabilizing mutations all result in more negative temperature coefficient values, indicating a decreased structural stability, while the pWT and stabilizing mutations all possess more positive temperature coefficients, indicating an increased structural stability. Lastly, the average temperature coefficients for the C-terminal residues are relatively consistent between all variants, with the exception of A4V, which is a mutant with a significantly destabilized dimer interface region.[119,122] Overall the changes in temperature coefficients for secondary structural elements correlate well with the changes in stability measured by other means and are consistent with the structural consequences of the mutations.

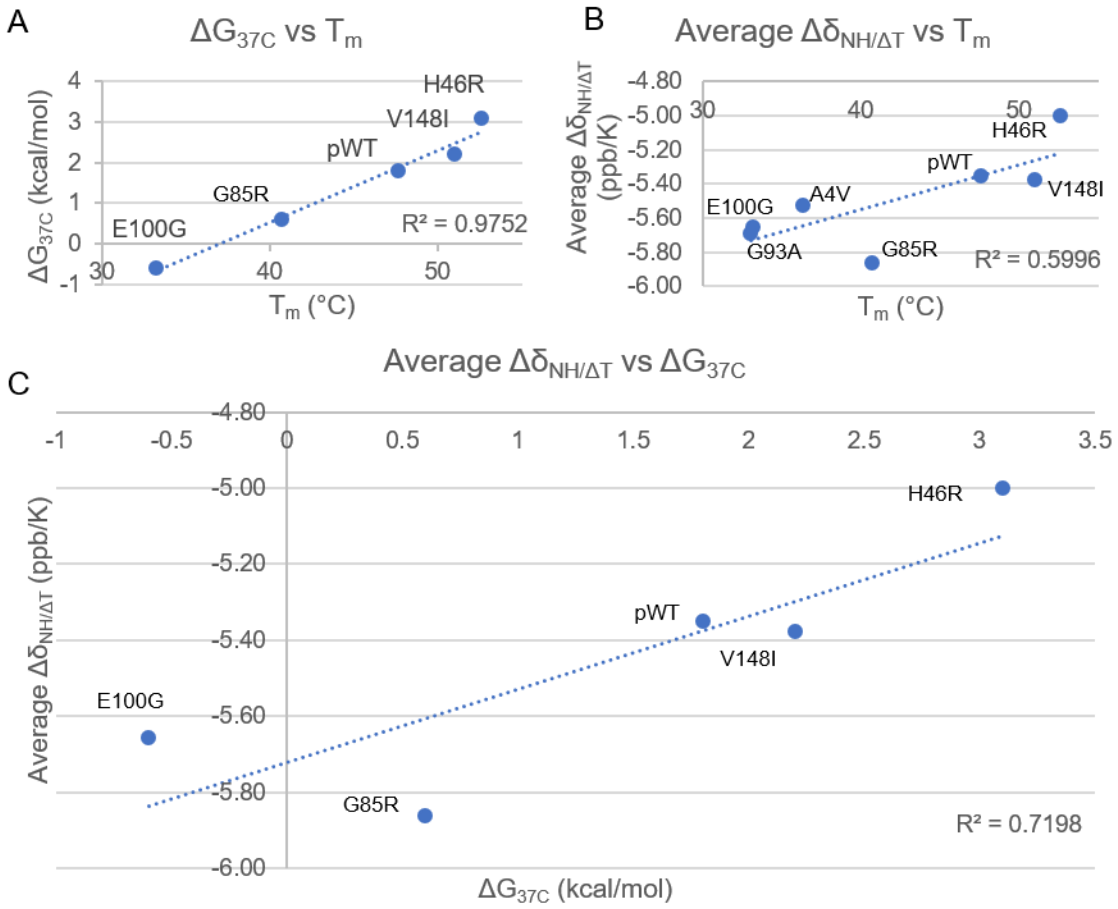

Figure 2.10: Apo2SH SOD1 Comparison of Thermodynamic Parameters. These graphs display the comparisons between the (A) ΔG_{37C} vs T_m values, (B) average temperature coefficients vs T_m, and (C) the average temperature coefficient vs ΔG_{37C} for the variants studied, where appropriate. The ΔG_{37C} and T_m values are found in Table 1 and were obtained from Vassall *et al.*[84]

Dimer Interface Mutants Affect Temperature Coefficients of Other Residues in the Dimer Interface, A4V Also Affects the Hydrophobic Residues Pointing Into the Core of the Protein

Displayed in Figure 2.11 are the differences in temperature coefficients for the dimer interface mutants A4V and V148I, relative to apo2SH pWT SOD1. Figure 2.11 (A) shows the change in temperature coefficients due to the A4V mutation. Residues that are coloured increasingly deep shades of red are destabilized upon the mutation, while residues coloured increasingly deep shades of blue are stabilized upon mutation. Residues coloured dark grey do not experience changed temperature coefficients and residues coloured white cannot be compared due to a lack of data in one or both variants. From Figure 2.11 (A), the majority of the residues in A4V do not exhibit changes temperature dependences, suggesting that the structure and stability of these residues are similar to pWT, which matches expectations since the two variants are related and should have generally similar structures, as seen in the data presented in Section 2.3.2. Also, there are more residues destabilized by the A4V mutation (16 in total) than stabilized (11 in total). Many of the destabilized residues in apo2SH A4V SOD1 are in the dimer interface region, which is destabilized in A4V, and near the site of mutation.[119] For example, as discussed earlier, L106 and I113 are disturbed the most in the structure of A4V. Residues at or around these sites experience changes temperature dependences, such as S105, L106, S107, R115, and T116 all with more negative temperature coefficients, and G114 with a more positive temperature coefficient. These data are consistent with the previous structural findings and the observation that mutations disrupting the dimer interface, such as A4V and I113T, may weaken the hydrogen bonding of G114, a residue involved in intermolecular hydrogen bonding with the other SOD1 monomer at the dimer interface, strengthening the dimer interface.[116,122]

Another residue affected in the structure of A4V is F20, a hydrophobic residue pointing into the hydrophobic core of the protein.[116] While the temperature coefficient of F20 does not change, the temperature coefficient of the proceeding residue, N19, suggests it is stabilized by the A4V mutation. There is a similar pattern in some of the other residues, where the temperature coefficient of either a hydrophobic residue whose sidechain points into the core of the protein, such as F45 and I149, or a residue nearby to those hydrophobic residues, such

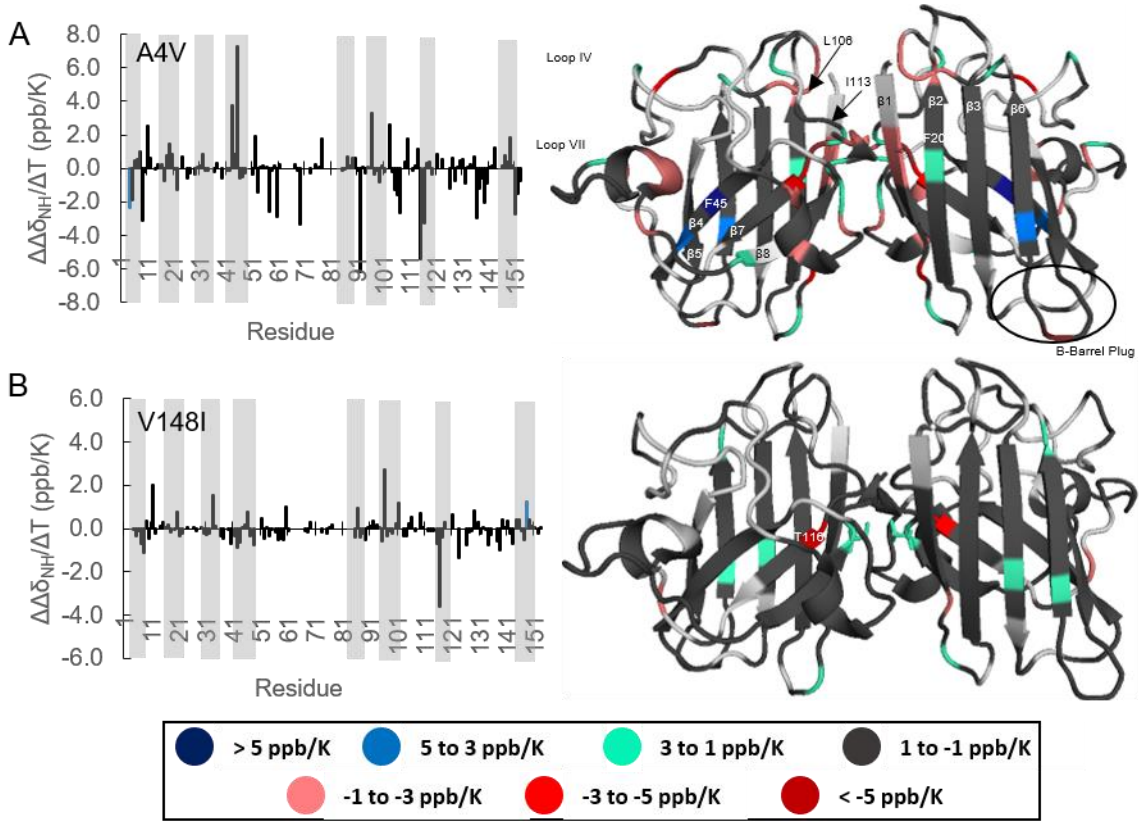

Figure 2.11: Changes in Temperature Coefficients for Dimer Interface Mutants Relative to pWT. This figure displays the changes in temperature coefficients, relative to apo2SH pWT, for (A) A4V and (B) V148I. Residues coloured white occur where no comparisons could be made. The sites of mutation are shown as blue bars in the graphs and the sidechains are shown as sticks in the structural representations of the data. Figures were made using PyMOL and PDB code 1HL5.[70,72]

as N19, H43, and D96, is altered. This may indicate that the A4V mutation, whose sidechain points into the core of the protein, creates a stronger hydrophobic environment in the interior of apo2SH SOD1. It should also be noted here that there are a small cluster of destabilized residues in the electrostatic loop, demonstrating that it is most likely less structured in apo2SH A4V than pWT SOD1.

The other dimer interface mutant studied is V148I, a mutation that introduces a larger, more hydrophobic residue to the dimer interface region. The thermodynamic stability of this mutant has been shown to be similar to that of pWT SOD1, which is reflected in the average temperature coefficients of these two apo2SH variants.[63,84] From Figure 2.11 (B), it is observed that some residues are affected slightly, while most are not affected at all. This further supports

the similar stabilities seen in other studies.[63,84] For the residues that are affected (8 in total), the majority are stabilized (5 residues), most notably the site of mutation, I148. Other stabilized residues are found in loop I and the first β-sheet, with two of these residues in β-strand 6. This may indicate a long range effect of the V148I mutation that protects the edge strand β6. This increased protection may partially explain the decreased aggregation propensity of this mutant.[84,133,134] The most destabilized is T116, which is found in β-strand 7 and is directly beside I148 in the structure of SOD1.

H46R Displays Increased Stability in the Metal-Binding Region

The next set of mutants studied are the metal-binding mutations H46R and G85R. For H46R, the changes in temperature coefficients relative to pWT are shown in Figure 2.12 (A). Similar to V148I, this mutation stabilizes apo2SH SOD1; however, in later maturation states, this mutant does not bind metals in the copper-binding site.[84,123] The average temperature coefficient of this mutant is the most positive of all the apo2SH SOD1 variants studied, consistent with it having the highest stability. While the majority of residues do not experience a change in temperature coefficient, those that do are more often stabilized by the mutation (17 of 22 affected residues). The majority of these changes are clustered around the site of mutation and the metal binding region. In the copper-binding region, the mutant residue and the metal-binding region are all stabilized. These changes are all in the vicinity of copper-binding ligands in pWT, H46R, H48, and H120, as well as the catalytically important R143.[68,87] This may indicate that the R46 sidechain, which is now positively charged, may act similarly to the copper ion that normally binds in pWT SOD1, stabilizing the copper-binding region. That said, the increased size of this sidechain may be what prevents the copper ion from binding this mutant.[123] Also, similar to the pattern observed in V148I, the same two residues in β-strand 6 are stabilized, potentially resulting in an increased protection of this edge strand.

From previous structural studies on H46R SOD1, this mutation is thought to disturb the H63, D124, and T137 sidechains, weakening the interactions between the metal binding region and the electrostatic loop.[124–126] Through these temperature coefficients, changes are seen for T137 (decreased local stability) and the surrounding area, notably N139 and K136, as

well as other residues in the electrostatic loop, L126, G127, and K128, and G44 in the metal-binding region. The residue with the most negative change in temperature coefficient in H46R is A145. This residue is found at the edge of the copper-binding site, and may be destabilized due to potential nearby structural changes.

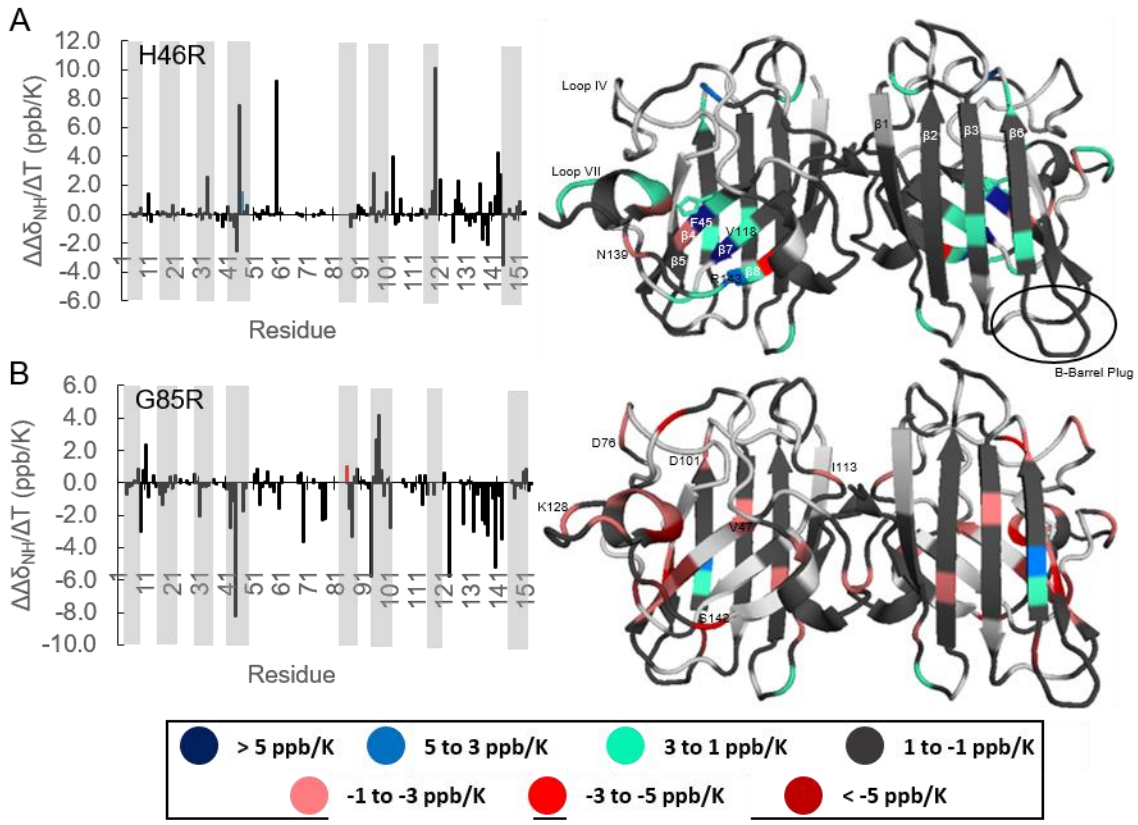

Figure 2.12: Changes in Temperature Coefficients for Metal-Binding Mutants Relative to pWT. This figure displays the changes in temperature coefficients, relative to apo2SH pWT, for (A) H46R and (B) G85R. Residues coloured white occur where no comparisons could be made. R46 is shown as a blue bar and R85 appears as a red bar (signifying there is no data for this residue) in the respective graphs and the sidechains are shown as sticks in the structural representations of the data. Figures were made using PyMOL and PDB code 1HL5.[70,72]

The G85R Mutation Greatly Affects Residues in the Metal-Binding Region, Zinc-binding and Electrostatic Loops, and the β5-β6 Hairpin

The temperature coefficients of the second metal-binding mutant studied, G85R, can be viewed in Figure 2.12 (B). This mutation has been shown to greatly decrease metal ion affinity, destabilize the β5-β6 hairpin, and affect the hydrogen bond network between β4 and

β5.[68,112,127] This mutant possesses the most negative average temperature coefficient of the variants studied and also possesses the most changes in temperature coefficients (>1ppb/K). The majority of these changes (25 of the 28) are in the negative direction, indicating a decrease in local structural stability. The most obvious changes occur around the site of mutation, in β-strand 5, in the metal-binding region, and the electrostatic loop. As mentioned above, the hydrogen bond network is disrupted between β4 and β5 in the oxidized apo crystal structure, which may be manifested by the appearance of more negative temperature coefficients in this region. The electrostatic loop also possesses a decreased structural stability in many residues, mostly in the residues that participate in the transient formation of the small helical structure.[112] In holo and E,Zn2SH pWT SOD1, this helical structure faces the zinc-binding site and is stabilized by bound zinc.[121] The decreased local structural stability of these residues in the apo2SH state may indicate that this loop does not transiently form, especially since zinc binding is weakened in this mutant.[127]

Other residues of interest that display altered temperature coefficients are those in the zinc-binding region, and D101, at the top of β6. In the zinc-binding region of the zinc-binding loop, residues R69, which is close to the zinc-coordinating residue H71, as well as D76 and E77, all exhibit more negative temperature coefficients in G85R. Most interesting are D76 and E77, both of which are between P74 and R79. Both P74 and R79 form important hydrogen bonds that tether the zinc-binding loop to the β-barrel. More specifically, P74 forms a bond with R79, which also forms a bond with D101, one of the residues that shows decreased local stability in G85R.[127] Furthermore, in crystal structural studies on D101 mutants, it was found that residue D76 in the zinc-binding loop participates in a bond with K128 in the electrostatic loop, helping to associate these two loops. This residue falls between P74 and R79, and the bond between D76 and K128 may be influenced by the conformation of the zinc-binding loop.[131,132] In apo2SH G85R SOD1, the temperature coefficient for K128 is also more negative than in pWT. The temperature coefficient patterns observed in these regions of G85R may be indicating that these structurally important hydrogen bonds are disrupted, and the loops have dissociated from each other and the β-barrel of the protein. These results agree with a previously proposed aggregation model, in which the zinc-binding and electrostatic loops are

disordered, as often found in metal-deficient pathogenic SOD1, and form non-native interactions with SOD1 monomers at unprotected edge strands β5 and β6.[112] These non-native interactions can lead to the formation of linear filamentous fibrils. In the case of G93A, and potentially G85R and E100G, the β5-β6 hairpin is destabilized leading to the formation of these fibrils.[112] In addition, this aggregation model is supported by the crystal structure of oxidized apo-H46R, which shows non-native interactions between the β5-β6 hairpin and the electrostatic loop of the adjacent monomer.[125]

The long range effects of the G85R mutation, as apparent from altered temperature coefficients, affect both the dimer interface region and the copper-binding site. In this mutant, there is a slight destabilization in the dimer interface, indicated by the more negative temperature coefficients for residues N53, A60, and I113. As discussed for A4V above, the change in the temperature coefficient of I113 may slightly affect the hydrogen bonding pattern of G114.[116,122] With respect to the copper-binding site in G85R, it has been shown previously that G85R has a decreased affinity of the copper ion, lowering its catalytic activity.[159] Residues whose temperature coefficients may be reporting on the decreased stability of the copper-binding site, include V47 and S142. The first of these residues, V47, is between two residues involved in binding copper, H46 and H48, as well as being directly beside H63, another copper-binding ligand, in the structure of SOD1. The other residue, S142, is directly beside the catalytically important R143, which increases the positive charge density required for substrate binding.[87] Overall, the temperature coefficient patterns observed in apo2SH G85R SOD1 appear to be reporting on numerous structural changes that occur as a result of the G85R mutation.

Decreased Stability in the Electrostatic Loop for G93A and E100G, E100G Mutation Results in a Large Destabilization of the Surrounding Area

The last two mutations studied, G93A and E100G, are in the β5-β6 hairpin, as is with the G85R mutation. The temperature coefficient patterns for these two variants are found in Figure 2.13. The first of these mutations, G93A, is in loop V, between β-strands 5 and 6, and is next to the β-barrel plug in loop III that stabilizes the structure of the folded SOD1.[116,129]

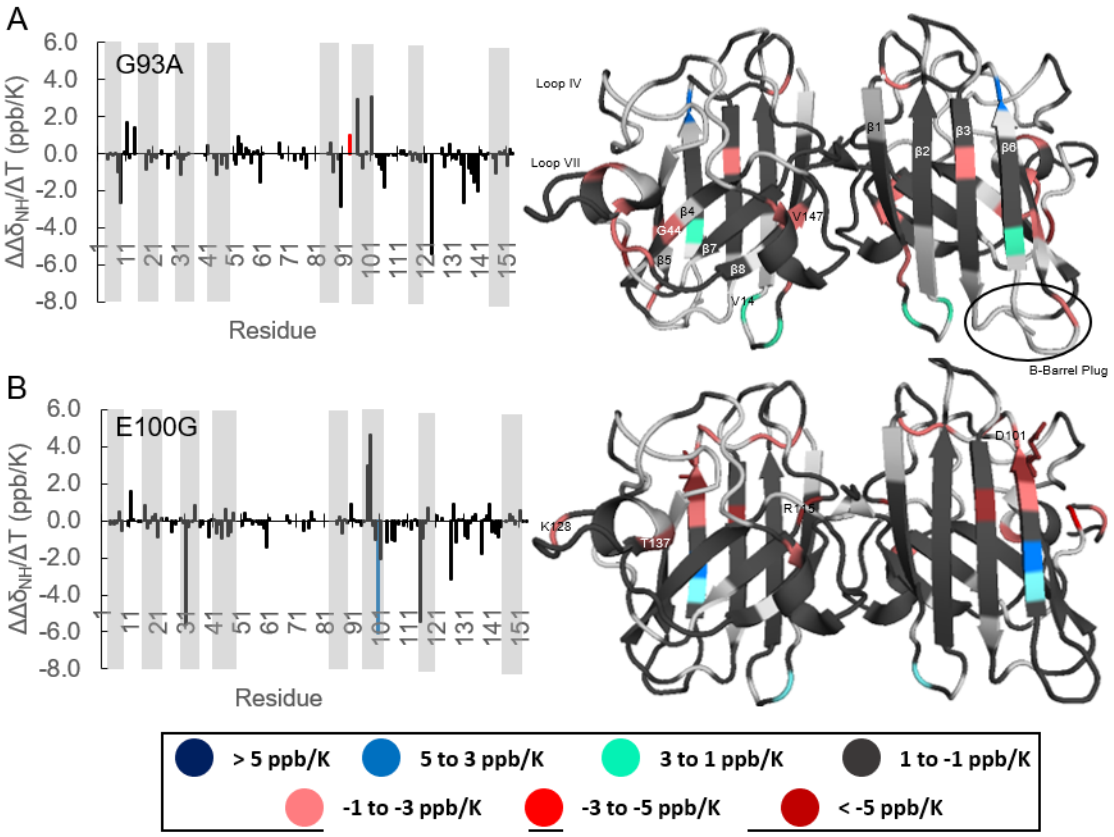

Figure 2.13: Changes in Temperature Coefficients for Other β5-β6 Hairpin Mutants Relative to pWT. This figure displays the changes in temperature coefficients, relative to apo2SH pWT, for (A) G93A and (B) E100G. Residues coloured white occur where no comparisons could be made. A93 is shown as a red bar (signifying there is no data for this residue) and G100 appears as a blue bar in the respective graphs and the sidechains are shown as sticks in the structural representations of the data. Figures were made using PyMOL and PDB code 1HL5.[70,72]

The average temperature coefficient of this variant is the second-lowest among the variants studied, consistent with its low T_m. The majority of the changed temperature coefficients correspond to a decrease in local structural stability, with three main regions of destabilization (Figure 2.13 A). The first of these regions is at the site of mutation, and includes the end of β5, the beginning of loop V, and loop III. In this region, especially in loops III and V, a large number of assignments were lost, indicating a potentially different or disordered structure for the β-barrel plug. The second region of destabilization is in the electrostatic loop and G44. As discussed for apo2SH G85R, the disordered zinc-binding and electrostatic loops have been shown in G93A to form non-native interactions in crystal structures with SOD1 monomers at

the unprotected edge strands, resulting in the formation of linear filamentous fibrils.[112] The temperature coefficient patterns seen here in the electrostatic loop of apo2SH G93A SOD1 may be presaging the destabilization of the electrostatic loop, allowing it to interact with other SOD1 monomers. The third region of destabilization is in the dimer interface region, which is indeed weakened in later maturation states of G93A.[119] The residues whose temperature coefficients report this destabilization are L8, K9, A60, and G147. Interestingly, a few residues showing increased local stability can be found in loop I, D11 and V14, and at the beginning of β6, D96. V14 is also beside the β-barrel plug and may be showing a propagating effect of the G93A mutation. This mutation introduces a more hydrophobic residue in the loop, which may assist in associating the nearby loops, especially loop III, which contains L38, another fairly hydrophobic amino acid that is beside V14 in loop I.

The last mutation studied in the β5-β6 hairpin, E100G, is located at the top of the β5-β6 hairpin beside D101, whose importance in bridging the β5-β6 hairpin has been discussed above. Mutations near D101, such as E100G, could have an effect on the formation of the bond between the D101 and R79 sidechains and affect the structure of the β5-β6 hairpin and the zinc-binding loop.[131] Also, the E100G mutation could disrupt the electrostatic network along the surface of the first β-sheet, as it forms a salt bridge with residue K30.[63,131] Apo2SH E100G SOD1 possesses one of the lower average temperature coefficient of the variants studied, along with the second lowest T_m of the group.[84] From the changes in temperature coefficients brought about by this mutation, as seen in Figure 2.13 (B), the majority of the changes are in the negative direction. Most of these changes are localized at the site of mutation, in β-strand 6, loop VI, and the top of β-strand 3. These changes may be representing disruptions in the SOD1 structure, such as a broken hydrogen bond between D101 and R79, and a broken salt bridge between K30 and what was E100 in pWT SOD1, now G100. There are also a few residues with decreased stability in loop VI, likely indicating that the loop is more flexible due to the substitution of a residue involved in a salt bridge with a glycine. Another region that shows altered temperature coefficients in E100G is the electrostatic loop, specifically residues K128, the residue that bonds to D76 to associate the zinc-binding and electrostatic loops, T137, the residue that points at the zinc-binding site as a part of the structured helix in holo SOD1, and

L126. In NMR studies on the formation of this helix in apo2SH SOD1, it was found that in E100G and the metal-binding mutants, the helix did not transiently form, and that T137 was one of the residues that reported on the formation of this helix.[112] A more negative temperature coefficient for T137 may indicate disruption of transient helix formation. With respect to H46R and G85R, the temperature coefficient of this residue was also more negative than in pWT. In E100G, the decreased temperature coefficient for K128 may be reporting on the decreased stability due to a broken bond between K128 and D76, potentially resulting in the dissociation of the zinc-binding and electrostatic loops.[131,132] This may further favour the process of aggregation previously discussed for G85R and G93A.[112,125] Lastly, in E100G, there are a couple residues in the dimer interface region, R115 and A60, with more negative temperature coefficients. This may support the destabilization of the dimer interface in E100G seen in later maturation states.[119]

Overall, the amide proton temperature coefficients for these variants of apo2SH SOD1 have provided valuable information regarding the changes in local structural stability that occur as the result of various mutations. The temperature coefficient patterns observed in these variants also well support previous structural, thermodynamic, and dynamics investigations, especially those that revealed the dynamics of functionally important SOD1 structural features, proposed aggregation pathways, and determined altered dimer interface stability, metal-binding affinities, and sidechain positions.

2.3.4 Amide Nitrogen Temperature Coefficients

Previous studies by Tomlinson & Williamson and Doyle *et al.* have investigated the use of amide nitrogen temperature coefficients ($\Delta\delta_N/\Delta T$) for the B1 domain of protein G and holo SOD1 variants, respectively. These studies found that there were no discernable patterns in the amide nitrogen temperature coefficients, when compared to amino acid type or structural feature, and a weak correlation with amide proton temperature coefficients. They concluded that further investigations were required to determine their potential uses.[58,63] In order to determine the uses of amide nitrogen temperature coefficients, Dr. Kyle Trainor proposed referencing them to their amide nitrogen random coil temperature coefficients, to deconvolute

the temperature coefficients from their sequence-dependence. These referenced amide nitrogen temperature coefficients are referred to as secondary amide nitrogen temperature coefficients (2° $\Delta\delta_N/\Delta T$). [61] This sequence dependence arises from a variety of factors, including electron withdrawal by adjacent side chains, dihedral angles, and hydrogen bonding.[59,60] By taking the sequence-dependence of the amide nitrogen chemical shifts into account, Dr. Trainer found that amide nitrogen temperature coefficients are extremely sensitive to deviations from random coil and may be used as a measure of structure.[61]

Amide Nitrogen Temperature Coefficients Must be Referenced to Random Coil to Provide Structural Interpretations

Dr. Trainor's experiments determining the uses of amide nitrogen temperature coefficients were performed on adnectins. To see if secondary amide nitrogen temperature coefficients provide useful and interpretable results for SOD1, secondary amide nitrogen temperature coefficients were first determined for the holo SOD1 variants, pWT, G93A, E100G, and V148I, using the amide nitrogen temperature coefficients collected by Doyle *et al.*[63] Figure 2.14 displays the amide nitrogen temperature coefficients for holo pWT SOD1 before and after referencing to random coil temperature coefficients measured for GGXAGG peptides, where X is any residue, using the script made by Dr. Trainor.[61,161]

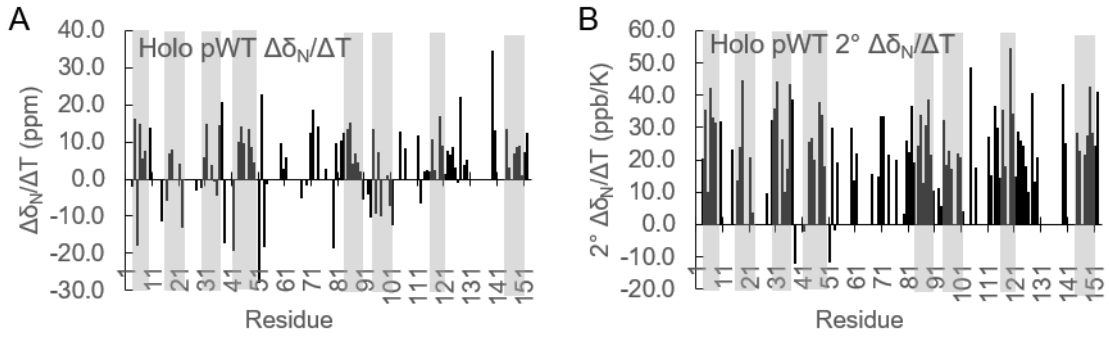

Figure 2.14: Referencing of ^{15}N Temperature Coefficients for Holo pWT SOD1. These graphs display (A) the raw amide nitrogen temperature coefficients calculated from tracked peaks, and (B) the secondary ^{15}N temperature coefficients following referencing to random coil for holo pWT SOD1. Dark grey bars indicate the presence of β-strands. Data obtained from Doyle *et al.*[63]

From Figure 2.14 (A), it is observed that there are no obvious patterns between the amide nitrogen temperature coefficients and the existence of secondary structure. Following referencing to random coil temperature coefficients to remove their sequence-dependence, the secondary amide nitrogen temperature coefficients start to show more discernable patterns, as seen in Figure 2.14 (B). For example, residues that are present in β-strands or structured loops, tend to possess amide nitrogen temperature coefficients of large magnitude, while less structured regions have temperature coefficients closer to zero. Figure 2.15 displays the secondary amide nitrogen temperature coefficients for mutant holo SOD1, while Figure 2.16 shows the changes between mutant and pWT SOD1 absolute secondary amide nitrogen temperature coefficients as a result of the mutation. Changes in absolute temperature coefficients are analyzed since not much is known about the effects of the sign of the temperature coefficients. Therefore, residues in mutant SOD1 with temperature coefficients larger in magnitude than pWT are considered to be more structured. Conversely, residues with temperature coefficients smaller in magnitude in mutant SOD are considered less structured.

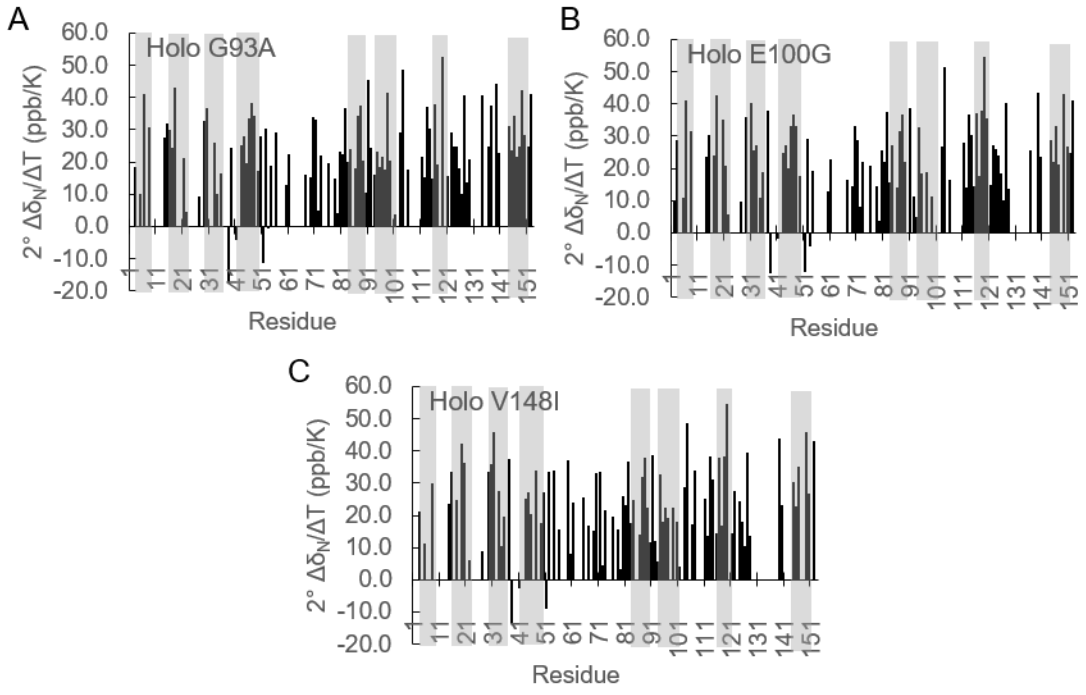

Figure 2.15: Holo SOD1 Mutant Secondary ^{15}N Temperature Coefficients. These graphs display the secondary ^{15}N temperature coefficients for (A) G93A, (B) E100G, and (C) V148I. Dark grey bars indicate the presence of β-strands. Raw ^{15}N temperature coefficient data obtained from Doyle *et al.*[63]

Residues in β-strands Exhibit Larger Secondary Amide Nitrogen Temperature Coefficients Than Those in Structured Loops or Random Coil

Table 6 displays the average secondary amide nitrogen temperature coefficient for each structural feature found in the holo SOD1 variants. Generally the average secondary amide nitrogen temperature coefficients for the β-strands are larger than those in loops; however, since holo SOD1 is a well structured protein, loops such as the zinc-binding and electrostatic loops, as well as loop III, are also well structured. In holo SOD1, the loops tend to possess average temperature coefficients around or less than 20 ppb/K, while β-strands generally possess values around or above 25 ppb/K. Many of the structural features possess similar temperature coefficients across the holo SOD1 variants. For example, of the average temperature coefficients for β-strand 1, V148I has the lowest value, indicating this strand may be less structured than pWT and the other variants. Holo V148I also has the largest temperature coefficient for β-strand 2. The temperature coefficients are relatively consistent in loop II, and in β-strand 3, both G93A and E100G display lower average temperature coefficients. In loop III, G93A shows a decrease in average temperature coefficient, as this loop is immediately beside the site of mutation. Next, V148I shows a decreased temperature coefficient in β-strand4, and a greatly increased temperature coefficient in the first portion of loop IV, which is near the site of mutation and passes through the dimer interface of holo SOD1. Through both the C-terminal part of loop IV and β-strand 5, the average temperature coefficient values are fairly consistent. In loop V, the average temperature coefficient for pWT is surprisingly low; however, the value for G93A is significantly larger than the others, which may indicate that this loop is more structured following the addition of the hydrophobic residue. Moving from β-strand 6 through loop VII, the average temperature coefficients are consistent across the holo SOD1 variants. For β-strand 8 and the C-terminus, differences in average temperature coefficient are observed for V148I, which is where the site of mutation is located. Overall, the relatively consistent patterns of the average secondary amide nitrogen temperature coefficients likely demonstrate that the structure of holo SOD1 is well-conserved across variants, with exceptions in structure most likely to occur near the site of mutation, if at all.

	pWT	G93A	E100G	V148I
N	N/A	N/A	9.29 (1)	N/A
β1	28.73 (6)	24.91 (4)	27.81 (4)	20.44 (3)
Loop I	31.77 (1)	N/A	N/A	N/A
β2	21.51 (5)	25.86 (6)	25.83 (6)	27.64 (5)
Loop II	9.53 (1)	9.31 (1)	9.56 (1)	8.73 (1)
β3	29.82 (7)	24.21 (5)	26.25 (6)	28.67 (6)
Loop III	25.32 (2)	20.85 (2)	25.01 (2)	25.15 (2)
β4	23.35 (7)	24.91 (8)	24.13 (8)	20.95 (6)
Loop IV Part 1	18.20 (7)	19.00 (8)	16.50 (6)	23.31 (8)
Loop IV Part 2	22.62 (10)	20.36 (12)	20.37 (12)	20.95 (13)
β5	25.70 (7)	25.62 (6)	24.30 (6)	24.63 (6)
Loop V	8.94 (3)	23.92 (4)	18.02 (3)	16.78 (4)
β6	19.57 (7)	20.73 (7)	20.11 (4)	19.38 (7)
Loop VI	29.06 (6)	28.34 (7)	28.90 (7)	29.41 (8)
β7	31.26 (5)	30.98 (4)	32.58 (6)	32.15 (5)
Loop VII	23.96 (11)	26.05 (14)	24.07 (11)	23.67 (9)
β8	27.82 (7)	28.68 (8)	28.37 (7)	31.98 (5)
C	41.09 (1)	41.07 (1)	40.93 (1)	43.06 (1)

Table 6: Holo SOD1 Secondary ^{15}N Temperature Coefficients by Structural Feature. Average secondary ^{15}N temperature coefficient data (ppb/K) for each structural feature of the holo SOD1 variants studied by Doyle *et al.* are summarized here, with the number of residues for which data is available found in parentheses.[63] Loop IV is separated into two parts, the first passes through the dimer interface region while the second is involved in metal binding.

Holo SOD1: Mutations Affect the Structure of a Few Nearby Residues

Figure 2.16 displays the changes in absolute temperature coefficients, as a result of mutation, for the holo G93A, E100G, and V148I. With respect to the number of changes in absolute temperature coefficient, there are relatively few, further supporting that holo SOD1 structure is highly conserved across mutations. In each of these mutants, the changes in temperature coefficient generally occur close to the site of mutation. For example, in holo G93A, there are changes found at the end of β-strand 5 and in loops III and V, where the mutation is found. These changes may be suggesting an alternate structure of the β-barrel plug in G93A. Also affected in holo G93A is residue G16, which is found at the beginning of β-strand 2, close to loop I, which is in turn near the β-barrel plug, and S111, a residue near the dimer interface region. In the second mutant, E100G, the residue with the most changed temperature coefficient is I99, immediately beside the site of mutation. Unfortunately, there are less assignments in this region of holo E100G; however, this may indicate a different

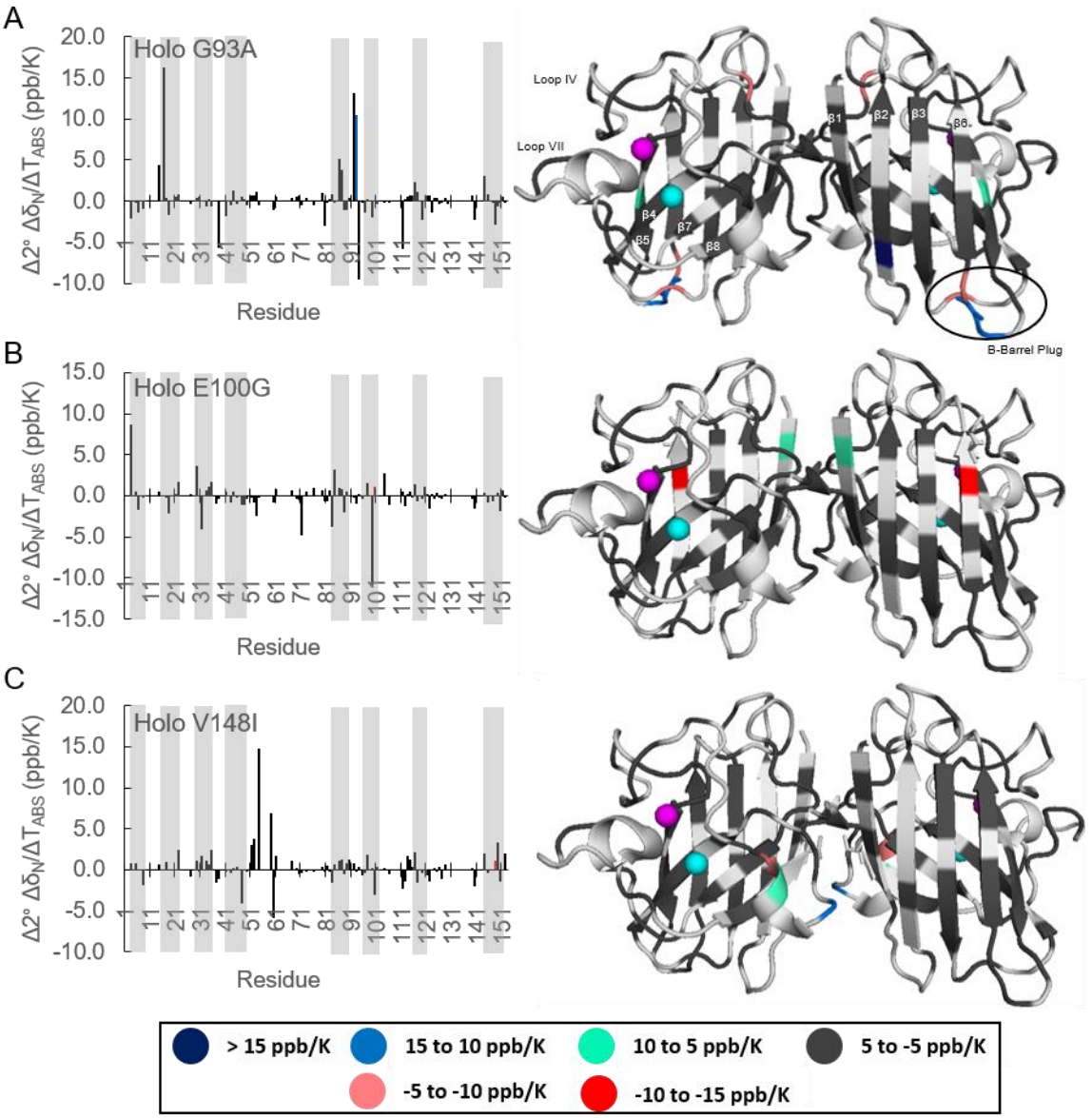

Figure 2.16: Holo Secondary ^{15}N Temperature Coefficients Compared to pWT SOD1. This figure displays the difference between the absolute ^{15}N temperature coefficients of holo (A) G93A, (B) E100G, and (C) V148I and pWT SOD1. Residues coloured white cannot be compared; zinc and copper ions are coloured magenta and cyan, respectively. A93 is shown as a blue bar and both G100 and I148 appears as red bars in the respective graphs (signifying there is no data for these residues). The sidechains are shown as sticks in the structural representations of the data. Figures made using PyMOL and PDB 1HL5.[70,72]

structure for this region of the protein. The decrease in I99's absolute temperature coefficient indicates a loss of structure, potentially meaning that the end of β-strand 6 is more flexible in

the mutant, due to the inserted glycine and broken salt bridge with K30. The other residue affected in E100G is K3, found in the dimer interface of the protein. In the last mutant, V148I, the changes are also localized to the site of mutation. Here, residues T54, S59, and A60 all show changed temperature coefficients, and all are present in the dimer interface. From these data on holo SOD1 variants, secondary amide temperature coefficients appear to be strong indicators of structure in a well-structured protein, and can be used to report on the effects mutations may have on the structure of a protein.

Following the determination of amide nitrogen temperature coefficients for holo SOD1, these were determined for the apo2SH SOD1 variants discussed earlier to investigate whether amide nitrogen temperature coefficients may act as indictors of structure in less structured proteins and, if so, if the structure of apo2SH SOD1 is conserved across a variety of mutants. Figure 2.17 shows the calculated secondary amide nitrogen temperature coefficients for the apo2SH SOD1 variants and E,Zn2SH SOD1. Figure 2.18, Figure 2.19, and Figure 2.20 all show the changes in absolute secondary amide nitrogen temperature coefficients of the respective mutations plotted onto the structure of holo SOD1.[70] Changes in secondary amide nitrogen temperature coefficients as SOD1 matures from apo2SH to E,Zn2SH will be discussed later in Section 3.3.3. With respect to these temperature coefficients for E,Zn2SH SOD1, they appear similar to holo SOD1, with structured β-strands and loops present throughout the structure.

Apo2SH SOD1: Temperature Coefficients for Residues in β-strands and Structured Loops are Similar to Those Determined in Holo SOD1 and Mutations Affect Nearby Structural Elements

Table 7 summarizes the average secondary amide nitrogen temperature coefficient for each structural feature in SOD1 for each of the apo2SH SOD1 variants studies. In general, the more-structured β-strands show significantly larger average temperature coefficients than the unstructured loops found in apo2SH SOD1. The average temperature coefficients for the β-strands are generally larger than 25 ppb/K, while the loops generally possess average temperature coefficients less than 20 ppb/K, the same values as seen in the holo SOD1 variants. In β-strand 1, the average temperature coefficients are relatively consistent across all variants, with the exception of A4V, which is where the mutation occurs that introduces a more

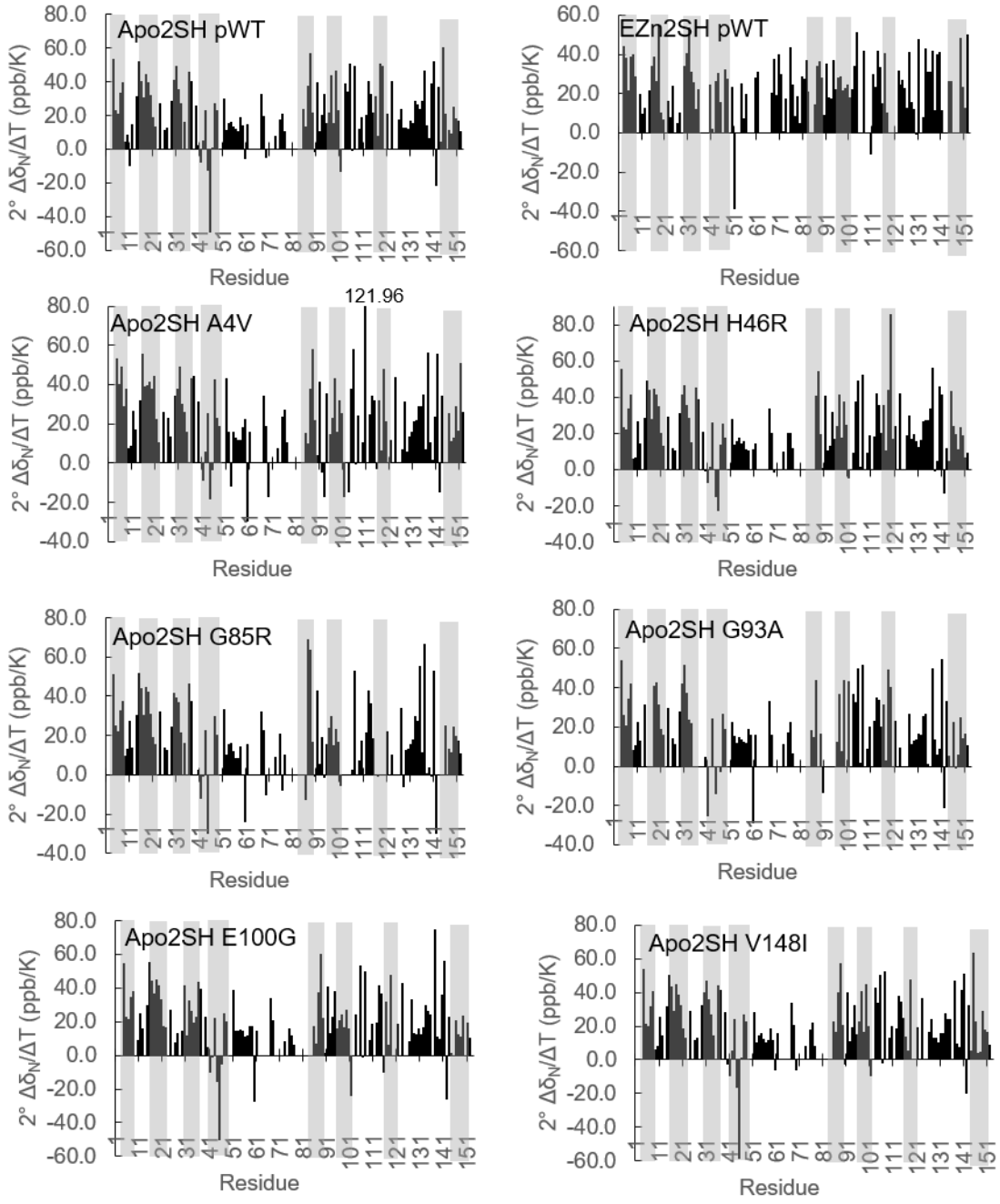

Figure 2.17: Apo2SH SOD1 and E,Zn2SH pWT SOD1 Secondary ^{15}N Temperature Coefficients. These graphs display the secondary ^{15}N temperature coefficients for the apo2SH form of each of the SOD1 mutants studied and E,Zn2SH pWT SOD1. Dark grey bars indicate the presence of β-strands in holo SOD1.[70]

hydrophobic residue pointing into the core of the protein. The temperature coefficients are also consistent across loop I, β-strand 2, and loop II, with the only significant change occurring in

β-strand 2 of G93A, where there are also three less assignments than the other variants. In β-strand 3, the only variant showing an altered average temperature coefficient is E100G, inwhich the site of mutation is directly next to, and forms a salt bridge in the other variants, with the beginning of β-strand 3. In loop III, the two mutants in which the structure appears to be altered are A4V and G93A. With respect to G93A, there are a loss of assignments in this region, which may in fact be suggesting an altered structure, but the one temperature coefficient determined in this loop is consistent with the values for that residue in the other variants. The next β-strand, β4, has the lowest average temperature coefficient of all the β-strands, which matches expectations, since this strand is primarily involved in metal coordination, which does not occur in apo2SH SOD1. With respect to the β4 data, H46R, which is present in this strand, is the only mutation that results in a changed average temperature coefficient, indicating slightly less structure here.

Through the entirety of loop IV, the average temperature coefficients are consistent, with the exception of A4V, where both values are slightly larger than those in the other variants. Next, the temperature coefficients are highly variable in β-strand 5, with the metal-binding mutants, H46R and G85R, both possessing larger values than others, and G93A displaying a smaller value. This strand is involved in zinc-coordination, contains the site of mutation in G85R, and is near the G93A mutation. In loop V, the average temperature coefficients are again consistent across the apo2SH variants, except G93A, which displays a lower average value, indicating a less structured region. With that said, there is also only one assignment in this loop, indicating that there may be a different structure of this loop and the β-barrel plug in this mutant. The average temperature coefficient of the next strand, β6, is affected in two mutants, G85R and E100G. The G85R mutation has been thought to disrupt the hydrogen bond that forms between R79 and D101, associating the two edge strands, and the E100G mutation is present directly beside D101 and may also affect this bond, altering the structure of β6 relative to the other SOD1 variants.[127] The following loop, loop VI, appears to be more structured in A4V, as this loop contains the hydrophobic residues L106 and I113, both of which have been shown to be displaced in other structural studies.[116] In the next strand, β7, the average temperature coefficient values are quite varied. In A4V, G85R, E100G, and V148I,

the values are smaller than pWT, indicating less structure. The beginning of this strand is directly beside both the A4V and V148I mutations, and is involved in copper-coordination, which is weakened in G85R.[159]

	pWT	A4V	H46R	G85R	G93A	E100G	V148I
N	N/A	N/A	N/A	N/A	N/A	N/A	N/A
β1	34.00 (5)	41.45 (5)	34.86 (5)	33.40 (5)	35.29 (5)	33.90 (5)	33.24 (5)
Loop I	9.19 (4)	14.78 (4)	13.04 (4)	15.73 (4)	13.42 (4)	16.22 (3)	13.37 (4)
β2	33.39 (9)	35.57 (9)	33.47 (9)	34.15 (9)	29.87 (6)	35.20 (9)	33.30 (9)
Loop II	17.00 (3)	20.54 (3)	16.71 (3)	19.29 (3)	18.00 (3)	15.91 (3)	17.46 (3)
β3	34.43 (7)	33.47 (7)	34.59 (7)	32.19 (7)	33.89 (6)	26.35 (8)	34.08 (7)
Loop III	22.51 (3)	37.44 (2)	19.69 (3)	19.75 (2)	4.62 (1)	22.06 (3)	23.76 (3)
β4	18.35 (8)	18.09 (8)	15.98 (8)	19.04 (6)	18.49 (6)	18.35 (8)	20.30 (8)
Loop IV Part 1	14.60 (11)	18.76 (11)	15.01 (10)	15.58 (10)	16.43 (11)	17.64 (11)	13.92 (11)
Loop IV Part 2	16.08 (7)	19.59 (7)	16.58 (7)	15.97 (7)	17.63 (6)	15.88 (6)	16.35 (7)
β5	30.52 (5)	28.46 (5)	37.94 (3)	40.33 (4)	23.15 (4)	28.60 (5)	31.23 (5)
Loop V	17.78 (4)	16.67 (4)	16.17 (4)	16.73 (4)	13.22 (1)	19.19 (4)	18.01 (4)
β6	26.34 (8)	25.56 (8)	24.56 (8)	16.19 (8)	28.72 (5)	22.54 (8)	25.02 (8)
Loop VI	29.67 (10)	35.66 (10)	27.12 (10)	25.55 (7)	29.21 (10)	27.82 (9)	30.28 (10)
β7	32.01 (5)	21.87 (5)	35.22 (6)	9.28 (2)	28.60 (5)	23.73 (4)	22.65 (4)
Loop VII	23.95 (19)	22.55 (19)	24.68 (19)	22.54 (18)	19.65 (17)	25.70 (18)	22.95 (18)
β8	22.38 (9)	25.38 (7)	17.84 (9)	18.39 (6)	15.25 (8)	15.74 (7)	21.63 (9)
C	10.07 (1)	25.58 (1)	9.25 (1)	10.52 (1)	10.54 (1)	9.99 (1)	8.58 (1)

Table 7: Apo2SH SOD1 Secondary ^{15}N Temperature Coefficients by Structural Feature. Average secondary ^{15}N temperature coefficient data (ppb/K) for each structural feature of the apo2SH SOD1 variants studied are summarized here, with the number of residues for which data is available found in parentheses. Loop IV is separated into two parts, the first passes through the dimer interface region while the second is involved in metal binding.

Next, the average temperature coefficients in the electrostatic loop (loop VII), are all generally consistent, matching with expectations since the electrostatic loop has been shown to be largely disordered in apo2SH SOD1.[112,121] Moving into the last β-strand, β8, the average temperature coefficients are lower in H46R, G85R, G93A, and E100G, most of which are destabilizing mutations and result in altered dimer interface stabilities in later maturation states.[119] It should also be noted that the apo2SH temperature coefficients for this strand are quite lower than the values obtained for holo SOD1 variants, most likely due to the fact that the dimer interface is not formed in apo2SH SOD1. Lastly, the only mutation that affects the

temperature coefficients obtained for the C-terminus is A4V, which is directly beside this in the protein.

Apo2SH SOD1: Mutations Can Affect the Structure of a Large Number of Residues, Match Well with Structural Information from Previously Reported Crystal Structures

When the changes in absolute secondary amide nitrogen temperature coefficients between the mutant and pWT SOD1 are plotted onto the structure of SOD1, informative patterns appear. In general, as previously seen in many of the results discussed so far, there are often changes in temperature coefficients values near the site of mutation; however, these secondary amide nitrogen temperature coefficient patterns may reveal long-range structural effects, due to mutations. These changes can be viewed in Figure 2.18, Figure 2.19, and Figure 2.20 for each of the apo2SH variants studied here. The changes in temperature coefficient patterns for the first mutation studied, A4V, can be seen in Figure 2.18 (A). Here, there appears to be numerous changes in the protein's temperature coefficients. As expected, a good portion of them appear in the dimer interface and loops immediately around the site of mutation. For example, in loop VI, residues S105, S107, I113, and R115 all show altered temperature coefficients. Two of these residues, S105 and S107, are directly beside L106, which along with I113 have been shown to be displaced in A4V.[116] The other two residues, I113 and R115, can be found in the dimer interface region and are beside G114, a residue involved in forming an intermolecular hydrogen bonding with another SOD1 monomer at the dimer interface, strengthening the dimer interface.[122] Therefore, a loss of structure around residue G114 may contribute to the destabilization of the dimer interface observed in these mutants.[119,122] Another residue that experiences a change in temperature coefficient and has previously been shown to be slightly displaced in A4V is F20.[116]

The other regions that appear to be affected in A4V are the metal-binding region, the β5-β6 hairpin, and the electrostatic loop. The first of these regions, the metal binding region, contains F45, another hydrophobic residue that points into the core of the protein. It appears that the residues surrounding F45 in the structure, G44, H46, G85, and V119 also all experience a change in temperature coefficient as well. This may be a result of an altered hydrophobic core, which affects the large hydrophobic side chains pointing into the core, as well as the

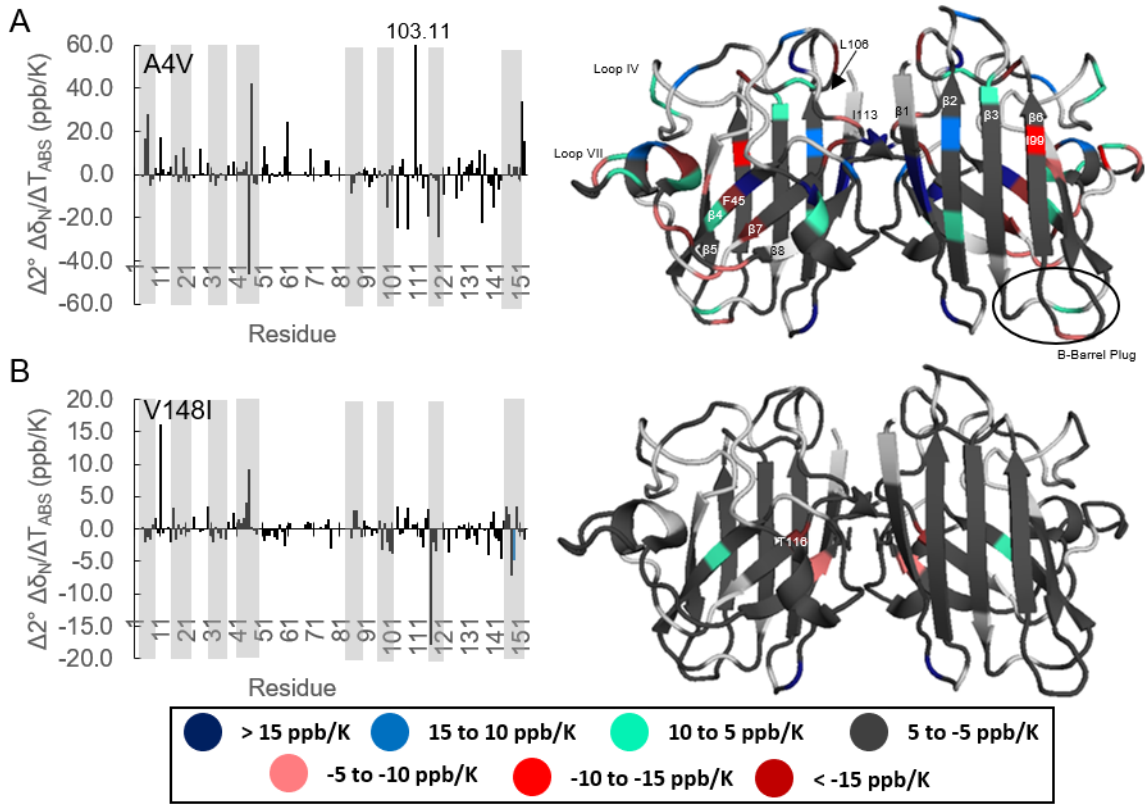

Figure 2.18: Changes in ^{15}N Temperature Coefficients for Dimer Interface Mutants Relative to pWT. This figure displays the changes in secondary ^{15}N temperature coefficients, relative to apo2SH pWT, for (A) A4V and (B) V148I. Residues coloured white occur where no comparisons could be made. The sites of mutation are shown as blue bars in the graphs and the sidechains are shown as sticks in the structural representations of the data. Figures were made using PyMOL and PDB code 1HL5.[70,72]

residues immediately surrounding them. The next region in which a change in structure is seen is the β5-β6 hairpin. Here, two residues at the widest point of the hairpin, G85 and I99, both have decreased temperature coefficients in A4V, as well as D92, found in loop V. These altered temperature coefficients may be reporting on a slight change in structure and loss of protection of these edge strands, relative to pWT. The last region of the protein that shows numerous changes in absolute secondary amide nitrogen temperature coefficients is the electrostatic loop. It has been established that this loop is not fully structured in apo2SH SOD1; however, a small helix transiently is formed in 2% of the protein, with a lifetime of 13 ms.[112]

The second mutant displayed in Figure 2.18 is V148I, a mutant that is expected to possess a structure similar to that of pWT SOD1. From Figure 2.18 (B), there are only a few

residues that experience changes in absolute secondary amide nitrogen temperature coefficients. Two of these residues, T116 and G147, are found directly next to the site of mutation in the structure and display a decrease in temperature coefficient, indicating a slight loss of structure here. The other two residues are located farther from the site of mutation and both indicate an increase in local structure. As most of the temperature coefficients for V148I mirror those of pWT SOD1, it may be demonstrating that the structure of V148I is extremely similar to that of pWT SOD1.

The next two mutants studied, H46R and G85R, are both metal-binding mutants, and their changes in temperature coefficients relative to pWT SOD1 can be found in Figure 2.19 (A) and (B), respectively. In apo2SH H46R SOD1, the changes in temperature coefficients mostly occur around the site of mutation and in the electrostatic loop. It is observed that there is a general decrease in temperature coefficients around the site of mutation and in the copper-binding site. Interestingly, we see changes in temperature coefficients for the copper-binding ligands in pWT, H48 and H46 (which has been mutated to R46), V119, a residue beside the copper-binding ligand H120, and around the catalytically important R143. These changes in temperature coefficients are likely reporting on an highly altered copper-binding site, that does not allow the copper ion to bind to H46R SOD1 in later maturation states.[123] This mutation has also been thought to disturb the H63, D124, and T137 sidechains, weakening the interactions between the metal-binding region and the electrostatic loop.[112,124] This may explain the altered temperature coefficients found throughout the electrostatic loop. Lastly, there is also a few changes in temperature coefficients at the end of β-strand 6, notably residue D101 whose sidechain bridges the β5-β6 hairpin, indicating a loss of structure here. These changes, combined with the loss of assignments at the beginning of β5, may be reporting on the formation of linear filamentous fibrils formed from non-native interactions between the electrostatic loop of one SOD1 monomer and the unprotected edge strands, β5 and β6, of the other. This aggregation model is supported by the crystal structure of apo-oxidized H46R, which shows non-native interactions between the β5-β6 hairpin and the electrostatic loop of the adjacent monomer.[112,125]

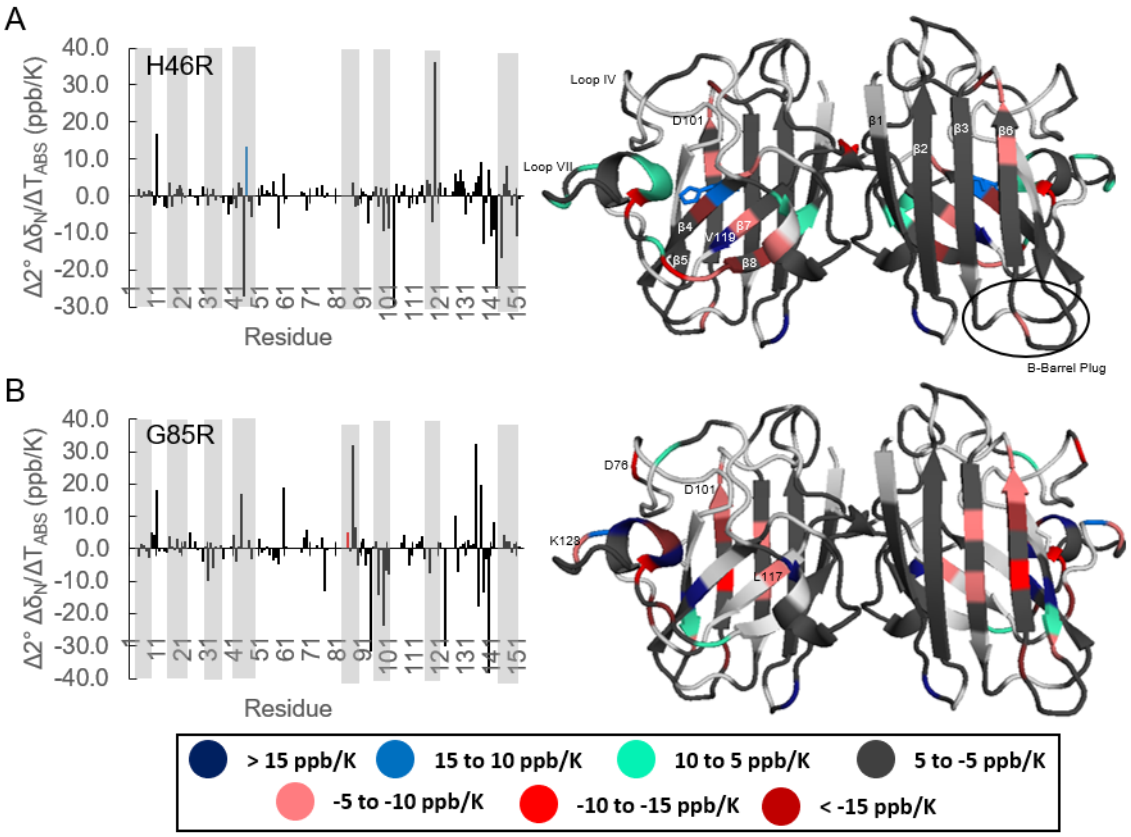

Figure 2.19: Changes in ^{15}N Temperature Coefficients for Metal-Binding Mutants Relative to pWT. This figure displays the changes in secondary ^{15}N temperature coefficients, relative to apo2SH pWT, for (A) H46R and (B) G85R. Residues coloured white occur where no comparisons could be made. R46 is shown as a blue bar and R85 appears as a red bar (signifying there is no data for this residue) in the respective graphs and the sidechains are shown as sticks in the structural representations of the data. Figures were made using PyMOL and PDB code 1HL5.[70,72]

The change in absolute secondary amide nitrogen temperature coefficients for the G85R can be viewed in Figure 2.19 (B). Once again, there are many changes in temperature coefficients, and many of these changes occur around the site of mutation. Around the site of mutation, especially through the entirety of β-strand 6, there are a large number of decreased temperature coefficients, indicating a loss of structure. These data may be a result of the bond between R79 and D101, one that usually bridges the β5-β6 hairpin at its widest point, being broken and resulting in a loss of protection of the edge strands and the dissociation of the zinc-binding loop from the β-barrel.[125,127] Also affected are the temperature coefficients for D76 and K128, two residues that are proposed to form a bond that associated the zinc-binding loop

and the electrostatic loop.[131,132] This may help to explain some of the altered temperature coefficients in the electrostatic loop, for which has been shown to not transiently form the short helix discussed earlier.[112] Another region which should be discussed is the copper-binding site, as G85R has a decreased affinity for copper.[159] Here, there is a large loss of assignments through the end of β-strand 6 and through β-strand 7, which combined contain three of the four copper-binding ligands. Of the two residues assigned in this region, one of them, L117, is directly beside the copper-binding ligand H48 and displays a decreased temperature coefficient. This in combination with the loss of assignments may be demonstrating that the copper-binding site in G85R is disturbed.

The changes in temperature coefficients for the last two mutants studied, G93A and E100G, both of which are present in the β5-β6 hairpin, can be found in Figure 2.20 (A) and (B), respectively. With respect to G93A, there are a large number of changes in throughout the β5-β6 hairpin, the majority of which have decreased in value relative to pWT SOD1. As discussed under H46R and G85R, these data may be reporting on a decreased protection of these edge strands, allowing them to form non-native interactions with the electrostatic loop of an adjacent monomer, promoting the formation of linear filamentous fibrils.[112,125] Also of interest, is the loss of assignments throughout loops III and V, suggesting an altered packing structure for the residues forming the β-barrel plug.[116] Lastly, there are also a few decreased temperature coefficients found in the dimer interface region, most notably I113, demonstrating a general decrease in structure here.[119]

The last mutant examined in this section, E100G, also displays changes in temperature coefficients around the site of mutation, the majority of which have decreased in value relative to apo2SH pWT SOD1. From Figure 2.20 (B), it is observed that there are numerous changes throughout β-strands 3, 5, and 6. The decrease in temperature coefficients through β5 and β6, may be reporting on an altered structure of the β5-β6 hairpin, similar to what was observed in H46R, G85R, and G93A. The decrease in temperature coefficients at the beginning of β-strand 3 is likely reporting on the broken salt bridge between E100 and K30 in pWT SOD1, now that the G100 mutation has been introduced. Outside of this region, the most notable residue that experiences a changes temperature coefficient is D76. As discussed for G85R, this residue is

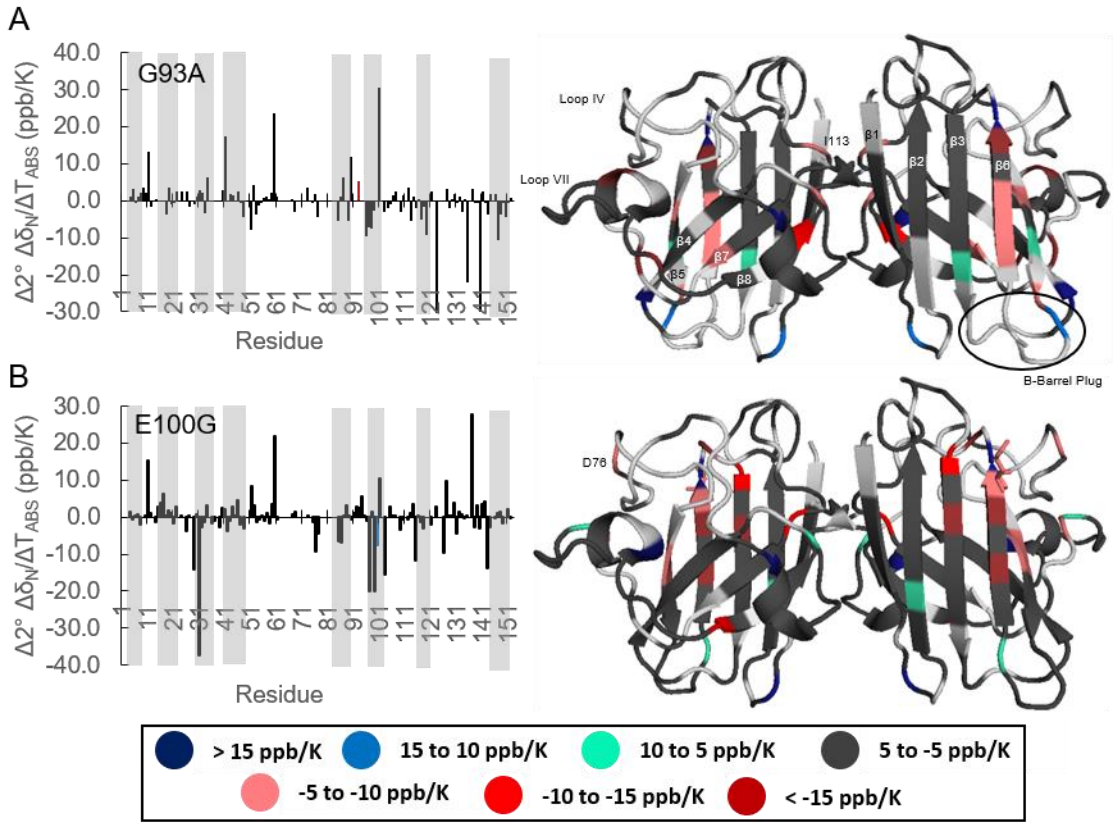

Figure 2.20: Changes in ^{15}N Temperature Coefficients for Other β5-β6 Hairpin Mutants Relative to pWT. This figure displays the changes in secondary ^{15}N temperature coefficients, relative to apo2SH pWT, for (A) G93A and (B) E100G. Residues coloured white occur where no comparisons could be made. A93 is shown as a red bar (signifying there is no data for this residue) and G100 appears as a blue bar in the respective graphs and the sidechains are shown as sticks in the structural representations of the data. Figures were made using PyMOL and PDB code 1HL5.[70,72]

proposed to form a bond with K128 in the electrostatic loop, associating the zinc-binding loop with the electrostatic loop.[131,132] Due to the decreased temperature coefficient for D76, this bond may be broken and the two loops dissociated from each other. This may help to explain why the electrostatic loop in apo2SH E100G does not show evidence of transiently forming a short helix, unlike pWT SOD1.[112] Overall, amide nitrogen temperature coefficients appear to be extremely sensitive to deviations from random coil and are useful for reporting on the local structure present in both highly structured proteins, such as holo SOD1, and less structured proteins, such as apo2SH SOD1. These temperature coefficients also appear to corroborate data previously acquired in both structural and dynamics studies performed on SOD1 mutants.

2.3.5 Conformational Heterogeneity

As discussed earlier in Section 1.2.7, temperature coefficients are predominately linear; however, some studies have shown the existence of curved temperature dependences.[56,62–65] The curvature originates from a temperature-dependent shift in population from the native state to a low-energy excited state.[62] This observed curvature is therefore able to report on the conformational heterogeneity of a protein, which may be vital for structural stability or functions such as binding, allostery, and catalysis.[14,63,66] Previously, conformational heterogeneity has been examined for the amide proton temperature found in holo SOD1 by Doyle *et al.*, as discussed in Section 2.1.2.[63] Also discussed in Section 2.1.2 are alternate states that have been found for apo2SH SOD1 variants through dynamics-based experiments by Sekhar *et al.*[112,135] This section aims to investigate the conformational heterogeneity found in the apo2SH SOD1 variants through the analysis of curvature in the temperature dependences, the changes in curvature patterns as a result of mutation, and the effects that heating a protein to its T_m may have on the observed curvature patterns. Curvature in both amide proton and amide nitrogen temperature coefficients will be analyzed and discussed, for which no work to date has been reported, to my knowledge, on curved amide nitrogen temperature coefficients.

Decreased Curvature in Mutant SOD1 Amide Proton Temperature Dependences Supports Disrupted Structures and Processes

Table 8 summarizes the curvature present in both the ^{1}H and ^{15}N temperature coefficients of the SOD1 variants studied. Generally, curvature is present between approximately 25-35% of the temperature coefficients for the residues that have been assigned. The residues that exhibit curved ^{1}H temperature dependences are plotted onto the structure of SOD1 in Figure 2.21. In the majority of the apo2SH SOD1 variants, most of the residues exhibiting curved ^{1}H temperature dependences are present in the dimer interface region of the protein, the electrostatic loop, the β5-β6 hairpin, and spread across the first β-sheet. The presence of curvature in the dimer interface region of many of these mutants is expected, despite apo2SH SOD1 existing in a monomeric form. Studies by Sekhar *et al.* have previously shown that one excited state of apo2SH SOD1 corresponds to a dimeric form, similar to what is present in holo SOD1, that is populated by roughly 3% of the protein, with

	pWT	A4V	H46R	G85R	G93A	E100G	V148I	E,Zn2SH
^{1}H Curvature								
Curved	41	29	31	31	20	27	34	43
Total Ass.	119	116	117	104	100	113	117	112
Percent (%)	34	25	26	30	20	24	29	38
^{1}H Curved Extended Temperature Range								
Curved	N/A	34	N/A	N/A	N/A	31	N/A	68
Percent (%)	N/A	29	N/A	N/A	N/A	27	N/A	61
^{15}N Curvature								
Curved	35	29	27	34	25	25	31	39
Total Ass.	119	116	117	104	100	113	117	112
Percent (%)	29	25	23	33	25	22	26	35
^{15}N Curved Extended Temperature Range								
Curved	N/A	36	N/A	N/A	N/A	28	N/A	62
Percent (%)	N/A	31	N/A	N/A	N/A	25	N/A	55

Table 8: Curvature Data for SOD1 Variants Studied. This table summarizes the number of curved residues found in each of the SOD1 variants studied, as well as the total resides assigned in each variant and the percentage of curved residues with respect to those assignments. The temperature ranges used for these experiments are summarized in Table 3.

a lifetime of 3 ms. This study also showed the presence of a second excited state, in which a short helix in the electrostatic loop is transiently formed, pointing at the zinc-binding site. This state is populated by roughly 2% of the protein and has a lifetime of 13 ms.[112] This explains the presence of extensive curvature in many of the variants' electrostatic loops. With respect to the electrostatic loop of E,Zn2SH SOD1, there appears to be less curvature present; however, that is mainly due to the fact that the short helix is fully formed and the electrostatic loop has become structured following the binding of zinc to SOD1.[121] Changes in curvature patterns as a result of SOD1 maturation will be further discussed in Section 3.3.4. With respect to the β5-β6 hairpin, curvature present here could be the result of an excited conformation in which the unstructured zinc-binding and electrostatic loops have slightly dissociated from the β-barrel,

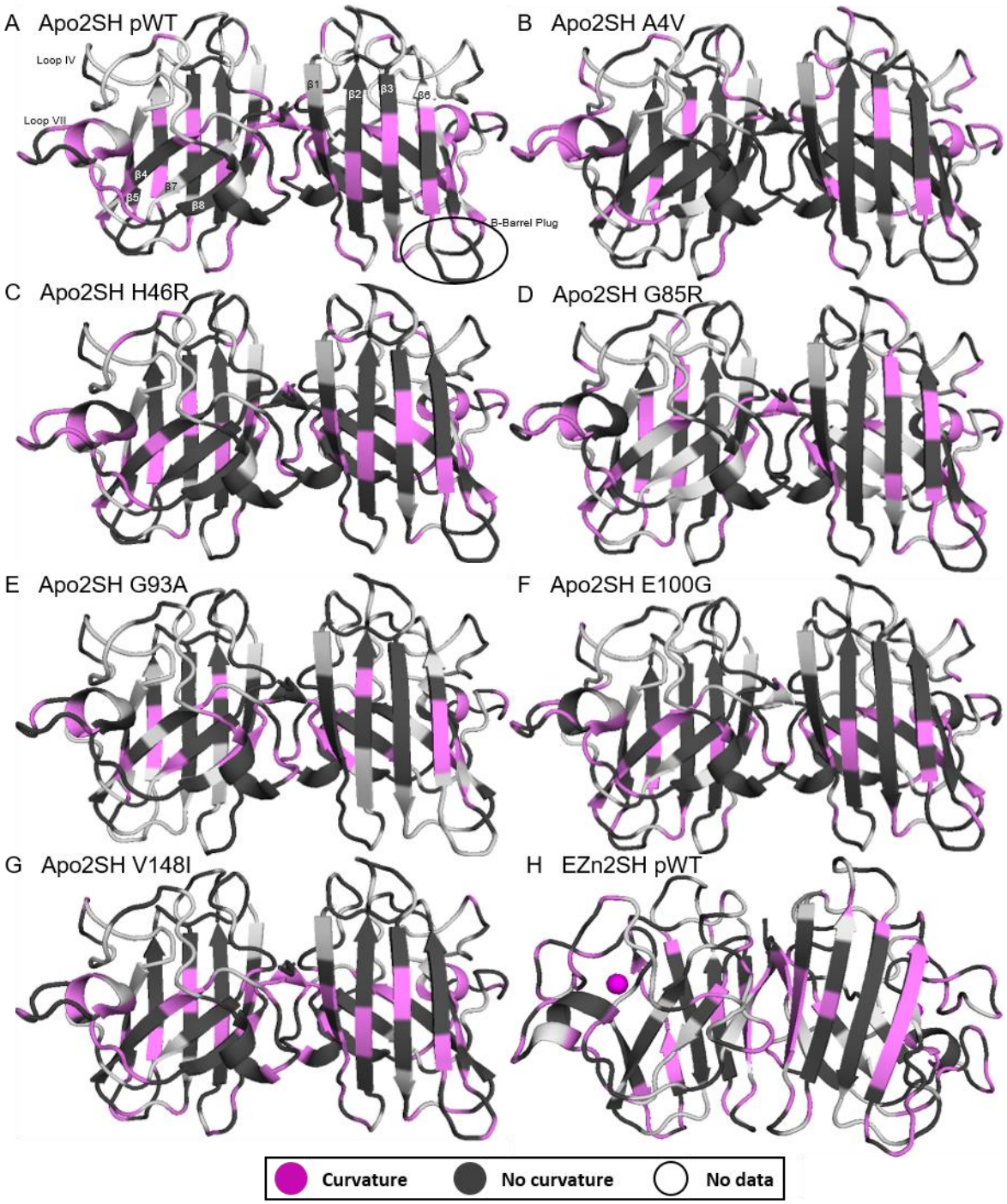

Figure 2.21: ^{1}H Curvature Found in apo2SH Variants and E,Zn2SH pWT SOD1. Displayed are the curvature found in the ^{1}H temperature coefficients for apo2SH SOD1 variants (A) pWT, (B) A4V, (C) H46R, (D) G85R, (E) G93A, (F) E100G, and (G) V148I, and (H) E,Zn2SH pWT SOD1. The zinc ion in E,Zn2SH SOD1 is coloured magenta. Figures were made using PyMOL and PDB codes 1HL5 (apo2SH SOD1) and 2AF2 (E,Zn2SH pWT SOD1).[70,72,160]

resulting in slightly less structure and protection of the edge strands.[125,127,131,132] In contrast, the curvature patterns observed across the first β-sheet may be a result of "breathing" motions that have been proposed for other proteins consisting of β-sheets.[162] It should be noted that the majority of ^{1}H curved temperature dependences start with more positive values and transition to more negative values, indicating a loss of stability as temperature increases.

A4V: Disrupted Ability to Dimerize, Curvature Also Lost in Residues that Form the Hydrophobic Core

To investigate how mutations to apo2SH SOD1 affect the curvature patterns found in the ^{1}H temperature coefficients, the difference between the residues exhibiting curved temperature dependences have been plotted onto the structure of SOD1. Figure 2.22, Figure 2.23, and Figure 2.24 all plot these differences for each of the mutants studied. In Figure 2.22 (A), the curvature patterns of A4V are compared to those of apo2SH pWT SOD1. In general, we see a large loss of curvature present around the site of mutation, in the dimer interface. This matches expectations, as apo2SH A4V SOD1 has been previously shown to not populate the dimeric excited state of apo2SH SOD1.[112] There is also a loss of curvature in β-strand 4, which contains hydrophobic residues F45 and V47, that could potentially stabilize the β-strand through increased hydrophobic interactions within the core of the protein. This is also supported by the slight loss of curvature across the first β-sheet. Two of these residues, I18 and I99, also point into the core of the protein and could be in close contact with F45, within the interior of the protein. The third residue that experiences a loss of curvature here, W32, is between these two residues in the structure of the protein. Outside of these regions, there are sporadic gains and losses of curvature throughout other structural elements, not clearly implicating any elements in excursions to excited states. For example, while the electrostatic loop still exhibits curvature in apo2SH A4V SOD1, the net change in the number of residues experiencing changes in curvature is roughly zero.

V148I: Similar Curvature Patterns to pWT

The second mutant, V148I, whose ^{1}H curvature patterns are compared to those of pWT in Figure 2.22 (B), show similar patterns of curvature to those in pWT SOD1. For example, in

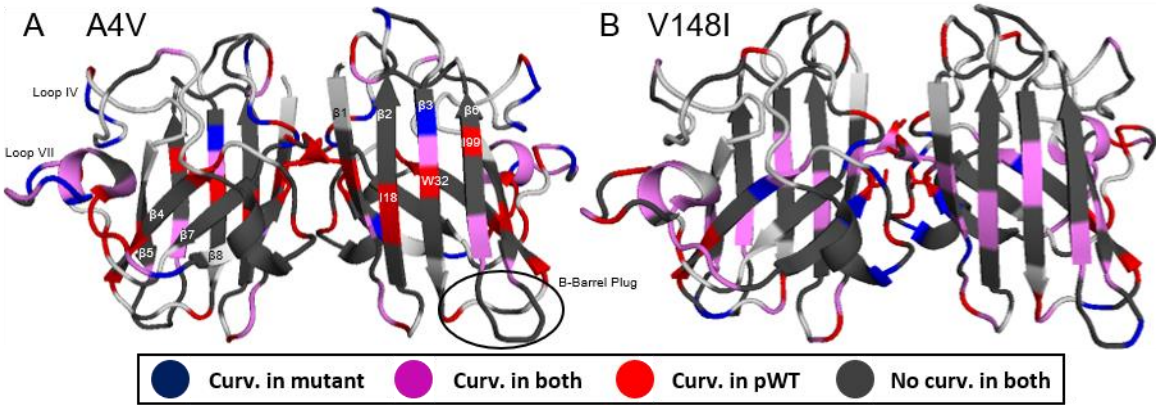

Figure 2.22: Changes of Curvature in ^{1}H Temperature Coefficients for Dimer Interface Mutants Relative to pWT. This figure displays the changes of curvature in ^{1}H temperature coefficients, relative to apo2SH pWT, for (A) A4V and (B) V148I. Residues coloured white occur where no comparisons could be made. The sidechains of the mutated residues are shown as sticks. Figures were made using PyMOL and PDB code 1HL5.[70,72]

the dimer interface region, where the site of mutation is located, the net change in the number of residues experiencing changes in curvature is roughly zero, indicating that V148I is able to transiently form a dimer. This is also the case across both β-sheets, and throughout the β5-β6 hairpin. Interestingly, this mutant shows a decrease in the amount of curvature present throughout the electrostatic loop; however, the residues that report on, and participate in, the transient formation of the short helix all exhibit curved temperature dependences, indicating that this helix still forms.[112]

H46R: Decreased Ability to Form the Transient Helix in Loop VII and Loss of Curvature in a Copper Ligand

The curvature patterns of the third mutant studied, H46R, are compared to pWT SOD1 in Figure 2.23 (A). This mutation, which like V148I is another stabilizing mutation, shows similar curvature patterns to pWT SOD1.[84,106] The curvature present across the first β-sheet is retained in this mutant, as well as the curvature in the β5-β6 hairpin. Unlike pWT, there is a small region of residues present in the dimer interface region that displays a loss of curvature. While there is still an appropriate amount of curvature present to indicate that this mutant still transiently forms a dimer, these changes in curvature may be prefacing the weaker dimer interface seen in later maturation states.[119] Also, in this mutant, there appears to be a loss of curvature in V47 and H48, one of the copper ligands. This loss of curvature may result in the

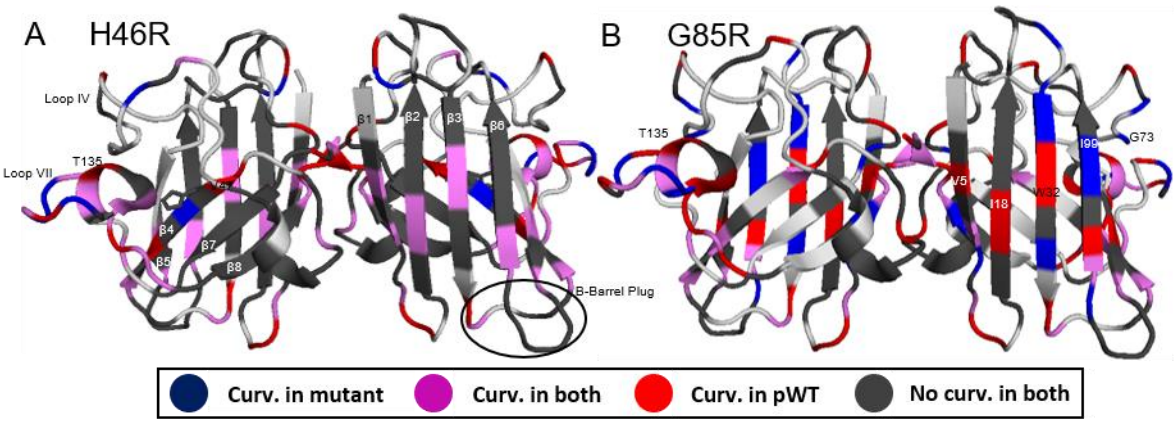

Figure 2.23: Changes of Curvature in ^{1}H Temperature Coefficients for Metal-Binding Mutants Relative to pWT. This figure displays the changes of curvature in ^{1}H temperature coefficients, relative to apo2SH pWT, for (A) H46R and (B) G85R. Residues coloured white occur where no comparisons could be made. The sidechains of the mutated residues are shown as sticks. Figures were made using PyMOL and PDB code 1HL5.[70,72]

inability of H48 to become excited to a functionally important state, involved in the binding of copper, as it has been established that H46R SOD1 is unable to bind copper at the copper-binding site.[123] Surprisingly, there are still numerous residues experiencing curvature in the electrostatic loop of this mutant, which has been previously shown to be largely unstructured and unable to transiently form the short helix described earlier in metal-binding mutants and E100G. With that said, one of the two residues, T135, that are reporters on the formation of this helix have lost their curvature.[112] This may indicate that the helix does not form in this mutant, even though curvature is present throughout the electrostatic loop.

G85R: Altered Patterns in the β5-β6 Hairpin, Dimer Interface and Electrostatic Loop

The fourth mutant, G85R, is another metal-binding mutant and has its curvature patterns compared to pWT SOD1's in Figure 2.23 (B). Unlike H46R, whose curvature patterns were relatively similar to pWT, this mutant displays vastly difference patterns. For example, there are extensive changes of curvature in the electrostatic loop, the β5-β6 hairpin, and across the first β-sheet. With respect to the electrostatic loop, there is a large loss of curvature throughout the loop, namely in residues T135 and T137, the two residues that report on the formation of the short helix mentioned earlier. This loss of curvature supports that in G85R, this helix does not transiently form.[112] There are also changes in curvature found in the β5-β6 hairpin, especially near the end of β-strand 6, which may be indicating the deprotection of these

two strands as a result of an altered hydrogen bond between R79 and D101.[127] This change in hydrogen bonding pattern may affect the sidechain position of D101, which could then point more towards the hydrophobic core of the protein. This would affect the residues involved in forming the hydrophobic core of the protein, for which the effect could propagate through. Hydrophobic residues that are present around D101 or point into the core of the protein that exhibit altered curvature patterns are I18, V29, V31, and I99. In addition, many of the residues directly beside these hydrophobic residues also experience altered curvature patters, for example: V5, I17, K30, W32, S34, and S98. Also observed in this mutant is the gain of curvature in both G73 and K75, residues on either side of P74, a residue that has been established to be disrupted by the G85R mutation.[127] Lastly, there is also a slight loss of curvature in the dimer interface region of the protein, suggesting that its ability to dimerize has been altered.

G93A: Decreased Curvature in the Dimer Interface, Electrostatic Loop, and Surrounding the β-Barrel Plug

The curvature patterns of the fifth mutant studied, G93A, compared to pWT can be found in Figure 2.24 (A). This mutant experiences a large loss of curvature across most of its structural elements when compared to pWT SOD1. For example, there is a loss of curvature in the dimer interface region, indicating a weakened ability to dimerize, and through the electrostatic loop, indicating that it is largely unstructured. In addition, there is a loss of curvature in loop I, the only loop along the "bottom" of the structure with assignments remaining. This may be reporting on a more structured arrangement of these loops, following the G93A mutation. It is also important to note that there is an increase in the amount of curvature present in β-strand 6. Previous experiments on G93A have shown that the β5-β6 hairpin is destabilized, leading to the formation of linear filamentous fibrils, through non-native interactions with the electrostatic loop of another SOD1 monomer.[112] This altered curvature pattern may be prefacing the loss of protection at the edge strands, which would then be available to form these non-native interactions. This mutant also displays changes in curvature across β-sheet 1, although to a lesser extent than what is observed for G85R and E100G. This could potentially be reporting on the rearrangements of the edge strands, that

result in a decrease in protection, having long-range effects that propagate through the backbone hydrogen bonds of the first β-sheet.

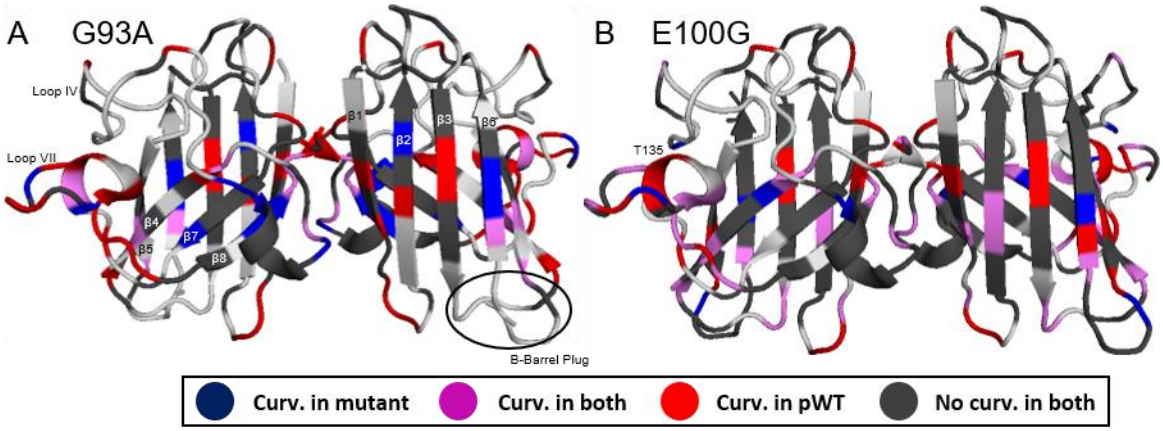

Figure 2.24: Changes of Curvature in ^{1}H Temperature Coefficients for Other β5-β6 Hairpin Mutants Relative to pWT. This figure displays the changes of curvature in ^{1}H temperature coefficients, relative to apo2SH pWT, for (A) G93A and (B) E100G. Residues coloured white occur where no comparisons could be made. The sidechains of the mutated residues are shown as sticks. Figures were made using PyMOL and PDB code 1HL5.[70,72]

E100G: Decreased Curvature in the Electrostatic Loop and Dimer Interface, Slight Changes in the β5-β6 Hairpin

The last mutant studied, E100G, experiences changes in temperature coefficient patterns similar to what is observed for apo2SH G93A SOD1. These patterns can be viewed in Figure 2.24 (B). Some of the most noticeable changes in this mutant occur in the dimer interface and electrostatic loop of the protein. In both regions, while curvature is still present, there is a loss of curvature. Not surprisingly, there is a loss of curvature in T135, one of the reporters of transient helix formation in the electrostatic loop, that was also observed in the H46R and G85R data sets. Sekhar *et al.* has previously shown that this helix does not form in E100G.[112] There are also some changes to the curvature patterns observed in the β5-β6 hairpin and across the first β-sheet, have been discussed above as potentially reporting on the destabilizing effects as a result of the loss of protection of the edge strands. Overall, the curvature patterns observed in the ^{1}H temperature coefficients of apo2SH SOD1 variants have provided useful results that correlate well to data obtained in previous studies.

Curvature in Amide Nitrogen Temperature Dependences Generally Indicate a Loss of Structure

Next, the curvature patterns observed in the ^{15}N temperature coefficients of apo2SH SOD1 variants and E,Zn2SH SOD1 were investigated. This was done to determine the extent that ^{15}N temperature coefficients can be used, and what they can potentially report on. Figure 2.25 displays the residues exhibiting curved ^{15}N temperature dependences for all apo2SH variants studied and E,Zn2SH pWT SOD1. Typically, these temperature dependences curve from a larger value towards a smaller value, indicating a loss of structure at these residues. Generally, the curvature found in the ^{15}N temperature coefficients is present throughout the β-barrel and the electrostatic loops, with few residues exhibiting curvature in the unstructured loops in apo2SH SOD1. Curvature present in the electrostatic loop most likely indicates the transient formation of the short helix and curvature present in the dimer interface could indicate transient dimer formation, as described in Sekhar *et al.*[112]

A4V: Loss of Curvature in the Dimer Interface and Residues That Form the Hydrophobic Core

Figure 2.26 (A) displays the differences in ^{15}N curvature patterns between apo2SH A4V and pWT SOD1. In A4V, there are numerous changes in curvature relative to pWT. For example, there appears to be a loss of curvature in the middle of the β-strand, and a slight increase in curvature at the ends of the strands, suggesting that the edges of some strands are fraying. Also, for many of the residues exhibiting curvature changes in the loops, residues that have lost curvature as a result of mutation are directly beside residues that have gained curvature, resulting in a roughly net zero change for most of the loops. There also appears to be a slight loss of curvature in the dimer interface, supporting the finding that apo2SH A4V SOD1 does not form a transient dimer.[112] Residues of interest that display a loss of curvature in this mutant are L117 and F45, two hydrophobic residues that point into the core of the protein, V5 and A6, residues immediately beside the site of mutation, and I113. As discussed earlier, changes in the structure of residue I113 may affect the hydrogen bonding pattern of G114, a residue involved in intermolecular hydrogen bonding with another SOD1 monomer at the dimer interface, in later maturation states.[116,122] If the structure of this region is altered, as

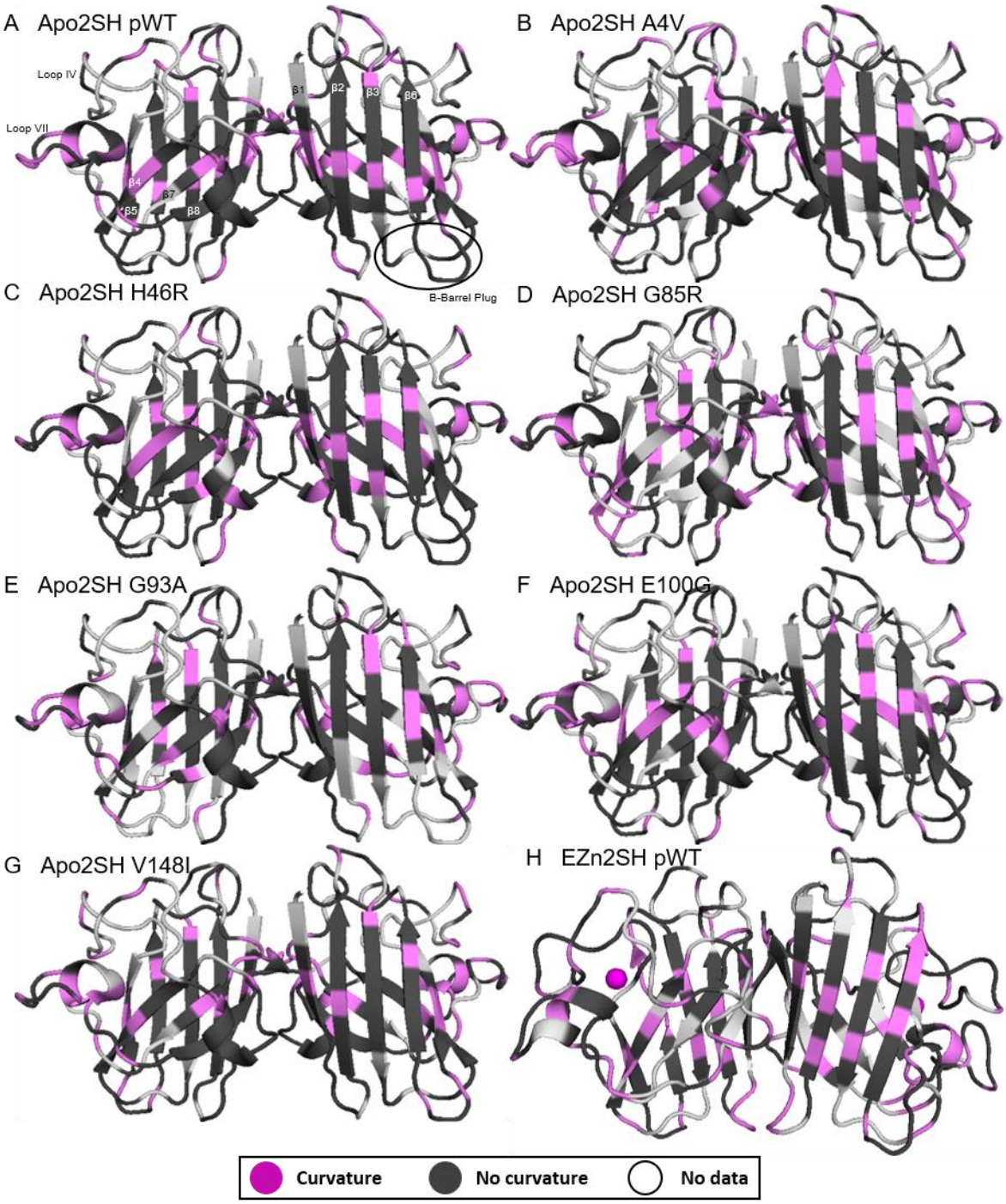

Figure 2.25: ^{15}N Curvature Found in apo2SH Variants and E,Zn2SH pWT SOD1. Displayed are the curvature found in the ^{15}N temperature coefficients for apo2SH SOD1 variants (A) pWT, (B) A4V, (C) H46R, (D) G85R, (C) G93A, (F) E100G, and (G) V148I, and (H) E,Zn2SH pWT SOD1. The zinc ion in E,Zn2SH SOD1 is coloured magenta. Figures were made using PyMOL and PDB codes 1HL5 (apo2SH SOD1) and 2AF2 (E,Zn2SH pWT SOD1).[70,72,160]

suggested by the A4V ^{15}N curvature patterns, this may help to explain why A4V is not able to properly form a dimer.[119]

V148I: Curvature Patterns Indicate Increased Structure Near the Site of Mutation

The ^{15}N curvature patterns of the second mutant studied, V148I, can be viewed in Figure 2.26 (B). Here, the curvature patterns are much more similar to pWT than A4V. The majority of the curvature found throughout the electrostatic loop and the β-barrel is retained. Regions that experience a slight loss of curvature include the "bottom" of the first β-sheet and the loops found across the "top" of the structure. Since this mutation results in an increased stability, the loss of curvature in this region, for which the majority of the curvature represents transitions from a structured state to an unstructured state, most likely indicated a more structured β-barrel. This would also be the case for the curvature lost in β4 and β7 in A4V (Figure 2.26 A), as the residues in these areas point into the hydrophobic core and would be most likely be more structured by the increased hydrophobicity. Back in V148I, there is a net zero change in curvature in the dimer interface, indicating that the protein is still able to transiently dimerize; however, both the site of mutation, I148, and two of its neighbors, I149 and A6, experience a loss in curvature, suggesting that this mutation increases the level of structure in this region.

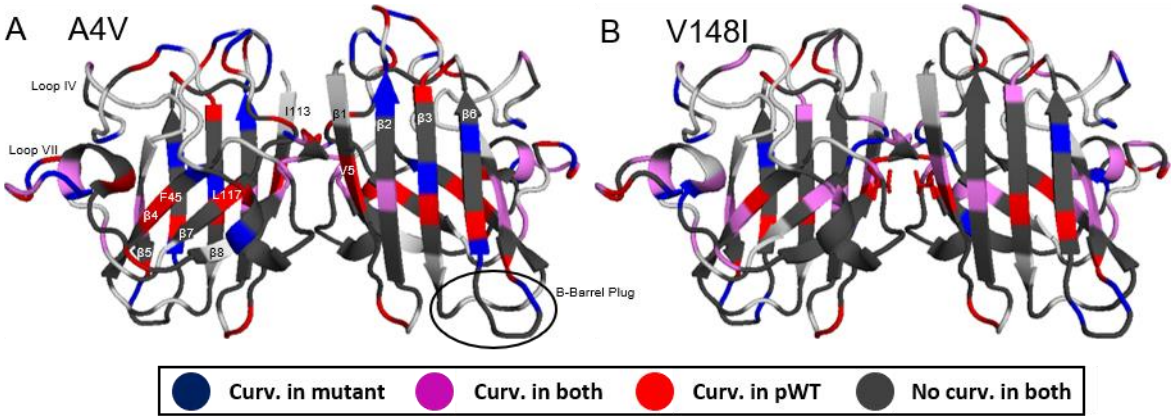

Figure 2.26: Changes of Curvature in ^{15}N Temperature Coefficients for Dimer Interface Mutants Relative to pWT. This figure displays the changes of curvature in ^{15}N temperature coefficients, relative to apo2SH pWT, for (A) A4V and (B) V148I. Residues coloured white occur where no comparisons could be made. The sidechains of the mutated residues are shown as sticks. Figures were made using PyMOL and PDB code 1HL5.[70,72]

H46R: Curvature Patterns Indicate Increased Structure of the β-barrel

Figure 2.27 (A) displays the ^{15}N curvature patterns for apo2SH H46R SOD1. In this mutant, there is a general loss of curvature in many of the structural elements. This mutation, like V148I, is stabilizing and since the curvature is in the direction of unfolding, a loss of curvature may be reporting on the increased stability in many of these structural elements. For example, , there is a loss of curvature in many of the strands that make up the β-barrel and the loops across the "top" of the structure, just like the pattern found in V148I. There also is a decrease in curvature in the dimer interface region, which may indicate a weaker dimer interface in later maturation states, as seen in Broom *et al.*[119] There is also a gain in curvature at the site of mutation, R46, and the following residue, V47. This may be reporting on fraying at the end of the strand due to mutation, which in turn would affect the positions of the ligands that bind copper in pWT, resulting in an altered copper-binding site in H46R SOD1. It has been previously shown that H46R SOD1 does not bind metals at the copper-binding site.[123]

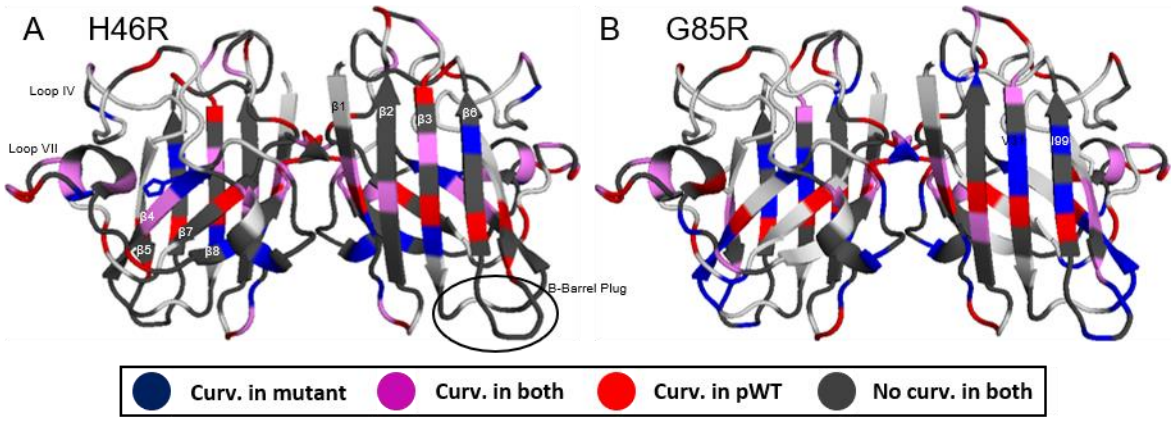

Figure 2.27: Changes of Curvature in ^{15}N Temperature Coefficients for Metal-Binding Mutants Relative to pWT. This figure displays the changes of curvature in ^{15}N temperature coefficients, relative to apo2SH pWT, for (A) H46R and (B) G85R. Residues coloured white occur where no comparisons could be made. The sidechains of the mutated residues are shown as sticks. Figures were made using PyMOL and PDB code 1HL5.[70,72]

G85R: Altered Curvature in the β5-β6 Hairpin and Metal-Binding Sites

The ^{15}N curvature patterns for the second metal-binding mutant, apo2SH G85R SOD1 can be viewed in Figure 2.27 (B). This mutant shows an increase in curvature in many of the

structural elements. For example, there is an increase in curvature in the β5-β6 hairpin, at the beginning of β4, and across the first β-sheet. The increase in curvature in each of these elements match expectations, as this mutation has been shown to disrupt the bond between R79 and D101, resulting in a loss of protection of the edge strands and the release of the D101 sidechain which points somewhat into the core of the protein.[127] This would affect the residues involved in forming the hydrophobic core of the protein, causing them to transition from a folded structure to an unfolded structure as temperature increases, especially at higher temperatures. This is supported by hydrophobic residues that are present around D101 and point into the core of the protein exhibiting altered curvature patterns. These residues are V97, I99, and V31. The increase of curvature at the beginning of β4 may likely be attributed to the weakened hydrogen bonding network between β4 and β5, causing the beginning of the strand to unfold as temperature increases.[127] Lastly, there is also a slight loss of curvature in the dimer interface region of the protein, suggesting that its ability to dimerize has been altered.

G93A: Changes in Curvature Indicate a Potential Rearrangement of the β5-β6 Hairpin and Electrostatic Loop

The curvature patterns of the next two mutants, G93A and E100G, compared to pWT can be viewed in Figure 2.28. The pattern of the first of these mutations, G93A, is very different from that of pWT. Some of the most noticeable changes occur around the site of mutation, for which there is a loss of curvature at the end of β5 and the beginning of β6, indicating a more structured loop. Oppositely, residues through the rest of β6 experience a gain in curvature, indicating that this mutation causes significant rearrangements in the β5-β6 hairpin. This in combination with the increased curvature in the electrostatic loop, indicating a less structured loop, supports the finding that the β5-β6 hairpin is destabilized, leading to the formation of linear filamentous fibrils through non-native interactions with the electrostatic loop of another SOD1 monomer.[112] In addition, there are numerous residues that experience a gain in curvature at the edges of the β-strands, signifying that the ends of the strands are less structured and unfold as temperature increases. Lastly, in G93A, there is a extensive losses of curvature in the dimer interface region, prefacing this mutant's weakened ability to dimerize in later maturation states.[119]

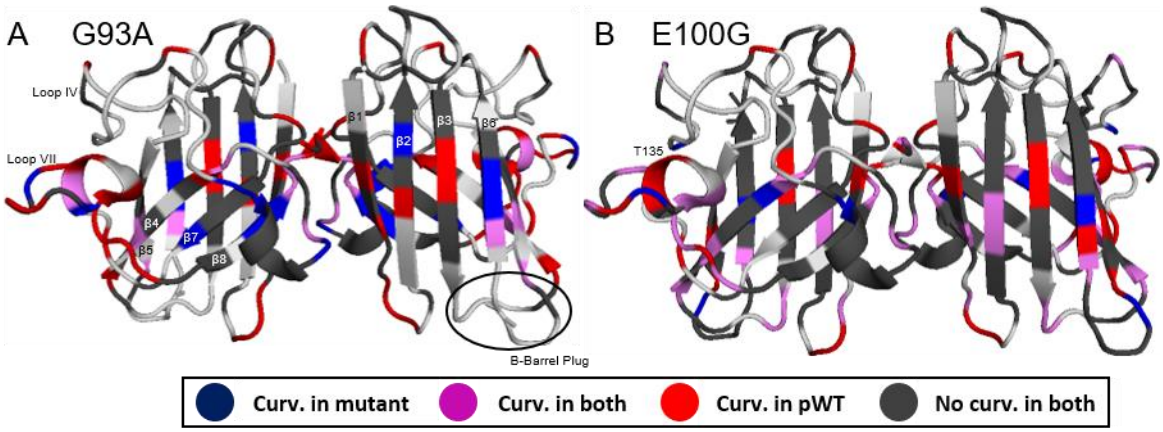

Figure 2.28: Changes of Curvature in ^{15}N Temperature Coefficients for Other β5-β6 Hairpin Mutants Relative to pWT. This figure displays the changes of curvature in ^{15}N temperature coefficients, relative to apo2SH pWT, for (A) G93A and (B) E100G. Residues coloured white occur where no comparisons could be made. The sidechains of the mutated residues are shown as sticks Figures were made using PyMOL and PDB code 1HL5.[70,72]

E100G: Altered Curvature Patterns Near the Site of Mutation and in the Dimer Interface

The last mutant, E100G, also experiences changed curvature patterns, compared to those in apo2SH pWT SOD1. As seen in other mutants, there are extensive changes in curvature near the site of mutation. More specifically, there is an increase in curvature across the middle to top of β3, β5, and β6. This pattern most likely reports on similar processes in G85R, where the end of the strand is more flexible due to a disrupted bond between R79 and D101.[127] The electrostatic loop is another region that appears to possess numerous curvature changes. With that said, the residues that experience an increase in curvature are most commonly directly beside a residue that experiences a loss in curvature. Interestingly, the loops across the "top" of the structure contain many residues that experience a loss of curvature. This would indicate that they are either more structured in this mutation; or, this mutation causes significant rearrangement in these loops, in which the loops are never structured to begin with, and therefore, could not further unfold as temperature is increased. Lastly, similar to the curvature patterns observed in most of the other mutants, E100G experiences a loss of curvature in the dimer interface, indicating a weaker dimer interface region in more mature forms of the protein.[119] Overall, the ^{15}N curvature patterns appear to be useful for determining if residues in a protein populate excited states due to various mutations and what those states may be, given previous structural and dynamics studies; as well as extracting information regarding the changes in structural features as a protein unfolds.[63,112,119]

Number of Curved Temperature Dependences Increases as the Temperature Range is Extended Closer to the T_m, Optimal Experimental Range Ends 10 to 15 °C Below the T_m

The final series of experiments aimed at observing the conformational heterogeneity found in temperature coefficients aim at examining the effects of heating different mutations and maturation states of immature SOD1 to their respective melting temperatures. These results will inform on the range of temperatures that can be studied in future temperature coefficient-based experiments, and if curved temperature dependences will appear due to global unfolding events, convoluting the results of local unfolding events with global unfolding events. In a previous study by Baxter & Williamson, it was demonstrated that when bovine pancreatic trypsin inhibitor is heated to its T_m, many of the linear temperature dependences show significant deviation from linearity, starting at approximately 15 °C below the T_m. They interpreted these results as the beginning of a global unfolding events.[56]

The first mutant that this experiment was performed on was apo2SH A4V SOD1, using the extended temperature range shown in Table 3. The changes in curvature patterns for both ^{1}H and ^{15}N temperature coefficients, as a result of heating to the T_m, are shown in Figure 2.29 (A) and (B), respectively. With respect to the curvature changes in the ^{1}H temperature coefficients, there appear to numerous changes in curvature throughout the structure. Generally, residues that experience a gain in curvature (blue) are found in the β-strands, while the majority of the residues that experience a loss in curvature (red) are found in the unstructured loops. It is important to note here that, starting at 26 °C, the intensities of the peaks corresponding to many of the residues found in the loops progressively decrease, as temperature increases towards the T_m. This makes finding the center of the peak increasingly difficult if the peak remains visible in the spectra, or if the peak completely disappears, makes the curvature comparisons more complicated. Many of these losses in curvature appear to be a result of decreased peak intensity. While the intensities of the peaks for residues found in the β-strands also decreased as the temperature was brought up to the T_m, the intensity did not decrease to the extent of the residues in the loops, and the peaks were still generally well resolved and the center of the peaks could be easily found. Many of the gains in curvature are found at the ends of the β-strands, indicating further fraying at the edge of the strands,

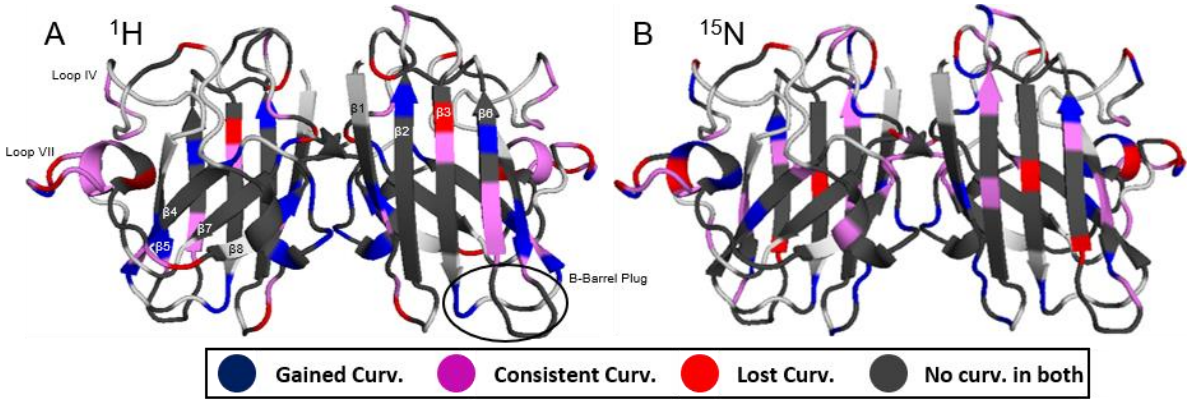

Figure 2.29: Effects of Heating Apo2SH A4V to T_m. This figure shows the change in curvature patterns in A4V's (A) ^{1}H and (B) ^{15}N temperature coefficients when the protein is heated to its T_m. Residues that appear curved over the entire temperature range are compared to residues that appear curved over the shorter temperature ranges from Figure 2.21 (B). Residues coloured white occur where no comparisons could be made. Figures were made using PyMOL and PDB code 1HL5.[70,72]

sometimes extending into the middle of the strands, such as what is observed in β1, β4, and β5. Also, these gains in curvature are mostly the result of the last few temperatures, resulting in a much sharper and asymmetric curve rather than the smooth curves observed in the shorter temperature range. These sharp asymmetric curves may be indicating the onset of a global unfolding event. Similar to the ^{1}H curvature patterns, in the ^{15}N curvature patterns, many of the losses in curvature appear for residues in unstructured loops that exhibit a decrease in peak intensity as temperature is increased. Also, the residues that experience a gain in curvature, signifying a transition from a more structured state to an unfolded state, are found at the edges of strands. For both ^{1}H and ^{15}N curvature patterns, a noticeable amount of curvature is retained from the shorter temperature range, especially around the edges of the strands.

The curvature patterns of the second mutant these experiments were performed on is apo2SH E100G SOD1. These changes in curvature patterns for both ^{1}H and ^{15}N temperature coefficients, as a result of heating to the T_m, are shown in Figure 2.30 (A) and (B), respectively. Interestingly, in the extended temperature experiments, there are few changes in curvature patterns for both ^{1}H and ^{15}N temperature coefficients. In the ^{1}H temperature coefficients, the increase in curvature is found at the bottom of β-stand 5, going through loop V, and in loop VI. These two regions are suspected to be affected by mutation. In the ^{15}N temperature coefficients, there are more changes in curvature patterns, with the majority present in middle

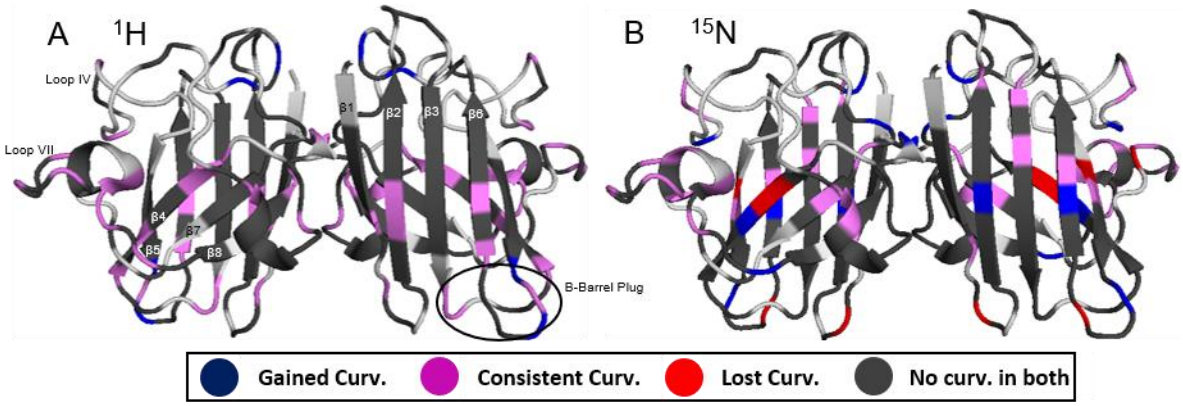

Figure 2.30: Effects of Heating Apo2SH E100G to T_m. This figure shows the change in curvature patterns in E100G's (A) ^{1}H and (B) ^{15}N temperature coefficients when the protein is heated to its T_m. Residues that appear curved over the entire temperature range are compared to residues that appear curved over the shorter temperature ranges from Figure 2.21 (F). Residues coloured white occur where no comparisons could be made. Figures were made using PyMOL and PDB code 1HL5.[70,72]

of the β-strands or in the dimer interface region, indicating further temperature-dependent loss of structure in many of these cases.

The last SOD1 variant these experiments were performed on was E,Zn2SH pWT SOD1, which has a much higher T_m than the other two variants. The changes in curvature patterns for ^{1}H and ^{15}N temperature coefficients, as a result of heating to the T_m, are shown in Figure 2.31 (A) and (B), respectively. In both sets of temperature coefficients, there are a large number of residues that experience gain in curvature, as displayed in Table 8. Similar to the patterns observed in apo2SH A4V SOD1, many of the residues that gain curvature are found at the edges of the β-strands, sometimes extending into the interior of the strands, signifying that the edges of the strands may be fraying and that the hydrogen bonding network across the β-sheets are being disrupted. In addition to the curvature found in the β-strands, a significant amount of curvature was gained in the zinc-binding and electrostatic loops, that have been shown to be well-structured in E,Zn2SH pWT SOD1.[121] The most likely explanation for this gain in curvature is that the increased temperature results in zinc being released from the zinc binding site, causing the zinc-binding and electrostatic loops to become unstructured. Lastly, as in the case of A4V, the majority of gained curvature is due to the last temperatures, resulting in sharper and asymmetric curves that may be indicating the onset of a global unfolding event.

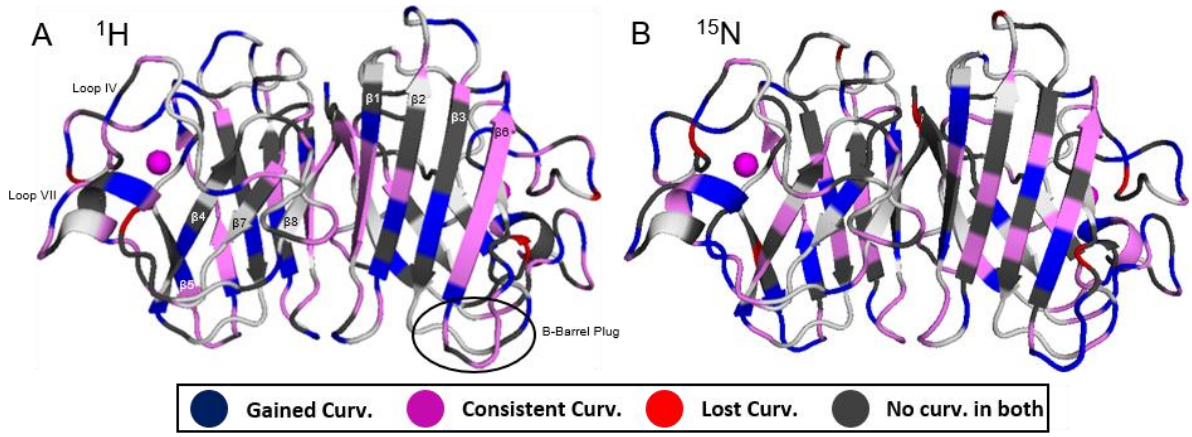

Figure 2.31: Effects of Heating E,Zn2SH pWT SOD1 to T_m. This figure shows the change in curvature patterns in E,Zn2SH pWT's (A) ^{1}H and (B) ^{15}N temperature coefficients when the protein is heated to its T_m. Residues that appear curved over the entire temperature range are compared to residues that appear curved over the shorter temperature ranges from Figure 2.21 (H). Residues coloured white occur where no comparisons could be made. Figure was made using PyMOL and PDB code 2AF2.[72,160]

In A4V, these sharp curves started to appear approximately 10 °C below the T_m, while here in E,Zn2SH pWT, the sharp curves start to appear approximately 15 °C below the T_m. This increase in curvature as the temperature approaches the T_m, along with the sharp asymmetric curves resulting from the peak positions in the last handful of temperatures, match well to the data acquired by Baxter and Williamson, suggesting that studies using temperature coefficients should avoid collecting or analyzing temperatures that start to approach the T_m of the protein. This is mainly due to the increase in curvature most likely resulting from global unfolding events, rather than local unfolding events.[56]

2.4 Conclusions

In this chapter, variable temperature NMR experiments were performed, resulting in high resolution data used to analyze the local structure and stability of 7 apo2SH SOD1 variants and E,Zn2SH SOD1. More specifically, these data were used to analyze the local structural elements found in immature SOD1 through amide proton secondary shifts and secondary amide nitrogen temperature coefficients. Local stability on a residue-specific level was also investigated through the use of amide proton temperature coefficients and conformational heterogeneity, observed by curved temperature-dependences. These analyses were performed

for each SOD1 variant and various patterns were compared to determine the effects mutations have on the local structure and stability of immature SOD1.

This chapter starts out by describing an alternate purification protocol, created by Dr. Tridib Mondal at the Weizmann Institute of Science that is currently in development. This procedure aims to eliminate the use of the hydrophobic interaction column and the subsequent dialyses, to remove the large amount of ammonium sulfate, in an effort to improve the yield of SOD1, as well as reducing the time and cost of the purification process. This protocol was tested on A4V SOD1, a mutant with a relatively high T_m. This purification procedure worked relatively well on this mutant, and will most likely work well for other highly thermostable variants, such as holo pWT, G93A, E100G, and V148I. With that said, it may not be appropriate to use for less thermostable variants, such as the metal-binding mutants H46R and G85R, as metal-binding mutants may have decreased structural stability due to a lack of one or both metals. In these cases, the heat treatment step would have to be performed at a lower temperature, which may increase the number of contaminant proteins found in the final concentrated protein, reducing the protocol's effectiveness.[82,84]

The second results section of this chapter describes the amide proton secondary shifts for each of the holo, E,Zn2SH and apo2SH SOD1 variants, and attempts to use them as indicators of secondary structure elements to determine low-resolution structural information for apo2SH SOD1 using well-established methods.[47–49,152,156] The regions of the protein that are suggested to participate in secondary structure elements by the amide proton secondary shifts are in strong agreement with the regions determined by crystal structures for holo pWT SOD1.[70] When the secondary chemical shift data for the mutant SOD1 was compared to pWT, almost all of the secondary chemical shift values do not change, indicating a conserved SOD1 structure across these mutations. The regions in which changes are seen in the secondary chemical shifts are almost exclusively at or near that sites of mutations. When these analyses were performed on apo2SH SOD1 variants, there were clear distinctions between regions suggested to participate in secondary structure elements and those that are known to form unstructured loops.[68,112,121,135] The location of these secondary structure elements are in almost identical positions as the ones in holo SOD1, indicating a structured β-barrel, and the effects

on the secondary chemical shifts were mostly localized to the site of mutation. In the future, the amide proton secondary shifts should be investigated for all apo2SH SOD1 mutants to help determine any significant changes in structure due to mutation, as this may assist in the interpretation of temperature coefficients and curvature.

The third section of this chapter focuses on amide proton temperature coefficients for the SOD1 variants studied, as well as the changes in local stability that occur as a result of mutation. The results discussed in this section support that amide proton temperature coefficients can be used as both indicators of intramolecular hydrogen bonding and as indicators of local stability. Many of the changes in temperature coefficients, as a result of mutation to apo2SH SOD1, occur around either the site of mutation or in functionally/structurally important sites that have been highlighted in previous structural and dynamics studies.[63,119,125,127,135] The large majority of these changes in temperature coefficients support previous data acquired on SOD1, and may result in a deeper understanding of many of the disrupted processes in mutant SOD1 by highlighting key residues and regions in apo2SH that are perturbed. One region of particular interest is the β5-β6 hairpin, which is consistently highlighted in the destabilizing SOD1 mutations as a region with decreased stability and has been shown to interact with another monomer's electrostatic loop in some mutants to form linear filamentous fibrils.[112,125]

The fourth section of this chapter discusses the uses of amide nitrogen temperature coefficients, whose interpretations have previously been convoluted by their sequence-dependence.[59–61] Following their referencing to random coil, the secondary amide nitrogen temperature coefficients appear to be extremely sensitive to structural deviations from random coil and are useful for reporting on the local structure present in both holo and apo2SH SOD1. Similar to what was observed in the amide proton temperature coefficients, the majority of changes in nitrogen temperature coefficients are located around the sites of mutation, and other functionally/structurally important regions. Not surprisingly, the apo2SH SOD1 temperature coefficients consistently indicate the altered structure of the β5-β6 hairpin in many of the destabilizing and metal-binding mutants studied. The structural information obtained through the analysis of the secondary amide nitrogen temperature coefficients also appear to

corroborate data previously acquired in structural and dynamics studies performed on these SOD1 mutants.[63,119,125,127,135]

In the last results section, the conformational heterogeneity in the apo2SH SOD1 variants was investigated through curved ^{1}H and ^{15}N temperature coefficients. It was determined that curvature patterns in many of these mutants reflect excursions to the excited states discussed by Sekhar *et al.*[112] When mutant curvature patterns were compared to the data acquired for apo2SH pWT SOD1, the effects of each individual mutation were shown to report on the associated disruption of various structures and functionally important processes, such as dimerization, electrostatic loop formation, and metal-binding. These data also matches well to previously acquired dynamics and stability data.[63,112,119,121,135]Again, these data highlighted the temperature-dependent loss of folded structure in the β5-β6 hairpin, through increased curvature, showing a transition from a more stable to a less stable state in many of the ^{1}H temperature coefficients and a transition from a more structured state to a random coil-like state in many of the ^{15}N temperature coefficients in this region. Experiments were also performed to examine the effects of heating the protein to its T_m on the conformational heterogeneity of the protein. It was determined that as the temperature approaches the T_m of the protein, approximately 10 to 15°C below the T_m, there is an increase of curvature due to the last few data points, which corroborates previous findings from Baxter and Williamson.[56] This results in sharp asymmetric curves, mostly present at the edges of the β-strands signifying that the edges of the strands are fraying. In some cases, this curvature extends to the middle of these strands, which may be reporting on the disruption of the hydrogen bonding network across the β-sheets. A large gain of curvature is also present surrounding the zinc-binding site in E,Zn2SH SOD1, potentially indicating that as the protein is heated, the zinc ion is less tightly bound, or is released, resulting in a decrease of structure in the zinc-binding and electrostatic loops. It is recommended for future experiments that temperature coefficients are only analyzed up to 10-15 °C, to avoid convolution of local unfolding events with the onset of a global unfolding event.

2.5 Chapter Acknowledgements

I would like to thank Jan Venne, David Beriashvili, Dr. Duncan Mackenzie, and Dalia Naser for all of their assistance with the NMR experiments and NMR processing. I would also like to thank Dr. Kyle Trainor for writing the many scripts used to analyze the NMR data and Harmeen Deol for demonstrating protein expression and purification techniques. Lastly, I would like to thank Catherine Crockett, who assisted in parts of the apo2SH G85R temperature coefficient analysis.

Chapter 3

Effects of Maturation on SOD1 Studied by NMR

3.1 Introduction

Following translation, many metalloproteins need to undergo numerous posttranslational processes to become fully mature and functional. SOD1 is one such protein, as it is initially an unmetallated monomer with reduced sulfhydryl groups and unstructured loops. Subsequently, the protein binds a structural zinc ion and a catalytic copper ion, has a disulfide bond formed between Cys57 and Cys146, and dimerizes.[68,78,79] Previously, the apo2SH SOD1 has been shown to start its journey down its maturation pathway through the binding of the structural zinc ion that greatly stabilizes the SOD1, resulting in a predominantly dimeric species, as determined using gel filtration assays by Furukawa *et al.*[86] In a study by Culik *et al.,* the effects of maturation from apo2SH to E,Zn2SH on the free energy landscape of SOD1 were examined. This study found that following the binding of zinc, the electrostatic loop undergoes extensive structural changes and forms the fully mature structure found in holo SOD1, complete with a short helix pointing towards the zinc-binding site, that does not transition to any excited conformers.[121] This study also found that the binding of zinc strongly promotes dimerization, with roughly 15% of the protein existing as a monomer; however, this dimer is weaker than more structured forms of the protein.[88,121]

The acquisition of zinc by SOD1 also increases the affinity for binding the CCS, which will bind to the small proportion of E,Zn2SH SOD1 monomers in solution. Interestingly, the CCS will only bind E,Zn2SH SOD1 and will not bind the disulfide oxidized version, EZnSS.[86] The CCS is a 28 kDa homodimeric protein with each subunit comprised of three domains that loads the E,Zn2SH SOD1 with copper and assists in the formation of the disulfide bond.[78,87] The first domain of the CCS contains a copper-binding motif that binds Cu^{1+} and transfers the ion to the E,Zn2SH SOD1, while the second domain is highly homologous to SOD1 and is involved in forming a heterodimer with E,Zn2SH SOD1.[78,87] In human CCS, the second domain binds an equimolar amount of zinc, that is essential for the proper functioning of the CCS.[87] The last domain of the CCS consists of a short polypeptide used to oxidize the disulfide

bond in SOD1.[78] Following the addition of copper and the formation of the disulfide bond by the CCS, SOD1 forms a tight dimer, resulting in the final functional form of the holo protein. As mentioned previously holo SOD1 is highly structured, with a defined dimer interface and structured zinc-binding and electrostatic loops, and displays high global stability.[68,70,101,112,121]

Currently, little is known about the method in which SOD1 acquires zinc and little high resolution, residue-specific data exists for this maturation state. For these reasons, it is of great interest to determine the changes in local structure and stability as a result of maturation from apo2SH to E,Zn2SH state, since the E,Zn2SH state appears to be key to the proper maturation of SOD1. By extension, it is also of interest to determine the effects that accompany maturation from E,Zn2SH to holo SOD1. Please refer to Section 2.1 for information regarding the structure of each mutant and previous temperature coefficient and conformational heterogeneity experiments performed.

The aim of this chapter is to investigate the effects of maturation on the local structure and stability of SOD1, using high resolution NMR data. Also examined are the effects that mutations (G93A, E100G, and V148I) have on the maturation of the protein, from the apo2SH state to the holo state. Specifically, the NMR data yielded information regarding the changes in amide proton secondary chemical shifts, amide proton and secondary nitrogen temperature coefficients, and patterns of curved temperature dependences as a result of maturation. From the secondary amide proton chemical shift and amide nitrogen temperature coefficient data, a widespread increase in structure is apparent as a result of metal binding, disulfide bond formation, and dimerization. Interestingly, there are a small subset of hydrophobic residues in the dimer interface and core of the protein that show decreases in structure. These residues may be reporting on either strain or an altered packing structure resulting from dimerization. From the amide proton temperature coefficients, the largest increase in structural stability throughout the protein occurs when the protein matures from the apo2SH to the E,Zn2SH form. In mutated SOD1, these temperature coefficient patterns report on altered processes that occur as a result of the mutation. For example, in G93A, the β-barrel plug is not stabilized during the maturation process. Lastly, the effects of maturation on the curvature patterns of individual temperature dependences were studied. As the SOD1 matures, there is a decrease in curvature

throughout the protein, especially in the electrostatic loop, zinc-binding loop, and metal binding regions following the binding of zinc, and the dimer interface following maturation to the holo form. When mutations were introduced, there is an increase in curvature in the dimer interface (in the holo form relative to the apo2SH form) that propagates to the β5-β6 hairpin through loop VI. These data describe the weakened dimer interface present in the mutant SOD1 and identify the β5-β6 hairpin as a dynamic hotspot.

3.2 Methods

Please refer to Section 2.2 for the methods used in this work. Holo SOD1 chemical shift data, raw temperature coefficients, and curvature patterns were obtained from Doyle *et al.*[63]

3.3 Results and Discussion

3.3.1 Amide Proton Secondary Shift

As discussed earlier in Sections 1.2.4 and 2.3.2, chemical shifts and secondary chemical shifts are useful information that can provide insight into the local secondary structure elements contained within a protein.[46,49] Since there is a lack of high resolution structural data on apo2SH SOD1, it is of interest to determine how the structure of SOD1 changes over the course of the maturation process, from apo2SH to holo SOD1. One method to investigate these changes utilizes ^{1}H secondary chemical shift.[47,156] Previously, it has been established that apo2SH SOD1 maintains a β-barrel fold, with unstructured loops, and holo SOD1 also exists in a structured β-barrel; however, with well-structured loops.[63,70,135] By observing the difference between the ^{1}H secondary chemical shifts of the different maturation states of SOD1 variants pWT, G93A, E100G, and V148I, it will be possible to gain a better an understanding, on a residue-specific level, of the structural changes occurring during protein maturation.

Apo2SH to EZn2SH pWT: Increased Dimer Interface, Zinc-Binding Loop, and Electrostatic Loop Structure.

According to the differences in ^{1}H secondary chemical shifts, maturation from apo2SH to E,Zn2SH pWT SOD1 results in an increase of structure for residues found in the β-strands and loops that make up the dimer interface and the zinc-binding loop. The differences in ^{1}H

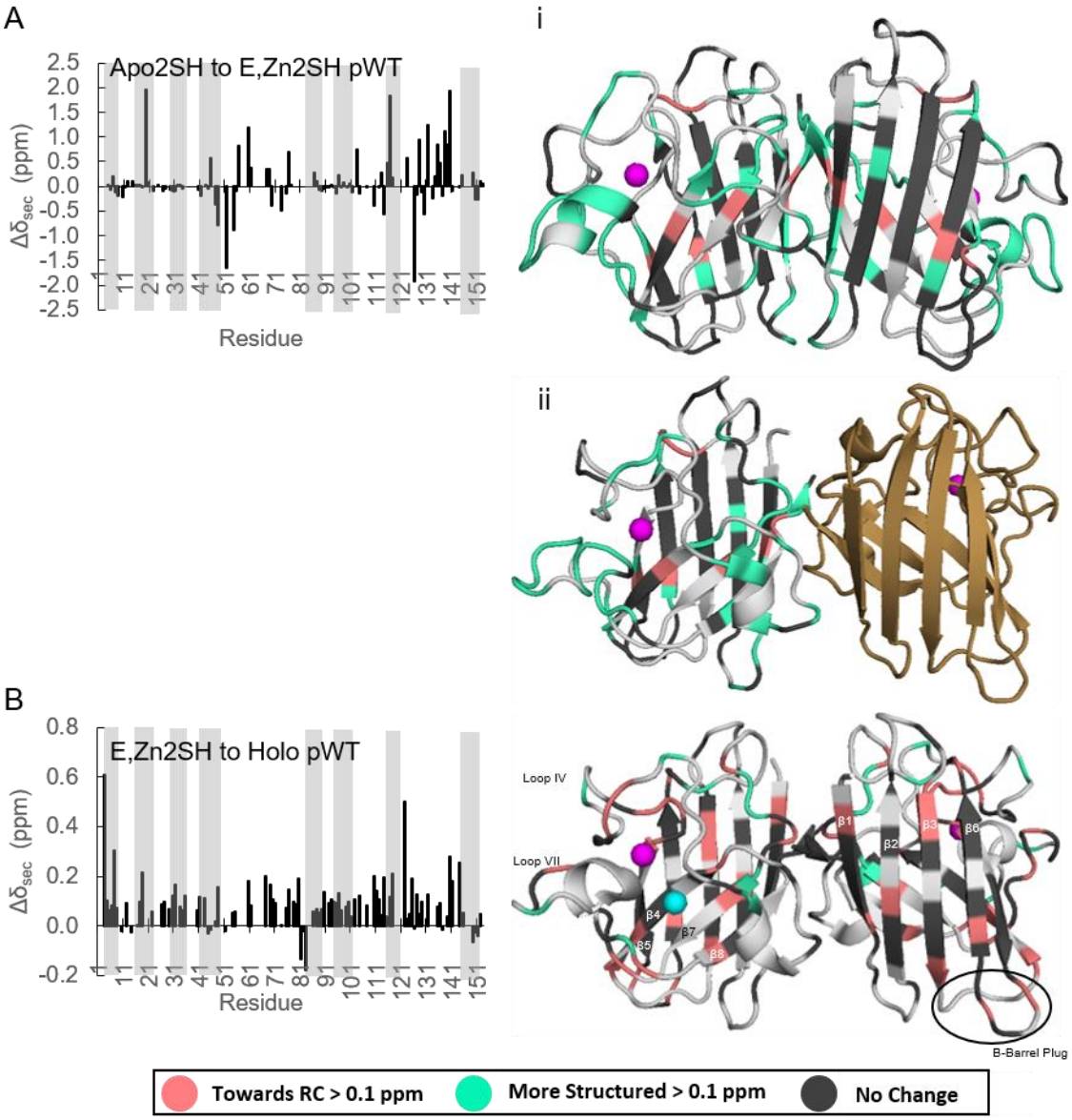

Figure 3.1: Changes in pWT Secondary Chemical Shifts During Maturation. This figure displays the changes in pWT SOD1 secondary chemical shift as the protein matures from (A) apo2SH to E,Zn2SH, plotted on the structure of i) E,Zn2SH pWT and ii) E,Zn2SH pWT with CCS, and (B) E,Zn2SH to holo SOD1. Residues coloured white occur where no comparisons could be made. Zinc and copper ions are coloured magenta and cyan, respectively. The CCS is sand-coloured. Figures were made using PyMOL and PDB codes 2AF2, 6FOL, and 1HL5.[70,72,160,164]

secondary chemical shifts between apo2SH and E,Zn2SH pWT can be viewed in Figure 3.1 (A). In general, increases in ^{1}H secondary chemical shifts (x > 0.1 ppm) in β-strands report on a loss of structure, while increase in loops report on increased structure for those specific

residues. By extension, decreases in chemical shifts for residues in β-strands indicate an increase in structure, and a decrease in those for loops indicate a loss of structure. In Figure 3.1 (A), there are extensive increases in secondary chemical shift for many of the residues involved in the loops that form the dimer interface and electrostatic loop of E,Zn2SH SOD1. These data indicate an increase in structure, as a result of the binding of the zinc ion to each monomer. With respect to the electrostatic loop, the largest increases in secondary chemical shift occur in the region of the short helix that occurs in holo SOD1, indicating that this structure is formed in E,Zn2SH SOD1.[121] Interestingly, a small subset of residues in the loops that form the dimer interface in E,Zn2SH SOD1 show a decrease in secondary chemical shift, from values indicative of random coil to those indicative of β-strand structure. These residues include G51, G114, and G151, all of which form intermolecular hydrogen bond with the other SOD1 monomer at the dimer interface.[163] It is likely that large changes in chemical shifts that indicate β-strand structure for residues found in loops signify that these residues are involved in strong intramolecular hydrogen bonds or intermolecular bond with another SOD1 monomer. Other residues that show increased structure in E,Zn2SH SOD1 include residues found in the strands involved in the dimer interface and metal-binding regions. In short, these ^{1}H secondary chemical shifts have reported on the increased structure, as a result of zinc-binding, found in many structurally and functionally important regions of SOD1 as the protein matures.

E,Zn2SH to Holo pWT: Increased Flexibility in the β-Barrel Plug, Copper-Binding Region, and Electrostatic Loop.

The maturation process from E,Zn2SH to holo pWT SOD1 results in many unexpected changes in ^{1}H secondary chemical shift values. These results may be due to differences in the chemical shift referencing of the holo SOD1 data, acquired by Doyle *et al.*[63] If this is not the case, these results indicate a slight decrease in structure for residues found in the β-barrel plug, copper-binding region, and electrostatic loop. In the majority of these cases, the secondary chemical shift values still indicate that the residues participate in either the β-strand or structured loop that they are expected to; however, their chemical shifts are consistently slightly shifted towards random coil. These changes can be viewed in Figure 3.1 (B) and may be suggesting an increase in flexibility for these regions that may be required for the catalysis

of superoxide radicals. This slight increase in flexibility may arise from the motions of the electrostatic loop, which forms an electrostatic funnel that helps guide the superoxide radicals towards the active site that possesses the copper ion.[165–167] From these comparisons, some of the largest changes in secondary chemical shift occur at the beginning and end of the electrostatic loop, which are close in structure to the catalytically important R143, which is linked to H48, another residue that displays increased flexibility, through hydrogen bonds to the carbonyl-oxygen of G61.[68,71] It should be noted that these data do not contradict previous findings that these regions possess extensive hydrogen-bonding patterns, as these data still suggest that these regions are highly structured in holo SOD1.[68,71,86] With respect to the increase in flexibility in the β-barrel plug, this may be a result of the increased breathing motions of SOD1 that are observed when the protein forms a dimer.[168] In conclusion, the difference ^{1}H secondary chemical shifts as a result of maturation from E,Zn2SH to holo pWT SOD1, could be reporting on the increased flexibility regions of SOD1 that are functionally important for catalysis.

Evidence of Strain and Structural Changes as a Result of Maturation are Similar for Mutant and pWT SOD1.

In each of the mutants studied, the changes in ^{1}H secondary chemical shifts as a result of maturation from apo2SH to holo SOD1 are near identical to the changes occurring in pWT, suggesting similar structural rearrangements during maturation. Figure 3.2 and Figure 3.3 displays the differences in ^{1}H secondary chemical shifts as a result of maturation from apo2SH to holo SOD1 for pWT, G93A, E100G, and V148I. In each of these SOD1 variants, residues throughout the structure of the protein experience an increase in structure. This is especially noticeable throughout the dimer interface, zinc-binding loop, and the electrostatic loop. In the dimer interface, residues G51, G114, and G151 experience a change from a random coil-like structure to a β-strand-like structure, similar to the patterns observed in the maturation from apo2SH to EZn2SH pWT. This demonstrates that the intermolecular hydrogen bonds these residues form in holo SOD1 result in an increase in local structure. In the zinc-binding loop and electrostatic loops, many of the residues experience an increase in structure following the binding of metals and the formation of the disulfide bond, as expected.

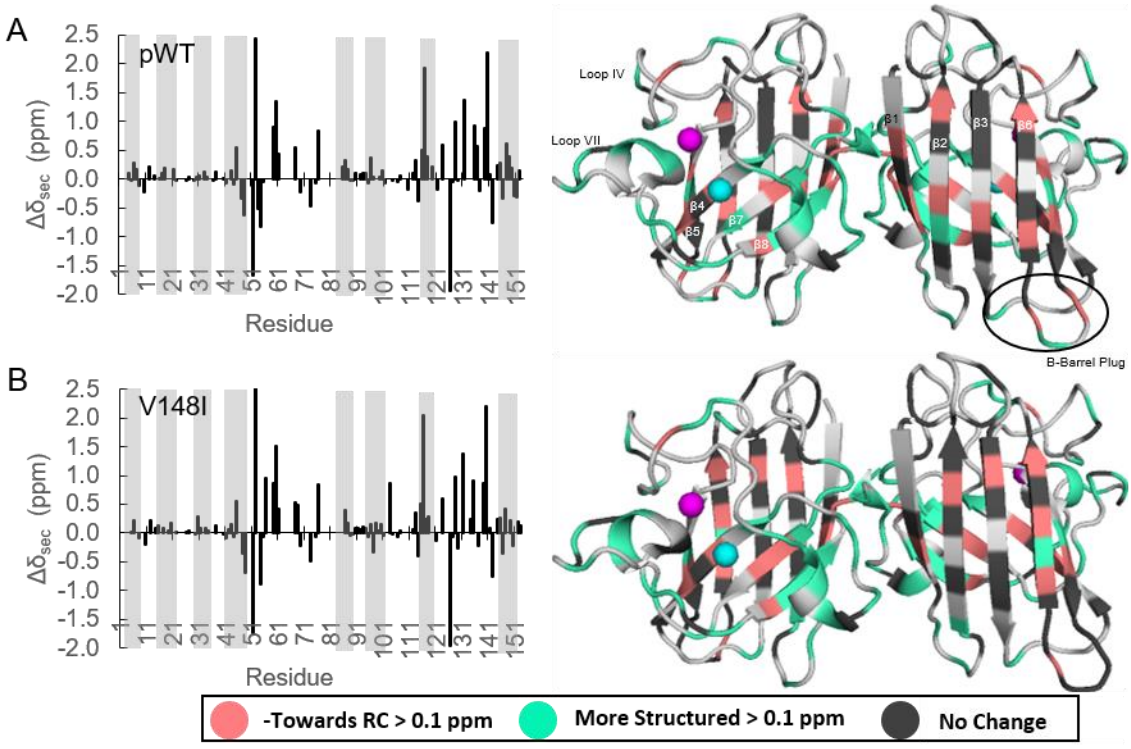

Figure 3.2: Changes in pWT and V148I Secondary Chemical Shifts During Maturation. This figure displays the changes in secondary chemical shift data as the protein matures from apo2SH to holo SOD1 for (A) pWT and (B) V148I SOD1. The dark grey bars on the graphs correspond to the location of the 8 β-strands that make up the SOD1 β-barrel.[70] Residues coloured white occur where no comparisons could be made. Zinc and copper ions are coloured magenta and cyan, respectively. Figures were made using PyMOL and PDB code 1HL5.[70,72]

Interestingly, in many of the variants, a small subset of residues found in the dimer interface experience a slight loss of structure during maturation. These residues, V5, A6, V7, V148, and I149 (depending on the assignments in the holo variants), generally show a decrease in structure, as well as F20 and F45. These residues are all hydrophobic and either point into either the core of the protein or the dimer interface. These results suggest that the process of dimerization results in a slightly different packing of the residues in the dimer interface that is able to propagate through the structure of the protein to other hydrophobic residues. Another region that, according to amide proton shifts, shows slight decreases in structure relative to apo2SH SOD1 is the β5-β6 hairpin. The ^{1}H secondary chemical shifts generally indicate the same secondary structure for each of the holo SOD1 residues as their apo2SH counterparts; however, they are often shifted slightly towards random coil. These may be the results of

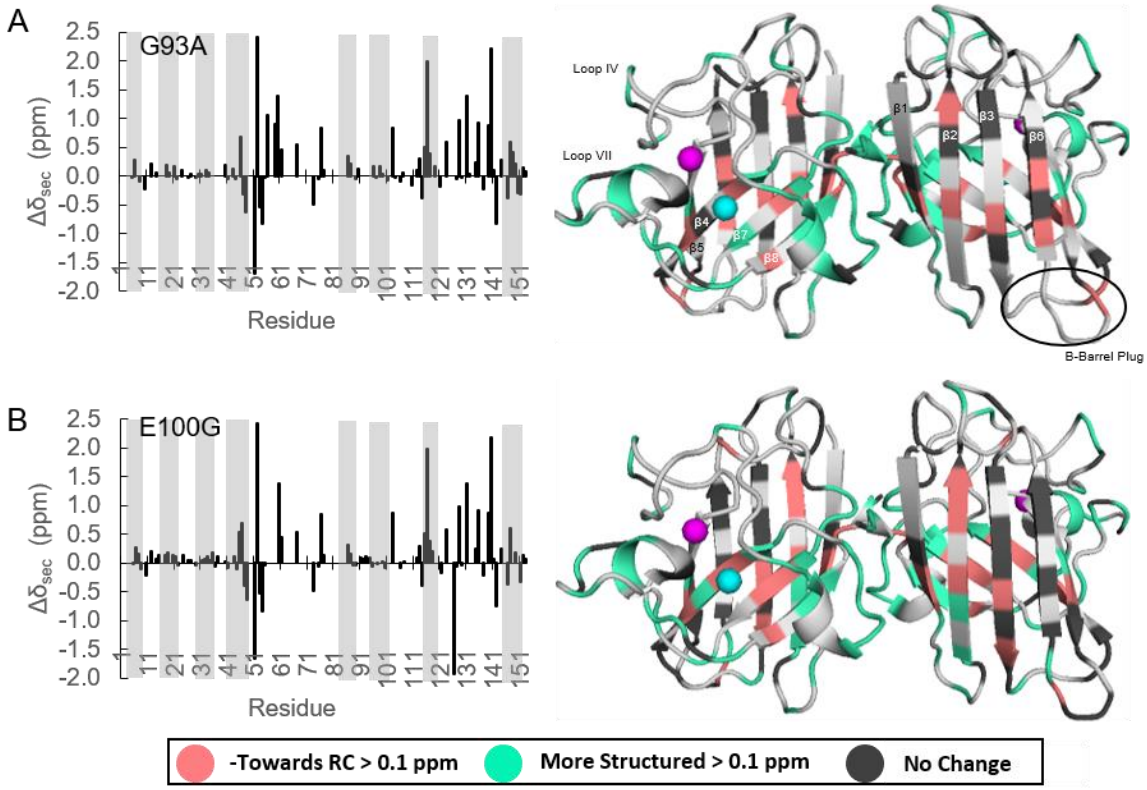

Figure 3.3: Changes in G93A and E100G Secondary Chemical Shifts During Maturation. This figure displays the changes in secondary chemical shift data as the protein matures from apo2SH to holo SOD1 for (A) G93A and (B) E100G SOD1. The dark grey bars on the graphs correspond to the location of the 8 β-strands that make up the SOD1 β-barrel.[70] Residues coloured white occur where no comparisons could be made. Zinc and copper ions are coloured magenta and cyan, respectively. Figures were made using PyMOL and PDB code 1HL5.[70,72]

propagating effects from the dimerization or metal-binding processes, or may be reporting on the increased breathing motions observed in dimeric SOD1.[168] The β5-β6 hairpin consists of two edge strands, one from each of the two β-sheets. As a result, breathing motions that affect the structure of the β-sheets, may become more pronounced at the edge strands, resulting in an observed slight decrease in structure of the residues forming the hairpin, even if many of the residues show increased stability using other methods. Since ^{1}H secondary chemical shifts are collected at one temperature, they are able to provide more structural information about a protein at that given temperature, than other NMR methods, such as the ^{1}H temperature coefficients, which observe the changes in local hydrogen bonding patterns and local structural stability over a temperature range. This may explain why a residue might show decreased

structure at a given temperature, yet still show increased stability in ^{1}H temperature coefficients. In summary, all of the SOD1 variants studied show increased structure throughout the dimer interface and zinc-binding and electrostatic loops, show signs of strain or altered packing structures in hydrophobic residues forming the dimer interface or the core of the protein, and show slightly decreased structure in the β5-β6 hairpin relative to their apo2SH counterparts.

3.3.2 Amide Proton Temperature Coefficients

Using the ^{1}H temperature coefficients, the effects that SOD1 maturation have on the local structural stability of residues can be investigated. First, the changes in the ^{1}H temperature coefficients are examined for pWT SOD1, as the protein matures from apo2SH to E,Zn2SH SOD1, and then from E,Zn2SH to holo SOD1. Then, the effects of maturation, from apo2SH to holo SOD1, have on the ^{1}H temperature coefficients of mutant SOD1 are examined.

pWT Maturation: Increased Stability over the Maturation Process.

As pWT SOD1 matures, from apo2SH to E,Zn2SH and from E,Zn2SH to holo SOD1, the average temperature coefficients of the entire protein, and of each structural element, increase. This demonstrates that the protein and many of the structural features become increasingly stable the farther down the maturation process the protein is. Table 9 displays the average temperature coefficients for each of the maturation states of pWT SOD1 studies, and those of the individual structural elements. In general, the temperature coefficients of the structural features are the most negative in the apo2SH state and the most positive in the holo state. This indicates the increased structural stability throughout the protein, resulting from the binding of zinc and copper, the formation of the disulfide bond between C57 and C146, and dimerization. The most notable areas that exhibit large increases in structural stability as the protein matures are the β-barrel plug, loop IV, the strands involved in metal-binding, and the electrostatic loop. Each of these regions are structurally or functionally important and, therefore, it is expected that they would exhibit increased stability during SOD1 maturation. Interestingly, the structural stability of the first three β-strands, forming the majority of the first β-sheet, and the first two loops did not increase as much as the other structural elements over

	Apo2SH	EZn2SH	Holo
Temperature Coefficient Summary			
Average (ppb/K)	-5.35	-4.05	-3.24
# Res	119	112	97
T_m (°C)	47.6	55	92.7
Average Temperature Coefficient for Structural Features (ppb/K)			
N	N/A	N/A	N/A
β1	-4.21 (5)	-3.50 (6)	-3.66 (6)
Loop I	-5.71 (4)	-6.41 (3)	-4.73 (1)
β2	-2.25 (9)	-3.34 (8)	-2.64 (7)
Loop II	-6.03 (3)	-6.13 (4)	-5.12 (1)
β3	-3.26 (7)	-3.27 (7)	-2.76 (7)
Loop III	-11.26 (3)	-7.34 (1)	-4.02 (2)
β4	-6.73 (8)	-5.02 (6)	-3.08 (7)
Loop IV Part 1	-6.68 (11)	-3.44 (7)	-3.27 (7)
Loop IV Part 2	-5.71 (7)	-4.24 (15)	-3.66 (11)
β5	-5.61 (5)	-3.97 (5)	-3.05 (7)
Loop V	-4.02 (4)	-3.69 (4)	-2.76 (3)
β6	-5.75 (8)	-4.91 (8)	-4.69 (7)
Loop VI	-4.47 (10)	-4.28 (9)	-2.61 (7)
β7	-2.84 (5)	-2.82 (3)	-1.78 (5)
Loop VII	-6.51 (19)	-3.67 (19)	-3.09 (11)
β8	-4.38 (9)	-2.53 (5)	-3.39 (7)
C	-7.42 (2)	-3.60 (2)	-0.70 (1)

Table 9: ^{1}H Temperature Coefficients Summary for pWT SOD1 Maturation States. Temperature coefficient data for each pWT SOD1 maturation state are summarized here. The first portion of the table describes the average temperature coefficients and the number of residues that data is available for. The second portion of the table describes the average temperature coefficient for each structural feature of SOD1, with the average temperature coefficient found beside the parentheses containing the number of residues for which data is available. Holo temperature coefficient data and thermostability data was obtained from previous publications.[63,82,84]

the maturation process. This may suggest that the hydrogen bond network across the first β-sheet is not as affected by SOD1 maturation as the second β-sheet, which is involved in binding metals and contains the intramolecular disulfide bond. Overall, as SOD1 matures, the protein and its individual structural elements becomes increasingly stable.

Apo2SH to E,Zn2SH pWT: Increased Stability Throughout the Protein.

As expected, the majority of the residues in E,Zn2SH pWT SOD1 experience an increase in local stability, especially those found in structural elements surrounding the zinc-binding site. Figure 3.4 (A) displays the changes in temperature coefficients of E,Zn2SH pWT relative to apo2SH pWT SOD1 on the structure of dimeric E,Zn2SH pWT SOD1 and monomeric E,Zn2SH complexed with domain II of the CCS.[160,164] Here, large positive changes in temperature coefficients are seen in residues throughout the dimer interface, β-strand 4, the zinc-binding loop (loop IV), the β5-β6 hairpin, and the electrostatic loop (loop VII). These data agree with previous results that have shown an increased structure of these regions as a result of zinc-binding.[121] Interestingly, there is a small "pocket" of destabilized residues found across the top of β-strands 2, 3, and 6. These destabilized residues, and a couple of destabilized residues in the loops connecting these strands, may report on a slightly altered hydrogen bonding network, as a result of dimerization and zinc-binding, as this region would not be stabilized by the strengthened hydrogen bonding network in the areas involved in zinc-binding and dimerization.[63,107,121,163] Lastly, while residues G51 and G151, two of three residues involved in forming intermolecular hydrogen bonds with either another monomer of SOD1 or the CCS, are stabilized upon zinc binding, the third residue, G114, is destabilized. This may be reporting on an altered hydrogen bonding network in the dimer interface of dimeric E,Zn2SH SOD1 that allows the dimer to transiently dissociate, resulting in monomeric E,Zn2SH SOD1. This monomeric E,Zn2SH SOD1 can then interact with the CCS and continue further down the maturation pathway.[86,160] In summary, the ^{1}H temperature coefficient patterns resulting from the maturation of pWT SOD1 from the apo2SH to the E,Zn2SH state display an increase in local stability throughout the structure, as well as some structurally important destabilization near the dimer interface that may allow the protein to dissociate, a process needed to continue down the SOD1 maturation pathway.

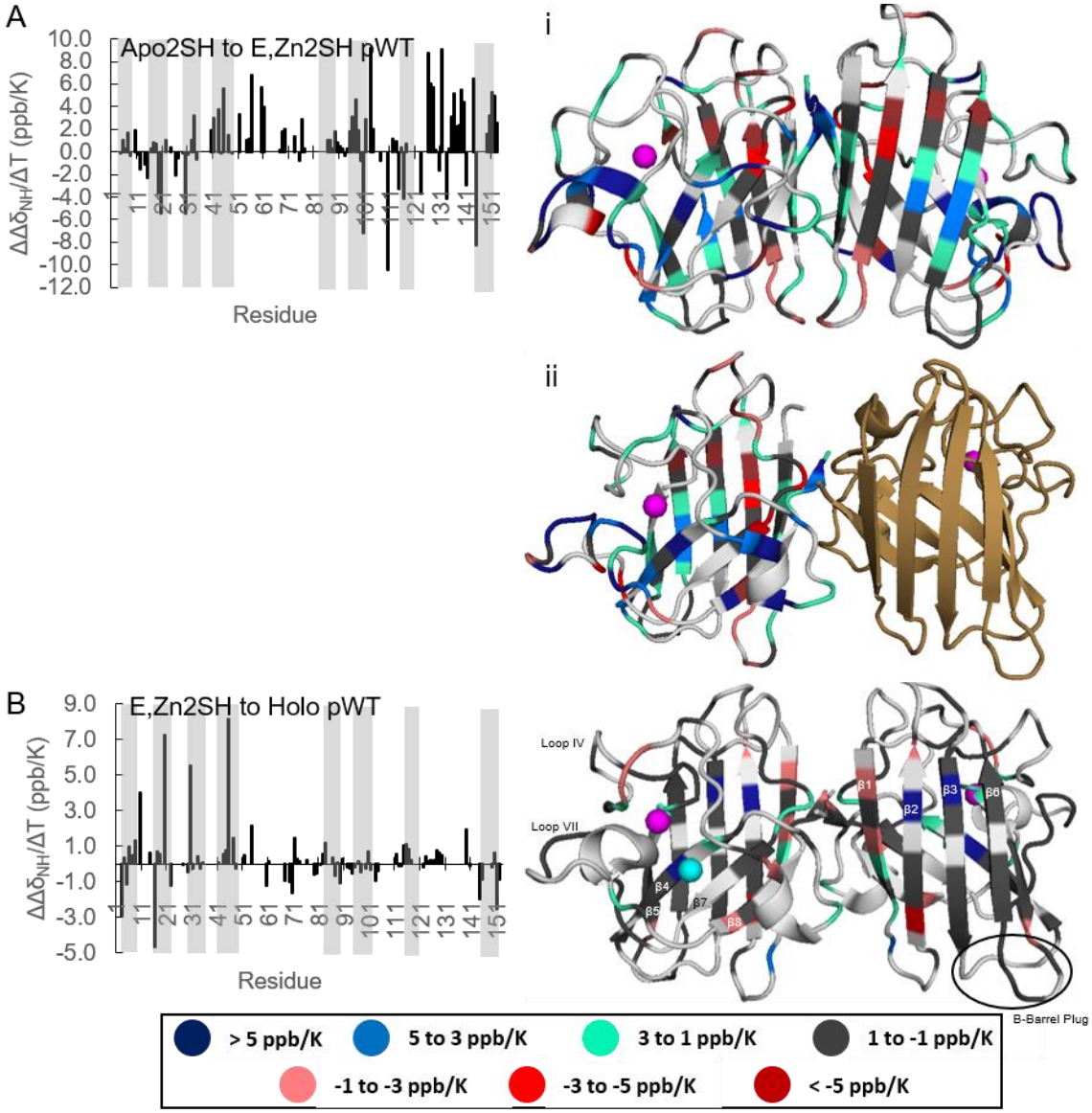

Figure 3.4: Changes in pWT ^{1}H Temperature Coefficients During Maturation. This figure displays the changes in ^{1}H temperature coefficients as the protein matures from (A) apo2SH to E,Zn2SH, plotted on the structure of i) E,Zn2SH pWT and ii) E,Zn2SH pWT with CCS, and (B) E,Zn2SH to holo SOD1. Residues coloured white occur where no comparisons could be made. Zinc and copper ions are coloured magenta and cyan, respectively. The CCS is sand-coloured. Figures were made using PyMOL and PDB codes 2AF2, 6FOL, and 1HL5.[70,72,160,164]

E,Zn2SH to Holo pWT: Increased Stability in the Metal-Binding Region and Recovered Stability of G114.

The temperature coefficients of residues assigned in both E,Zn2SH and holo pWT SOD1 indicate an increase of structural stability in the metal-binding region and G114, a

structurally important residue that forms intermolecular hydrogen bonds in the dimer interface. More specifically, the local stability of two of the zinc-binding ligands, H71 and D83, are increased in holo pWT, as well as two of the residues directly beside the copper-binding ligands H46 and H48. Also, the stability of residue G114 has increased in holo pWT relative to E,Zn2SH pWT, suggesting the residue's ability to form intermolecular hydrogen bonds in the dimer interface has returned, resulting in the tight dimer observed for holo SOD1.[82] While there are a small subset of residues in the dimer interface of holo pWT SOD1 that show a slight decrease in stability, some of these are directly beside residues stabilized by maturation from E,Zn2SH pWT. Those that are not may be reporting on increased strain in this region, due to the formation of the dimer. Lastly, many of the residues that can be compared between the two states possess near-identical temperature coefficients. This pattern is different from the pattern seen during the maturation from apo2SH to E,Zn2SH pWT, where most of the residues show significantly more positive temperature coefficients. This demonstrates that the binding of zinc confers the majority of the structural stability observed in holo SOD1. Overall, maturation from E,Zn2SH to holo pWT SOD1 results in an increase of structural stability around the metal-binding region, and a return of G114 stability, indicating a more structurally stable dimer interface.

Effects of Mutation on the Maturation of SOD1 Occur Locally.

The average temperature coefficients for each of the mutant SOD1 and their individual structural elements show increased stability upon maturation from apo2SH to holo SOD1. The average temperature coefficients for each of these mutants and their structural features for both apo2SH and holo states are summarized in Table 10. The increase in stability in each structural feature generally mirrors the change in average temperature coefficients of those features in pWT SOD1. The changes in temperature coefficients from apo2SH to holo SOD1 for pWT are plotted onto the structure of SOD1 in Figure 3.5 (A). Here, positive increases in temperature coefficients can be seen throughout the structure of SOD1, with few residues experiencing decreases. The residues that experience decreases in stability are directly beside residues experiencing increases in stability and are scattered throughout the structure of SOD1. From

	Apo2SH G93A	Holo G93A	Apo2SH E100G	Holo E100G	Apo2SH V148I	Holo V148I
Temperature Coefficient Summary						
Average (ppb/K)	-5.69	-3.43	-5.66	-3.37	-5.38	-3.03
# Res	100	101	113	93	117	92
T_m (°C)	33	87.7	33.2	86.2	51	92.7
Average Temperature Coefficient for Structural Features (ppb/K)						
N	N/A	N/A	N/A	-8.97 (1)	N/A	N/A
β1	-4.49 (5)	-4.03 (4)	-4.33 (5)	-3.92 (4)	-4.67 (5)	-4.48 (3)
Loop I	-5.99 (4)	N/A	-5.99 (3)	N/A	-5.29 (4)	N/A
β2	-3.77 (6)	-2.13 (8)	-2.24 (9)	-2.52 (7)	-2.18 (9)	-1.97 (7)
Loop II	-6.28 (3)	-5.16 (1)	-6.24 (3)	-5.32 (1)	-6.04 (3)	-4.93 (1)
β3	-3.54 (6)	-2.93 (5)	-3.66 (8)	-2.81 (6)	-3.18 (7)	-2.46 (6)
Loop III	-9.29 (1)	-10.07 (2)	-11.59 (3)	-4.22 (2)	-11.66 (3)	-3.98 (2)
β4	-5.47 (6)	-2.91 (8)	-6.99 (8)	-2.95 (8)	-6.97 (8)	-2.57 (6)
Loop IV (Part 1)	-6.73 (11)	-3.37 (8)	-6.86 (11)	-3.77 (6)	-6.78 (11)	-2.05 (8)
Loop IV (Part 2)	-5.95 (6)	-4.08 (12)	-5.84 (6)	-4.24 (12)	-5.72 (7)	-3.99 (13)
β5	-5.65 (4)	-3.47 (6)	-5.75 (5)	-3.54 (6)	-5.74 (5)	-3.29 (6)
Loop V	-8.59 (1)	-4.24 (4)	-3.80 (4)	-2.77 (3)	-3.83 (4)	-3.15 (4)
β6	-5.98 (5)	-4.05 (7)	-6.02 (8)	-3.96 (4)	-5.38 (8)	-4.47 (7)
Loop VI	-4.80 (10)	-2.61 (7)	-4.93 (9)	-2.86 (7)	-4.43 (10)	-2.70 (8)
β7	-3.03 (5)	-1.95 (4)	-3.30 (4)	-1.90 (6)	-2.94 (4)	-1.71 (5)
Loop VII	-7.04 (17)	-2.79 (15)	-6.83 (18)	-2.70 (11)	-6.66 (18)	-2.14 (9)
β8	-6.11 (8)	-3.61 (8)	-5.55 (7)	-3.46 (7)	-4.21 (9)	-3.08 (5)
C	-7.25 (2)	-4.18 (2)	-7.45 (2)	-4.31 (2)	-7.52 (2)	-3.72 (2)

Table 10: ^{1}H Temperature Coefficients Summary for Mutant SOD1 Maturation States. Temperature coefficient data for each mutant SOD1 maturation state are summarized here. The first portion of the table describes the average temperature coefficients and the number of residues that data is available for. The second portion of the table describes the average temperature coefficient for each structural feature of SOD1, with the average temperature coefficient found beside the parentheses containing the number of residues for which data is available. Holo temperature coefficient data and thermostability data was obtained from previous publications.[63,82,84]

the changes in temperature coefficients upon the maturation of V148I, G93A, and E100G seen in Figure 3.5 and Figure 3.6, the changes closely mirror those observed in pWT SOD1.

From the differences in temperature coefficients summarized in Table 10 and shown in Figures 3.5 and 3.6, each of the mutants show slightly different patterns of stabilization. When compared to differences in temperature coefficients between the apo2SH and holo states of the other mutations, V148I shows slightly increased stability in the dimer interface and the electrostatic loop. This is likely a result of the stabilizing effect of this mutation. In contrast, E100G displays a decrease in the change of average temperature coefficients for the zinc-binding loop. This may be a result of an altered bond between D101 and R79, which confers

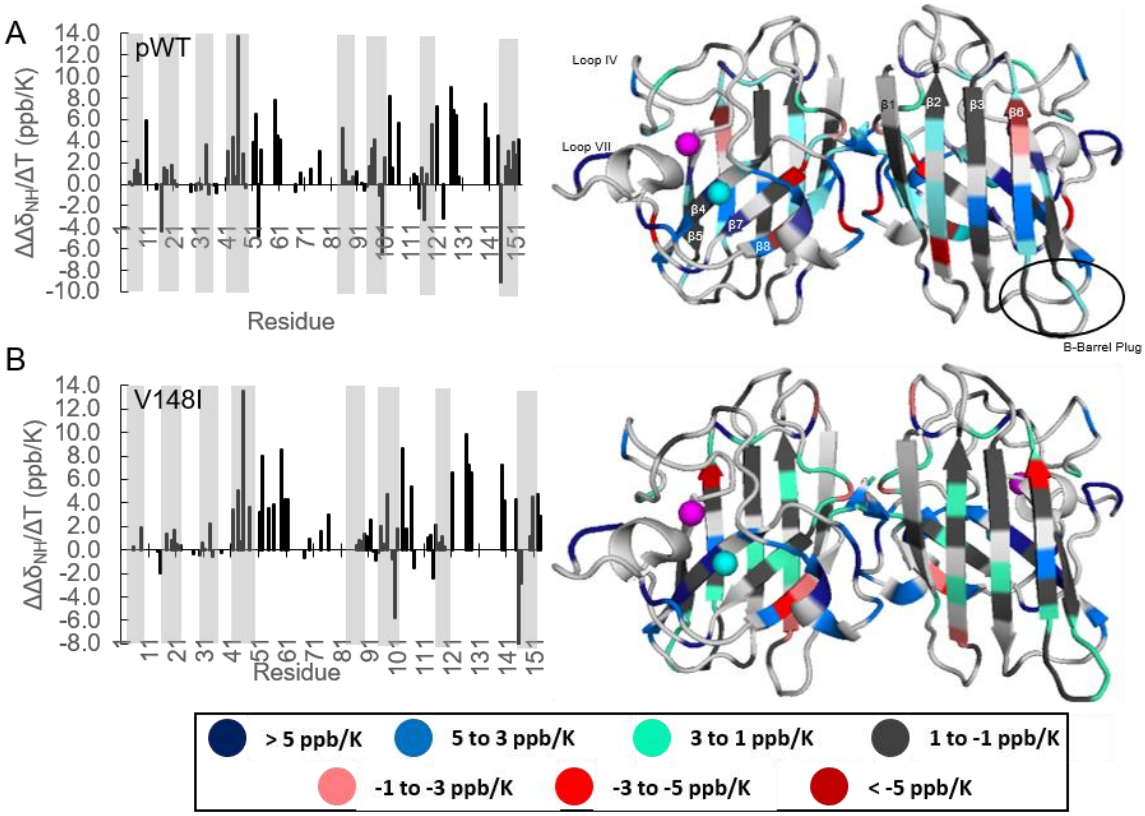

Figure 3.5: Changes in pWT and V148I ^{1}H Temperature Coefficients During Maturation. This figure displays the changes in ^{1}H temperature coefficients as the protein matures from apo2SH to holo SOD1 for (A) pWT and (B) V148I. Residues coloured white occur where no comparisons could be made. Zinc and copper ions are coloured magenta and cyan, respectively. Figures were made using PyMOL and PDB code 1HL5.[70,72]

stability to the zinc-binding loop by tethering it to the β-barrel.[127] Also noted is the decrease in local stability at the beginning of β-strand 3, which is usually connected to the end of β-strand 6 through a salt bridge between K30 and E100. This decrease likely indicates that the end of this strand is still frayed in holo SOD1. Lastly, during the maturation of G93A, it is displayed in Table 10 that loop III, which contains the β-barrel plug, is not stabilized upon maturation. This is likely due to the altered conformation of the β-barrel plug in the structure of G93A.[116] In summary, the effects of mutations on the maturation process from apo2SH to holo SOD1 are minimal, with slight differences occurring near the sites of mutation, as the temperature coefficient patterns are similar to those observed for pWT SOD1.

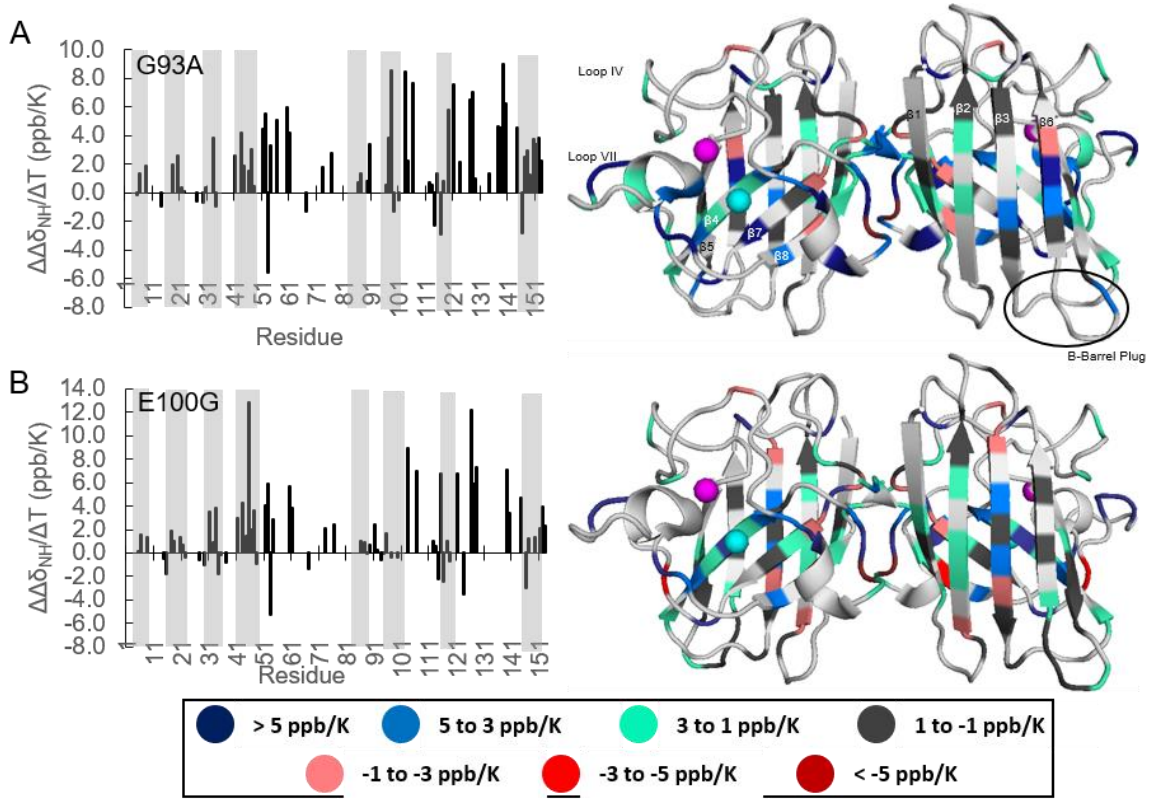

Figure 3.6: Changes in G93A and E100G ^{1}H Temperature Coefficients During Maturation. This figure displays the changes in ^{1}H temperature coefficients as the protein matures from apo2SH to holo SOD1 for (A) G93A and (B) E100G. Residues coloured white occur where no comparisons could be made. Zinc and copper ions are coloured magenta and cyan, respectively. Figures were made using PyMOL and PDB code 1HL5.[70,72]

3.3.3 Amide Nitrogen Temperature Coefficients

As discussed in Section 2.3.4, amide nitrogen temperature coefficients are extremely sensitive to structural deviations from random coil and may be used as a measure of structure for each residue in the protein.[61] This section aims to determine the effects that mutation have on the maturation of SOD1, as determined by amide nitrogen temperature coefficients. First, the maturation process of pWT SOD1 is investigated to determine how the structure of SOD1 changes as the protein matures. Following analysis of pWT, the structure observed in the apo2SH and holo states of mutants G93A, E100G, and V148I are compared.

pWT Maturation: Increased Structure in the Dimer Interface and Metal-Binding Region, Decreased Structure Across β-Sheet 1.

As pWT SOD1 matures from apo2SH to E,Zn2SH and from E,Zn2SH to holo SOD1, the structure of the protein increases around the metal-binding regions and in some of the structural elements that form the dimer interface. Oppositely there is a pattern of destabilization across the first β-strand. The average secondary ^{15}N temperature coefficients for each of the pWT maturation states studied are summarized in Table 11. As expected, the binding of metals and the formation of the disulfide bond have a positive effect on the structure of the zinc-binding loop and β-strands 4 and 8. Other regions that become more structured are the first loop and the β-barrel plug. The pattern of structural changes upon maturation will be discussed in the next two subsections.

Apo2SH to E,Zn2SH SOD1: Increased Structure in the Dimer Interface, Decreased Structure in Hydrophobic Residues Pointing into the Core of the Protein.

As the protein matures from apo2SH to E,Zn2SH SOD1, numerous residues found throughout the β-strands and loops that make up the dimer interface and the zinc-binding loop. The differences in absolute secondary ^{15}N temperature coefficients between apo2SH and E,Zn2SH pWT can be viewed in Figure 3.7 (A) on the structures of E,Zn2SH pWT and E,Zn2SH pWT with CCS. The increases in structure in the dimer interface, notably in G51, a residue that forms intermolecular hydrogen bonds with the other SOD1 monomer, is due to the formation of the SOD1 dimer. In extension, the increases in structure of the zinc-binding

	Apo2SH	EZn2SH	Holo
N	N/A	N/A	N/A
β1	34.00 (5)	34.91 (6)	28.73 (6)
Loop I	9.19 (4)	13.90 (3)	31.77 (1)
β2	33.39 (9)	25.87 (8)	21.51 (5)
Loop II	17.00 (3)	11.42 (4)	9.53 (1)
β3	34.43 (7)	31.17 (7)	29.82 (7)
Loop III	22.51 (3)	24.20 (1)	25.32 (2)
β4	18.35 (8)	22.13 (6)	23.35 (7)
Loop IV Part 1	14.60 (11)	24.60 (7)	18.20 (7)
Loop IV Part 2	16.08 (7)	23.67 (15)	22.62 (10)
β5	30.52 (5)	26.44 (5)	25.70 (7)
Loop V	17.78 (4)	19.93 (4)	8.94 (3)
β6	26.34 (8)	25.21 (8)	19.57 (7)
Loop VI	29.67 (10)	31.72 (9)	29.06 (6)
β7	32.01 (5)	21.77 (3)	31.26 (5)
Loop VII	23.95 (19)	25.75 (19)	23.96 (11)
β8	22.38 (9)	27.27 (5)	27.82 (7)
C	10.07 (1)	50.03 (1)	41.09 (1)

Table 11: ^{15}N Temperature Coefficients Summary for Mutant SOD1 Maturation States. Secondary amide nitrogen **t**emperature coefficient data for each pWT SOD1 maturation state are summarized here. This describes the average temperature coefficient for each structural feature of SOD1, with the average temperature coefficient found beside the parentheses containing the number of residues for which data is available.

and electrostatic loops are the result of the binding of zinc, which has been shown to increase the structure of the zinc-binding loop and causes the formation of the short-helix observed in the electrostatic loop.[121] Interestingly, the differences in ^{15}N temperature coefficients also display a decrease in structure in many of the residues that form the hydrophobic core of the protein. For example, residues A4, F20, F45, V97, and I99, all of which point into the core of the protein show a decrease in structure. As discussed in Section 3.3.1, the decreased structure

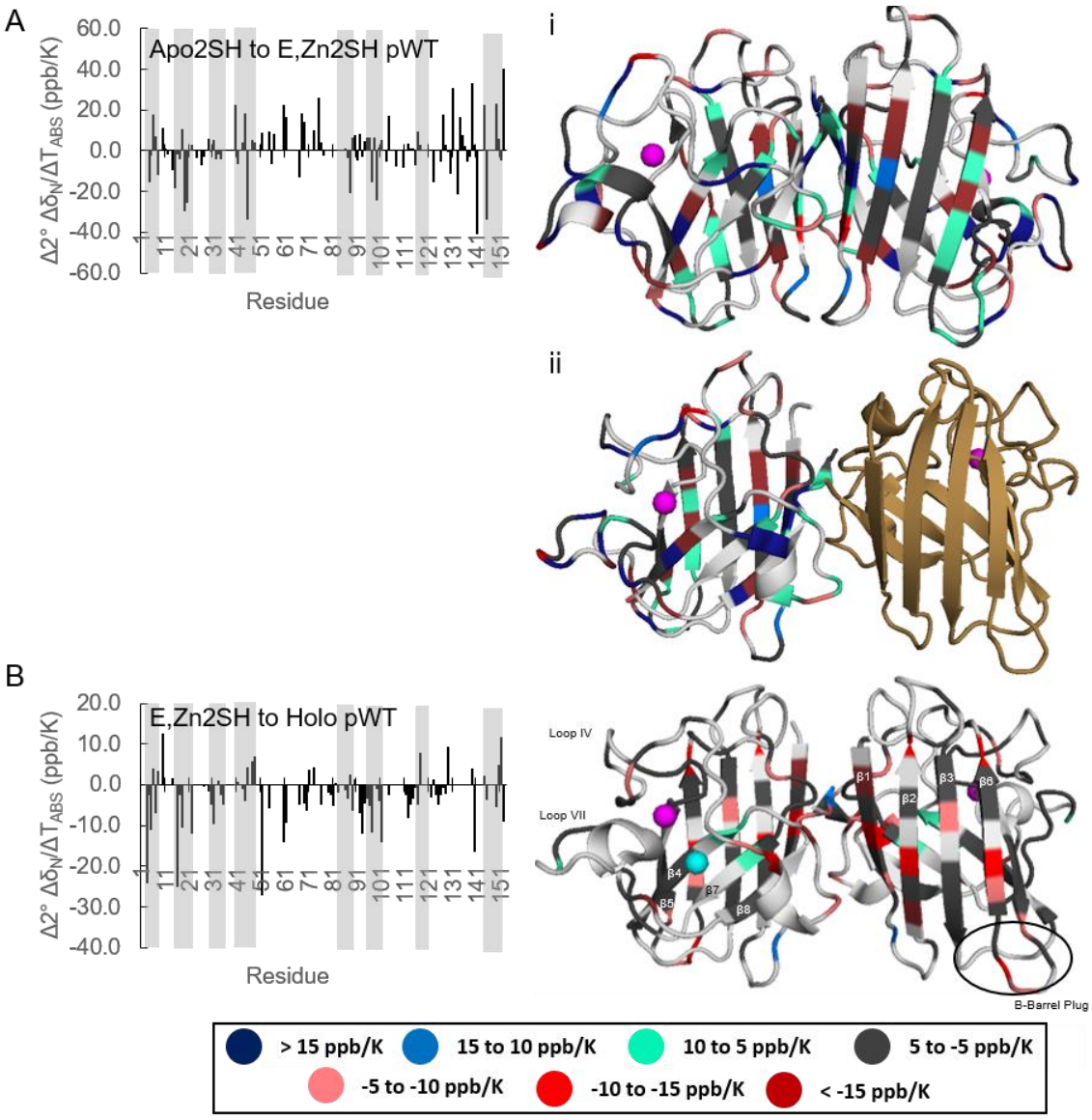

Figure 3.7: Changes in pWT ^{15}N Temperature Coefficients During Maturation. This figure displays the changes in absolute secondary ^{15}N temperature coefficients as the protein matures from from (A) apo2SH to E,Zn2SH, plotted on the structure of i) E,Zn2SH pWT and ii) E,Zn2SH pWT with CCS, and (B) E,Zn2SH to holo SOD1. Residues coloured white occur where no comparisons could be made. Zinc and copper ions are coloured magenta and cyan, respectively. The CCS is sand-coloured. Figures were made using PyMOL and PDB codes 2AF2, 6FOL, and 1HL5.[70,72,160,164]

in this region may be either a result of the increased breathing motions of SOD1, observed in the dimeric form of the protein, or the process of dimerization results in a slightly different packing of the residues in the dimer interface that is able to propagate through the structure of the protein to other hydrophobic residues.[168]

E,Zn2SH to Holo SOD1: Increased Structure Surrounding the Copper-Binding Site and Further Decreased Structure Across β-Sheet 1.

Following the binding of copper and the formation of the intermolecular disulfide bond of SOD1 by the CCS, the protein shows increased structure around the copper binding site, specifically in residue H48, a copper-binding ligand. Another residue that experiences an increase in structure is G151, found in the dimer interface. This residue is one of the three that forms intermolecular hydrogen bonds and its increased structure may indicate a tighter dimer in holo SOD1.[82] In contrast, some of the hydrophobic residues, such as V5, V7, I149, and A152, that form the dimer interface experience a decrease in structure. Furthermore, additional hydrophobic residues that point into the core of the protein, such as I18 and V31, experience a decrease in structure. This decreased structure is likely the result of a strengthened dimer interface in holo SOD1 that further disrupts the packing structure of the hydrophobic residues that form the core of the protein. In short, these ^{15}N secondary temperature coefficients report on the increased structure found surrounding the zinc binding site as a result of zinc-binding, and the decreased structure of residues found in the dimer interface and across the first β-sheet as a result of dimerization.

Mutant SOD1 Exhibit Locally-Occurring Effects on SOD1 Maturation Compared to pWT.

Each of the SOD1 variants studied show similar ^{15}N temperature coefficient patterns during maturation from the apo2SH state to holo state as pWT SOD1. The average ^{15}N temperature coefficients for each structural feature in the protein are summarized in Table 12. These temperature coefficients are also plotted onto the structure of holo SOD1 in Figure 3.8 (pWT and V148I maturation) and Figure 3.9 (G93A and E100G maturation). During maturation from apo2SH to holo pWT SOD1, there are large increases in structure of residues surrounding the metal-binding region and many of the residues found in the dimer interface. Notable residues that experience an increase in structure include H48, V119, and G151, along with hydrophobic residues in the dimer interface such as A6, V148, I149, and A152. These support the increased structure in the metal-binding region and the dimer interface of holo SOD1 compared to apo2SH SOD1.[63,82,121]

	Apo2SH G93A	Holo G93A	Apo2SH E100G	Holo E100G	Apo2SH V148I	Holo V148I
N	N/A	N/A	N/A	9.29 (1)	N/A	N/A
β1	35.29 (5)	24.91 (4)	33.90 (5)	27.81 (4)	33.24 (5)	20.44 (3)
Loop I	13.42 (4)	N/A	16.22 (3)	N/A	13.37 (4)	N/A
β2	29.87 (6)	25.86 (6)	35.20 (9)	25.83 (6)	33.30 (9)	27.64 (5)
Loop II	18.00 (3)	9.31 (1)	15.91 (3)	9.56 (1)	17.46 (3)	8.73 (1)
β3	33.89 (6)	24.21 (5)	26.35 (8)	26.25 (6)	34.08 (7)	28.67 (6)
Loop III	4.62 (1)	20.85 (2)	22.06 (3)	25.01 (2)	23.76 (3)	25.15 (2)
β4	18.49 (6)	24.91 (8)	18.35 (8)	24.13 (8)	20.30 (8)	20.95 (6)
Loop IV (Part 1)	16.43 (11)	19.00 (8)	17.64 (11)	16.50 (6)	13.92 (11)	23.31 (8)
Loop IV (Part 2)	17.63 (6)	20.36 (12)	15.88 (6)	20.37 (12)	16.35 (7)	20.95 (13)
β5	23.15 (4)	25.62 (6)	28.60 (5)	24.30 (6)	31.23 (5)	24.63 (6)
Loop V	13.22 (1)	23.92 (4)	19.19 (4)	18.02 (3)	18.01 (4)	16.78 (4)
β6	28.72 (5)	20.73 (7)	22.54 (8)	20.11 (4)	25.02 (8)	19.38 (7)
Loop VI	29.21 (10)	28.34 (7)	27.82 (9)	28.90 (7)	30.28 (10)	29.41 (8)
β7	28.60 (5)	30.98 (4)	23.73 (4)	32.58 (6)	22.65 (4)	32.15 (5)
Loop VII	19.65 (17)	26.05 (14)	25.70 (18)	24.07 (11)	22.95 (18)	23.67 (9)
β8	15.25 (8)	28.68 (8)	15.74 (7)	28.37 (7)	21.63 (9)	31.98 (5)
C	10.54 (1)	41.07 (1)	9.99 (1)	40.93 (1)	8.58 (1)	43.06 (1)

Table 12: ^{15}N Temperature Coefficients Summary for Mutant SOD1 Maturation States. Secondary amide nitrogen **t**emperature coefficient data for each mutant SOD1 maturation state are summarized here. This describes the average temperature coefficient for each structural feature of SOD1, with the average temperature coefficient found beside the parentheses containing the number of residues for which data is available.

With respect to the SOD1 mutants V148I, G93A, and E100G , each experience altered ^{15}N temperature coefficients around the sites of mutations. For example, in V148I, changes in the temperature patterns from those of pWT occur around the site of mutation, where the structure of residues found in β-strand 8 and the first part of the zinc-binding loop, which passes through the dimer interface, are stabilized. There is also a decrease in average temperature coefficient of the first β-strand, likely as result of the increased size of the I148 residue. In

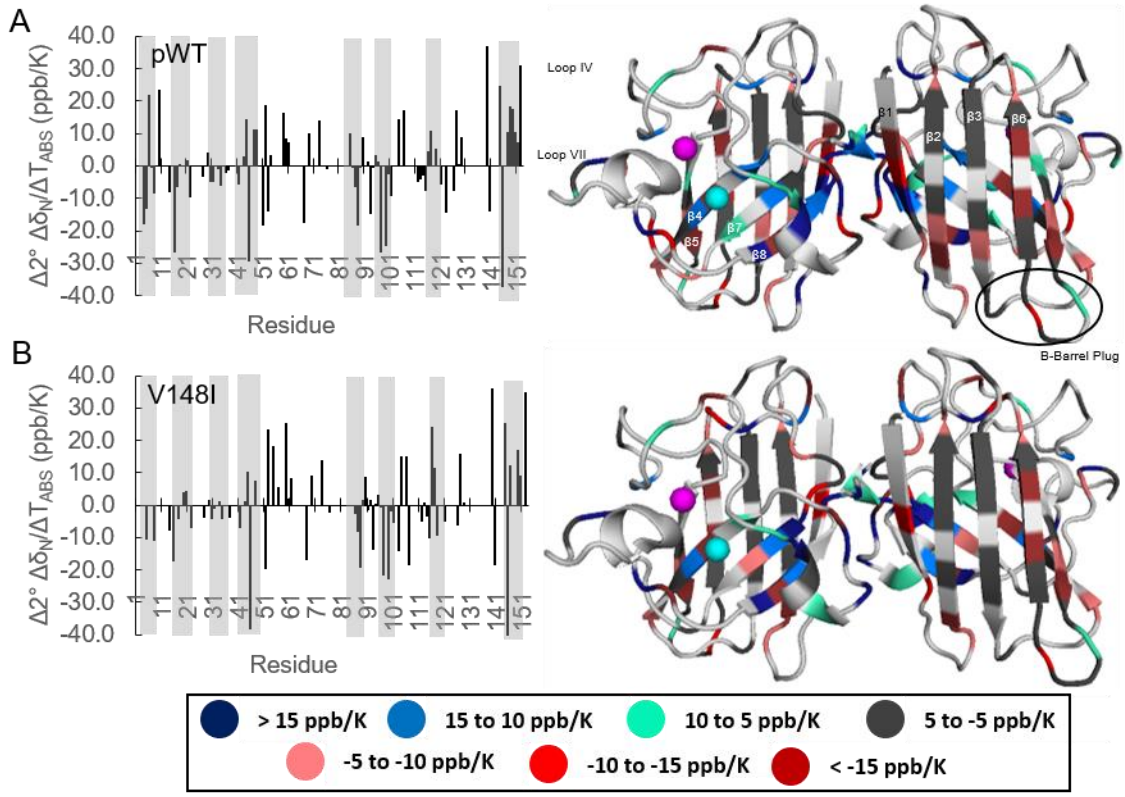

Figure 3.8: Changes in pWT and V148I ^{15}N Temperature Coefficients During Maturation. This figure displays the changes in absolute secondary ^{15}N temperature coefficients as the protein matures from apo2SH to holo SOD1 for (A) pWT and (B) V148I. Residues coloured white occur where no comparisons could be made. Zinc and copper ions are coloured magenta and cyan, respectively. Figures were made using PyMOL and PDB code 1HL5.[70,72]

G93A, there is a large increase of structure in loops III and V, as well as β-strand 5, that is not observed during pWT maturation. These changes in structure are most likely a result of the increased hydrophobic interactions that A93 has with the other hydrophobic residues that make up the β-barrel plug, including L38.[116] Lastly, in E100G, the largest effects on maturation, that do not occur in pWT, are located at the top of β-strand 3 in Figure 3.9 (B), which shows an increased structure as the protein matures. In summary, the amide nitrogen temperature coefficients are able to report on changes in structurally important features of the SOD1, and how mutations affect the structure of SOD1, as the protein matures from its most immature to mature form.

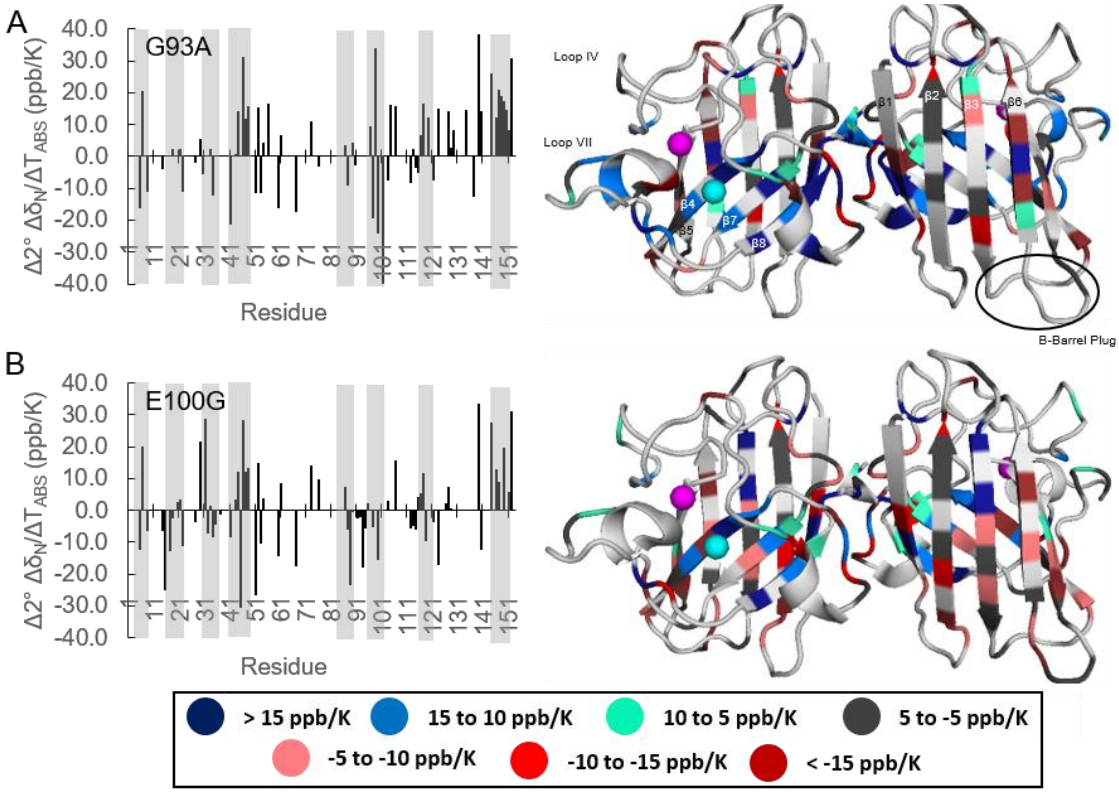

Figure 3.9: Changes in G93A and E100G ^{15}N Temperature Coefficients During Maturation. This figure displays the changes in absolute secondary ^{15}N temperature coefficients as the protein matures from apo2SH to holo SOD1 for (A) G93A and (B) E100G. Residues coloured white occur where no comparisons could be made. Zinc and copper ions are coloured magenta and cyan, respectively. Figures were made using PyMOL and PDB code 1HL5.[70,72]

3.3.4 Conformational Heterogeneity

As discussed earlier in Sections 1.2.7 and 2.3.5, temperature coefficients are predominately linear; however, some studies have shown the existence of curved temperature dependences.[56,62–65] The deviation from linearity, also known as curvature, originates from a temperature-dependent shift in population from the native state to a low-energy excited state.[62] This observed curvature is able to report on the conformational heterogeneity of a protein, which may be vital for structural stability or functions such as binding, allostery, and catalysis.[14,63,66] This section aims to investigate the change in observed curvature patterns and the SOD1 variants mature from the apo2SH state to the holo state. The number of curved residues found in each maturation state of pWT, G93A, E100G, and V148I SOD1 are displayed in Table 13.

^{1}H Curvature in Apo2SH SOD1 Variants					
	pWT		**G93A**	**E100G**	**V148I**
Curved	41		20	27	34
Assignments	119		100	113	117
% Curved	34		20	24	29
^{1}H Curvature in Matured SOD1 Variants					
	E,Zn2SH pWT	**Holo pWT**	**Holo G93A**	**Holo E100G**	**Holo V148I**
Curved	43	28	44	37	19
Assignments	112	97	101	93	92
% Curved	38	29	44	40	21
^{15}N Curvature in Apo2SH and E,Zn2SH pWT					
	Apo2SH	**E,Zn2SH**			
Curved	35	39			
Assignments	119	112			
% Curved	29	35			

Table 13: Curvature Changes in SOD1 Variants During Maturation. This table displays the curvature information for the different maturation states of SOD1 variants studied. The percentage of curved residues is calculated by dividing the number of curved residues by the number of assignments in the protein. Holo SOD1 variant data was obtained from Doyle *et al.*[63]

Decreased Curvature During pWT Maturation a Result of Increased Structure.

As pWT SOD1 matures from apo2SH to E,Zn2SH, and from E,Zn2SH to holo SOD1, there is a loss of curvature in many of the structural elements of the protein. These losses of curvature are likely a result of the increased structure in some of the structural features. For example, when apo2SH pWT matures to E,Zn2SH pWT SOD1, as viewed in Figure 3.10 (A), there are losses in curvature throughout the electrostatic loop and the metal-binding region. This is a result of the zinc ion conferring structural stability to this region, especially in the electrostatic loop, where the short helix forms.[121] In E,Zn2SH pWT SOD1, many of the residues that are found in the dimer interface experience gains in curvature, relative to apo2SH pWT. These increases in curvature report on the dissociation of the dimer to form monomeric E,Zn2SH SOD1, which is then able to interact with the CCS.[86] Interestingly, there is an

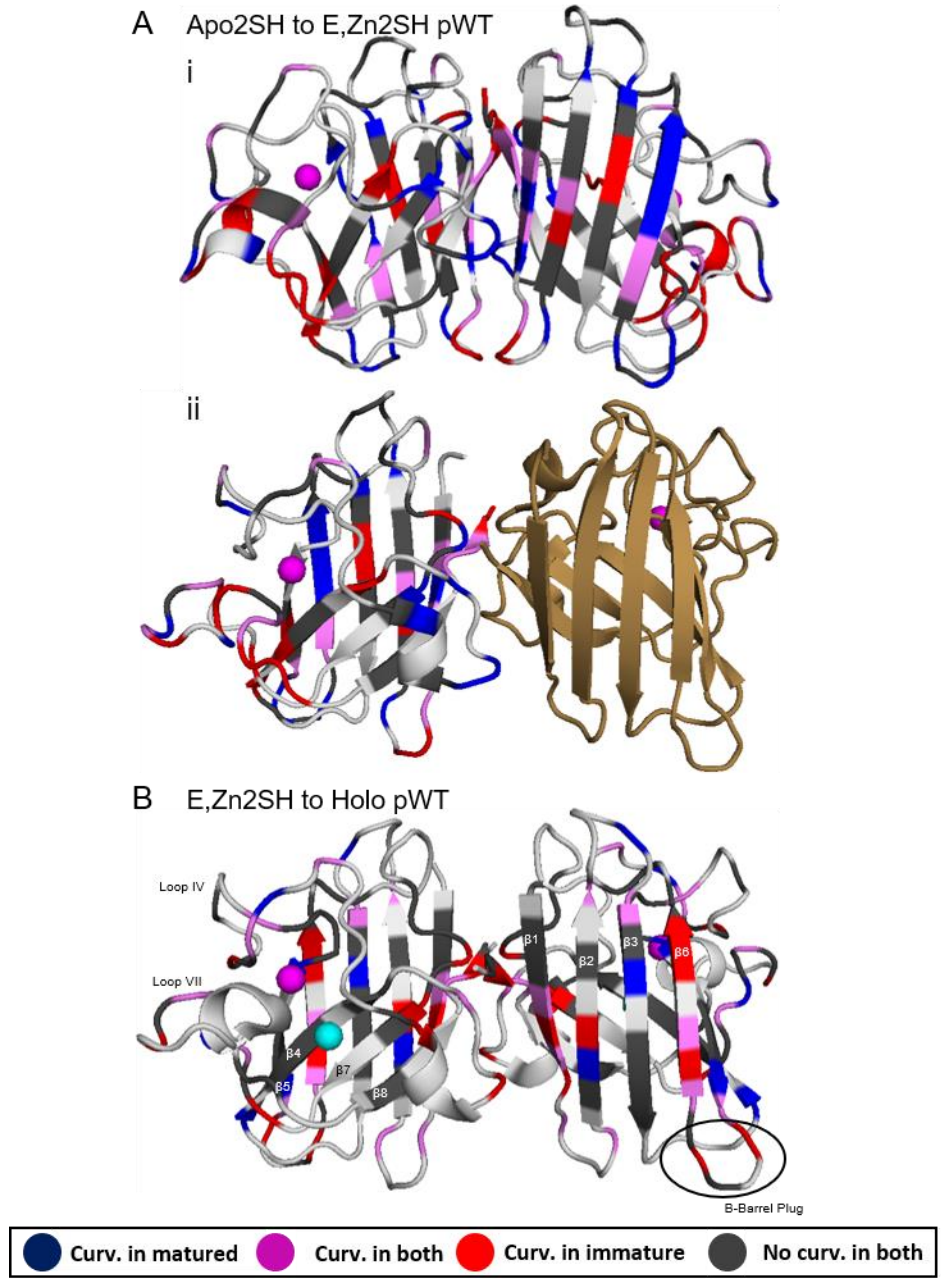

Figure 3.10: Changes in pWT ^{1}H Curvature Patterns During Maturation. This figure displays the changes in ^{1}H curvature patterns as the protein matures from (A) apo2SH to E,Zn2SH, plotted on the structure of i) E,Zn2SH pWT and ii) E,Zn2SH pWT with CCS, and (B) E,Zn2SH to holo SOD1. Residues coloured white occur where no comparisons could be made. Zinc and copper ions are coloured magenta and cyan, respectively. The CCS is sand-coloured. Figures were made using PyMOL and PDB codes 2AF2, 6FOL, and 1HL5.[70,72,160,164]

increase in curvature in across the "top" of β-sheet 1, most notably in β6. These increases in curvature may be reporting on an alternate state, where the loops across the top of the β-barrel become more structured following the binding of zinc and dimerization.

Following maturation from E,Zn2SH to holo pWT SOD1, there is an observed loss of curvature in the dimer interface of the protein and at the end of β-strand 6. The loss of curvature in the dimer interface reports on the formation of a tight dimer in holo SOD1.[82] Throughout the rest of the structure of the protein, residues that experience a gain in curvature are usually directly beside residues that experience losses in curvature, resulting in a net zero change in curvature for given regions. This indicates that the largest changes in structure between E,Zn2SH and holo SOD1 occur in the dimer interface. In summary, the binding of zinc to apo2SH SOD1 confers structural stability to the electrostatic loop and metal-binding region of the protein, observed as a loss of curvature, and an increase in curvature in the dimer interface as a result of increased transitions between monomeric and dimeric E,Zn2SH SOD1. In addition, when the protein further matures to holo pWT SOD1, the protein experiences an extensive loss of curvature in the dimer interface, owing to the formation of a tight dimer.

Mutations to SOD1 Result in Increased Curvature in the Dimer Interface During Maturation that Propagates to the β5-β6 Hairpin.

For each of the SOD1 variants, where the maturation to holo from apo2SH SOD1 can be studied, there is an increase in curvature present in the dimer interface. The difference in the curvature patterns between apo2SH and holo SOD1 can be found in Figure 3.11. During the maturation of pWT, from apo2SH to holo SOD1, there is a loss of curvature found in the dimer interface, as well as around both metal binding sites and in the electrostatic loop. These data signify the increased stability of each of these regions due to the binding of zinc and copper, the formation of the disulfide bond, and the formation of a tight dimer. Similarly, each of the SOD1 variants display a loss of curvature in the electrostatic loop and metal-binding sites; however, there is an increase of curvature found in the dimer interface of all of these mutants. This increase in curvature likely reports on the decreased strength of the dimer interface in mutant SOD1, allowing the protein to transiently monomerize.[101,119] In general,

from the results in Section 2.3.5, the apo2SH mutant SOD1 possess less curvature in the dimer interface region than pWT, indicating a decreased ability to transiently dimerize due to a weakened dimer interface region. Since this curvature appears in holo SOD1, of which there should be very little in the dimer interface if it is well-structured and maintained, it again indicates the weakening of the dimer interface in mutant SOD1. In addition, compared to the changes in curvature due to pWT maturation, there is an increase in curvature at the top of the β5-β6 hairpin and throughout loop VI during mutant SOD1 maturation. This increase in curvature in holo SOD1 likely appears due to the weakening of the dimer interface and decreased structure of loop VI in mutant SOD1, increasing the flexibility of the loop and allowing it to adopt alternate conformations. In summary, these altered curvature patterns show that mutant SOD1 weaken the dimer interface of the holo protein, which is propagated to β5-β6 hairpin through increased flexibility in loop VI.

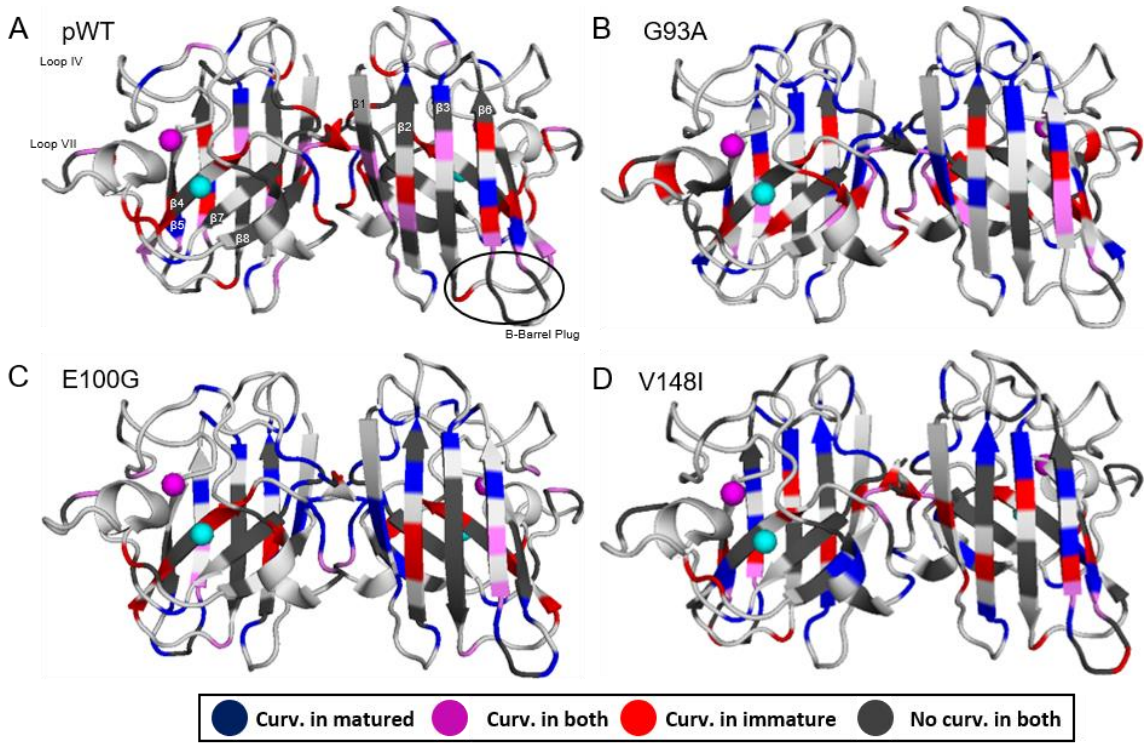

Figure 3.11: Changes in ^{1}H Curvature Patterns During Maturation of SOD1 Variants. This figure displays the changes in ^{1}H curvature patterns as the protein matures from apo2SH to holo SOD1 for (A) pWT, (B) G93A, (C) E100G and (D) V148I. Residues coloured white occur where no comparisons could be made. Zinc and copper ions are coloured magenta and cyan, respectively. Figures were made using PyMOL and PDB code 1HL5.[70,72]

Increased Structure in Metal-Binding Region and Dimer Interface in E,Zn2SH SOD1 Viewed by ^{15}N Curvature Patterns.

As a result of zinc-binding to apo2SH pWT SOD1, there is an increase in structure surrounding the metal-binding region and the dimer interface, as determined by the loss of curvature in the ^{15}N temperature coefficients of these locations. Figure 3.12 displays these changes in curvature patterns on the structure of E,Zn2SH SOD1 and E,Zn2SH complexed with the CCS.[160,164] These data match with previous results discussed throughout this chapter, as a short helix forms in the electrostatic loop and the zinc-binding loop becomes more ordered as a result of the binding of the zinc ion and dimerization.[121]

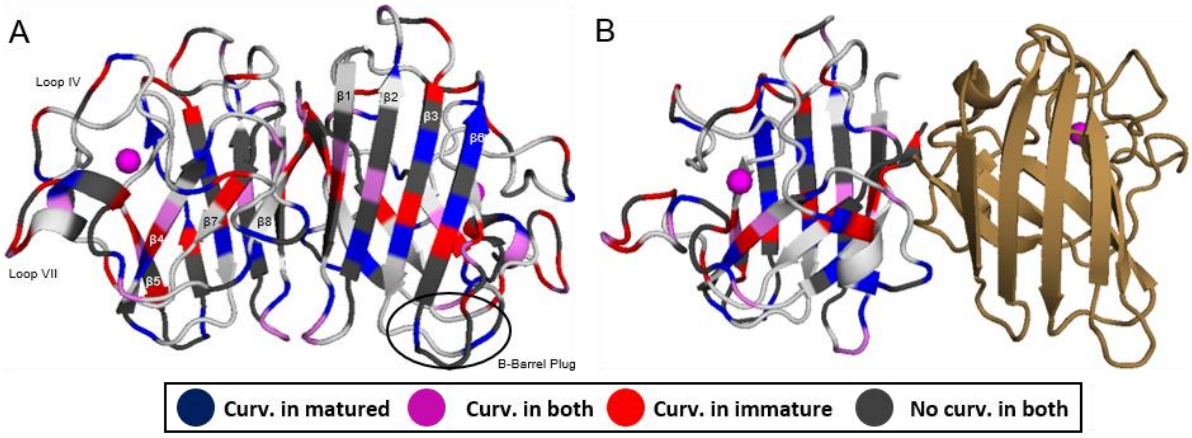

Figure 3.12: Changes in pWT ^{15}N Curvature Patterns During Maturation. This figure displays the changes in ^{15}N curvature patterns as the protein matures from apo2SH to E,Zn2SH SOD1. Comparisons plotted onto the structures of (A) E,Zn2SH pWT SOD1 and (B) E,Zn2SH pWT SOD1 with CCS. The CCS is sand-coloured. Residues coloured white occur where no comparisons could be made. Figures were made using PyMOL and PDB codes 2AF2 and 6FOL.[72,160,164]

3.4 Conclusions

In this chapter, high resolution data acquired from variable temperature NMR experiments have been used to analyze the effects of mutations on the maturation process of SOD1 and the changes in local structure and stability that SOD1 variants experience as a result of maturation. More specifically, local structural changes were investigated through amide proton secondary shifts and secondary amide nitrogen temperature coefficients, while changes in local stability have been investigated using amide proton temperature coefficients and

conformational heterogeneity, observed by curved temperature-dependences. These analyses were performed on SOD1 variants for which the above data has been acquired for various maturation states (pWT, G93A, E100G, and V148I).

Through the use of ^{1}H secondary chemical shifts, the changes in the local and secondary structure of residues can be investigated. As the pWT SOD1 matures from apo2SH to EZn2SH, there is an increase in structure in the dimer interface, zinc-binding loop, and electrostatic loop. As the protein further matures from E,Zn2SH to holo SOD1, there is evidence of increased flexibility in the β-barrel plug, copper-binding region, and electrostatic loop. These data are likely reporting on the increased flexibility that may be required for the catalysis of superoxide radicals and the increased breathing motions of SOD1 that are observed when the protein forms a dimer.[168] When the protein is mutated, the changes in structure during maturation are nearly identical to the changes occurring in pWT, suggesting similar structural rearrangements during maturation. Interestingly, there are a small subset of hydrophobic residues in the dimer interface and core of the protein that show decreases in structure. This suggests that the dimerization of SOD1 causes slight strain in some regions that results in the altered packing of hydrophobic sidechains that may propagate and, in turn, result in a slightly decreased structure in the β5-β6 hairpin in the holo protein relative to their apo2SH counterparts.

From the amide proton temperature coefficients, the effects of maturation on the local stability of residues in pWT and mutant SOD1 were examined. From these studies, it has been confirmed that maturation from apo2SH to E,Zn2SH results in the largest increase of structural stability throughout the protein, especially in the zinc-binding region, electrostatic loop, and dimer interface, despite some evidence of decreased stability of key residues involved in the formation of a tight dimer, allowing the protein to transiently monomerize and interact with the CCS. When the protein further matures to the holo states, there is a further increase in stability surrounding the metal-binding region and there is recovered stability in the residues involved in intermolecular hydrogen bonding to form a tight dimer. The effects of mutation largely occur locally and report on their respective stabilizing or destabilizing effects. For example, in G93A, the β-barrel plug is not stabilized during the maturation process, suggesting an alternate, more stable structure of this region in the mutant.[116] In E100G, the temperature

coefficient changes suggest an altered stability of the zinc-binding loop and β-strand 3 during maturation that result in a decreased stability of these regions, likely due to altered bonds that tether the zinc-binding loop to the β-barrel and connect the tops of β3 and β6. Lastly, in V148I displays a stabilizing effect on the maturation of the protein, by increasing the stability of residues found in the dimer interface.

Using ^{15}N secondary temperature coefficients, the structural changes in SOD1 variants were examined as the protein matured. With respect to pWT SOD1, as the protein matures from apo2SH to E,Zn2SH, it has been found that there is an increase in structure for many of the residues involved in forming the electrostatic loop and the dimer interface; however, one propagating effect of this increased structure in the dimer interface likely results in the altered packing of hydrophobic sidechains pointing into the core of the protein, decreasing their structure. As the protein matures from E,Zn2SH to holo SOD1, there is an increase in structure surrounding the copper-binding site and there is evidence of decreased structure across the first β-sheet, a result of the formation of a tight dimer that further affects the packing of hydrophobic residues. As expected, when mutations are introduced into SOD1, the effects they have on the protein occur near the site of mutation. Most notably, in G93A there is a large increase in structure in loops III and V that suggest increased hydrophobic interactions that A93 has with the other hydrophobic residues that make up the β-barrel plug, including L38.[116] Also, the V148I mutation, a stabilizing mutation, appears to stabilize residues present in the first portion of the zinc-binding loop and β-strand 8, while E100G affects the residues located directly beside the site of mutation at the top of β-strand 3. Overall, the amide nitrogen temperature coefficients have been proved to be sensitive to changes in structure as a result of maturation, and the effects that mutations have on the maturation process are shown to affect the structure of the protein most intensely near the site of mutation.

Lastly, using the presence of curvature in amide proton and nitrogen temperature coefficients, the changes in conformational heterogeneity during the maturation process of SOD1 were investigated. It has been determined that as the protein matures and becomes more structured, there is a decrease in curvature in pWT SOD1. For example, when the protein binds zinc, both the metal-binding region (including the zinc-binding loop) and the electrostatic loop

experience a loss of curvature, indicating that they are more stable and exist in one conformation. Oppositely, there is a gain of curvature in many of the residues found in the dimer interface that report on the dissociation of the dimer to form monomeric E,Zn2SH SOD1, which is then able to interact with the CCS.[86] As the protein matures to holo SOD1, there is a loss curvature in the dimer interface of the protein and at the end of β-strand 6 that reports on the formation of a tight dimer in holo SOD1.[82] Upon mutation, there is an increase in the amount of curvature present in the dimer interface in the holo state of the SOD1 variants, relative to the apo2SH state. This curvature propagates through the entirety of loop VI to the β5-β6 hairpin. This increased curvature describes the weakened dimer interfaces present in mutant SOD1 and assists in identifying the β5-β6 hairpin as a dynamic hotspot.[63,119] Finally, through comparisons of the secondary amide nitrogen temperature coefficients for apo2SH and E,Zn2SH pWT SOD1, it was further enforced that losses of curvature in these temperature coefficients report on the increased structure of a specific residue, as the curvature most often trends from a structured state to an unfolded or random coil-like state. These curvature patterns described the increased structure found in the metal-binding region and dimer interface following the binding of zinc to the protein.

3.5 Future Work for Temperature Coefficient and Conformational Heterogeneity Experiments

In these past two chapters, the usefulness of amide proton secondary shifts and temperature coefficients for determining the effects that mutations and maturation have on the local structure and stability of residues throughout the SOD1 structure have been discussed. In addition, the uses and extent of usefulness of amide nitrogen temperature coefficients have been examined. For future experiments, it would be of interested to investigate the ^{1}H and ^{15}N temperature coefficient and curvature patterns for more apo2SH SOD1 variants; for example, V148G and I113T, both of which have disrupted dimer interface regions. In addition, E,Zn2SH data should be collected for the mutants studied in this chapter, as holo and apo2SH data have already been collected and extensively analyzed. These experiments would assist in determining if maturation patterns are generally conserved during the process of zinc-binding and later processes involving the CCS. Additionally, it would be of great interest to acquire

E,Zn2SH and holo data for the other mutants studied in Chapter 2, especially the metal-binding mutants H46R and G85R, as they should provide valuable insight into the changes of local structure and stability associated with decreased metal affinities. Many mutations result in decreased metal-binding affinities, regardless of if the mutation is near the metal-binding sites, and investigations into the metal-binding mutants may help to greatly inform on effects observed in other mutations.

Chapter 4
Properties of SOD1 Studied by CIEF

4.1 Introduction

Isoelectric focusing is an electrophoretic method in which amphoteric compounds, such as proteins, are separated along a pH gradient by their isoelectric points (pI). This results from the net charge of a protein being determined by the pH of its local environment, meaning that proteins can carry a positive, negative, or neutral charge.[169,170] The net charge of a protein is the sum of all its positive and negative charges, most of which stem from the acidic and basic side chains of various amino acids. The pI of a protein corresponds to the pH at which that protein is net neutral. If the pH of the environment is less than the pI of a protein, the protein will be positively charged. Similarly, if the pH of the environment is above the pI of a protein, the protein will be negatively charged.[171]

When placed in a pH gradient and subjected to an electric field, a protein will migrate towards the oppositely charged electrode. During this migration, the protein will either acquire or lose protons, thus changing its net charge and mobility. The protein will stop migrating when it reaches the pH at which it is net neutral.[169] While the electric field is applied, if the protein should diffuse away from its pI, it will acquire a charge and migrate back towards its pI. This process is called "focusing" and following its completion, a protein will be condensed into a sharp band in the linear pH gradient, at its respective pI.[169–171] One of the most important factors in acquiring high quality focusing data is the formation of a stable, linear pH gradient. The most common method of forming the pH gradient for capillary isoelectric focusing (CIEF) experiments involves the use of solution containing carrier ampholytes, a mixture of numerous small compounds ranging from 300-1000 Da. These compounds contain multiple amino and carboxylate groups that have a high buffering capacity at their pKa values.[169,171] These compounds do not bind to proteins as they are highly hydrophilic.[171]

Traditionally, isoelectric focusing experiments were performed using gel electrophoresis techniques; however, these methods are time consuming and unable to be automated, despite providing high resolution data. To combat these issues, CIEF methods were

developed. In CIEF, proteins are first focused in a short column, generally 5 cm long, into stable bands. This focusing period typically takes approximately 5 minutes.[170,172] During the focusing process, there are three main challenges that need to be overcome. The first is the decrease in the solubility of a protein at its pI. The second is the compression of the pH gradient due to the presence of salt. The third issue is the heating of the column due to a high electrical current. These issues can all be overcome by the dilution of the protein during sample preparation.[170,172] Following focusing, the concentrated protein "peaks" are detected, for example, by UV absorbance. There are two main techniques used to image the focused peaks. The first method, single point detection, utilized a camera that images the end of the column, while the focused sample is pushed through the column by solvent. One of the major drawbacks of the single point detection method is that it takes 10-40 minutes to image all of the focused peaks. During this mobilization period, the focused samples are able to diffuse, broadening the peaks and decreasing the peak heights, which in turn affects the separation of the proteins and the sensitivity of the method.[172] The second method, whole-column imaging detection (WCID), uses a charge-coupled device camera to image the whole column over the course of the focusing period. The main benefit of WCID is that it allows real-time monitoring of the focusing process and offers resolution of 0.03 pH units.[170,172]

In addition to determining the pIs of proteins, it is also possible to use CIEF in combination with whole-column imaging detection to determine the diffusion coefficients (D) and molecular weights of proteins.[170,173] The diffusion coefficient can be determined by imaging the column after the voltage in the CIEF instrument has been turned off. A protein's D can then be calculated by using the Einstein equation (Equation 1), where σ^2 represents the peak variance and t represents the diffusion time. The molecular weight (M) of the protein can then be determined from the D using Equation 2, where A is a function of temperature (T) and viscosity (η).[170] Using the methods here it is possible determine and compare the pI and diffusion coefficients of related proteins, which has not yet been explored in depth.[170]

$$1)\ \sigma^2=2Dt$$

$$2)\ D=A(T,\eta)M^{-1/3}$$

Previously, studies on some of the electrophoretic properties of SOD1 have been performed by the Shaw Group at Baylor University.[103,174] The first of these studies, utilizing protein charge ladders and capillary electrophoresis, examined the effects that metal binding has on the net charge of SOD1.[174] This study concluded that the binding of zinc and copper, as well as the formation of the intramolecular disulfide bond, reduce the net negative charge of the protein. The theoretical pIs of the metal-free SOD1 and holo SOD1 were also calculated to be 5.9 and 5.3, respectively. In addition, the protein resisted charge inversion at pH 5.3, remaining negatively charged. These results indicated that the net-negative surface charge of holo SOD1 is vital for catalysis, especially around the catalytically active R143.[174] Building upon the above study, the Shaw group then focused on the effects that ALS-associated mutations have on the net charge of SOD1, most notably the "cryptic mutations" that lower the negative surface potential of SOD1, such as D90A and E100K.[103] This study found that the net charge of the protein upon mutation was lower than predicted for metal-free SOD1 and that the binding of zinc to the protein decreased the charge gap between the WT protein and the ALS-variants. This study also found that the ALS mutations did not prevent the protein from regulating its net charge. These results point to the ability of SOD1 to resist reductions of its negative charge, suggesting that this property is functionally relevant to maximizing solubility, protein-protein interactions, and catalytic activity.[103] Other studies, such as the experiments performed on recombinant human SOD1 by Wenisch *et al.*, have utilized gel isoelectric focusing experiments to show the presence of three isoforms of with pI values of 4.80, 4.92, and 5.07, with the protein at pI 5.07 corresponding to the holo SOD1.[175]

The purpose of this study is to determine if CIEF can be used as a diagnostic tool for determining the mutations and maturation states present in patient samples, given the pI of SOD1 variants. In order to for this to occur, a complete set of pI values for each mutant and maturation state are needed for SOD1 variants expressed in the WT background. It would also be of interest to determine if SOD1 expressed in the pWT background could be used in place of WT SOD1, due to its increased solubility, for the set of pI values; however, that requires investigation into both WT and pWT pI values for SOD1 variants. It would also be of interest to determine the size of soluble aggregates or oligomers, which could be inferred from the

diffusion coefficients of the SOD1 maturation states and of soluble oligomers in WT SOD1, if the oligomers stay soluble during the CIEF experiments.

The method development portion of this chapter, in which the conditions for experiments were established, concluded that the SOD1 concentrations needs to be approximately 0.4 mg/mL for a good signal to noise ratio, pI markers should not focus between pI 5 and pI 7, SOD1 focusing should occur at 3 kV for approximately 7 minutes, and diffusion should be monitored for roughly 20 minutes to determine diffusion coefficients. In addition, the level of waste in the bottles on either side of the capillary need to be equalized prior to running the experiment to avoid the drift of peaks during the diffusion process. The data obtained from the CIEF studies on SOD1 expressed in the pWT background indicate that the pI of the protein decreases as SOD1 matures, charge mutations are reflected in the experimentally determined pI values, and during these experiments the SOD1 is likely present in a dimeric form as a result of high concentration during the focusing process. With respect to the SOD1 expressed in the WT background, all SOD1 samples aggregated during focusing. The aggregation of these samples may be a result of the free cysteines in WT SOD1.

4.2 Methods

4.2.1 Growth and Expression of SOD1 for CIEF Experiments

Pseudo-wildtype SOD1 was grown and expressed for CIEF experiments using methods described previously by Broom *et al.*.[120] In this procedure, SOD-/- cells, which are resistant to kanamycin and chloramphenicol, are transformed with the pHSOD1ASlacI1, which contains the ampicillin resistance gene, by electroporation. The transformed cells are selected for, grown, and induced as described in Section 2.2.1, using LB media instead of M9 minimal media. Kanamycin and chloramphenicol were each added to a final concentration of 0.03 mg/mL.[83,137] The induced cells are grown for 8 hours before being harvested. SOD1 variants expressed in the WT background, were grown and expressed as described above and in Trainor *et al.*, with the following modifications. SOD1 will be expressed in a WT background using BL21 (DE3) *E.coli* cells that contain a pLysS plasmid, that confers resistance to chloramphenicol, and pET21 vector that confers resistance to ampicillin. The volume of M9

minimal media is scaled down to 250 mL and the culture is grown for 6 hours after the induction at 25°C.[176] Samples were grown with and without the addition of 0.1 mM ZnSO4. All cells were harvested by 15 minutes of centrifugation at 4000 g and the resulting cell pellets were stored at -80°C until further processing.

4.2.2 Protein Purification

SOD1 samples are purified and prepared using the methods outlined in Sections 2.2.2, 2.2.4, and 2.2.5. Protein expressed in the WT background, for which the supernatant (SUP) of the cells was used in experiments, were purified using freeze-thaw methods. Following harvesting, cell pellets containing the overexpressed WT SOD1 were resuspended in 7.5 mL of TEN buffer (20 mM Tris, 1 mM EDTA, 100 mM NaCl, pH 8.0) and repeatedly freeze-thawed in liquid nitrogen and a 37°C water bath. After the first cycle, DNase was added and incubated at 4°C for 40 minutes to remove any DNA contamination. Following the third cycle, the sample was centrifuged at 14800 g for 10 minutes to remove cell pellets and aggregated protein, and yields the SUP samples to be used in the CIEF experiments. All protein was aliquoted into 50 μL aliquots and stored at -80 °C until experiments were performed.

4.2.3 Preparation of the CIEF Samples

The preparation of various SOD1 samples for analysis by CIEF were performed as described in Wu *et al*.[172] The SOD1 protein of interest, was diluted to a final concentration of 0.3 - 0.4 mg/mL, with a mixture of carrier ampholyte solution (pH 3-10) containing methylcellulose and the appropriate pI markers that focus on both sides of SOD1 (Protein Simple, San Jose CA, USA). The carrier ampholytes and methylcellulose were added to a final concentration of 4% and 0.35%, respectively. The sample is made up to 100 μL with metal-free MilliQ water. For samples that do not possess metals, all solutions were treated with Chelex ® 100 Resin prior to the addition of the protein (Bio-Rad, Hercules, CA, USA). Lastly, bubbles were eliminated from the sample by centrifugation at 3200 rpm for 5 minutes.

4.2.4 Additional WT SOD1 CIEF Samples Prepared

For WT SUP samples, additional experiments needed to be performed to determine experimental conditions that kept the WT SOD1 soluble throughout the focusing process, to accurately determine the respective pI and diffusion coefficient. The samples that were prepared involved performing buffer exchanges on the samples to increase or decrease the ionic strength of solution, performing a titration with the non-ionic reducing agent dithiothreitol (DTT), performing the experiment using a smaller range of carrier ampholytes, and performing the experiments on WT SOD1 protein grown in the presence of zinc. Each set of samples were performed at numerous protein concentrations, from roughly 0.3 mg/mL to below the detection limit of the instrument, to determine conditions that would, if at all, allow for analysis.

4.2.5 CIEF Experiments

Experiments were performed on a iCE280 analyzer (Convergent Bioscience, Toronto ON, Canada) with a UV-WCID at 280 nm and a fluorocarbon internally coated fused-silica capillary separation column.[170] Before each run, the column was conditioned with 0.5% methylcellulose. At the beginning of an experiment, 50 μL of a protein sample is loaded into the injector loop, with care taken to avoid introducing bubbles in the lines. The sample is injected into the column at a rate of 0.36 mL/hour for 2 minutes before being allowed to equilibrate for 2 minutes. Following this equilibration time, a scan of the capillary is performed to perform a baseline correction in later scans. Samples were then focused for roughly 7 minutes at 3 kV before the voltage was turned off and the protein was allowed to diffuse for roughly 30 minutes. Scans of the capillary using the CCD camera were taken every 57 seconds and the internal temperature of the instrument was recorded to ensure the temperature during the experiments stayed consistent. Each sample was run in triplicate. Following each run, the capillary was washed for 300 seconds with 0.5% methylcellulose.

4.2.6 CIEF Data Analysis

The analysis of the focusing data from the CIEF experiments to obtain the pIs and diffusion coefficients of SOD1 variants were performed as described in Liu *et al*.[170] First, using

the peak positions of the pI markers, a calibration curve representing the pH gradient was built and used to find the pI of SOD1. Next, the peak variance, obtained from the diffusion data, was plotted against separation time to determine the diffusion coefficient of SOD1 sample using a program written by Dr. Victor Galievsky, which also performs a baseline correction for each scan. The pI and diffusion coefficients were calculated by averaging the results of triplicate experiments on each respective protein.

4.3 Results and Discussion

4.3.1 Experiment Optimization

SOD1 Concentration Needs to be ~0.4 mg/mL and pI Markers Should not Focus Between pI = 5 and pI = 7.

Before experiments determining SOD1 pIs and diffusion coefficients could be run using the iCE280 analyzer, initial experiments needed to be performed to optimize some of the parameters. These parameters included the flow rate and injection time of the protein, concentration of SOD1 and pI markers, focusing voltage and time, and diffusion time. With respect to the determination of the flow rate and injection time of the protein, initial experiments found that at a flow rate of 0.36 mL/hour for 2 minutes, the region of the capillary that is scanned using the UV-WCID has been completely filled with the protein solution to be analyzed. Next, the concentration of SOD1 the pI markers to be used in experiments needed to be determined. The concentration experiments were performed using holo E100K SOD1, which when tested at a concentration of 0.1 mg/mL did not show a good signal to noise ratio. The concentration was then increased to 0.4 mg/mL, which showed the presence of a sharp symmetrical peak, allowing for the accurate determination of peak position. These tests further continued with the addition of various pI markers to determine which would be most suitable for use with SOD1 variants. According to previous experiments, holo SOD1 focusses at approximately pI = 5.3, while the holo E100K, a double charge mutant, focusses at approximately pI = 7. For this reason, pI markers that focus between pI 5 and pI 7 are not appropriate to use, as they may interfere with the SOD1 signal. The pI markers used throughout many of the following experiments focus at pI 3.59 and pI 8.4; however, in earlier experiments

a pI marker at pI 7.4 was used as we had not received the pI 8.4 marker yet and did not possess one that focused at a higher pI (Protein Simple, San Jose CA, USA).

SOD1 Focusing can Occur at 3 kV for ~7 Minutes.

Following the determination of protein concentration and pI markers to use in these experiments, it was necessary to determine the appropriate focusing voltage and time. If there is a high concentration of salt present in these samples, focusing at a lower voltage is preferable to avoid joule heating; however, this results in a longer focusing time.[170] The iCE280 allows the user to choose between two focusing voltages, 0.5 kV and 3 kV. Both voltages were tested and neither voltage caused the current running through the sample to rapidly increase, indicating that salt levels were low enough to use either voltage. Since SOD1, especially mutant SOD1, has a high aggregation propensity, it was decided to use a 3 kV focusing voltage to avoid SOD1 being highly concentrated for a long period of time.[84,133] Further tests at the 3 kV focusing voltage concluded that the SOD1 samples and the pI markers had focused by

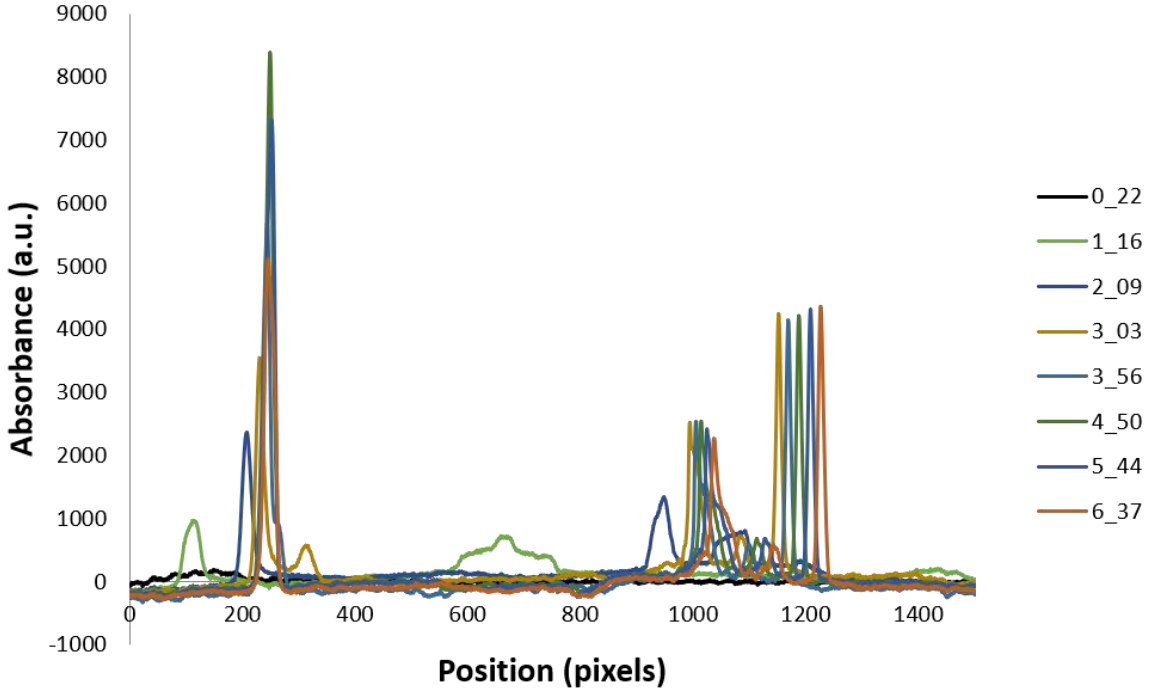

Figure 4.1: Focusing of E100K and pI Markers. The focusing of peaks corresponding to the pI 3.59 marker (left), E100K (middle) and pI 7.4 marker (right) are displayed over the focusing time.

6 minutes and 37 seconds, indicating this was the time at which the voltage could be turned off and the observation of protein diffusion could start. The focusing of E100K and the pI markers 3.59 and 7.4 can be seen in Figure 4.1.

Diffusion is Monitored for ~20 Minutes and Waste Bottle Levels Need to be Equalized to Avoid Drift of SOD1 During Diffusion.

After suitable conditions for focusing had been established as a precondition for observing diffusion, a set of experiments were performed to determine how long the diffusion process should be followed. In order to provide a large number of data points (approximately 20) to calculate the diffusion coefficient from, the diffusion process was monitored for roughly 20 minutes. This provided enough points to plot the peak variance against the diffusion time to determine the diffusion coefficient. The area gain of each peak over the diffusion time is also plotted as a control, as it should remain constant over the diffusion process of one peak. The peak variance and area gain of the E100K peak are plotted in Figure 4.2 (A) and (B), respectively. From Figure 4.2 (A) and (B) it is observed that the peak variance is linear, indicating diffusion of the protein, and the peak area gain over the diffusion process is constant. As noticed in Figure 4.2 (C), during the diffusion there is a slow drift of the peaks. This was later determined to be a result of uneven liquid levels of the two waste bottles on either side of the capillary. These uneven levels caused a slight “siphoning” effect from one bottle to another which moved the peaks over the 20 minute diffusion time. The drifting of peaks did not affect the calculation of the diffusion coefficient, except in extreme cases where the peaks drifted to a part of the capillary that could not be imaged with the CCD camera, preventing diffusion analysis. This drift was eliminated once the levels of liquid in the waste bottles were equalized.

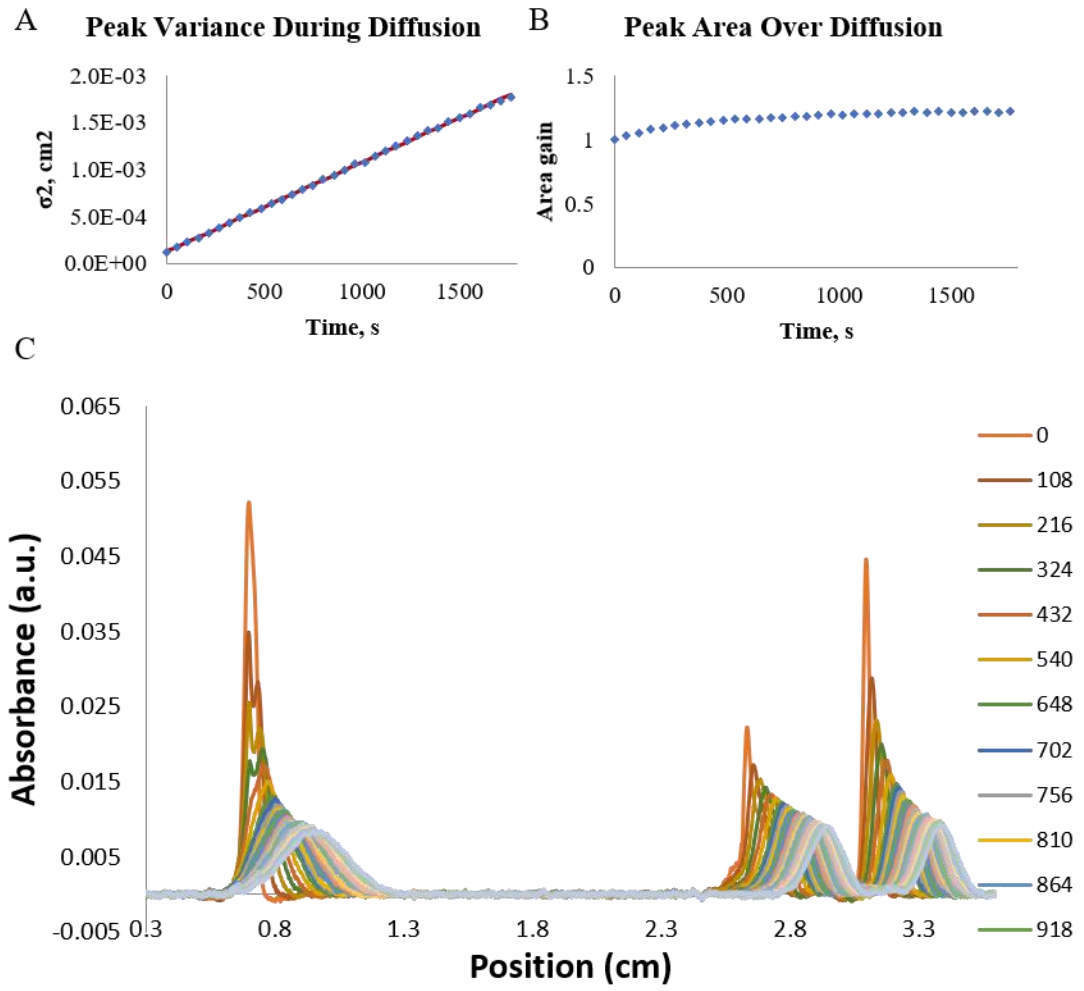

Figure 4.2: Diffusion of E100K and pI Markers. This figure displays the (A) peak variance and (B) area gain of the E100K peak, as well as (C) the diffusion of the pI markers (pI 3.59 and 7.4) and E100K over the diffusion process.

4.3.2 CIEF on SOD1 Expressed in pWT Background

pI Decreases as SOD1 Matures.

From the determined pI values found in Table 14 it is apparent that as pWT matures from apo2SH to holo SOD1, the pI decreases. Earlier experiments in the Meiering Lab on holo pWT SOD1 found a pI of 5.3 (Hwang, unpublished), matching the theoretical pI calculated by Shi *et al.*[174] This also indicates that the pI value of WT and pWT should be identical, as the experimentally determined pI for holo pWT SOD1 matches the theoretical value for holo WT SOD1. Applying these assumptions to the theoretical apo oxidized (apoSS) WT pI value, there

would be a decrease in pI from apo2SH to apoSS and then further from apoSS to holo pWT SOD1. This trend is expected as, in apo2SH SOD1, there are no metals bound to the protein and the disulfide bond is reduced, which will change the structure and net charge of SOD1.[174] This trend can be seen when comparing the apo oxidized and apo2SH E100K samples; however, interestingly, the holo E100K data does not fit the previously described trend. This may be the result of an issue with the pI markers or the calibration curve used for this state as the trend should not be different from that found in pWT. If E100K did indeed deviate from the general trend, this would imply that its structure is significantly distorted, which appears unlikely, given the previous structural characterizations by NMR..[112,121,135] Overall, there appears to be a trend of declining pI concomitant with metal binding and disulfide formation.

Charge Mutations Are Reflected in the Experimentally Determined pI Values.

From the remaining data contained in Table 14, it is observed that changes to the charge of SOD1 through mutations are reflected in the pI value. For example, when comparing apo2SH and apoSS E100K to pWT, which the change in formal net charge is +2, the pI increases by approximately 0.4 and 0.2 units, respectively. In addition, when comparing the pI values of holo G85R and pWT/WT, in which there is a change in formal net charge of +1, the pI increases by 0.12. Therefore, mutations that change the net charge of the protein will also change the pI of the protein in the expected direction.

All SOD1 Maturation States Likely Predominantly in a Dimeric Form.

From the diffusion coefficient data contain in Table 14, the diffusion coefficients for all of the SOD1 variants and their respective states are relatively similar. Since the diffusion coefficient is related to the molecular mass of a protein, this indicates that the molecular mass of these states are near identical.[170] This likely demonstrates that, in the CIEF experiments, all maturation states can be found as a dimer, as a result of the high concentration of protein found in a peak due to focusing. It has been established that apo2SH SOD1 is able to transiently form a dimer, and these results suggest that if the concentration is high enough, apo2SH SOD1 could potentially be found predominantly in a dimeric form.[112,135]

Mutant	Maturation State	Average pI	Average D (s/cm^2)
pWT	Apo2SH	6.24	9.16×10^{-7}
	Holo	5.3	N.D
WT	ApoSS*	5.9	N.D
	Holo*	5.3	N.D
E100K	Apo2SH	6.62	8.22×10^{-7}
	ApoSS	6.14	1.07×10^{-6}
	Holo	7.02	9.89×10^{-7}
G85R	Holo	5.42	8.05×10^{-7}
I113T	ApoSS	5.70	9.31×10^{-7}

Table 14: Focusing and Diffusion Data for Various SOD1 Mutants and States. This table displays the CIEF results obtained from triplicate experiments. Maturation states denoted with an asterick are theoretical results obtained by Shi *et al.*[174] Holo pWT data was obtained in a previous experiment in the Meiering lab (Hwang, unpublished). "N.D" denotes that diffusion has not been studied for these states.

4.3.3 CIEF on SOD1 Expressed in WT Background

WT SOD1 Obtained from SUP Samples Likely Aggregate During CIEF Due to Free Cysteines.

Following the study above, successfully showing that pWT SOD1 can be stays soluble during the CIEF process and is able to diffuse, experiments were performed on WT SOD1 samples obtained from the SUP of cells. First, the WT SUP CIEF samples were prepared the same as the pWT SOD1 samples above; however, in each experiment, after roughly 3 minutes a large extremely intense peak appeared around the area that SOD1 focuses and did not move or diffuse during the remainder of the experiments. The appearance of this peak and loss of migration and diffusion indicates that the SOD1 in the WT SUP has aggregated. These experiments were repeated with decreasing concentrations of WT SOD1 until they were not detectable by the iCE280. In each experiment, the protein still aggregated. To determine if this aggregation was a result of other proteins or contaminants in the SUP sample, a pWT SUP sample was prepared. This sample appeared to show a focused SOD1 peak that diffuses; however, there smaller peaks are present in the surrounding area that convolute the diffusion

of the protein. This suggests that the reason behind the aggregation of the WT SOD1 is inherent to the protein.

Next, experiments were performed that slightly increased the ionic strength of the CIEF sample through the addition of NaCl, to increase the solubility of the protein, and decreased ionic strength through a buffer exchange into water, to potentially reduce the effects of joule heating if there are any. Again, these experiments all yielded aggregated WT SOD1, even when the protein concentration was increasingly reduced to below detectable levels. Following these experiments, experiments were performed with increasing amounts of thiol-reducing agent, DTT, and experiments with a constant amount of DTT and decreasing amounts of protein to a level that was not detectable. In these experiments, the WT SOD1 always aggregated; however, this may be due to the fact that DTT does not stay covalently bound to a free cysteine once it is reduced, so when the voltage is turned on the DTT migrates to its own pI and does not stay in the vicinity of WT SOD1, rendering it useless. While a reducing agent that covalently binds the free thiol groups of cysteines may appear useful, this would not fall under the purpose of this study as it would change both the charge and the size of the protein, resulting in altered pI values and diffusion coefficients for the protein.

The last set of experiments performed on SOD1 expressed in the WT background involved the focusing of WT SOD1 grown with zinc, as zinc has been shown to rescue the protein from aggregation.[138] These experiments were performed with decreasing amounts of protein, until it was no longer detectable by the instrument, and in each experiment the protein aggregated within the capillary. The combination of these results indicates that the free cysteines in the protein are heavily implicated in WT SOD1 aggregation, as experiments attempting to stabilize other regions of the protein or increase solubility do not show positive results. This likely occurs in tandem with the high concentration of protein in the “focused” peak, even though that amount is greatly decreased throughout each of these experiments. Unfortunately, since the SOD1 peak does not fully focus, or diffuse, the experimental pI value and the size of soluble oligomers, as determined by the diffusion coefficient, of WT SOD1 and other SOD1 variants expressed in the WT background can not be determined as the protein aggregates under all experimental conditions.

4.4 Conclusions

This chapter has focused on the patterns, or lack thereof, of pI values and diffusion coefficients for SOD1 variants, expressed in the pWT and WT background using established CIEF methods. In this work, it has been determined that the pI of SOD1 decreases as the protein matures due to changes to structure and net charge arising from metal-binding and disulfide bond formation. In addition, charge mutations to the protein have been shown to be reflected in the experimentally determined pI values. Another set of interesting data show that, from the diffusion coefficients of the maturation states of the SOD1 variants studied here, SOD1 predominantly exists as a dimer throughout the CIEF experiments, even for the apo2SH state. This is a result of the high concentration of protein during focusing, promoting dimerization.

Further experiments on WT SUP samples showed that, in a variety of experimental conditions, the WT SOD1 always aggregated. This is most likely a result of free cysteine participating in aberrant interactions that promote aggregation, in combination with the increased concentration of the protein during focusing. Unfortunately, this results in a lack of pI and diffusion coefficient data for WT SOD1, suggesting that this method is most likely not well-suited to determining the presence of SOD1 mutants, maturation states, and the sizes of soluble oligomers found in patient samples.

4.4.1 Future CIEF Work

In future CIEF experiments on SOD1, it would be of great interest to determine if WT SOD1 grown in eukaryotic systems, such as yeast, remain soluble in solution as a result of further post translational processing. In addition, further studies could be performed into other methods to keep WT SOD1 stable during focusing that do not change the pI or size of the protein. One experimental method that may be fruitful, is using immobilized pH gradients to study the focusing of SOD1.

4.5 Chapter Acknowledgements

I would like to thank Dr. Victor Galievsky of the Pawliszyn Group, whose efforts in preparing the iCE280 analyzer, writing the analysis program, and providing training on

preparing and running the CIEF samples made these CIEF studies possible. In addition, I would like to thank Gyana Mishra of the Meiering Lab for all of his assistance and training on growing and purifying the SOD1 samples expressed in the WT background.

References

1. Voet, D. & Voet, J. G. *Biochemistry*. (John Wiley & Sons Inc., 2011).
2. Onuchic, J. N., Luthey-Schulten, Z. & Wolynes, P. G. Theory of Protein Folding: The Energy Landscape Perspective. *Annu. Rev. Phys. Chem* **48**, 545–600 (1997).
3. Anfinsen, C. B. Principles that Govern the Folding of Protein Chains. *Science (80-.).* **181**, 223–230 (1973).
4. Waudby, C. A., Dobson, C. M. & Christodoulou, J. Nature and Regulation of Protein Folding on the Ribosome. *Trends Biochem. Sci.* **44**, 914–926 (2019).
5. Dill, K. A., Ozkan, S. B., Scott Shell, M. & Weikl, T. R. The Protein Folding Problem. *Annu. Rev. Biophys.* **37**, 289–316 (2008).
6. Rose, G. D., Fleming, P. J., Banavar, J. R. & Maritan, A. A backbone-based theory of protein folding. *PNAS* **103**, 16623–33 (2006).
7. Onuchic, J. N. & Wolynes, P. G. Theory of protein folding. *Curr. Opin. Struct. Biol.* **14**, 70–75 (2004).
8. Kim, P. S. & Baldwin, R. L. Specific Intermediates in the Folding Reactions of Small Proteins and the Mechanism of Protein Folding. *Annu. Rev. Biochem.* **51**, 459–489 (1982).
9. Ptitsyn, O. B. & Rashin, A. A. A model of myoglobin self-organization. *Biophys. Chem.* **3**, 1–20 (1975).
10. Karplus, M. & Weaver, D. L. Protein-folding dynamics. *Nature* **260**, 404–406 (1976).
11. Harrison, S. C. & Durbin, R. Is there a single pathway for the folding of a polypeptide chain? (native-like structure/microdomains/jigsaw-puzzle analogy/protein conformation/protein renaturation). *Proc. Nail. Acad. Sci. USA* **82**, 4028–4030 (1985).
12. Kanehisa, M. I. & Tsong, T. Y. Mechanisms of the multiphasic kinetics in the folding and unfolding of globular proteins. *J. Mol. Biol.* **124**, 177–194 (1978).
13. Ptitsyn, O. B. Protein folding: Hypotheses and experiments. *J. Protein Chem.* **6**, 273–293 (1987).
14. Tsai, C.-J., Kumar, S., Ma, B. & Nussinov, R. Folding funnels, binding funnels, and protein function. *Protein Sci.* **8**, 1181–1190 (1999).

15. Krupyanskii, Y. F. & Gol'danski, V. I. Dynamical properties and energy landscape of simple globular proteins. *Physics-Uspekhi* **45**, 1131–1151 (2002).

16. Zwanzig, R. Two-state models of protein folding kinetics. *Proc. Natl. Acad. Sci. U. S. A.* **94**, 148–150 (1997).

17. Chu, X., Gan, L., Wang, E. & Wang, J. Quantifying the topography of the intrinsic energy landscape of flexible biomolecular recognition. *Proc. Natl. Acad. Sci. U. S. A.* **110**, E2342–E2351 (2013).

18. Muñoz, V. & Sanchez-Ruiz, J. M. Exploring protein-folding ensembles: A variable-barrier model for the analysis of equilibrium unfolding experiments. *Proc. Natl. Acad. Sci. U. S. A.* **101**, 17646–17651 (2004).

19. Dobson, C. M. Principles of protein folding, misfolding and aggregation. *Semin. Cell Dev. Biol.* **15**, 3–16 (2004).

20. Li, Y. & Roberts, C. J. Lumry−Eyring Nucleated-Polymerization Model of Protein Aggregation Kinetics. 2. Competing Growth via Condensation and Chain Polymerization. *J. Phys. Chem. B* **113**, 7020–7032 (2009).

21. Kim, Y. E., Hipp, M. S., Bracher, A., Hayer-Hartl, M. & Hartl, F. U. Molecular Chaperone Functions in Protein Folding and Proteostasis. *Annu. Rev. Biochem.* **82**, 323–355 (2013).

22. Morris, A. M., Watzky, M. A. & Finke, R. G. Protein aggregation kinetics, mechanism, and curve-fitting: A review of the literature. *Biochim. Biophys. Acta - Proteins Proteomics* **1794**, 375–397 (2009).

23. Hendrick, J. P. & Hartl, F.-U. MOLECULAR CHAPERONE FUNCTIONS OF HEAT-SHOCK PROTEINS. *Annu. Rev. Biochem.* **62**, 349–384 (1993).

24. Bartolini, M. & Andrisano, V. Strategies for the Inhibition of Protein Aggregation in Human Diseases. *ChemBioChem* **11**, 1018–1035 (2010).

25. Burmann, B. M., Gerez, J. A., Matečko-Burmann, I., Campioni, S., Kumari, P., Ghosh, D., Mazur, A., Aspholm, E. E., Šulskis, D., Wawrzyniuk, M., Bock, T., Schmidt, A., Rüdiger, S. G. D., Riek, R. & Hiller, S. Regulation of α-synuclein by chaperones in mammalian cells. *Nature* **577**, 132 (2020).

26. Chiti, F. & Dobson, C. M. Protein Misfolding, Functional Amyloid, and Human Disease.

Annu. Rev. Biochem. **75**, 333–66 (2006).

27. Luk, K. C., Song, C., O'Brien, P., Stieber, A., Branch, J. R., Brunden, K. R., Trojanowski, J. Q. & Lee, V. M. Y. Exogenous α-synuclein fibrils seed the formation of Lewy body-like intracellular inclusions in cultured cells. *Proc. Natl. Acad. Sci. U. S. A.* **106**, 20051–20056 (2009).

28. Huang, R., Ripstein, Z. A., Augustyniak, R., Lazniewski, M., Ginalski, K., Kay, L. E. & Rubinstein, J. L. Unfolding the mechanism of the AAA+ unfoldase VAT by a combined cryo-EM, solution NMR study. *Proc. Natl. Acad. Sci. U. S. A.* **113**, E4190 (2016).

29. Sugiki, T., Kobayashi, N. & Fujiwara, T. Modern Technologies of Solution Nuclear Magnetic Resonance Spectroscopy for Three-dimensional Structure Determination of Proteins Open Avenues for Life Scientists. *Comput. Struct. Biotechnol. J.* **15**, 328–339 (2017).

30. Wüthrich, K. Protein Structure Determination in Solution by NMR Spectroscopy. *JOURNAL. Biol. Chem.* **265**, 22059–22062 (1990).

31. Wong, L. E., Kim, T. H., Muhandiram, D. R., Forman-Kay, J. D. & Kay, L. E. NMR Experiments for Studies of Dilute and Condensed Protein Phases: Application to the Phase-Separating Protein CAPRIN1. *J. Am. Chem. Soc.* **142**, 2471–2489 (2020).

32. Jensen, M. R., Zweckstetter, M., Huang, J. R. & Blackledge, M. Exploring free-energy landscapes of intrinsically disordered proteins at atomic resolution using NMR spectroscopy. *Chem. Rev.* **114**, 6632–6660 (2014).

33. Balbach, J., Forge, V., Van Nuland, N. A. J., Winder, S. L., Hore, P. J. & Dobson, C. M. Following protein folding in real time using NMR spectroscopy. *Nat. Struct. Biol.* **2**, 865–870 (1995).

34. Howard, M. J. Protein NMR spectroscopy. *Curr. Biol.* **8**, R331–R333 (1998).

35. Wüthrich, K. NMR with Proteins and Nucleic Acids. *Eur. News* **17**, 11–13 (1986).

36. Cavanagh, J., Fairbrother, W. J., Palmer, A. G., Skelton, N. J. & Rance, M. *Protein NMR Spectroscopy: Principles and Practice . Protein NMR Spectroscopy* (Elsevier Inc., 2007). doi:10.1016/B978-0-12-164491-8.X5000-3.

37. Günther, H. *NMR Spectroscopy : Basic Principles, Concepts and Applications in Chemistry.* (John Wiley & Sons Inc., 2013).

38. Rule, G. S. & Hitchens, T. K. *Fundamentals of Protein NMR Spectroscopy*. (Springer, 2006).

39. Jones, C. J. & Thornback, J. *Medicinal applications of coordination chemistry*. (Royal Society of Chemistry, 2007).

40. Doucleff, M., Hatcher-Skeers, M. & Crane, N. J. *Pocket Guide to Biomolecular NMR*. (Springer Berlin Heidelberg, 2011). doi:10.1007/978-3-642-16251-0.

41. Noggle, J. H. & Schirmer, R. E. *The Nuclear Overhauser Effect: Chemical Applications*. (Academic Press Inc., 1971).

42. Asakura, T., Taoka, K., Demura, M. & Williamson, M. The relationship between amide proton chemical shifts and secondary structure in proteins. *J. Biomol. NMR* **6**, 227–236 (1995).

43. Chen, K., Freedberg, D. I. & Keire, D. A. NMR profiling of biomolecules at natural abundance using 2D1H-15N and1H-13C multiplicity-separated (MS) HSQC spectra. *J. Magn. Reson.* **251**, 65–70 (2015).

44. Frueh, D. P. Practical aspects of NMR signal assignment in larger and challenging proteins. *Prog. Nucl. Magn. Reson. Spectrosc.* 47–75 (2014) doi:10.1016/j.pnmrs.2013.12.001.

45. Skinner, A. L. & Laurence, J. S. High-field solution NMR spectroscopy as a tool for assessing protein interactions with small molecule ligands. *J. Pharm. Sci.* **97**, 4670–4695 (2008).

46. Mielke, S. P. & Krishnan, V. V. Characterization of protein secondary structure from NMR chemical shifts. *Prog. Nucl. Magn. Reson. Spectrosc.* **54**, 141–165 (2009).

47. Wishart, D. S., Sykes, B. D. & Richards, F. M. The Chemical Shift Index : A Fast and Simple Method for the Assignment of Protein Secondary Structure Through NMR Spectroscopy. *Biochemistry* **31**, 1647–1651 (1992).

48. Wishart, D. S., Sykes, B. D. & Richards, F. M. Relationship between nuclear magnetic resonance chemical shift and protein secondary structure. *J. Mol. Biol.* **222**, 311–333 (1991).

49. Schwarzinger, S., Kroon, G. J. A., Foss, T. R., Chung, J., Wright, P. E. & Dyson, H. J. Sequence-dependent correction of random coil NMR chemical shifts. *J. Am. Chem. Soc.* **123**, 2970–2978 (2001).

50. Pfuhl, M., Gautel, M., Politou, A. S., Joseph, C. & Pastore, A. Secondary structure determination by NMR spectroscopy of an immunoglobulin-like domain from the giant

muscle protein titin. *J. Biomol. NMR* **6**, 48–58 (1995).

51. Kleckner, I. R. & Foster, M. P. An Introduction to NMR-based approaches for measuring protein dynamics. *Biochim. Biophys. Acta - Proteins Proteomics* **1814**, 942–968 (2011).

52. Ohnishi, M. & Urry, D. W. Temperature dependence of amide proton chemical shifts: The secondary structures of gramicidin S and valinomycin. *Biochem. Biophys. Res. Commun.* **36**, 194–202 (1969).

53. Andersen, N. H., Neidigh, J. W., Harris, S. M., Lee, G. M., Liu, Z. & Tong, H. Extracting Information from the Temperature Gradients of Polypeptide NH Chemical Shifts. 1. The Importance of Conformational Averaging. *J. Am. Chem. Soc.* **119**, 8547–8561 (1997).

54. Keller, R. Optimizing the Process of Nuclear Magnetic Resonance Spectrum Analysis and Computer Aided Resonance Assignment. (Swiss Federal Institute of Technology, 2005).

55. Williamson, M. P., Hall, M. J. & Handa, B. K. 1H-NMR assignment and secondary structure of a Herpes simplex virus glycoprotein D-1 antigenic domain. *Eur. J. Biochem.* **158**, 527–536 (1986).

56. Baxter, N. J. & Williamson, M. P. Temperature dependence of 1H chemical shifts in proteins. *J. Biomol. NMR* **9**, 359–369 (1997).

57. Cierpicki, T. & Otlewski, J. Amide proton temperature coefficients as hydrogen bond indicators in proteins. *J. Biomol. NMR* **21**, 249–261 (2001).

58. Tomlinson, J. H. & Williamson, M. P. Amide temperature coefficients in the protein G B1 domain. *J. Biomol. NMR* **52**, 57–64 (2012).

59. Wang, Y. & Jardetzky, O. Predicting 15N chemical shifts in proteins using the preceding residue-specific individual shielding surfaces from φ, ψi-1, and χ1 torsion angles. *J. Biomol. NMR* **28**, 327–340 (2004).

60. Wang, Y. & Jardetzky, O. Investigation of the neighboring residue effects on protein chemical shifts. *J. Am. Chem. Soc.* **124**, 14075–14084 (2002).

61. Trainor, K. Adnectin Solubility and Dynamics (PhD Thesis). (University of Waterloo, 2019).

62. Baxter, N. J., Hosszu, L. L. ., Waltho, J. P. & Williamson, M. P. Characterisation of low free-energy excited states of folded proteins. *J. Mol. Biol.* **284**, 1625–1639 (1998).

63. Doyle, C. M., Rumfeldt, J. A., Broom, H. R., Sekhar, A., Kay, L. E. & Meiering, E. M. Concurrent Increases and Decreases in Local Stability and Conformational Heterogeneity in Cu, Zn Superoxide Dismutase Variants Revealed by Temperature-Dependence of Amide Chemical Shifts. *Biochemistry* **55**, 1346–1361 (2016).

64. Veltri, T., De Oliveira, G. A. P., Bienkiewicz, E. A., Palhano, F. L., Marques, M. D. A., Moraes, A. H., Silva, J. L., Sorenson, M. M. & Pinto, J. R. Amide hydrogens reveal a temperature-dependent structural transition that enhances site-II Ca2+-binding affinity in a C-domain mutant of cardiac troponin C. *Sci. Rep.* **7**, 691 (2017).

65. Williamson, M. P. Many residues in cytochrome c populate alternative states under equilibrium conditions. *Proteins Struct. Funct. Genet.* **53**, 731–739 (2003).

66. Pallara, C., Rueda, M., Abagyan, R. & Fernández-Recio, J. Conformational Heterogeneity of Unbound Proteins Enhances Recognition in Protein−Protein Encounters. *J. Chem. Theory Comput.* **12**, 3236–3249 (2016).

67. Mackenzie, D. W. S. Stability and Strain in Hisactophilin and the Mechanism of the Myristoyl Switch (PhD Thesis). (University of Waterloo, 2019).

68. Valentine, J. S., Doucette, P. A. & Zittin Potter, S. Copper-Zinc Superoxide Dismutase and Amyotrophic Lateral Sclerosis. *Annu. Rev. Biochem.* **74**, 563–593 (2005).

69. Banci, L., Bertini, I., Boca, M., Girotto, S., Martinelli, M., Valentine, J. S. & Vieru, M. SOD1 and amyotrophic lateral sclerosis: mutations and oligomerization. *PLoS One* **3**, e1677 (2008).

70. Strange, R. W., Antonyuk, S., Hough, M. A., Doucette, P. A., Rodriguez, J. A., Hart, P. J., Hayward, L. J., Valentine, J. S. & Hasnain, S. S. The Structure of Holo and Metal-deficient Wild-type Human Cu, Zn Superoxide Dismutase and its Relevance to Familial Amyotrophic Lateral Sclerosis. *J. Mol. Biol.* **328**, 877–891 (2003).

71. Rakhit, R. & Chakrabartty, A. Structure, folding, and misfolding of Cu,Zn superoxide dismutase in amyotrophic lateral sclerosis. *Biochim. Biophys. Acta - Mol. Basis Dis.* **1762**, 1025–1037 (2006).

72. The PyMOL Molecular Graphics System, Version 2.0 Schrodinger, LLC.

73. Broom, H. R. Stability and Aggregation Studies of Immature Superoxide Dismutase (PhD Thesis). (University of Waterloo, 2015).

74. Getzoff, E. D., Tainer, J. A., Weiner, P. K., Kollman, P. A., Richardson, J. S. & Richardson, D. C. Electrostatic recognition between superoxide and copper, zinc superoxide dismutase. *Nature* **306**, 287–290 (1983).

75. Barber, S. C., Mead, R. J. & Shaw, P. J. Oxidative stress in ALS: A mechanism of neurodegeneration and a therapeutic target. *Biochim. Biophys. Acta - Mol. Basis Dis.* **1762**, 1051–1067 (2006).

76. Fridovich, I. Biological effects of the superoxide radical. *Arch. Biochem. Biophys.* **247**, 1–11 (1986).

77. Kehrer, J. P. Free Radicals as Mediators of Tissue Injury and Disease. *Crit. Rev. Toxicol.* **23**, 21–48 (1993).

78. Banci, L., Bertini, I., Cantini, F., Kozyreva, T., Massagni, C., Palumaa, P., Rubino, J. T. & Zovo, K. Human superoxide dismutase 1 (hSOD1) maturation through interaction with human copper chaperone for SOD1 (hCCS). *Proc. Natl. Acad. Sci. U. S. A.* **109**, 13555–60 (2012).

79. Lindberg, M. J., Normark, J., Holmgren, A. & Oliveberg, M. Folding of human superoxide dismutase: disulfide reduction prevents dimerization and produces marginally stable monomers. *Proc. Natl. Acad. Sci. U. S. A.* **101**, 15893–8 (2004).

80. Banks, C. J., Rodriguez, N. W., Gashler, K. R., Pandya, R. R., Mortenson, J. B., Whited, M. D., Soderblom, E. J., Thompson, J. W., Moseley, M. A., Reddi, A. R., Tessem, J. S., Torres, M. P., Bikman, B. T. & Andersen, J. L. Acylation of Superoxide Dismutase 1 (SOD1) at K122 Governs SOD1-Mediated Inhibition of Mitochondrial Respiration. *Mol. Cell. Biol.* **37**, e00354-17 (2017).

81. Proctor, E. A., Ding, F. & Dokholyan, N. V. Structural and Thermodynamic Effects of Post-translational Modifications in Mutant and Wild Type Cu, Zn Superoxide Dismutase. *J. Mol. Biol.* **408**, 555–567 (2011).

82. Stathopulos, P. B., Rumfeldt, J. A. O., Karbassi, F., Siddall, C. A., Lepock, J. R. & Meiering, E. M. Calorimetric Analysis of Thermodynamic Stability and Aggregation for Apo and Holo Amyotrophic Lateral Sclerosis-associated Gly-93 Mutants of Superoxide Dismutase. *J. Biol. Chem.* **281**, 6184–93 (2006).

83. Stathopulos, P. B., Rumfeldt, J. A. O., Scholz, G. A., Irani, R. A., Frey, H. E., Hallewell, R.

A., Lepock, J. R. & Meiering, E. M. Cu/Zn superoxide dismutase mutants associated with amyotrophic lateral sclerosis show enhanced formation of aggregates in vitro. *Proc. Natl. Acad. Sci. U. S. A.* **100**, 7021–7026 (2003).

84. Vassall, K. A., Stubbs, H. R., Primmer, H. A., Tong, M. S., Sullivan, S. M., Sobering, R., Srinivasan, S., Briere, L.-A. K., Dunn, S. D., Colón, W. & Meiering, E. M. Decreased stability and increased formation of soluble aggregates by immature superoxide dismutase do not account for disease severity in ALS. *Proc. Natl. Acad. Sci. U. S. A.* **108**, 2210–2215 (2011).

85. Parge, H. E., Hallewellt, R. A. & Tainer, J. A. Atomic structures of wild-type and thermostable mutant recombinant human Cu,Zn superoxide dismutase (hydrogen bonds/protein design/helix dipole/metafloenzyme/protein conformation). *Proc. Natl. Acad. Sci. USA* **89**, 6109–6113 (1992).

86. Furukawa, Y., Torres, A. S. & O'halloran, T. V. Oxygen-induced maturation of SOD1: a key role for disulfide formation by the copper chaperone CCS. *EMBO J.* **23**, 2872–2881 (2004).

87. Furukawa, Y. & O'halloran, T. V. Posttranslational Modifications in Cu,Zn-Superoxide Dismutase and Mutations Associated with Amyotrophic Lateral Sclerosis. *Antioxid Redox Signal* **8**, 847–867 (2006).

88. Khare, S. D., Caplow, M. & Dokholyan, N. V. The rate and equilibrium constants for a multistep reaction sequence for the aggregation of superoxide dismutase in amyotrophic lateral sclerosis. *PNAS* **101**, 15094–15099 (2004).

89. Zarei, S., Carr, K., Reiley, L., Diaz, K., Guerra, O., Altamirano, P. F., Pagani, W., Lodin, D., Orozco, G. & Chinea, A. A comprehensive review of amyotrophic lateral sclerosis. *Surg. Neurol. Int.* **6**, 171 (2015).

90. Bruijn, L. I., Miller, T. M. & Cleveland, D. W. Unraveling the Mechanisms Involved in Motor Neuron Degeneration in ALS. *Annu. Rev. Neurosci* **27**, 723–749 (2004).

91. Abel, O., Shatunov, A., Jones, A. R., Andersen, P. M., Powell, J. F. & Al-Chalabi, A. Development of a Smartphone App for a Genetics Website: The Amyotrophic Lateral Sclerosis Online Genetics Database (ALSoD). *JMIR mHealth uHealth* **1**, e18 (2013).

92. Bruijn, L. I., Houseweart, M. K., Kato, S., Anderson, K. L., Anderson, S. D., Ohama, E., Reaume, A. G., Scott, R. W. & Cleveland, D. W. *Aggregation and Motor Neuron Toxicity of*

an ALS-Linked SOD1 Mutant Independent from Wild-Type SOD1. *Science* vol. 281 https://www-jstor-org.proxy.lib.uwaterloo.ca/stable/pdf/2895798.pdf?refreqid=excelsior%3A5acc7a8bef509756a7355466a3b35706 (1998).

93. Beckman, J. S., Carson, M., Smith, C. D. & Koppenol, W. H. ALS, SOD and peroxynitrite. *Nature* **364**, 584–584 (1993).

94. Saccon, R. A., Bunton-Stasyshyn, R. K. A., Fisher, E. M. C. & Fratta, P. Is SOD1 loss of function involved in amyotrophic lateral sclerosis? *Brain* **136**, 2342–58 (2013).

95. Reaume, A. G., Elliott, J. L., Hoffman, E. K., Kowall, N. W., Ferrante, R. J., Siwek, D. R., Wilcox, H. M., Flood, D. G., Beal, M. F., Brown, R. H., Scott, R. W. & Snider, W. D. Motor neurons in Cu/Zn superoxide dismutase-deficient mice develop normally but exhibit enhanced cell death after axonal injury. *Nat. Genet.* **13**, 43–47 (1996).

96. Gurney, M., Pu, H., Chiu, A., Canto, M. D., Polchow, C., Alexander, D., Caliendo, J., Hentati, A., Kwon, Y., Deng, H. & et, al. Motor neuron degeneration in mice that express a human Cu,Zn superoxide dismutase mutation. *Science (80-.).* **264**, 1772–1775 (1994).

97. Joyce, P. I., Fratta, P., Fisher, E. M. C. & Acevedo-Arozena, A. SOD1 and TDP-43 animal models of amyotrophic lateral sclerosis: recent advances in understanding disease toward the development of clinical treatments. *Mamm. Genome* **22**, 420–448 (2011).

98. Münch, C. & Bertolotti, A. Exposure of hydrophobic surfaces initiates aggregation of diverse ALS-causing superoxide dismutase-1 mutants. *J. Mol. Biol.* **399**, 512–25 (2010).

99. Rakhit, R., Crow, J. P., Lepock, J. R., Kondejewski, L. H., Cashman, N. R. & Chakrabartty, A. Monomeric Cu,Zn-superoxide Dismutase Is a Common Misfolding Intermediate in the Oxidation Models of Sporadic and Familial Amyotrophic Lateral Sclerosis. *J. Biol. Chem.* **279**, 15499–15504 (2004).

100. Rakhit, R., Cunningham, P., Furtos-Matei, A., Dahan, S., Qi, X. F., Crow, J. P., Cashman, N. R., Kondejewski, L. H. & Chakrabartty, A. Oxidation-induced misfolding and aggregation of superoxide dismutase and its implications for amyotrophic lateral sclerosis. *J. Biol. Chem.* **277**, 47551–47556 (2002).

101. Vassall, K. A., Stathopulos, P. B., Rumfeldt, J. A. O., Lepock, J. R. & Meiering, E. M.

Equilibrium Thermodynamic Analysis of Amyotrophic Lateral Sclerosis-Associated Mutant Apo Cu,Zn Superoxide Dismutases. *Biochemistry* **45**, 7366–7379 (2006).

102. Hwang, Y. M., Stathopulos, P. B., Dimmick, K., Yang, H., Badiei, H. R., Tong, M. S., Rumfeldt, J. A. O., Chen, P., Karanassios, V. & Meiering, E. M. Nonamyloid aggregates arising from mature copper/zinc superoxide dismutases resemble those observed in amyotrophic lateral sclerosis. *J. Biol. Chem.* **285**, 41701–41711 (2010).

103. Shi, Y., Abdolvahabi, A. & Shaw, B. F. Protein charge ladders reveal that the net charge of ALS-linked superoxide dismutase can be different in sign and magnitude from predicted values. *Protein Sci.* **23**, 1417–33 (2014).

104. Chiti, F., Calamai, M., Taddei, N., Stefani, M., Ramponi, G. & Dobson, C. M. Studies of the aggregation of mutant proteins in vitro provide insights into the genetics of amyloid diseases. *PNAS* **99**, 16419–16426 (2002).

105. Doyle, C. M., Rumfeldt, J. A., Broom, H. R., Broom, A., Stathopulos, P. B., Vassall, K. A., Almey, J. J. & Meiering, E. M. Energetics of oligomeric protein folding and association. *Arch. Biochem. Biophys.* **531**, 44–64 (2013).

106. Wang, Q., Johnson, J. L., Agar, N. Y. . & Agar, J. N. Protein Aggregation and Protein Instability Govern Familial Amyotrophic Lateral Sclerosis Patient Survival. *PLoS Biol.* **6**, e170 (2008).

107. Broom, H. R., Rumfeldt, J. A. O. & Meiering, E. M. Many roads lead to Rome? Multiple modes of Cu,Zn superoxide dismutase destabilization, misfolding and aggregation in amyotrophic lateral sclerosis. *Essays Biochem.* **56**, 149–165 (2014).

108. Collier, A. M., Nemtsova, Y., Kuber, N., Banach-Petrosky, W., Modak, A., Sleat, D. E., Nanda, V. & Lobel, P. Lysosomal protein thermal stability does not correlate with cellular half-life: Global observations and a case study of tripeptidyl-peptidase 1. *Biochem. J.* **477**, 727–745 (2020).

109. Nagasundaram, N., Zhu, H., Liu, J., Karthick, V., Doss, G. P. C., Chakraborty, C. & Chen, L. Analysing the Effect of Mutation on Protein Function and Discovering Potential Inhibitors of CDK4: Molecular Modelling and Dynamics Studies. *PLoS One* **10**, e0133969 (2015).

110. Qiao, W., Akhter, N., Fang, X., Maximova, T., Plaku, E. & Shehu, A. From mutations to

mechanisms and dysfunction via computation and mining of protein energy landscapes. *BMC Genomics* **19**, 671 (2018).

111. Reva, B., Antipin, Y. & Sander, C. Predicting the functional impact of protein mutations: application to cancer genomics. *Nucleic Acids Res.* **39**, e118 (2011).

112. Sekhar, A., Rumfeldt, J. A. O., Broom, H. R., Doyle, C. M., Sobering, R. E., Meiering, E. M. & Kay, L. E. Probing the free energy landscapes of ALS disease mutants of SOD1 by NMR spectroscopy. *Proc. Natl. Acad. Sci. U. S. A.* **113**, E6939–E6945 (2016).

113. Banci, L., Bertini, I., Durazo, A., Girotto, S., Gralla, E. B., Martinelli, M., Valentine, J. S., Vieru, M. & Whitelegge, J. P. Metal-free superoxide dismutase forms soluble oligomers under physiological conditions: A possible general mechanism for familial ALS. *Proc. Natl. Acad. Sci. U. S. A.* **104**, 11263–11267 (2007).

114. Wang, J., Xu, G. & Borchelt, D. R. Mapping superoxide dismutase 1 domains of non-native interaction: roles of intra- and intermolecular disulfide bonding in aggregation. *J. Neurochem.* **96**, 1277–1288 (2006).

115. Hallewell, R. A., Imlay, K. C., Lee, P., Fong, N. M., Gallegos, C., Getzoff, E. D., Tainer, J. A., Cabelli, D. E., Tekamp-Olson, P., Mullenbach, G. T. & Cousens, L. S. Thermostabilization of recombinant human and bovine CuZn superoxide dismutases by replacement of free cysteines. *Biochem. Biophys. Res. Commun.* **181**, 474–480 (1991).

116. Galaleldeen, A., Strange, R. W., Whitson, L. J., Antonyuk, S. V., Narayana, N., Taylor, A. B., Schuermann, J. P., Holloway, S. P., Hasnain, S. S. & Hart, P. J. Structural and biophysical properties of metal-free pathogenic SOD1 mutants A4V and G93A. *Arch. Biochem. Biophys.* **492**, 40–47 (2009).

117. Schmidlin, T., Kennedy, B. K. & Daggett, V. Structural Changes to Monomeric CuZn Superoxide Dismutase Caused by the Familial Amyotrophic Lateral Sclerosis-Associated Mutation A4V. *Biophys. J.* **97**, 1709–1718 (2009).

118. Rumfeldt, J. A. O., Stathopulos, P. B., Chakrabarrty, A., Lepock, J. R. & Meiering, E. M. Mechanism and Thermodynamics of Guanidinium Chloride-induced Denaturation of ALS-associated Mutant Cu,Zn Superoxide Dismutases. *J. Mol. Biol.* **355**, 106–123 (2006).

119. Broom, H. R., Rumfeldt, J. A. O., Vassall, K. A. & Meiering, E. M. Destabilization of the

dimer interface is a common consequence of diverse ALS-associated mutations in metal free SOD1. *Protein Sci.* **24**, 2081–2089 (2015).

120. Broom, H. R., Vassall, K. A., Rumfeldt, J. A. O., Doyle, C. M., Tong, M. S., Bonner, J. M. & Meiering, E. M. Combined Isothermal Titration and Differential Scanning Calorimetry Define Three-State Thermodynamics of fALS-Associated Mutant Apo SOD1 Dimers and an Increased Population of Folded Monomer. *Biochemistry* **55**, 519–533 (2016).

121. Culik, R. M., Sekhar, A., Nagesh, J., Deol, H., Rumfeldt, J. A. O., Meiering, E. M. & Kay, L. E. Effects of maturation on the conformational free-energy landscape of SOD1. *Proc. Natl. Acad. Sci. U. S. A.* **115**, E2546–E2555 (2018).

122. Hough, M. A., Grossmann, J. G., Antonyuk, S. V., Strange, R. W., Doucette, P. A., Rodriguez, J. A., Whitson, L. J., Hart, P. J., Hayward, L. J., Valentine, J. S. & Hasnain, S. S. Dimer destabilization in superoxide dismutase may result in disease-causing properties: Structures of motor neuron disease mutants. *Proc. Natl. Acad. Sci. U. S. A.* **101**, 5976–5981 (2004).

123. Liu, H., Zhu, H., Eggers, D. K., Nersissian, A. M., Faull, K. F., Goto, J. J., Ai, J., Sanders-Loehr, J., Gralla, E. B. & Valentine, J. S. Copper(2+) binding to the surface residue cysteine 111 of His46Arg human copper-zinc superoxide dismutase, a familial amyotrophic lateral sclerosis mutant. *Biochemistry* **39**, 8125–8132 (2000).

124. Winkler, D. D., Schuermann, J. P., Cao, X., Holloway, S. P., Borchelt, D. R., Carroll, M. C., Proescher, J. B., Culotta, V. C. & Hart, P. J. Structural and biophysical properties of the pathogenic SOD1 variant H46R/H48Q. *Biochemistry* **48**, 3436–3447 (2009).

125. Elam, J. S., Taylor, A. B., Strange, R., Antonyuk, S., Doucette, P. A., Rodriguez, J. A., Hasnain, S. S., Hayward, L. J., Valentine, J. S., Yeates, T. O. & Hart, P. J. Amyloid-like filaments and water-filled nanotubes formed by SOD1 mutant proteins linked to familial ALS. *Nat. Struct. Biol.* **10**, 461–467 (2003).

126. Antonyuk, S., Elam, J. S., Hough, M. A., Strange, R. W., Doucette, P. A., Rodriguez, J. A., Hayward, L. J., Valentine, J. S., Hart, P. J. & Hasnain, S. S. Structural consequences of the familial amyotrophic lateral sclerosis SOD1 mutant His46Arg. *Protein Sci.* **14**, 1201–1213 (2005).

127. Cao, X., Antonyuk, S. V, Seetharaman, S. V, Whitson, L. J., Taylor, A. B., Holloway, S. P.,

Strange, R. W., Doucette, P. A., Selverstone Valentine, J., Tiwari, A., Hayward, L. J., Padua, S., Cohlberg, J. A., Samar Hasnain, S. & John Hart, P. Structures of the G85R Variant of SOD1 in Familial Amyotrophic Lateral Sclerosis . *J. Biol. Chem.* **283**, 16169–16177 (2008).

128. Kawamata, H. & Manfredi, G. Different regulation of wild-type and mutant Cu,Zn superoxide dismutase localization in mammalian mitochondria. *Hum. Mol. Genet.* **17**, 3303–3317 (2008).

129. Durazo, A., Shaw, B. F., Chattopadhyay, M., Faull, K. F., Nersissian, A. M., Selverstone Valentine, J. & Whitelegge, J. P. Metal-free Superoxide Dismutase-1 and Three Different Amyotrophic Lateral Sclerosis Variants Share a Similar Partially Unfolded-Barrel at Physiological Temperature. *J. Biol. Chem.* **284**, 34382–34389 (2009).

130. Bruns, C. K. & Kopito, R. R. Impaired post-translational folding of familial ALS-linked Cu, Zn superoxide dismutase mutants. *EMBO J.* **26**, 855–866 (2007).

131. Byström, R., Andersen, P. M., Gröbner, G. & Oliveberg, M. SOD1 Mutations Targeting Surface Hydrogen Bonds Promote Amyotrophic Lateral Sclerosis without Reducing Apo-state Stability. *J. Biol. Chem.* **285**, 19544–19552 (2010).

132. Tiwari, A. & Hayward, L. J. Mutant SOD1 Instability: Implications for Toxicity in Amyotrophic Lateral Sclerosis. *Neurodegener. Dis.* **2**, 115–127 (2005).

133. Prudencio, M., Hart, P. J., Borchelt, D. R. & Andersen, P. M. Variation in aggregation propensities among ALS-associated variants of SOD1: Correlation to human disease. *Hum. Mol. Genet.* **18**, 3217–3226 (2009).

134. Luchinat, E., Barbieri, L., Rubino, J. T., Kozyreva, T., Cantini, F. & Banci, L. In-cell NMR reveals potential precursor of toxic species from SOD1 fALS mutants. *Nat. Commun.* **5**, 5502 (2014).

135. Sekhar, A., Rumfeldt, J. A., Broom, H. R., Doyle, C. M., Bouvignies, G., Meiering, E. M. & Kay, L. E. Thermal fluctuations of immature SOD1 lead to separate folding and misfolding pathways. *Elife* **4**, e07296 (2015).

136. Shipp, E. L., Cantini, F., Bertini, I., Valentine, J. S. & Banci, L. Dynamic properties of the G93A mutant of copper-zinc superoxide dismutase as detected by NMR spectroscopy: Implications for the pathology of familial amyotrophic lateral sclerosis. *Biochemistry* **42**, 1890–1899 (2003).

137. Getzoff, E. D., Cabelli, D. E., Fisher, C. L., Parge, H. E., Viezzoli, M. S., Banci, L. & Hallewell, R. A. Faster superoxide dismutase mutants designed by enhancing electrostatic guidance. *Nature* **358**, 347–351 (1992).

138. Furukawa, Y. & O'Halloran, T. V. Amyotrophic lateral sclerosis mutations have the greatest destabilizing effect on the apo- and reduced form of SOD1, leading to unfolding and oxidative aggregation. *J. Biol. Chem.* **280**, 17266–74 (2005).

139. Hwang, T. L. & Shaka, A. J. Water Suppression That Works. Excitation Sculpting Using Arbitrary Wave-Forms and Pulsed-Field Gradients. *J. Magn. Reson. - Ser. A* **112**, 275–279 (1995).

140. Bodenhausen, G. & Ruben, D. J. Natural abundance nitrogen-15 NMR by enhanced heteronuclear spectroscopy. *Chem. Phys. Lett.* **69**, 185–189 (1980).

141. Piotto, M., Saudek, V. & Sklenar, V. Gradient-tailored excitation for single-quantum NMR spectroscopy of aqueous solutions. *J. Biomol. NMR* **2**, 661–665 (1992).

142. Sklenar, V., Piotto, M., Leppik, R. & Saudek, V. Gradient-Tailored Water Suppression for 1H-15N HSQC Experiments Optimized to Retain Full Sensitivity. *J. Magn. Reson. - Ser. A* **102**, 241–245 (1993).

143. Mori, S., Abeygunawardana, C., Johnson, M. O. & Van Zljl, P. C. M. Improved Sensitivity of HSQC Spectra of Exchanging Protons at Short Interscan Delays Using a New Fast HSQC (FHSQC) Detection Scheme That Avoids Water Saturation. *J. Magn. Reson. Ser. B* **108**, 94–98 (1995).

144. Zhang, O., Kay, L. E., Olivier, J. P. & Forman-Kay, J. D. Backbone 1H and 15N resonance assignments of the N-terminal SH3 domain of drk in folded and unfolded states using enhanced-sensitivity pulsed field gradient NMR techniques. *J. Biomol. NMR* **4**, 845–858 (1994).

145. Palmer, A. G., Cavanagh, J., Wright, P. E. & Rance, M. Sensitivity improvement in proton-detected two-dimensional heteronuclear correlation NMR spectroscopy. *J. Magn. Reson.* **93**, 151–170 (1991).

146. Kay, L. E., Keifer, P. & Saarinen, T. Pure Absorption Gradient Enhanced Heteronuclear Single Quantum Correlation Spectroscopy with Improved Sensitivity. *J. Am. Chem. Soc.* **114**,

10663–10665 (1992).

147. Schleucher, J., Schwendinger, M., Sattler, M., Schmidt, P., Schedletzky, O., Glaser, S. J., Sørensen, O. W. & Griesinger, C. A general enhancement scheme in heteronuclear multidimensional NMR employing pulsed field gradients. *J. Biomol. NMR* **4**, 301–306 (1994).

148. Keller, R. L. J. *The Computer Aided Resonance Assignment Tutorial*. (Cantina Verlag, 1996).

149. Trainor, K., Palumbo, J. A., MacKenzie, D. W. S. & Meiering, E. M. Temperature dependence of NMR chemical shifts: Tracking and statistical analysis. *Protein Sci.* **29**, 306–314 (2020).

150. Maltsev, A., Poulsen, F. & Bax, A. Poulsen IDP/IUP random coil chemical shifts. *Bax Group Website* https://spin.niddk.nih.gov/bax/nmrserver/Poulsen_rc_CS/ (2019).

151. Kjaergaard, M., Brander, S. & Poulsen, F. M. Random coil chemical shift for intrinsically disordered proteins: effects of temperature and pH. *J Biomol NMR* **49**, 139–149 (2011).

152. Kjaergaard, M. & Poulsen, F. M. Sequence correction of random coil chemical shifts: correlation between neighbor correction factors and changes in the Ramachandran distribution. *J. Biomol. NMR* **50**, 157–165 (2011).

153. Leinweber, B., Barofsky, E., Barofsky, D. F., Ermilov, V., Nylin, K. & Beckman, J. S. Aggregation of ALS mutant superoxide dismutase expressed in Escherichia coli. *Free Radic. Biol. Med.* **36**, 911–918 (2004).

154. Jaktaji, R. P. & Heidari, F. Study the expression of ompf gene in esherichia coli mutants. *Indian J. Pharm. Sci.* **75**, 540–544 (2013).

155. Wang, X., Teng, D., Guan, Q., Mao, R., Hao, Y., Wang, X., Yao, J. & Wang, J. Escherichia coli outer membrane protein F (OmpF): an immunogenic protein induces cross-reactive antibodies against Escherichia coli and Shigella. *AMB Express* **7**, 155 (2017).

156. Wishart, D. S., Bigam, C. G., Holm, A., Hodges, R. S. & Sykes, B. D. 1H, 13C and 15N random coil NMR chemical shifts of the common amino acids. I. Investigations of nearest-neighbor effects. *J. Biomol. NMR* **5**, 67–81 (1995).

157. Robustelli, P., Stafford, K. A. & Palmer, A. G. Interpreting protein structural dynamics from NMR chemical shifts. *J. Am. Chem. Soc.* **134**, 6365–6374 (2012).

158. Doyle, C. A Refined Method for Quantitation of Divalent Metal Ions in Metalloproteins and

Local Stability and Conformational Heterogeneity of Amyotrophic Lateral Sclerosis-Associated Cu, Zn Superoxide Dismutase (MSc Thesis). (University of Waterloo, 2014).

159. Hayward, L. J., Rodriguez, J. A., Kim, J. W., Tiwari, A., Goto, J. J., Cabelli, D. E., Valentine, J. S. & Brown, R. H. Decreased metallation and activity in subsets of mutant superoxide dismutases associated with familial amyotrophic lateral sclerosis. *J. Biol. Chem.* **277**, 15923–15931 (2002).

160. Banci, L., Bertini, I., Cantini, F., D'Amelio, N. & Gaggelli, E. Human SOD1 before Harboring the Catalytic Metal: Solution structure of copper-depleted, disulfide-reduced form. *J. Biol. Chem.* **281**, 2333–2337 (2006).

161. Lam, S. L. & Hsu, V. L. NMR identification of left-handed polyproline type II helices. *Biopolymers* **69**, 270–281 (2003).

162. Cheng, J. W., Lepre, C. A., Chambers, S. P., Fulghum, J. R., Thomson, J. A. & Moore, J. M. 15N NMR Relaxation Studies of the FK506 Binding Protein: Backbone Dynamics of the Uncomplexed Receptor. *Biochemistry* **32**, 9000–9010 (1993).

163. Tainer, J. A., Getzoff, E. D., Beem, K. M., Richardson, J. S. & Richardson, D. C. Determination and analysis of the 2 Å structure of copper, zinc superoxide dismutase. *J. Mol. Biol.* **160**, 181–217 (1982).

164. Sala, F. A., Wright, G. S. A., Antonyuk, S. V, Garrattid, R. C. & Hasnainid, S. S. Molecular recognition and maturation of SOD1 by its evolutionarily destabilised cognate chaperone hCCS. *PLoS Biol.* **17**, e3000141 (2019).

165. Das, A. & Plotkin, S. S. SOD1 exhibits allosteric frustration to facilitate metal binding affinity. *Proc. Natl. Acad. Sci. U. S. A.* **110**, 3871–3876 (2013).

166. Fisher, C. L., Cabelli, D. E., Tainer, J. A., Hallewell, R. A. & Getzoff, E. D. The role of arginine 143 in the electrostatics and mechanism of Cu, Zn superoxide dismutase: Computational and experimental evaluation by mutational analysis. *Proteins Struct. Funct. Genet.* **19**, 24–34 (1994).

167. Banci, L., Benedetto, M., Bertini, I., Del Conte, R., Piccioli, M. & Viezzoli, M. S. Solution structure of reduced monomeric Q133M2 copper, zinc superoxide dismutase (SOD). Why is SOD a dimeric enzyme? *Biochemistry* **37**, 11780–11791 (1998).

168. Banci, L., Bertini, I., Cramaro, F., Del Conte, R., Rosato, A. & Viezzoli, M. S. Backbone dynamics of human Cu,Zn superoxide dismutase and of its monomeric F50E/G51E/E133Q mutant: The influence of dimerization on mobility and function. *Biochemistry* **39**, 9108–9118 (2000).

169. Garfin, D. E. Gel Electrophoresis of Proteins. in *Essential Cell Biology, Volume 1: Cell Structure, A Practical Approach* (eds. John Davey & Mike Lord) 197–268 (Oxford University Press, 2003).

170. Liu, Z., Lemma, T. & Pawliszyn, J. Capillary Isoelectric Focusing Coupled with Dynamic Imaging Detection: A One-Dimensional Separation for Two-Dimensional Protein Characterization. *J. Proteome Res.* **5**, 1246–1251 (2006).

171. Righetti, P. G. *Isoelectric focusing : theory, methodology, and applications*. (Elsevier, 1983).

172. Wu, J., Wu, X.-Z., Huang, T. & Pawliszyn, J. Analysis of Proteins by CE, CIEF, and Microfluidic Devices With Whole-Column-Imaging Detection. in *Capillary Electrophoresis of Proteins and Peptides* 229–252 (Humana Press, 2004). doi:10.1385/1-59259-798-X:229.

173. Zarabadi, A. S. & Pawliszyn, J. Accurate Determination of the Diffusion Coefficient of Proteins by Fourier Analysis with Whole Column Imaging Detection. *Anal. Chem.* **87**, 2100–2106 (2015).

174. Shi, Y., Mowery, R. A. & Shaw, B. F. Effect of Metal Loading and Subcellular pH on Net Charge of Superoxide Dismutase-1. *J. Mol. Biol.* **425**, 4388–4404 (2013).

175. Wenisch, E., Vorauer, K., Jungbauer, A., Katinger, H. & Righetti, P. G. Purification of human recombinant superoxide dismutase by isoelectric focusing in a multicompartment electrolyzer with zwitterionic membranes. *Electrophoresis* **15**, 647–653 (1994).

176. Trainor, K., Gingras, Z., Shillingford, C., Malakian, H., Gosselin, M., Lipovšek, D. & Meiering, E. M. Ensemble Modeling and Intracellular Aggregation of an Engineered Immunoglobulin-Like Domain. *J. Mol. Biol.* **428**, 1365–1374 (2016).

177. Vogt, C. 1999. Creating Long Documents using Microsoft Word. Published on the Web at the University of Waterloo.

Appendix A

Acquisition Parameters of the ^{1}H-^{15}N HSQC

Experiment
PULPROG hsqcfpf3gpphwg
AQ_mod DQD
FnTYPE traditional(planes)
FnMODE States-TPPI
TD 8192 128
DS 16
NS 8
TD0 1
TDav 0
Width
SW [ppm] 23.9411 44.0001
SWH [Hz] 14367.816
2675.984
IN_F [µsec] 373.69
AQ [sec] 0.2850816
0.0239164
FIDRES [Hz] 3.507768
41.812252
FW [Hz] 125000.000
Receiver
RG 128
DW [µsec] 34.800
DWOV [µsec] 0.040
DECIM 12
DSPFIRM sharp(standard)
DIGTYP #ADC+ (digitizer not
installed!)
DIGMOD digital
DR 17
DDR 0
DE [µsec] 6.00
NBL 1
HPPRGN normal
PRGAIN high
DQDMODE add
PH_ref [degree] 0
OVERFLW check
(1/14)
Thu Jun 11 15:51:49 CDT
2020
Nucleus 1
NUC1 1H
O1 [Hz] 2813.41 6993.22
O1P [ppm] 4.688 115.000
SFO1 [MHz] 600.1328134
60.8176382
BF1 [MHz] 600.1300000
60.8106450
Nucleus 2
NUC2 off
O2 [Hz] 0
O2P [ppm] 0
SFO2 [MHz] 600.1300000
BF2 [MHz] 600.1300000
Nucleus 3
NUC3 15N
O3 [Hz] 6993.22
O3P [ppm] 115.000
SFO3 [MHz] 60.8176382
BF3 [MHz] 60.8106450
Nucleus 4
NUC4 off
O4 [Hz] 0
O4P [ppm] 0
SFO4 [MHz] 600.1300000
BF4 [MHz] 600.1300000
Nucleus 5
NUC5 off
O5 [Hz] 0
O5P [ppm] 0
SFO5 [MHz] 600.1300000
BF5 [MHz] 600.1300000
Nucleus 6
NUC6 off
O6 [Hz] 0
O6P [ppm] 0
SFO6 [MHz] 600.1300000
BF6 [MHz] 600.1300000
Nucleus 7
NUC7 off
(2/14)
Thu Jun 11 15:51:50 CDT
2020
O7 [Hz] 0
O7P [ppm] 0
SFO7 [MHz] 600.1300000
BF7 [MHz] 600.1300000
Nucleus 8
NUC8 off
O8 [Hz] 0
O8P [ppm] 0
SFO8 [MHz] 600.1300000
BF8 [MHz] 600.1300000
Durations
P [µsec] [0]: 8.500 [1]: 9.140
[2]: 18.800
[3]: 0 [4]: 0 [5]: 16.500
[6]: 25.000 [7]: 50.000 [8]: 0
[9]: 0 [10]: 0 [11]: 1000.000
[12]: 2000.000 [13]: 32.500
[14]: 0
[15]: 250000.000 [16]:
1000.000 [17]: 1000.000
[18]: 10000.000 [19]: 500.000
[20]: 25.000
[21]: 37.000 [22]: 74.000 [23]:
0
[24]: 0 [25]: 500.000 [26]: 0
[27]: 8.500 [28]: 1000.000
[29]: 250.000
[30]: 0 [31]: 0 [32]: 0
[33]: 0 [34]: 0 [35]: 0
[36]: 0 [37]: 0 [38]: 0
[39]: 0 [40]: 0 [41]: 0
[42]: 0 [43]: 0 [44]: 0
[45]: 0 [46]: 0 [47]: 0
[48]: 0 [49]: 0 [50]: 0
[51]: 0 [52]: 0 [53]: 0
[54]: 0 [55]: 0 [56]: 0
[57]: 0 [58]: 0 [59]: 0
[60]: 0 [61]: 0 [62]: 0
[63]: 0
D [sec] [0]: 0.000003000[1]:
0.800000012[2]: 0.003450000
[3]: 0.002300000[4]:
0.001725000[5]: 0
[6]: 0 [7]: 0.483999997[8]: 0
[9]: 0.059999999[10]: 0 [11]:
0.029999999
[12]: 0.000020000[13]:
0.000003000[14]: 0
(3/14)
Thu Jun 11 15:51:50 CDT
2020
[15]: 0 [16]: 0.000500000[17]:
0
[18]: 0 [19]: 0 [20]: 0
[21]: 0 [22]: 0 [23]: 0
[24]: 0.002777778[25]: 0 [26]:
0

[27]: 0 [28]: 0 [29]: 0
[30]: 0 [31]: 0 [32]: 0
[33]: 0 [34]: 0 [35]: 0
[36]: 0 [37]: 0 [38]: 0
[39]: 0 [40]: 0 [41]: 0
[42]: 0 [43]: 0 [44]: 0
[45]: 0 [46]: 0 [47]: 0
[48]: 0 [49]: 0 [50]: 0
[51]: 0 [52]: 0 [53]: 0
[54]: 0 [55]: 0 [56]: 0
[57]: 0 [58]: 0 [59]: 0
[60]: 0 [61]: 0 [62]: 0
[63]: 0
IN [sec] [0]: 0.00018685 [1]:
0.00100000 [2]: 0.00100000
[3]: 0.00100000 [4]:
0.00100000 [5]: 0.00100000
[6]: 0.00100000 [7]:
0.00100000 [8]: 0.00100000
[9]: 0.00100000 [10]:
0.00100000 [11]: 0.00100000
[12]: 0.00100000 [13]:
0.00100000 [14]: 0.00100000
[15]: 0.00100000 [16]:
0.00100000 [17]: 0.00100000
[18]: 0.00100000 [19]:
0.00100000 [20]: 0.00100000
[21]: 0.00100000 [22]:
0.00100000 [23]: 0.00100000
[24]: 0.00100000 [25]:
0.00100000 [26]: 0.00100000
[27]: 0.00100000 [28]:
0.00100000 [29]: 0.00100000
[30]: 0.00100000 [31]:
0.00100000 [32]: 0.00100000
[33]: 0.00100000 [34]:
0.00100000 [35]: 0.00100000
[36]: 0.00100000 [37]:
0.00100000 [38]: 0.00100000
[39]: 0.00100000 [40]:
0.00100000 [41]: 0.00100000
[42]: 0.00100000 [43]:
0.00100000 [44]: 0.00100000
[45]: 0.00100000 [46]:
0.00100000 [47]: 0.00100000
[48]: 0.00100000 [49]:
0.00100000 [50]: 0.00100000
[51]: 0.00100000 [52]:
0.00100000 [53]: 0.00100000
[54]: 0.00100000 [55]:
0.00100000 [56]: 0.00100000
[57]: 0.00100000 [58]:
0.00100000 [59]: 0.00100000
[60]: 0.00100000 [61]:
0.00100000 [62]: 0.00100000
(4/14)
Thu Jun 11 15:51:50 CDT
2020
[63]: 0.00100000
INP [µsec] [0]: 0 [1]: 0 [2]: 0
[3]: 0 [4]: 0 [5]: 0
[6]: 0 [7]: 0 [8]: 0
[9]: 0 [10]: 0 [11]: 0
[12]: 0 [13]: 0 [14]: 0
[15]: 0 [16]: 0 [17]: 0
[18]: 0 [19]: 0 [20]: 0
[21]: 0 [22]: 0 [23]: 0
[24]: 0 [25]: 0 [26]: 0
[27]: 0 [28]: 0 [29]: 0
[30]: 0 [31]: 0 [32]: 0
[33]: 0 [34]: 0 [35]: 0
[36]: 0 [37]: 0 [38]: 0
[39]: 0 [40]: 0 [41]: 0
[42]: 0 [43]: 0 [44]: 0
[45]: 0 [46]: 0 [47]: 0
[48]: 0 [49]: 0 [50]: 0
[51]: 0 [52]: 0 [53]: 0
[54]: 0 [55]: 0 [56]: 0
[57]: 0 [58]: 0 [59]: 0
[60]: 0 [61]: 0 [62]: 0
[63]: 0
HDDUTY [%] 20.0
HDRATE 20
PCPD [µsec] [0]: 100 [1]: 70
[2]: 75
[3]: 190 [4]: 100 [5]: 100
[6]: 100 [7]: 100 [8]: 100
[9]: 100
V9 [%] 5.00
Power
PLW [W] [0]: -1 [1]: -1 [2]: -1
[3]: -1 [4]: -1 [5]: -1
[6]: -1 [7]: -1 [8]: -1
[9]: -1 [10]: -1 [11]: -1
[12]: -1 [13]: -1 [14]: -1
[15]: -1 [16]: -1 [17]: -1
[18]: -1 [19]: -1 [20]: -1
(5/14)
Thu Jun 11 15:51:50 CDT
2020
[21]: -1 [22]: -1 [23]: -1
[24]: -1 [25]: -1 [26]: -1
[27]: -1 [28]: -1 [29]: -1
[30]: -1 [31]: -1 [32]: -1
[33]: -1 [34]: -1 [35]: -1
[36]: -1 [37]: -1 [38]: -1
[39]: -1 [40]: -1 [41]: -1
[42]: -1 [43]: -1 [44]: -1
[45]: -1 [46]: -1 [47]: -1
[48]: -1 [49]: -1 [50]: -1
[51]: -1 [52]: -1 [53]: -1
[54]: -1 [55]: -1 [56]: -1
[57]: -1 [58]: -1 [59]: -1
[60]: -1 [61]: -1 [62]: -1
[63]: -1
PLdB [0]: [1]: [2]:
[3]: [4]: [5]:
[6]: [7]: [8]:
[9]: [10]: [11]:
[12]: [13]: [14]:
[15]: [16]: [17]:
[18]: [19]: [20]:
[21]: [22]: [23]:
[24]: [25]: [26]:
[27]: [28]: [29]:
[30]: [31]: [32]:
[33]: [34]: [35]:
[36]: [37]: [38]:
[39]: [40]: [41]:
[42]: [43]: [44]:
[45]: [46]: [47]:
[48]: [49]: [50]:
[51]: [52]: [53]:
[54]: [55]: [56]:
[57]: [58]: [59]:
[60]: [61]: [62]:
[63]:
PLSTRT [dB] -6
(6/14)
Thu Jun 11 15:51:50 CDT
2020
PLSTEP 0.1
SHAPE
SP [dB] = [0]: [1]: [2]:
[3]: [4]: [5]:
[6]: [7]: [8]:
[9]: [10]: [11]:
[12]: [13]: [14]:
[15]: [16]: [17]:
[18]: [19]: [20]:
[21]: [22]: [23]:
[24]: [25]: [26]:
[27]: [28]: [29]:
[30]: [31]:
SPOFFS [Hz] = [0]: 0 [1]: 0
[2]: 0
[3]: 0 [4]: 0 [5]: 0
[6]: 0 [7]: 0 [8]: 0
[9]: 0 [10]: 0 [11]: 0

[12]: 0 [13]: 0 [14]: 0
[15]: 0 [16]: 0 [17]: 0
[18]: 0 [19]: 0 [20]: 0
[21]: 0 [22]: 0 [23]: 0
[24]: 0 [25]: 0 [26]: 0
[27]: 0 [28]: 0 [29]: 0
[30]: 0 [31]: 0
SPOAL = [0]: 0.5 [1]: 0.5 [2]: 0.5
[3]: 0.5 [4]: 0.5 [5]: 0.5
[6]: 0.5 [7]: 0.5 [8]: 0.5
[9]: 0.5 [10]: 0.5 [11]: 0.5
[12]: 0.5 [13]: 0.5 [14]: 0.5
[15]: 0.5 [16]: 0.5 [17]: 0.5
[18]: 0.5 [19]: 0.5 [20]: 0.5
[21]: 0.5 [22]: 0.5 [23]: 0.5
[24]: 0.5 [25]: 0.5 [26]: 0.5
[27]: 0.5 [28]: 0.5 [29]: 0.5
[30]: 0.5 [31]: 0.5
SPNAM = [0]: [1]: [2]:
[3]: [4]: [5]:
[6]: [7]: [8]:
(7/14)
Thu Jun 11 15:51:50 CDT 2020
[9]: [10]: [11]:
[12]: [13]: [14]:
[15]: [16]: [17]:
[18]: [19]: [20]:
[21]: [22]: [23]:
[24]: [25]: [26]:
[27]: [28]: [29]:
[30]: [31]:
GRADIENT
GPX [%] = [0]: 0 [1]: 0 [2]: 0
[3]: 0 [4]: 0 [5]: 0
[6]: 0 [7]: 0 [8]: 0
[9]: 0 [10]: 0 [11]: 0
[12]: 0 [13]: 0 [14]: 0
[15]: 0 [16]: 0 [17]: 0
[18]: 0 [19]: 0 [20]: 0
[21]: 0 [22]: 0 [23]: 0
[24]: 0 [25]: 0 [26]: 0
[27]: 0 [28]: 0 [29]: 0
[30]: 0 [31]: 0
GPY [%] = [0]: 0 [1]: 0 [2]: 0
[3]: 0 [4]: 0 [5]: 0
[6]: 0 [7]: 0 [8]: 0
[9]: 0 [10]: 0 [11]: 0
[12]: 0 [13]: 0 [14]: 0
[15]: 0 [16]: 0 [17]: 0
[18]: 0 [19]: 0 [20]: 0
[21]: 0 [22]: 0 [23]: 0
[24]: 0 [25]: 0 [26]: 0
[27]: 0 [28]: 0 [29]: 0
[30]: 0 [31]: 0
GPZ [%] = [0]: 0 [1]: 80 [2]: -50
[3]: 50 [4]: 80 [5]: 30
[6]: 0 [7]: 0 [8]: 0
[9]: 0 [10]: 0 [11]: 0
[12]: 0 [13]: 0 [14]: 0
[15]: 0 [16]: 0 [17]: 0
[18]: 0 [19]: 0 [20]: 0
(8/14)
Thu Jun 11 15:51:50 CDT 2020
[21]: 0 [22]: 0 [23]: 0
[24]: 0 [25]: 0 [26]: 0
[27]: 0 [28]: 0 [29]: 0
[30]: 0 [31]: 0
GPNAM = [0]: [1]: [2]:
[3]: [4]: [5]:
[6]: [7]: [8]:
[9]: [10]: [11]:
[12]: [13]: [14]:
[15]: [16]: [17]:
[18]: [19]: [20]:
[21]: [22]: [23]:
[24]: [25]: [26]:
[27]: [28]: [29]:
[30]: [31]:
AMP [%] [0]: 100.00 [1]: 100.00 [2]: 100.00
[3]: 100.00 [4]: 100.00 [5]: 100.00
[6]: 100.00 [7]: 100.00 [8]: 100.00
[9]: 100.00 [10]: 100.00 [11]: 100.00
[12]: 100.00 [13]: 100.00 [14]: 100.00
[15]: 100.00 [16]: 100.00 [17]: 100.00
[18]: 100.00 [19]: 100.00 [20]: 100.00
[21]: 100.00 [22]: 100.00 [23]: 100.00
[24]: 100.00 [25]: 100.00 [26]: 100.00
[27]: 100.00 [28]: 100.00 [29]: 100.00
[30]: 100.00 [31]: 100.00
Program parameters
L [0]: 1 [1]: 1 [2]: 1
[3]: 1 [4]: 1 [5]: 1
[6]: 1 [7]: 1 [8]: 1
[9]: 1 [10]: 1 [11]: 1
[12]: 1 [13]: 1 [14]: 1
[15]: 1 [16]: 1 [17]: 1
[18]: 1 [19]: 1 [20]: 1
[21]: 1 [22]: 1 [23]: 1
[24]: 1 [25]: 1 [26]: 1
[27]: 1 [28]: 1 [29]: 1
[30]: 1 [31]: 1
(9/14)
Thu Jun 11 15:51:50 CDT 2020
CNST [0]: 1 [1]: 1 [2]: 90
[3]: 1 [4]: 94 [5]: 1
[6]: 1 [7]: 1 [8]: 1
[9]: 1 [10]: 1 [11]: 1
[12]: 1 [13]: 1 [14]: 1
[15]: 1 [16]: 1 [17]: 1
[18]: 1 [19]: 1 [20]: 1
[21]: 80 [22]: 30 [23]: 20
[24]: 1 [25]: 1 [26]: 1
[27]: 1 [28]: 1 [29]: 1
[30]: 1 [31]: 1 [32]: 1
[33]: 1 [34]: 1 [35]: 1
[36]: 1 [37]: 1 [38]: 1
[39]: 1 [40]: 1 [41]: 1
[42]: 1 [43]: 1 [44]: 1
[45]: 1 [46]: 1 [47]: 1
[48]: 1 [49]: 1 [50]: 1
[51]: 1 [52]: 1 [53]: 1
[54]: 1 [55]: 1 [56]: 1
[57]: 1 [58]: 1 [59]: 1
[60]: 1 [61]: 1 [62]: 1
[63]: 1
CPDPRG [0]: [1]: garp [2]: garp
[3]: mlev [4]: mlev [5]: mlev
[6]: mlev [7]: mlev
PHCOR [degree] [0]: 0 [1]: 0
[2]: 0
[3]: 0 [4]: 0 [5]: 0
[6]: 0 [7]: 0 [8]: 0
[9]: 0 [10]: 0 [11]: 0
[12]: 0 [13]: 0 [14]: 0
[15]: 0 [16]: 0 [17]: 0
[18]: 0 [19]: 0 [20]: 0
[21]: 0 [22]: 0 [23]: 0
[24]: 0 [25]: 0 [26]: 0
[27]: 0 [28]: 0 [29]: 0
[30]: 0 [31]: 0
SUBNAM [0]: "" [1]: "" [2]: ""
[3]: "" [4]: "" [5]: ""
(10/14)

Thu Jun 11 15:51:50 CDT 2020
[6]: "" [7]: "" [8]: ""
[9]: ""
ZGOPTNS
Probe
QNP 1
RO [Hz] 0
MASR [Hz] 4200
SPINCNT 0
TE [K] 298.2
TE1 [K] 300.0
TE2 [K] 300.0
TE3 [K] 300.0
TE4 [K] 300.0
TEG [K] 300.0
Lists
FQLIST [0]: [1]: [2]:
[3]: [4]: [5]:
[6]: [7]:
VALIST valist
VCLIST CCCCCCCCCCCCCCC
VDLIST DDDDDDDDDDDDDDD
VPLIST PPPPPPPPPPPPPPP
PHLIST
VTLIST TTTTTTTTTTTTTTT
NUS (Non Uniform Sampling) parameters
NusAMOUNT [%] 25
NusPOINTS 16
NusJSP [Hz] 0
NusT2 [sec] 1
NusSEED 54321
NUSLIST automatic
Wobble
WBSW [MHz] [0]: 8.0000000 [1]: 10.0000000 [2]: 10.0000000
[3]: 10.0000000 [4]: 10.0000000 [5]: 10.0000000
[6]: 10.0000000 [7]: 10.0000000
(11/14)
Thu Jun 11 15:51:50 CDT 2020
WBST 1024
Lock
LOCNUC 2H
SOLVENT D2O
Automation
AUNM au_getlinv
PYNM acqu.py
EXP
TUBE_TYPE
Miscellaneous
GRDPROG
CHEMSTR none
User parameters
USERA1 user
USERA2 user
USERA3 user
USERA4 user
USERA5 user
Routing
RSEL [0]: 0 [1]: 2 [2]: 0
[3]: 6 [4]: 0 [5]: 0
[6]: 0 [7]: 0 [8]: 0
[9]: 0 [10]: 0 [11]: 0
[12]: 0 [13]: 0 [14]: 0
[15]: 0 [16]: 0 [17]: 0
[18]: 0 [19]: 0 [20]: 0
[21]: 0 [22]: 0 [23]: 0
[24]: 0
RECCHAN [0]: -1 [1]: -1 [2]: -1
[3]: -1 [4]: -1 [5]: -1
[6]: -1 [7]: -1 [8]: -1
[9]: -1
PRECHAN [0]: -1 [1]: 1 [2]: -1
[3]: 0 [4]: 2 [5]: -1
[6]: -1 [7]: -1 [8]: -1
[9]: -1 [10]: -1 [11]: -1
[12]: -1 [13]: -1 [14]: -1
[15]: -1 [16]: -1 [17]: -1
(12/14)
Thu Jun 11 15:51:50 CDT 2020
[18]: -1 [19]: -1 [20]: -1
[21]: -1 [22]: -1 [23]: -1
[24]: -1 [25]: -1 [26]: -1
[27]: -1 [28]: -1 [29]: -1
[30]: -1 [31]: -1 [32]: -1
RECSEL [0]: 0 [1]: 0 [2]: 0
[3]: 0 [4]: 0 [5]: 0
[6]: 0 [7]: 0 [8]: 0
[9]: 0 [10]: 0 [11]: 0
[12]: 0 [13]: 0 [14]: 0
[15]: 0 [16]: 0 [17]: 0
[18]: 0 [19]: 0 [20]: 0
[21]: 0 [22]: 0 [23]: 0
[24]: 0
SELREC [0]: 0 [1]: 0 [2]: 0
[3]: 0 [4]: 0 [5]: 0
[6]: 0 [7]: 0 [8]: 0
[9]: 0 [10]: 0 [11]: 0
[12]: 0 [13]: 0 [14]: 0
[15]: 0 [16]: 0 [17]: 0
[18]: 0 [19]: 0 [20]: 0
[21]: 0 [22]: 0 [23]: 0
[24]: 0
RECPRFX [0]: -1 [1]: -1 [2]: -1
[3]: -1 [4]: -1 [5]: -1
[6]: -1 [7]: -1 [8]: -1
[9]: -1 [10]: -1 [11]: -1
[12]: -1 [13]: -1 [14]: -1
[15]: -1 [16]: -1 [17]: -1
[18]: -1 [19]: -1 [20]: -1
[21]: -1 [22]: -1 [23]: -1
[24]: -1 [25]: -1 [26]: -1
[27]: -1 [28]: -1 [29]: -1
[30]: -1 [31]: -1 [32]: -1
RECPRE [0]: -1 [1]: -1 [2]: -1
[3]: -1 [4]: -1 [5]: -1
[6]: -1 [7]: -1 [8]: -1
[9]: -1 [10]: -1 [11]: -1
(13/14)
Thu Jun 11 15:51:50 CDT 2020
[12]: -1 [13]: -1 [14]: -1
[15]: -1 [16]: -1 [17]: -1
[18]: -1 [19]: -1 [20]: -1
[21]: -1 [22]: -1 [23]: -1
[24]: -1
NLOGCH 1
SWIBOX [0]: 0 [1]: 1 [2]: 4
[3]: 0 [4]: 0 [5]: 0
[6]: 6 [7]: 7 [8]: 0
[9]: 0 [10]: 0 [11]: 0
[12]: 0 [13]: 0 [14]: 0
[15]: 0 [16]: 0 [17]: 0
[18]: 0 [19]: 0 [20]: 0
[21]: 0 [22]: 0 [23]: 0
[24]: 0 [25]: 0 [26]: 0
[27]: 0 [28]: 0 [29]: 0
[30]: 0 [31]: 0 [32]: 0
FCUCHAN [0]: 0 [1]: 1 [2]: 0
[3]: 3 [4]: 0 [5]: 0
[6]: 0 [7]: 0 [8]: 0
HPMOD [0]: FALSE [1]: FALSE [2]: FALSE
[3]: FALSE [4]: FALSE [5]: FALSE
[6]: FALSE [7]: FALSE [8]: FALSE

[9]: FALSE [10]: FALSE [11]: FALSE
[12]: FALSE [13]: FALSE
[14]: FALSE
[15]: FALSE [16]: FALSE
[17]: FALSE
[18]: FALSE [19]: FALSE
[20]: FALSE

[21]: FALSE [22]: FALSE
[23]: FALSE
[24]: FALSE [25]: FALSE
[26]: FALSE
[27]: FALSE [28]: FALSE
[29]: FALSE
[30]: FALSE [31]: FALSE
[32]: FALSE

MULEXPNO [0]: 0 [1]: 0 [2]: 0
[3]: 0 [4]: 0 [5]: 0
[6]: 0 [7]: 0 [8]: 0
[9]: 0 [10]: 0 [11]: 0
[12]: 0 [13]: 0 [14]: 0
[15]: 0
(14/14)

Appendix B

Processing Parameters of the ^{1}H-^{15}N HSQC

Reference
SI 4096 512
SF [MHz] 600.1299452 60.8106630
OFFSET [ppm] 16.74991 135.84680
SR [Hz] -54.81 18.00
HZpPT [Hz] 3.507768 4.736472
SPECTYP UNDEFINED
Window function
WDW QSINE QSINE
LB [Hz] -25.00 -25.00
GB 0.1 0.15
SSB 2 2
TM1 0 0.1
TM2 0 0.9
Phase correction
PHC0 [degrees] 266.058 0
PHC1 [degrees] -5.600 0
PH_mod pk no
Baseline correction
ABSG 5 5
ABSF1 [ppm] 1000.00000 1000.00000
ABSF2 [ppm] -1000.00000 -1000.00000
BCFW [ppm] 1.00000 1.00000
COROFFS [Hz] 0 0
BC_mod qpol no
Fourier transform
TDeff 4096 0
STSR 0 10
STSI 0 456
ME_mod no LPfc
NCOEF 0 18
LPBIN 0 320
TDoff 0 0
REVERSE FALSE FALSE
(1/3)
Thu Jun 11 15:45:05 CDT 2020
FCOR 0.5 0.5
PKNL TRUE
FT_mod no no
MC2 echo-antiecho
NUS (Non Uniform Sampling) parameters
Mdd_mod mdd
MddCEXP FALSE
MddCT_SP FALSE
MddF180 FALSE
MddNCOMP 0
MddPHASE 0
MddSRSIZE [ppm] 0
Peak picking / plotting
MI [rel] 0
MAXI [rel] 1.00
PSIGN pos.
F1P [ppm] 10.8824 133.742
F2P [ppm] 6 104.112
PPIPTYP parabolic
PPDIAG 0
PPRESOL 1
PPMPNUM 200
Automation
AUNMP proc_2dinv
PYNMP
LAYOUT
CURPLOT HPLaserJet5000
Miscellaneous
TI
ALPHA 0 0
GAMMA 1 1
LEV0 35.00
NLEV 6
TOPLEV [%] 100.00
SIGF1 [ppm] 0 0
SIGF2 [ppm] 0 0
XDIM 64 64
User parameters
(2/3)
Thu Jun 11 15:45:05 CDT 2020
USERP1 user
USERP2 user
USERP3 user
USERP4 user
USERP5 user
(3/3)

Appendix C

SOD1 Spectra at Reference Temperatures

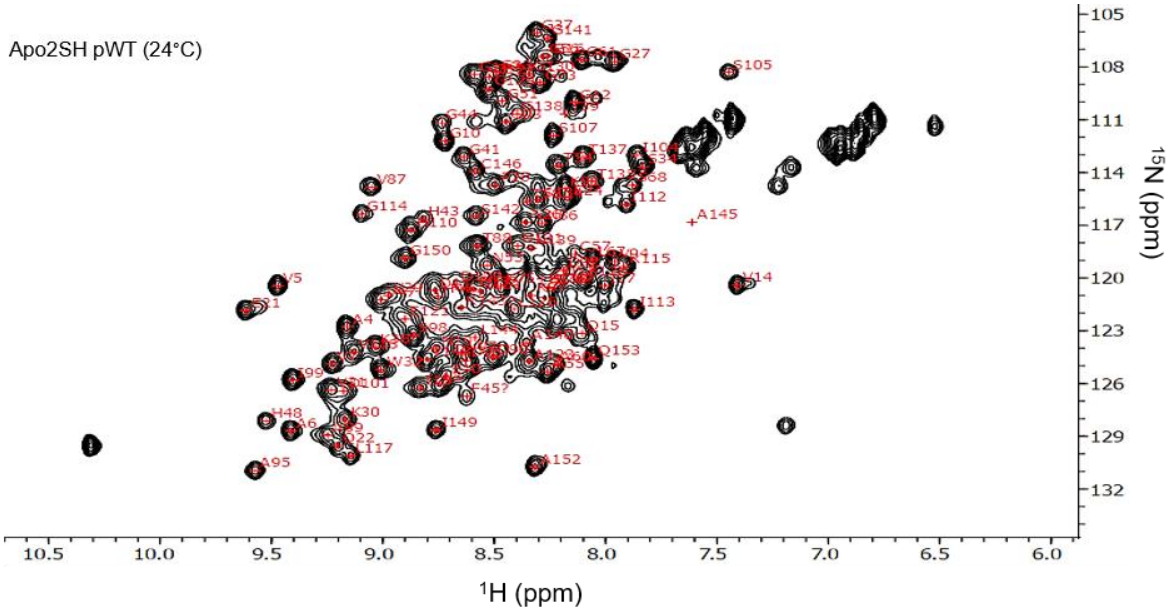

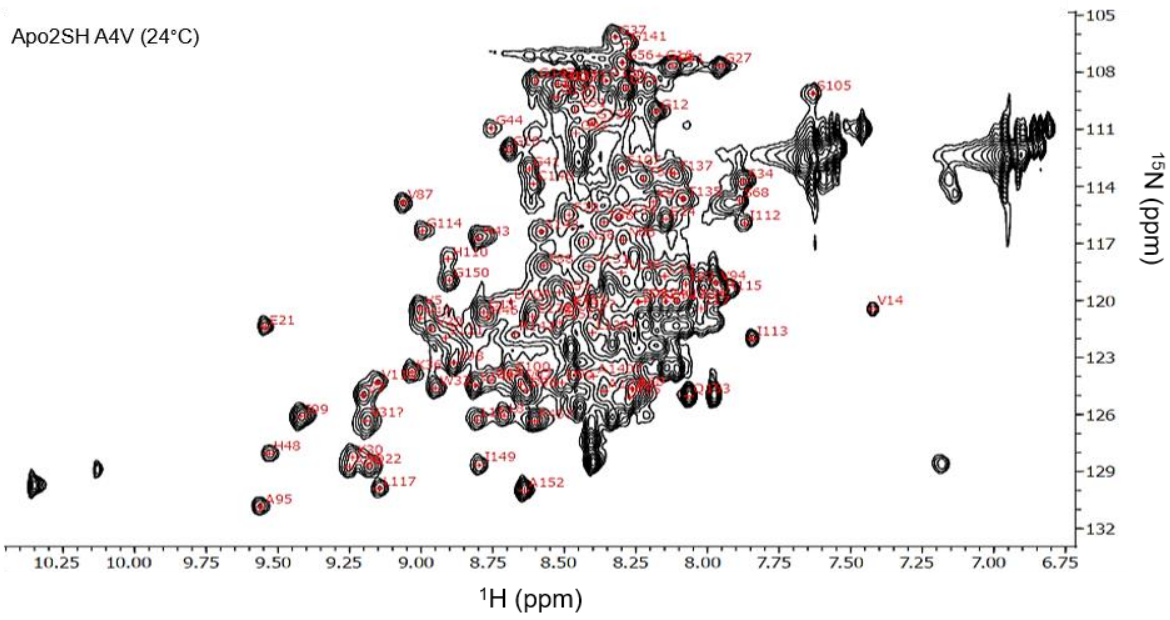

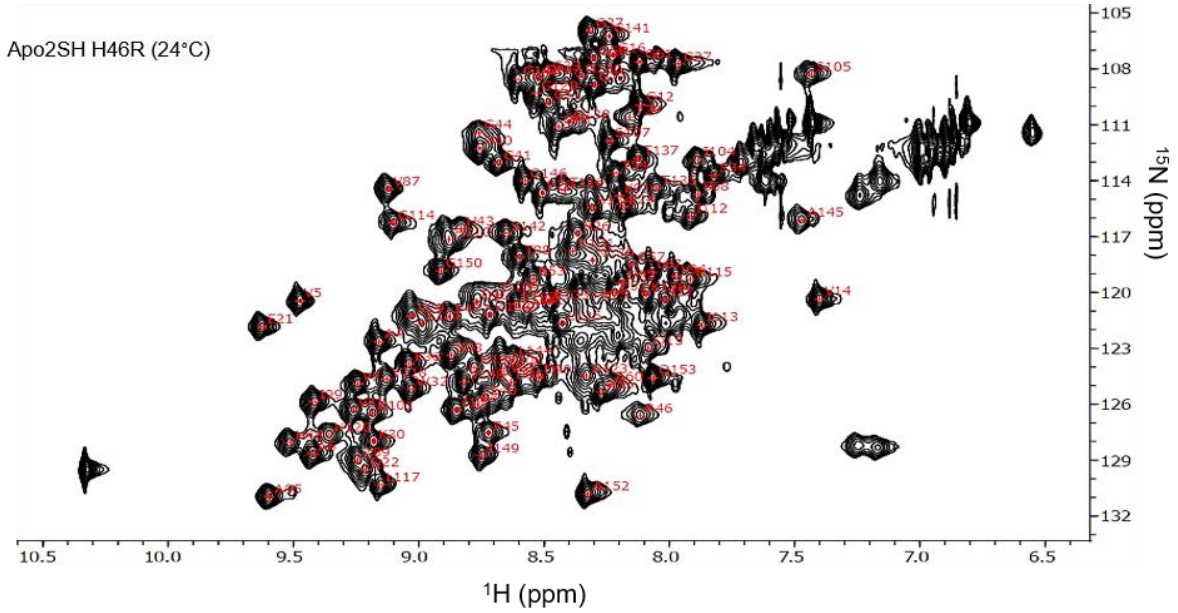
Apo2SH H46R (24°C)
105
108
111
114
117
120
123
126
129
132
15N (ppm)
10.5
10.0
9.5
9.0
8.5
8.0
7.5
7.0
6.5
1H (ppm)

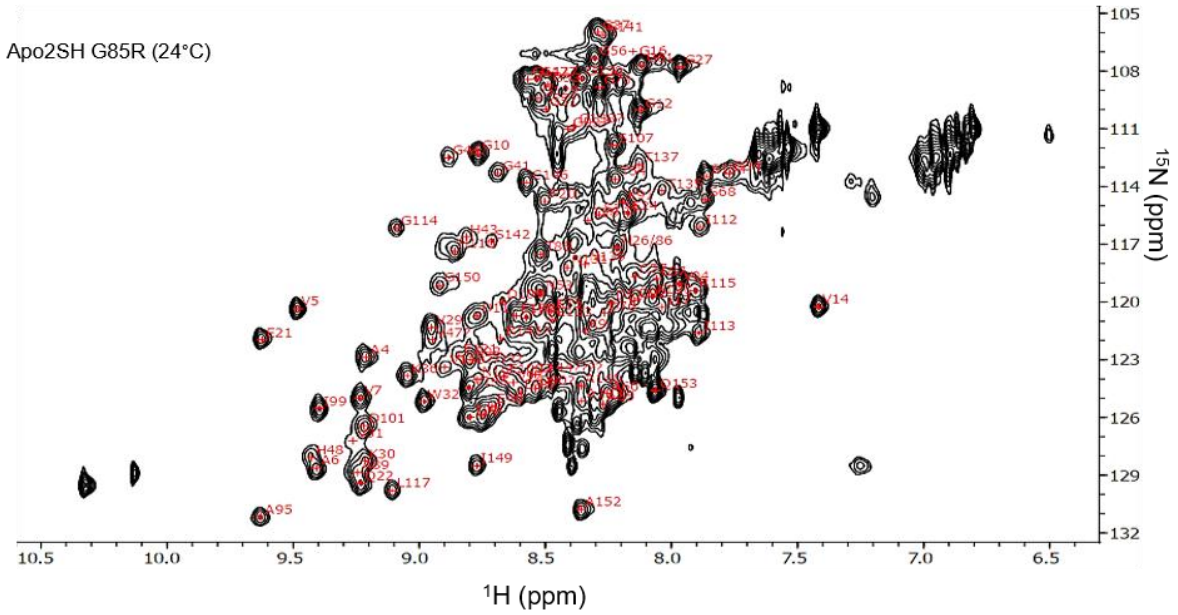
Apo2SH G85R (24°C)
105
108
111
114
117
120
123
126
129
132
15N (ppm)
10.5
10.0
9.5
9.0
8.5
8.0
7.5
7.0
6.5
1H (ppm)

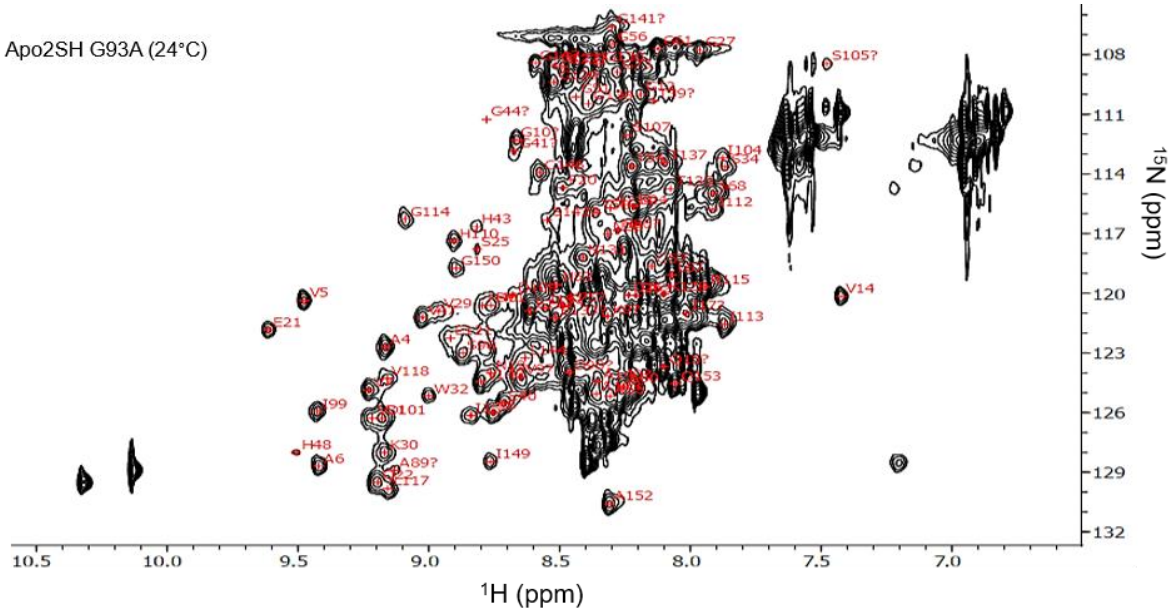
Apo2SH G93A (24°C)
^{15}N (ppm)
^{1}H (ppm)

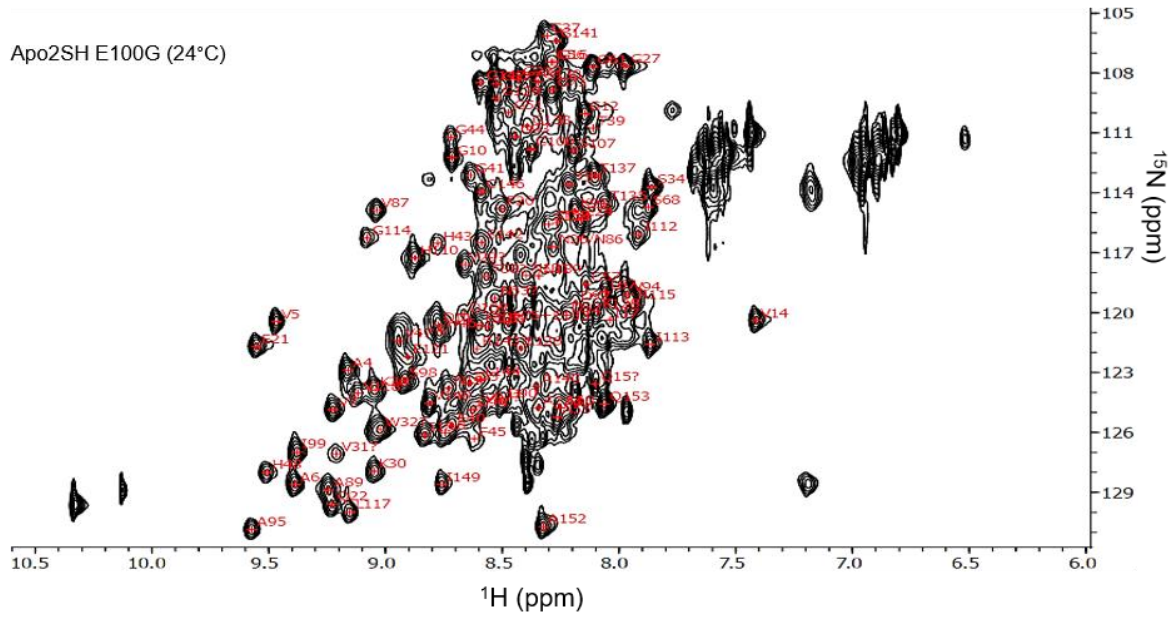
Apo2SH E100G (24°C)
^{15}N (ppm)
^{1}H (ppm)

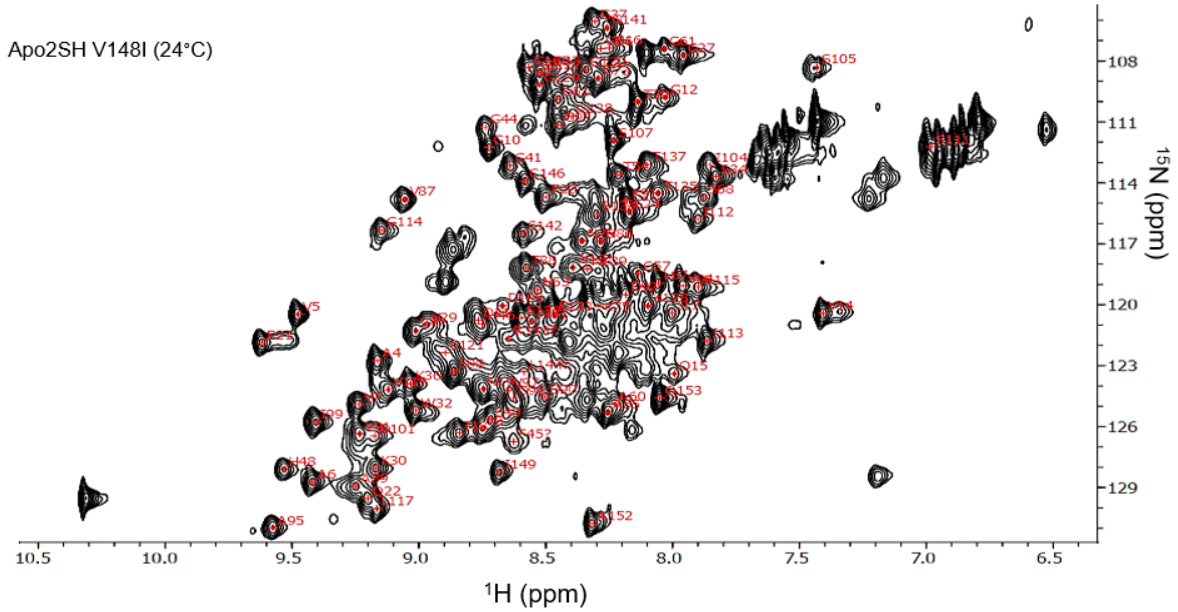
Apo2SH V148I (24°C)
^{15}N (ppm)
^{1}H (ppm)

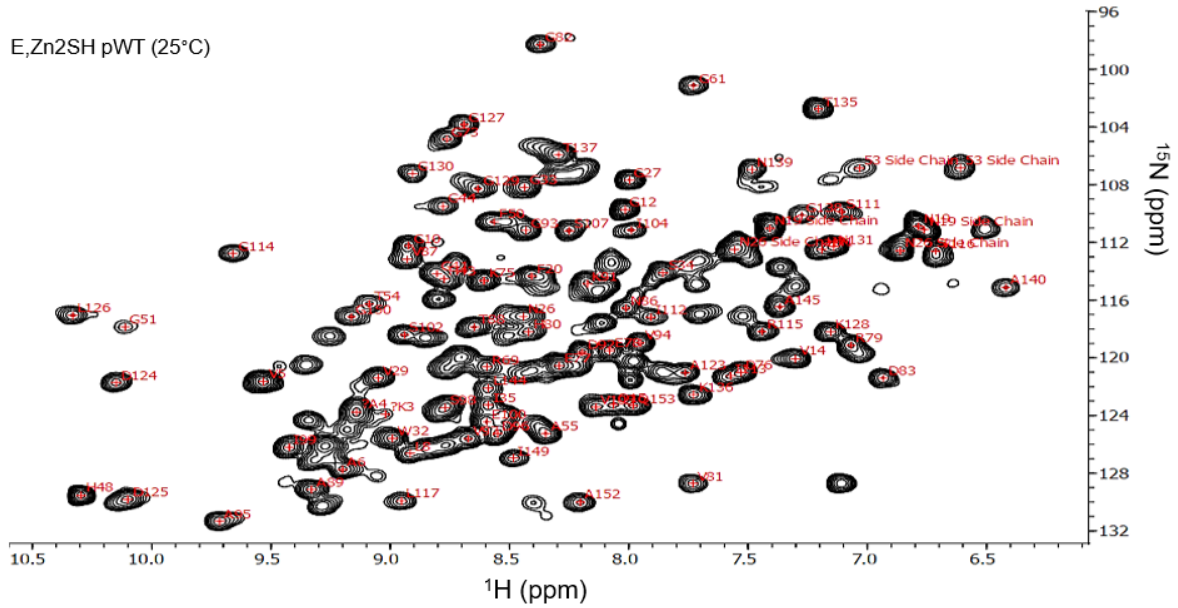
E,Zn2SH pWT (25°C)
^{15}N (ppm)
^{1}H (ppm)

Appendix D

Assignment Notes

Assignment Notes: 1. Crowded region (top of spectrum), 2. Crowded region (center of spectrum), 3. Crowded region (bottom of spectrum), 4. Minor overlap, 5. Major overlap, 6. Weak peak, 7. Ambiguous assignment, 8. More resolved following mutation, 9. More intense following mutation, 10. Less overlap following mutation, 11. Well resolved, 12. Well resolved (ambiguous assignment), "-" lost assignment.

Res #	RA pWT	RA A4V	RA H46R	RA G85R	RA G93A	RA E100G	RA V148I	E,Zn2SH pWT
1								
2								
3								3,4,6
4	11	5	11	11	11	11	11	3
5	11	4	11	11	11	11	11	11
6	11	5	11	11	11			3,4
7	11	11	11	11	11	11	11	
8		11		4				3,4
9	2,5	2,5	2,5	2,5	2,5	-	2,5	
10	11	11	11	11	11	11	11	4
11	5,6	5,6	5,6	5,6	5,6	5,6	5,6	4
12	11	11	11	11	11	11	11	11
13								
14	11	11	11	11	11	11	11	11
15	2,4,6	2,4,6	2,4,6	2,4,6	-	2,4,6	2,4,6	4
16	5	5	10	5	-	5	5	5
17					-			2
18		11						3,4
19								5
20	5	5	5	5	5	5	5	5
21		11	11	11	11			
22	11	11	11	11	11	11	11	4
23								6
24	4	4	4	4	4	4	4	2,5
25								
26								4
27								11
28								
29	4	4	4		4	4	4	4
30	11	11	11	11	11	8	11	3,5,6
31	4	5	4	11	5	5	4	3,4
32	11	11	11	11	11	11	11	

33	1,4	1,4	1,4	1,4	1,4	1,4	1,4	
34	4	4	4	4	4	4	4	11
35								3
36	11	11	11	11	-	11	11	
37	4	4	4	4	-	4	4	
38								
39	6	6	6	-	-	6	6	
40		-		4				3,4
41	11	11	11	11	6	11	11	5
42	2,5	2,5	2,5	2,5	-	2,5	2,5	
43	6,11	6,12	6,12	6,11	6,11	6,11	6,11	5
44	11	11	11	6,11	6,11	11	11	
45	6,11	9	11	-	-	6,11	6,11	
46	5,6	5,6	8	-	5,6	5,6	5,6	
47	4	4	8		4	4	4	11
48	11	11	11	11	11	11	11	11
49								
50								5
51	1	1	1	1	1	1	1	6,11
52	2,4	2,4	2,4	2,4	2,4	2,4	2,4	
53	11	4	11	4	11	11	11	
54	11	11	11	11	11	11	11	4
55								5
56	5	5	10	5		5	5	
57	6	6	6	6	6	6	6	
58	5	4	5	4	4	4	5	
59	2,6	2,6	2,6	-	2,6	2,6	2,6	
60	4	4	4	4	4	4	4	5
61								11
62								
63								
64								
65								
66								
67								
68	4	4	4	4	4	4	4	
69	2,5	2,5	2,5	2,5	-	-	2,5	2
70								4
71								5
72								
73	11	11	11	11	11	11	11	11
74								
75	4	4	4	4	4	4	4	
76	2,5	2,5	2,5	2,5	2,5	2,5	2,5	5
77	2,4	2,4	2,4	2,4	2,4	2,4	2,4	2,5

78								2
79								5
80								4
81								11
82								11
83								11
84								
85	1,4,6	1,4,6	-	1,4,6	1,4,6	1,4,6	1,4,6	
86			-					2,4
87	11	11	11	11	11	11	11	4
88	11	11	11	11	-	11	11	
89	11	11	11	11	6	11	11	4
90								3,4
91	4	4	4	4	-	4	4	2,5
92	2,4	2,4	2,4	2,4	-	2,4	2,4	2
93	1,4	1,4	1,4	1,4	-	1,4	1,4	4
94	4	4	4	4	-	4	4	2
95	11	11	11	11	-	11	11	4
96	3,5	3,5	3,5	3,5	3,5	3,5	3,5	3,4
97	3,5	3,5	3,5	3,5	3,5	3,5	3,5	3
98	11	11	5	11	11	11	11	
99	11	5	11	11	11		11	3
100	3,5,6	3,5,6	3,5,6	3,5,6	-	8	3,5,6	3,4
101	4,6	5	4,6	6	5	5	4,6	3
102								4
103	5,6	5,6	5,6	-	4,6	5,6	5,6	
104	4	4,6	4	-	4,6	-	4	4
105	6,11	11	6,11	-	6,11	6,11	6,11	
106	2,5	2,5	2,5	2,5	2,5	2,5	2,5	
107	11	11	11	11	11	11	11	
108								
109	6	6	6	6	6	6	6	
110	12	12	12	12	12	12	12	11
111								
112	11	11	11	11	11	11	11	
113	11	11	11	11	11	11	11	5
114	11	11	11	11	11	11	11	11
115	4	4	4	4	4	4	4	11
116	5,6	8,9	5,6	-	6	4,6	5,6	5
117	11	11	11	11	11	11	11	11
118	11	11	11	-	11	11	11	
119	2,5	2,5	2,5	-	2,4	-	-	
120			11					
121	5,6	4,6	5,6	4,6	4,6	5,6	5,6	
122								

123	3	3	3	3	3	3	3	4
124								11
125								4
126	4	4	4	-	-	4	4	4
127	1,4	1,4	1,4	5	1,4	1,4	1,4	11
128	2	2	2	2	2	2	2	
129	1,4	1,4	1,4	1,4	1,4	1,4	1,4	5
130	11	11	11	11	11	11	11	11
131	2	2	2	2	2	2	2	5
132	4	4	4	4	4	4	4	
133	4	4	4	4	4	4	4	4
134	5	4	5	4	4	4	5	2,5
135	11	11	11	11	11	11	11	11
136	2,5	2,5	2,5	2,5	-	-	-	11
137	11	11	11	11	11	11	11	5
138	1,4	1,4	1,4	1,4	1,4	1,4	1,4	
139	2,5,6	2,5,6	2,5,6	2,5,6	2,5,6	2,5,6	2,5,6	
140	6	6	6	6	6	6	6	11
141	4	4	4	4	4	4	4	5
142	11	11	11	11	11	11	11	
143	6	6	6	-	6	6	6	
144	3,6	-	3,6	-	3,6	3,6	3,6	3
145	6	-	6	-	-	-	6	
146	11	11	11	11	11	11	11	
147	1,4	1,4	1,4	5	1	1,4	1,4	
148							8	
149	11	11	11	11	11	11	11	
150	12	12	12	12	12	-	12	4
151	4	5	4	4	4	4	4	
152	11	11	11	11	11	11	11	11
153	11	11	11	11	11	11	11	4

[1]All data in this appendix is updated with respect to all other data and appendices in the thesis.

[2]Updated assignments with respect to earlier data: D96 (RA pWT), K30 (RA V148I), G129 (RA V148I).

Appendix E

Copyright and Permissions for Figure 1.2

Annual Reviews, Inc. - License Terms and Conditions

This is a License Agreement between Jeffrey Palumbo ("You") and Annual Reviews, Inc. ("Publisher") provided by Copyright Clearance Center ("CCC"). The license consists of your order details, the terms and conditions provided by Annual Reviews, Inc., and the CCC terms and conditions.

All payments must be made in full to CCC.

Order Date	05-May-2020	Type of Use	Republish in a thesis/dissertation
Order license ID	1032827-1		
ISSN	1545-4509	Publisher	ANNUAL REVIEWS
		Portion	Chart/graph/table/figure

LICENSED CONTENT

Publication Title	Annual review of biochemistry	Rightsholder	Annual Reviews, Inc.
		Publication Type	e-Journal
Date	01/01/1932	URL	http://arjournals.annualreviews.org/loi/biochem
Language	English		
Country	United States of America		

REQUEST DETAILS

Portion Type	Chart/graph/table/figure	Distribution	Worldwide
Number of charts / graphs / tables / figures requested	1	Translation	Original language of publication
		Copies for the disabled?	No
Format (select all that apply)	Electronic	Minor editing privileges?	Yes
Who will republish the content?	Academic institution	Incidental promotional use?	No
Duration of Use	Life of current edition	Currency	CAD
Lifetime Unit Quantity	Up to 499		
Rights Requested	Main product		

NEW WORK DETAILS

Title	Biophysical Properties of Immature Cu,Zn Superoxide Dismutase 1	Institution name	University of Waterloo
		Expected presentation date	2020-07-17
Instructor name	Prof. Elizabeth Meiering		

ADDITIONAL DETAILS

Order reference number	N/A	The requesting person / organization to appear on the license	Jeffrey Palumbo

REUSE CONTENT DETAILS

Title, description or numeric reference of the portion(s)	Figure 1	Title of the article/chapter the portion is from	Molecular Chaperone Functions in Protein Folding and Proteostasis
Editor of portion(s)	Annual Review of Biochemistry	Author of portion(s)	Yujin E. Kim, Mark S. Hipp, Andreas Bracher, Manajit Hayer-Hartl, and F. Ulrich Hartl
Volume of serial or monograph	82		
Page or page range of portion	325	Issue, if republishing an article from a serial	N/A
		Publication date of portion	2013-01-01

CCC Republication Terms and Conditions

1. Description of Service; Defined Terms. This Republication License enables the User to obtain licenses for republication of one or more copyrighted works as described in detail on the relevant Order Confirmation (the "Work(s)"). Copyright Clearance Center, Inc. ("CCC") grants licenses through the Service on behalf of the rightsholder identified on the Order Confirmation (the "Rightsholder"). "Republication", as used herein, generally means the inclusion of a Work, in whole or in part, in a new work or works, also as described on the Order Confirmation. "User", as used herein, means the person or entity making such republication.

2. The terms set forth in the relevant Order Confirmation, and any terms set by the Rightsholder with respect to a particular Work, govern the terms of use of Works in connection with the Service. By using the Service, the person transacting for a republication license on behalf of the User represents and warrants that he/she/it (a) has been duly authorized by the User to accept, and hereby does accept, all such terms and conditions on behalf of User, and (b) shall inform User of all such terms and conditions. In the event such person is a "freelancer" or other third party independent of User and CCC, such party shall be deemed jointly a "User" for purposes of these terms and conditions. In any event, User shall be deemed to have accepted and agreed to all such terms and conditions if User republishes the Work in any fashion.

3. Scope of License; Limitations and Obligations.

   3.1. All Works and all rights therein, including copyright rights, remain the sole and exclusive property of the Rightsholder. The license created by the exchange of an Order Confirmation (and/or any invoice) and payment by User of the full amount set forth on that document includes only those rights expressly set forth in the Order Confirmation and in these terms and conditions, and conveys no other rights in the Work(s) to User. All rights not expressly granted are hereby reserved.

   3.2. General Payment Terms: You may pay by credit card or through an account with us payable at the end of the month. If you and we agree that you may establish a standing account with CCC, then the following terms apply: Remit Payment to: Copyright Clearance Center, 29118 Network Place, Chicago, IL 60673-1291. Payments Due: Invoices are payable upon their delivery to you (or upon our notice to you that they are available to you for downloading). After 30 days, outstanding amounts will be subject to a service charge of 1-1/2% per month or, if less, the maximum rate allowed by applicable law. Unless otherwise specifically set forth in the Order Confirmation or in a separate written agreement signed by CCC, invoices are due and payable on "net 30" terms. While User may exercise the rights licensed immediately upon issuance of the Order Confirmation, the license is automatically revoked and is null and void, as if it had never been issued, if complete payment for the license is not received on a timely basis either from User directly or through a payment agent, such as a credit card company.

   3.3. Unless otherwise provided in the Order Confirmation, any grant of rights to User (i) is "one-time" (including the editions and product family specified in the license), (ii) is non-exclusive and non-transferable and (iii) is subject to any and all limitations and restrictions (such as, but not limited to, limitations on duration of

use or circulation) included in the Order Confirmation or invoice and/or in these terms and conditions. Upon completion of the licensed use, User shall either secure a new permission for further use of the Work(s) or immediately cease any new use of the Work(s) and shall render inaccessible (such as by deleting or by removing or severing links or other locators) any further copies of the Work (except for copies printed on paper in accordance with this license and still in User's stock at the end of such period).

3.4. In the event that the material for which a republication license is sought includes third party materials (such as photographs, illustrations, graphs, inserts and similar materials) which are identified in such material as having been used by permission, User is responsible for identifying, and seeking separate licenses (under this Service or otherwise) for, any of such third party materials; without a separate license, such third party materials may not be used.

3.5. Use of proper copyright notice for a Work is required as a condition of any license granted under the Service. Unless otherwise provided in the Order Confirmation, a proper copyright notice will read substantially as follows: "Republished with permission of [Rightsholder's name], from [Work's title, author, volume, edition number and year of copyright]; permission conveyed through Copyright Clearance Center, Inc. " Such notice must be provided in a reasonably legible font size and must be placed either immediately adjacent to the Work as used (for example, as part of a by-line or footnote but not as a separate electronic link) or in the place where substantially all other credits or notices for the new work containing the republished Work are located. Failure to include the required notice results in loss to the Rightsholder and CCC, and the User shall be liable to pay liquidated damages for each such failure equal to twice the use fee specified in the Order Confirmation, in addition to the use fee itself and any other fees and charges specified.

3.6. User may only make alterations to the Work if and as expressly set forth in the Order Confirmation. No Work may be used in any way that is defamatory, violates the rights of third parties (including such third parties' rights of copyright, privacy, publicity, or other tangible or intangible property), or is otherwise illegal, sexually explicit or obscene. In addition, User may not conjoin a Work with any other material that may result in damage to the reputation of the Rightsholder. User agrees to inform CCC if it becomes aware of any infringement of any rights in a Work and to cooperate with any reasonable request of CCC or the Rightsholder in connection therewith.

4. Indemnity. User hereby indemnifies and agrees to defend the Rightsholder and CCC, and their respective employees and directors, against all claims, liability, damages, costs and expenses, including legal fees and expenses, arising out of any use of a Work beyond the scope of the rights granted herein, or any use of a Work which has been altered in any unauthorized way by User, including claims of defamation or infringement of rights of copyright, publicity, privacy or other tangible or intangible property.

5. Limitation of Liability. UNDER NO CIRCUMSTANCES WILL CCC OR THE RIGHTSHOLDER BE LIABLE FOR ANY DIRECT, INDIRECT, CONSEQUENTIAL OR INCIDENTAL DAMAGES (INCLUDING WITHOUT LIMITATION DAMAGES FOR LOSS OF BUSINESS PROFITS OR INFORMATION, OR FOR BUSINESS INTERRUPTION) ARISING OUT OF THE USE OR INABILITY TO USE A WORK, EVEN IF ONE OF THEM HAS BEEN ADVISED OF THE POSSIBILITY OF SUCH DAMAGES. In any event, the total liability of the Rightsholder and CCC (including their respective employees and directors) shall not exceed the total amount actually paid by User for this license. User assumes full liability for the actions and omissions of its principals, employees, agents, affiliates, successors and assigns.

6. Limited Warranties. THE WORK(S) AND RIGHT(S) ARE PROVIDED "AS IS". CCC HAS THE RIGHT TO GRANT TO USER THE RIGHTS GRANTED IN THE ORDER CONFIRMATION DOCUMENT. CCC AND THE RIGHTSHOLDER DISCLAIM ALL OTHER WARRANTIES RELATING TO THE WORK(S) AND RIGHT(S), EITHER EXPRESS OR IMPLIED, INCLUDING WITHOUT LIMITATION IMPLIED WARRANTIES OF MERCHANTABILITY OR FITNESS FOR A PARTICULAR PURPOSE. ADDITIONAL RIGHTS MAY BE REQUIRED TO USE ILLUSTRATIONS, GRAPHS, PHOTOGRAPHS, ABSTRACTS, INSERTS OR OTHER PORTIONS OF THE WORK (AS OPPOSED TO THE ENTIRE WORK) IN A MANNER CONTEMPLATED BY USER; USER UNDERSTANDS AND AGREES THAT NEITHER CCC NOR THE RIGHTSHOLDER MAY HAVE SUCH ADDITIONAL RIGHTS TO GRANT.

Effect of Breach. Any failure by User to pay any amount when due, or any use by User of a Work beyond the scope of the license set forth in the Order Confirmation and/or these terms and conditions, shall be a material breach of the license created by the Order Confirmation and these terms and conditions. Any breach not cured within 30 days of written notice thereof shall result in immediate termination of such license without further notice. Any unauthorized (but licensable) use of a Work that is terminated immediately upon notice thereof may be liquidated by payment of the Rightsholder's ordinary license price therefor; any unauthorized (and unlicensable) use that is not terminated immediately for any reason (including, for example, because materials containing the Work cannot reasonably be recalled) will be subject to all remedies available at law or in equity, but in no event to a payment of less than three times the Rightsholder's ordinary license price for the most closely analogous licensable use plus Rightsholder's and/or CCC's costs and expenses incurred in collecting such payment.

8. Miscellaneous.

8.1. User acknowledges that CCC may, from time to time, make changes or additions to the Service or to these terms and conditions, and CCC reserves the right to send notice to the User by electronic mail or otherwise for the purposes of notifying User of such changes or additions; provided that any such changes or additions shall not apply to permissions already secured and paid for.

8.2. Use of User-related information collected through the Service is governed by CCC's privacy policy, available online here:https://marketplace.copyright.com/rs-ui-web/mp/privacy-policy

8.3. The licensing transaction described in the Order Confirmation is personal to User. Therefore, User may not assign or transfer to any other person (whether a natural person or an organization of any kind) the license created by the Order Confirmation and these terms and conditions or any rights granted hereunder; provided, however, that User may assign such license in its entirety on written notice to CCC in the event of a transfer of all or substantially all of User's rights in the new material which includes the Work(s) licensed under this Service.

8.4. No amendment or waiver of any terms is binding unless set forth in writing and signed by the parties. The Rightsholder and CCC hereby object to any terms contained in any writing prepared by the User or its principals, employees, agents or affiliates and purporting to govern or otherwise relate to the licensing transaction described in the Order Confirmation, which terms are in any way inconsistent with any terms set forth in the Order Confirmation and/or in these terms and conditions or CCC's standard operating procedures, whether such writing is prepared prior to, simultaneously with or subsequent to the Order Confirmation, and whether such writing appears on a copy of the Order Confirmation or in a separate instrument.

8.5. The licensing transaction described in the Order Confirmation document shall be governed by and construed under the law of the State of New York, USA, without regard to the principles thereof of conflicts of law. Any case, controversy, suit, action, or proceeding arising out of, in connection with, or related to such licensing transaction shall be brought, at CCC's sole discretion, in any federal or state court located in the County of New York, State of New York, USA, or in any federal or state court whose geographical jurisdiction covers the location of the Rightsholder set forth in the Order Confirmation. The parties expressly submit to the personal jurisdiction and venue of each such federal or state court.If you have any comments or questions about the Service or Copyright Clearance Center, please contact us at 978-750-8400 or send an e-mail to support@copyright.com.

1.1